UNIVERSITÀ
DEGLI STUDI
DI TRIESTE

Università degli studi di Trieste

XXXVII CICLO DEL DOTTORATO DI RICERCA IN

Ingegneria Industriale e dell'Informazione

Non-Invasive Biomarker Extraction and Predictive Modeling for Diagnosis and Prognosis in Cardiovascular and Neurovascular Diseases

Settore scientifico-disciplinare:

IBIO-01/A Bioingegneria

Dottoranda: **Katerina Iscra**

Coordinatore: **Prof. Fulvio Babich**

Supervisore di tesi: **Prof. Miloš Ajčević**

Co-supervisore di tesi: **Prof. Agostino Accardo**

Anno Accademico 2023/2024

Sommario

Introduzione. Le malattie cardiovascolari e neurovascolari rappresentano alcune delle principali cause di mortalità e disabilità a lungo termine. Per questo motivo, costituiscono un rilevante onere sia per il sistema sanitario sia per la società nel suo complesso. Nonostante i significativi progressi registrati negli ultimi anni in ambito preventivo, diagnostico e terapeutico, la diagnosi precoce e la previsione degli esiti funzionali continuano a rappresentare una sfida, in particolare nei casi clinici più complessi o quando gli strumenti diagnostici tradizionali non sono in grado di fornire risposte certe.

In ambito cardiovascolare, la cardiopatia ischemica (IHD) e la cardiomiopatia dilatativa (DCM) rappresentano due delle patologie più comuni e, al contempo, tra le più complesse dal punto di vista clinico. Una diagnosi differenziale precoce e accurata tra queste due condizioni è essenziale per ottimizzare il percorso terapeutico e migliorare la prognosi dei pazienti. Tuttavia, distinguere tra IHD e DCM può risultare particolarmente difficile in alcuni casi, specialmente quando la frazione di eiezione del ventricolo sinistro (LVEF) si trova nella cosiddetta 'grey zone' (40–50%), in cui entrambe le condizioni possono presentare caratteristiche ecocardiografiche sovrapponibili.

Parallelamente alle patologie cardiache, anche le malattie cerebrovascolari, in particolare gli ictus ischemici, continuano a rappresentare una delle principali cause di mortalità e disabilità a livello globale. Sebbene l'introduzione e la diffusione delle terapie di riperfusione abbiano significativamente migliorato gli esiti clinici, una quota rilevante di pazienti non riesce a ottenere un recupero funzionale completo, anche in presenza di una ricanalizzazione efficace. Una delle sfide più rilevanti nella gestione dell'ictus consiste proprio nella capacità di prevedere in modo accurato gli esiti funzionali a lungo termine, elemento cruciale per una pianificazione terapeutica personalizzata e per una migliore gestione del paziente.

Obiettivo. Alla luce delle condizioni fisiopatologiche e delle sfide cliniche descritte in ambito sia cardiovascolare sia neurovascolare, la presente tesi di dottorato si propone di identificare biomarcatori predittivi ottenuti attraverso l'elaborazione di bioimmagini e biosegnali acquisiti con modalità non invasive, con l'obiettivo di supportare il processo decisionale clinico e migliorare la gestione dei pazienti. A tal fine, sono state adottate tecniche di machine learning interpretabile, finalizzate allo sviluppo di modelli predittivi in grado di migliorare la diagnosi, la previsione degli esiti clinici e la caratterizzazione dei pazienti.

Metodi. Gli studi condotti si sono focalizzati sull'identificazione di parametri della variabilità della frequenza cardiaca (HRV), ottenuti mediante analisi lineare e non lineare del segnale, nonché di parametri ecocardiografici come il global longitudinal strain (GLS) e la LVEF, utili a supportare la classificazione differenziale tra DCM e IHD. Particolare attenzione è stata rivolta alla trasparenza dei modelli predittivi, con l'obiettivo di garantire la possibilità di interpretare le caratteristiche utilizzate durante il processo di sviluppo. Inoltre, è stato valutato l'impatto delle diverse fasi di preprocessing del segnale HRV sulle prestazioni diagnostiche dei parametri considerati.

Un ulteriore obiettivo degli studi è stato la valutazione di parametri estratti dall'elettroencefalogramma (EEG) in grado di supportare la stima degli esiti funzionali post-ictus, espressi tramite il punteggio della modified Rankin Scale (mRS) a tre mesi. Per migliorare la classificazione dei pazienti a rischio di attività EEG epilettiforme, è stato inoltre analizzato l'impatto di diverse strategie di bilanciamento del dataset, quali il sottocampionamento e il sovracampionamento, sulle prestazioni dei modelli predittivi. La tesi ha affrontato anche una delle sfide diagnostiche più critiche in neurologia acuta: la distinzione tra ictus ischemico e stroke mimics. A tal fine, è stata introdotta l'applicazione della tecnica di risonanza magnetica non invasiva Arterial Spin Labeling (ASL), impiegata per analizzare le variazioni temporali della perfusione cerebrale.

Pertanto, il presente progetto di dottorato ha indagato l'integrazione di biomarcatori fisiologici non invasivi, ottenuti mediante l'elaborazione di segnali e immagini, con modelli interpretabili di machine learning, al fine di affrontare alcune tra le principali sfide diagnostiche e prognostiche nelle malattie cardiovascolari e neurovascolari. Ponendo particolare attenzione alla trasparenza dei modelli, alla qualità dei dati e alla rilevanza clinica delle informazioni estratte, questo lavoro mira a contribuire allo sviluppo di strumenti decisionali pratici a supporto dei clinici, con l'obiettivo di migliorare la gestione dei pazienti sia in ambito cardiologico che neurologico.

Risultati. I risultati ottenuti dimostrano che l'integrazione dei parametri HRV con le misure di deformazione miocardica, in particolare il GLS, consente un significativo miglioramento nella diagnosi differenziale tra DCM e IHD, anche nei pazienti con frazioni di eiezione simili.

I parametri ottenuti da analisi lineari e non lineari del segnale HRV si sono rivelati utili per distinguere tra soggetti sani, pazienti affetti da DCM e pazienti con IHD. In particolare, i modelli sviluppati hanno raggiunto un'accuratezza del 70% rilevante per questa popolazione clinica. Inoltre, il GLS si è confermato un indicatore altamente sensibile della disfunzione miocardica, rafforzando la sua rilevanza clinica e sostenendone una più ampia applicazione nelle valutazioni ecocardiografiche di routine. I modelli basati su GLS rispetto al LVEF hanno infatti portato ad una migliore performance predittiva (86% vs 83%) nella diagnosi dei DCM.

Tali parametri si sono dimostrati efficaci nella discriminazione tra DCM e IHD nei soggetti con frazione di eiezione lievemente ridotta, condizione in cui la diagnosi differenziale risulta particolarmente complessa. I modelli di apprendimento automatico interpretabili sviluppati hanno consentito di identificare le interazioni complesse tra variabili demografiche, fisiologiche e cliniche, quali età, sesso, caratteristiche dell'HRV e parametri di strain miocardico, raggiungendo un'accuratezza del 76%, offrendo un supporto concreto al processo decisionale clinico particolarmente sfidante, come nei casi con LVEF compresa tra il 40% e il 50%.

Nel contesto neurovascolare, l'integrazione di caratteristiche derivate da tecniche di acquisizione non invasive, quali l'EEG e l'ASL-MRI, ha mostrato un potenziale significativo nel migliorare sia la diagnosi sia la previsione degli esiti clinici nei pazienti colpiti da ictus ischemico. In particolare, l'EEG quantitativo ha fornito informazioni neurofisiologiche oggettive che hanno arricchito le valutazioni cliniche e di imaging tradizionali, permettendo una stratificazione del rischio in tempo reale e contribuendo a orientare le decisioni terapeutiche. Il modello sviluppato sulla base dei parametri quantitativi dell'EEG ha raggiunto un'accuratezza di classificazione pari all'84%, superiore all'81% ottenuto considerando esclusivamente la presenza o l'assenza di IED. Inoltre, la tecnica ASL-MRI si è rivelata particolarmente efficace nell'identificazione di pattern di perfusione cerebrale indicativi di ictus o di stroke mimics nei casi di afasia isolata, in cui i segni neurologici possono risultare assenti o poco evidenti, rendendo essenziale una rapida definizione eziologica.

Conclusioni. In conclusione, l'analisi quantitativa dei segnali fisiologici HRV e EEG, ottenuti mediante strumenti non invasivi, ampiamente disponibili ma spesso sottoutilizzati nella pratica clinica, combinata con tecniche di imaging avanzate e con l'impiego di modelli interpretabili di machine learning, ha dimostrato un rilevante potenziale nel migliorare la diagnosi, la caratterizzazione e la prognosi delle patologie cardiovascolari e neurovascolari. Questo approccio integrato può rappresentare un progresso significativo verso un'assistenza clinica più precisa, personalizzata ed efficace.

Abstract

Introduction. Cardiovascular and neurovascular diseases are among the leading causes of morbidity, mortality, and long-term disability worldwide, posing a major burden on healthcare systems and societies. Despite remarkable advancements in prevention, diagnostics, and acute care, early diagnosis and personalized outcome prediction remain challenging, particularly in complex cases or when traditional diagnostic tools fall short.

In the cardiovascular domain, ischemic heart disease (IHD) and dilated cardiomyopathy (DCM) represent two of the most prevalent and clinically challenging conditions. Early and accurate differential diagnosis between these two conditions is critical for effective therapeutic decision-making and prognosis improvement. However, this remains difficult in many cases, especially when left ventricular ejection fraction (LVEF) lies within the so-called "grey zone" (40–50%), in which both DCM and IHD can present overlapping echocardiographic profiles.

Parallel to cardiac disorders, cerebrovascular diseases, particularly ischemic strokes, continue to rank among the top causes of death and disability globally. Despite the implementation of reperfusion therapies that have improved outcomes, a substantial number of patients fail to fully recover, even after successful recanalization. One of the major challenges in stroke management lies in accurately predicting long-term functional outcomes.

Objective. Considering the pathophysiological insights and clinical challenges in both the cardiovascular and neurovascular domains, this PhD thesis aimed to identify predictive biomarkers derived from image and signal processing of non-invasively acquired biosignals and bioimages, to support clinicians in improving patient management. Furthermore, interpretable machine learning (ML) techniques were employed to develop predictive models for enhanced diagnosis, outcome prediction, and patient characterization.

Methods. The conducted studies aimed to identify heart rate variability (HRV) features, estimated through linear and non-linear HRV signal analysis, as well as echocardiographic imaging parameters, such as global longitudinal strain (GLS) and LVEF, that support the classification of IHD and DCM, and to assess the influence of HRV preprocessing on diagnostic performance, focusing on feature explainability and model transparency.

Moreover, the studies aimed to asses EEG extracted parameters that can support the estimation of post-stroke functional outcomes, measured by modified Ranking Scale (mRS) scores at three months. To further enhance the classification of patients at risk of epileptiform EEG activity, we investigated the impact of dataset balancing strategies, such as under-sampling and over-sampling, on model performance. This thesis also addressed a critical diagnostic challenge in acute neurology, which is distinguishing true ischemic strokes from stroke mimics in acute setting by introducing the implementation of non-invasive Arterial Spin Labeling (ASL) MRI to investigate perfusion changes over time.

Thus, this doctoral project explored the integration of non-invasive physiological biomarkers extracted by signal and image processing, and interpretable machine learning models to address some of key diagnostic and prognostic challenges in cardiovascular and neurovascular diseases. By prioritizing transparency, data quality, and clinical relevance, this work contributes to the development of practical decision-support tools to enhance patient care in both cardiology and neurology.

Results. The findings demonstrate that the integration of HRV features with myocardial deformation measures, particularly GLS, significantly improves the differential diagnosis between DCM and IHD, even in patients with comparable ejection fraction values.

Both linear and nonlinear analyses of HRV signals proved to be valuable in distinguishing among healthy subjects, DCM patients, and those with IHD. Specifically, the developed models achieved an accuracy of 70%, which is notable for this clinical population.

Furthermore, GLS emerged as a highly sensitive indicator of myocardial dysfunction, reinforcing its clinical relevance and supporting its broader implementation in routine echocardiographic assessments. Models based on GLS, compared to those based on LVEF, yielded superior predictive performance (86% vs. 83%) in the diagnosis of DCM.

These parameters also proved effective in discriminating between DCM and IHD in subjects with mildly reduced ejection fraction, a condition in which differential diagnosis is particularly challenging. The developed interpretable machine learning models allowed for the identification of complex interactions among demographic, physiological, and clinical variables, such as age, sex, HRV characteristics, and myocardial strain parameters, achieving an accuracy of 76%. This provides concrete support to the clinical decision-making process, particularly in challenging cases, such as those with LVEF between 40% and 50%.

In the neurovascular domain, the introduction of non-invasive EEG and ASL-MRI derived features can improve both diagnosis and outcome prediction in patients with ischemic stroke. Quantitative EEG, in particular, provided objective, neurophysiological insights that complemented traditional clinical and imaging assessments, enabling real-time, bedside risk stratification and guiding treatment decisions. The developed model based on quantitative EEG parameters achieved a classification accuracy of 84%, outperforming the 81% obtained when considering only the presence or absence of IEDs. Furthermore, ASL-MRI proved especially valuable in detecting perfusion patterns indicative of stroke or stroke mimics in cases of isolated aphasia, where overt neurological signs may be absent and timely etiological clarification is critical.

Conclusion. In conclusion, the quantitative analysis of physiological signals such as HRV and EEG, obtained through non-invasive and widely available tools but often underused in clinical practice, combined with advanced imaging techniques and interpretable machine learning models, has shown strong potential to improve the diagnosis, characterization, and prognosis of cardiovascular and neurovascular diseases. This integrated approach may represent a significant step toward more precise, personalized, and effective patient care.

CONTENTS

List of Figures

List of Tables

List of Abbreviations

A-mode Amplitude Mode

A2C Apical Two-Chamber

A3C Apical Three-Chamber

A4C Apical Four-Chamber

AHA/ASA American Heart Association/American Stroke Association

AIF Arterial Input Function

ANN Artificial Neural Network

ANS Autonomic Nervous System

ASL Arterial Spin Labeling

ASPECT score Alberta Stroke Program Early CT Score

ATA Arterial Transit Artifact

ATT Arterial Transit Time

AUC Area Under the ROC Curve

betaExp Beta Exponent

CA Classification Accuracy

CAD Coronary Artery Disease

cASL continuous ASL

CBF Cerebral Blood Flow

CBV Cerebral Blood Volume

CFR Coronary Flow Reserve

CI Confidence Intervals

CMP Cardiomyopathy

CSF Cerebrospinal Fluid

CT Computed Tomography

CTA Computed Tomography Angiography

CTP CT Perfusion

DAR Delta/Alpha Ratio

DCM Dilated Cardiomyopathy

DSC Dynamic Susceptibility Contrast

DTABR (Delta + Theta)/(Alpha + Beta) Ratio

DWI-MRI Diffusion-weighted MRI

ECG Electrocardiogram

EEG Electroencephalography

EDV End-Diastolic Volume

ENN Edited Nearest Neighbours

ESO European Stroke Organisation

ESV End-Systolic Volume

EVT Endovascular Thrombectomy

FD Fractal Dimension

FN False Negatives

FP False Positives

FPR False Positive Rate

GLS Global Longitudinal Strain

GM Gray Matter

GR Information Gain Ratio

HC Healthy Controls

HF High-Frequency

HFn High Frequency normalized

HR Heart Rate

HRV Heart Rate Variability

IEDs Interictal Epileptiform Discharges

IG Information Gain

IHD Ischemic Heart Disease

IRF Impulse Residue Function

LACS Lacunar Syndromes

LF Low-Frequency

LF/HF Ratio between the LF and the HF

LFn Low Frequency normalized

LOF Local Outlier Factor

LVEF Left Ventricular Ejection Fraction

LV Left Ventricular

LVO Large Vessel Occlusion

M-mode Motion Mode

MC Motion Correction

MeanRR Mean RR intervals

ML Machine Learning

MNI Montreal Neurological Institute

MRI Magnetic Resonance Imaging

mRS modified Rankin Scale

MSE Mean Squared Error

MT Mechanical Thrombectomy

mTICI modified Thrombolysis in Cerebral Infarction

MTT Mean Transit Time

NCCT Non-Contrast Computed Tomography

NIHSS National Institutes of Health Stroke Scale

NN Normal-to-Normal

NN50 Number of pairs of successive NNs that differ by more than 50 ms

NSTE-ACS Non-ST Elevation Acute Coronary Syndrome

NYHA New York Heart Association

OR Odds Ratios

pASL pulsed ASL

PACS Partial Anterior Circulation Syndrome

pcASL pseudo-continuous ASL

PET Positron Emission Tomography

PLD Post-Labeling Delay

PNS Parasympathetic Nervous System

POCS Posterior Circulation Syndrome

PR Precision

PSD Power Spectral Density

PTP Pre-Test Probability

PVC Partial Volume Correction

qEEG quantitative EEG

RBF Radial Basis Function

ReLU Rectified Linear Unit

RF Radiofrequency

RMSSD Root mean square of RR intervals successive differences

ROC Receiver Operating Characteristic

ROI Regions of Interest

RSA Respiratory Sinus Arrhythmia

SAH Subarachnoid Hemorrhage

SDNN Standard Deviation of Normal-to-Normal RR intervals

SDs Standard Deviations

sICH Symptomatic intracranial hemorrhage

SMOTENC Synthetic Minority Over-sampling Technique for Nominal and Continuous

SNR Signal-To-Noise Ratio

SNS Sympathetic Nervous System

SP Specificity

SPECT Single Photon Emission Computed Tomography

STE Speckle Tracking Echocardiography

SVM Support Vector Machine

TACS Total Anterior Circulation Syndrome

TDC Time-Density Curve

TI Inversion Time

TIA Transient Ischemic Attack

TN True Negatives

TP True Positives

TPR True Positive Rate

TOAST Trial of Org 10172 in Acute Stroke Treatment

TTP Time to Peak

TR Repetition Time

VOF Venous Output Function

WHO World Health Organization

WM White Matter

INTRODUCTION

Cardiovascular and neurovascular diseases are among the leading causes of morbidity, mortality, and long-term disability worldwide [1,2], posing a major burden on healthcare systems and societies. Despite remarkable advancements in prevention, diagnostics, and acute care, early diagnosis and personalized outcome prediction remain challenging, particularly in complex cases or when traditional diagnostic tools fall short.

In the cardiovascular domain, ischemic heart disease (IHD) and dilated cardiomyopathy (DCM) represent two of the most prevalent and clinically challenging conditions. IHD, typically caused by an imbalance between myocardial oxygen supply and demand due to atherosclerotic coronary artery disease, often progresses silently before culminating in acute events such as myocardial infarction or sudden cardiac death. In contrast, DCM is a non-ischemic condition characterized by ventricular dilation and systolic dysfunction without coronary artery involvement.

Early and accurate differential diagnosis between these two conditions is critical for effective therapeutic decision-making and prognosis improvement. However, this remains difficult in many cases, especially when left ventricular ejection fraction (LVEF) lies within the so-called "grey zone" (40–50%), in which both DCM and IHD can present overlapping echocardiographic profiles [3]. Furthermore, current gold-standard diagnostic procedures, such as coronary angiography and cardiac MRI, are often invasive, costly, or not readily available in all clinical settings.

In this context, there is an urgent need to identify non-invasive, widely accessible biomarkers and develop automated diagnostic tools to support clinicians in the early differential diagnosis of IHD and DCM. Among the most promising parameters are global longitudinal strain (GLS), a measure of myocardial deformation derived from speckle-tracking echocardiography [4], and heart rate variability (HRV), which reflects autonomic nervous system modulation of cardiac rhythm [5]. Both have shown significant potential in identifying subclinical myocardial dysfunction and in stratifying risk among patients with cardiac pathologies [6–8].

HRV, in particular, has attracted growing research interest due to its sensitivity to the autonomic imbalances observed in both IHD and DCM. However, the interpretation of HRV remains complex and controversial, with ongoing debates regarding signal preprocessing steps, such as the treatment of ectopic beats, and their impact on diagnostic model performance [9,10]. Likewise, GLS has been demonstrated to outperform LVEF in detecting early systolic dysfunction, but its clinical integration remains hindered by variability in acquisition protocols and a lack of consensus on optimal thresholds.

Parallel to cardiac disorders, cerebrovascular diseases, particularly ischemic strokes, continue to rank among the top causes of death and disability globally. Approximately 17 million stroke cases are reported annually, with ischemic stroke accounting for roughly 85%

of all cases [11,12]. Despite the implementation of reperfusion therapies that have improved outcomes [13], a substantial number of patients fail to fully recover, even after successful recanalization.

One of the major challenges in stroke management lies in accurately predicting long-term functional outcomes. The variability in clinical presentations and recovery trajectories necessitates the exploration of biomarkers capable of capturing early brain function disturbances. Electroencephalography (EEG), through both qualitative and quantitative analysis, provides real-time insights into cortical function, offering a non-invasive and bedside-friendly tool for continuous monitoring [11,14].

Acute ischemic stroke leads to perfusion deficits that alter neuroelectrical activity, a phenomenon referred to as neurovascular coupling [15]. Quantitative EEG (qEEG) metrics, such as delta/alpha ratio (DAR) and DTABR, have shown strong correlations with CT perfusion measures and clinical outcomes, making them potential tools for guiding post-recanalization care [16–18]. Moreover, EEG changes, including widespread slowing, increased delta power, and decreased alpha power, have been shown to correlate with ischemic severity and predict functional outcomes measured by the modified Rankin Scale (mRS) and NIHSS [16–19].

In addition to slowing abnormalities, epileptiform EEG patterns, such as interictal epileptiform discharges (IEDs), are increasingly considered in acute stroke patients, even in the absence of clinical seizures or a prior epilepsy diagnosis [20,21]. Their presence has been linked to higher seizure risk and poorer outcomes, though their predictive value remains underexplored in early-phase stroke [21].

Considering the pathophysiological insights and clinical challenges in both the cardiovascular and neurovascular domains, this PhD thesis aimed to identify predictive biomarkers derived from image and signal processing of non-invasively acquired biosignals and bioimages, to support clinicians in improving patient management. Furthermore, interpretable machine learning (ML) techniques were employed to develop predictive models for enhanced diagnosis, outcome prediction, and patient characterization.

In particular, the conducted studies aimed to identify HRV features, estimated through linear and non-linear HRV signal analysis, as well as echocardiographic imaging parameters, such as GLS and LVEF, that support the classification of IHD and DCM, and to assess the influence of HRV preprocessing on diagnostic performance, focusing on feature explainability and model transparency.

Moreover, the studies aimed to assess EEG extracted parameters that can support the estimation of post-stroke functional outcomes, measured by mRS scores at three months. This included the analysis of quantitative EEG features estimated through spectral analysis in patients who underwent endovascular treatment, as well as the potential role of epileptiform features in patients who received riperfusion therapy. To further enhance the classification of patients at risk of epileptiform EEG activity, we investigated the impact of dataset balancing strategies, such as under-sampling and over-sampling, on model performance. This is particularly relevant given the typically imbalanced nature of clinical datasets, which tend to bias models toward majority classes [22].

This thesis also addressed a critical diagnostic challenge in acute neurology: distinguishing true ischemic strokes from stroke mimics in patients presenting with isolated aphasia, a symptom often caused by either ischemia or seizures [23]. While CT perfusion imaging supports early diagnosis, it cannot be performed repeatedly. Therefore, non-invasive perfusion imaging is desirable to assess potential perfusion pattern evolution following a suspected ischemic event. In this context, this thesis propose the implementation of non-invasive Arterial Spin Labeling (ASL) MRI to investigate perfusion changes over time in patients with isolated aphasia caused by either ischemia or seizure-related stroke mimics, with the aim of identifying imaging biomarkers that could support timely and accurate differential diagnosis in acute stroke care.

In conclusion, this doctoral project explored the integration of non-invasive physiological biomarkers extracted by signal and image processing, and interpretable machine learning models to address some of key diagnostic and prognostic challenges in cardiovascular and neurovascular diseases. By prioritizing transparency, data quality, and clinical relevance, this work contributes to the development of practical decision-support tools to enhance patient care in both cardiology and neurology.

This thesis is structured into five chapters. The first chapter provides a comprehensive overview of cardiovascular and neurovascular diseases, addressing their associated clinical pathways and the challenges encountered in diagnosis and prognosis. Furthermore, it presents the current state of the art regarding the instrumental techniques employed, the parameters extracted during the study, and the interpretable machine learning methodologies applied. The second chapter details the acquisition and analysis techniques utilized throughout the research activities conducted in this doctoral project. Chapter three reports the studies and results related to the identification of HRV features, alongside echocardiographic parameters such as GLS and LVEF, which support the differential diagnosis of IHD and DCM. Chapter four focuses on investigations aimed at enhancing the diagnosis and prognosis of stroke patients through the analysis of EEG signals and perfusion imaging derived from ASL-MRI. Finally, chapter five summarizes the main conclusions drawn from this research.

Chapter 1. CARDIOVASCULAR AND NEUROVASCULAR CONDITIONS: DIAGNOSTIC AND PROGNOSTIC CHALLENGES

Cardiovascular and neurovascular diseases are among the leading causes of death and long-term disability worldwide [1,2]. Although they primarily affect different organs, the heart and the brain, respectively, they share numerous risk factors (including hypertension, diabetes, smoking, and dyslipidemia) as well as common pathophysiological mechanisms, such as atherosclerosis, systemic inflammation, and endothelial dysfunction. Moreover, these conditions often coexist in the same patient, complicating both the clinical presentation and therapeutic management.

This chapter focuses on the main diseases investigated in this work: two cardiovascular conditions, dilated cardiomyopathy (DCM) and ischemic heart disease (IHD), and a neurovascular condition, stroke, in both its ischemic and hemorrhagic forms. Moreover, it summarizes the current state of the art regarding the instrumental techniques, the parameters extracted during the study, and the interpretable machine learning methodologies applied.

1.1 DILATED CARDIOMYOPATHY

Dilated cardiomyopathy (DCM) is a non-ischemic, non-valvular cardiac condition characterized by significant left ventricular or biventricular systolic dysfunction at the time of the diagnosis despite asymptomatic or scarcely symptomatic patients [24] reflecting a long period of asymptomatic silent disease progression [25]. It is one of the leading causes of heart failure, sudden cardiac arrest, and heart transplantation worldwide.

1.1.1 Epidemiology

Over the past four decades, the prognosis for patients with DCM has significantly improved. In 1980, when DCM was considered a terminal illness, the two-year mortality rate was approximately 50%. Today, the estimated 10-year survival rate without the need for heart transplantation has increased to around 85% [26]. Despite these advances, DCM remains the third most common cause of sudden cardiac arrest, with an estimated prevalence

of approximately 1 in 2,500 individuals [27,28], and it is the leading indication for heart transplantation.

Symptoms typically manifest between the ages of 20 and 60; however, the disease can also affect both pediatric and elderly populations [27,28]. In many cases, particularly those of genetic or idiopathic origin, patients may remain asymptomatic for extended periods, despite the presence of measurable pathological changes. In hereditary forms of DCM, ventricular dilation, reduced left ventricular ejection fraction (LVEF), and myocardial fibrosis may already be detectable in the early stages of the disease, even in the absence of evident clinical symptoms [27,29].

1.1.2 Pathophysiology

DCM can result from various etiological factors. In some cases, myocardial damage arises from nutritional deficiencies, endocrine disorders, or infectious agents, such as in Chagas cardiomyopathy. In many cases, however, no clear cause can be identified, and the condition is classified as idiopathic dilated cardiomyopathy. This form is generally attributed to an intrinsic dysfunction of the cardiac muscle, often of genetic origin.

DCM is characterized by left ventricular dilation, which may subsequently impair ventricular function. This structural remodeling is due to alterations in the structure and composition of cardiomyocytes. These changes, whether hereditary or acquired, lead to myocardial remodeling marked by the interspersion of necrotic cells, fibroblasts, and calcifications within the myocardium (Figure 1.1) [29]. This altered architecture results in elevated diastolic pressure and progressive ventricular dilation, ultimately leading to reduced LVEF [27,30].

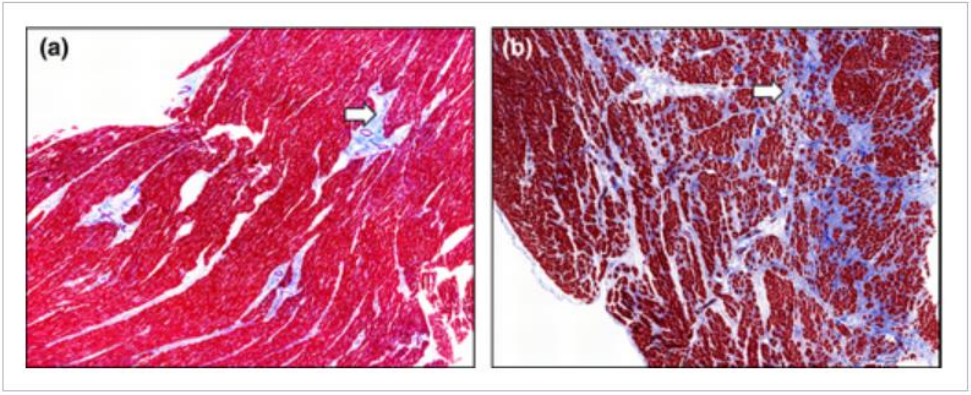

***Figure 1.1**. (a) healthy myocardial tissue; (b) myocardial tissue affected by DCM, obtained post-cardiac arrest. The fibrotic content is estimated at approximately 3% in non-diseased tissue and 30% in DCM-affected tissue [8].*

The clinical presentation of DCM varies widely. Patients may remain asymptomatic for long periods, particularly in hereditary forms, or present with symptoms typical of heart failure, such as dyspnea, orthopnea, palpitations, and non-specific precordial pain. In advanced stages, peripheral edema and hepatomegaly may also occur.

From a morphological perspective, left ventricular dilation is typically observed, followed by global chamber dilation in the later stages of the disease. The lateral ventricular

walls may thicken, and longitudinal, radial, and circumferential contractility are often reduced [31,32].

1.1.3 Diagnosis

Due to the etiological heterogeneity of DCM, diagnostic approaches must be tailored to each patient. In cases of suspected DCM, such as those involving cardiac arrest, family history, or abnormal findings during physical examination, a comprehensive evaluation typically includes an electrocardiogram (ECG) and transthoracic echocardiogram.

Echocardiography primarily provides prognostic insights and can reveal additional cardiac abnormalities, such as valvular disease. However, the most comprehensive assessment of cardiac anatomy and function is performed via cardiac magnetic resonance imaging (MRI) with gadolinium contrast. MRI allows precise measurement of chamber volumes and diameters, LVEF, and myocardial tissue characterization.

In recent years, the Speckle Tracking Echocardiography (STE) technique has emerged as a valuable, non-invasive alternative to MRI. STE provides comparable information, including measurements of chamber dimensions, particularly the LVEF and myocardial deformation parameters (longitudinal, radial, and circumferential strain) [31,32].

Identifying the underlying etiology is crucial, particularly in suspected genetic cases. Therapeutic strategies, both pharmacological and non-pharmacological, should be guided by the specific DCM phenotype, with the goal of promoting left ventricular reverse remodeling even during the preclinical phase.

For this reason, family screening is essential in all cases of DCM. In familial forms, early monitoring of first-degree relatives can significantly improve prognosis and life expectancy [33,34].

1.2 Ischemic Heart Disease

Ischemic heart disease (IHD), in its chronic and stable form, is a condition affecting the coronary arteries that develops gradually and often remains asymptomatic in its early stages. IHD arises from an imbalance between myocardial oxygen supply and demand, most commonly due to atherosclerosis. As the disease progresses, it can lead to unstable angina, myocardial infarction, or, in the most severe cases, sudden cardiac death. Early diagnosis is therefore essential to improve prognostic outcomes.

1.2.1 Epidemiology

Over the past decade, mortality due to IHD has decreased by 30% to 60% in high-income countries [35]. Despite this progress, IHD remains a major health burden, causing over 1.7 million deaths annually in Europe [35]. In the United States, it is estimated to be responsible for approximately 30% of all deaths among individuals aged 35 and older [36]. The incidence of coronary events increases significantly with age, and women typically experience rates similar to those of men who are ten years younger [37]. Additionally, the

incidence of IHD among individuals aged 65 to 95 is approximately three times higher for men and twice as high for women compared to those aged 35 to 64 [37].

1.2.2 Pathophysiology

IHD is primarily caused by atherosclerosis, a chronic inflammatory disease that leads to stenosis of the epicardial coronary arteries. Myocardial ischemia may result from two main mechanisms [38]:

- An increased oxygen demand that cannot be met due to stenotic lesions.
- Rupture of an atherosclerotic lipid plaque, potentially triggering thrombus formation and partial or complete vessel occlusion.

The severity of the clinical syndrome depends on the nature and combination of these mechanisms. Typically, the first scenario results in stable angina, while the second, more critical, often leads to myocardial infarction (Figure 1.2).

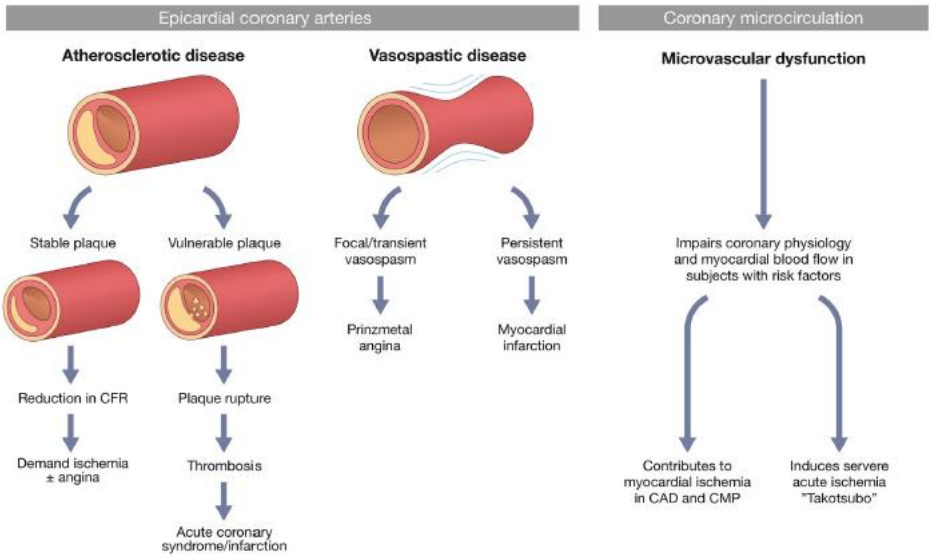

Figure 1.2. *Mechanisms of pathogenesis of IHD. On the left, coronary artery impairment due to atherosclerosis. In the center, impairment due to vascular spasm. On the right, impairment due to microvascular dysfunction [12].*

Other non-atherosclerotic causes of IHD include coronary vasospasm, microvascular dysfunction, coronary embolism, hypertension, reduced oxygen availability, or abnormal increases in myocardial oxygen demand [38].

In the context of chronic IHD, six distinct clinical scenarios can be identified based on symptomatology [38]:

- Stable angina and dyspnea.
- Patients with a history of cardiac arrest or evidence of left ventricular dysfunction.
- Asymptomatic or stable symptomatic individuals within one year following an acute IHD event.
- Asymptomatic or symptomatic patients who have undergone revascularization more than one year after the initial diagnosis.

- Patients with angina in whom coronary vasospasm or microvascular disease is suspected.
- Asymptomatic individuals diagnosed with IHD through screening procedures.

1.2.3 Diagnosis

The diagnosis of chronic IHD typically involves non-invasive functional or anatomical approaches selected based on the patient's individual characteristics. The goal is to assess the risk of obstructive IHD and to evaluate the potential need for revascularization.

The diagnostic pathway follows a structured approach. Initially, a thorough symptom assessment is performed to exclude the possibility of an acute IHD event. Subsequently, resting ECG and transthoracic echocardiography are conducted, along with the evaluation and exclusion of other cardiac conditions that may present with similar symptoms. In particular, resting ECG can reveal abnormalities in the electrical activity of the heart, such as ST segment depression, that are commonly observed in patients with chronic IHD. Laboratory tests, including hemoglobin levels, creatinine, lipid profile, HbA1c, and thyroid function, are also analyzed. These parameters help clarify the underlying cause of symptoms, influence the likelihood of chronic IHD, and assist in selecting the most appropriate imaging modality or treatment strategy.

Echocardiography plays a key role in the assessment of ventricular function, particularly by measuring LVEF and detecting myocardial wall motion abnormalities, which are often impaired in the presence of IHD. It can also help identify alternative diagnoses, such as valvular heart disease or hypertrophic obstructive cardiomyopathy, thereby excluding IHD as the primary cause of symptoms.

Once preliminary evaluations are complete, the clinical probability of chronic IHD is estimated. A pre-test probability (PTP) is calculated based on the patient's age, sex, and symptom characteristics. Depending on the PTP value, an appropriate diagnostic test is selected. For patients with a PTP >15%, non-invasive imaging is recommended. The choice of imaging modality depends in part on local availability. According to current guidelines [39], computed tomography angiography (CTA) is the preferred option due to its widespread use and high negative predictive value. In cases where the clinical probability is high, or CTA results are inconclusive, invasive coronary angiography is indicated to provide a definitive diagnosis.

In conclusion, early diagnosis of coronary artery disease is essential to improving clinical outcomes, although it is often challenging. Clinical assessment is primarily based on patient-reported symptoms as well as pathological findings on ECG and echocardiography. However, in many cases, only invasive coronary angiography, which involves the use of potentially nephrotoxic contrast agents, can provide a definitive diagnosis.

1.3 CEREBRAL STROKE

Stroke is one of the most significant neurological emergencies worldwide, currently ranking as the second leading cause of death globally [2]. According to the World Health Organization (WHO), stroke is characterized by the sudden onset of focal neurological

symptoms that persist for more than 24 hours or result in death within a shorter time frame, with no identifiable cause other than a vascular origin [40].

In parallel, a transient ischemic attack (TIA) is a brief episode of focal neurological dysfunction, typically lasting less than 24 hours, caused by a temporary reduction in blood flow to a specific region of the brain or retina. The symptoms, although reversible, are suggestive of an underlying vascular origin and are confined to the territory of a single artery [41,42]. Despite its transient nature, TIA is widely recognized as a strong predictor of stroke, particularly within the first 48 hours after the event. The ABCD2 score is a clinical tool used to estimate the short-term risk of stroke following a TIA.

In 2009, the definition of stroke was revised by a committee of the American Heart Association/American Stroke Association (AHA/ASA), adopting a tissue-based approach. According to this updated definition, TIA is described as "an episode of neurological dysfunction caused by focal cerebral, spinal cord, or retinal ischemia, without evidence of acute infarction" [43]. This paradigm shift was later extended to the definition of stroke itself, which now includes silent infarcts and cerebral, spinal, or retinal hemorrhages, emphasizing an instrumental diagnostic basis (e.g., imaging) over a purely time-based criterion.

1.3.1 Epidemiology

Stroke is the second leading cause of death worldwide and the third leading cause when considering both death and disability. According to 2019 data, there were 12.2 million new cases and 101 million existing cases. Of these, 62.4% were ischemic strokes, 27.9% intracerebral hemorrhages, and 9.7% subarachnoid hemorrhages [2].

Although ischemic strokes are the most frequent, hemorrhagic strokes are more likely to result in fatal outcomes and greater disability-adjusted life years lost [44].

The INTERSTROKE study, conducted across 22 countries, identified 10 modifiable risk factors that account for nearly 90% of all strokes: hypertension (≥160/90 mmHg), smoking, high waist-to-hip ratio, poor diet, physical inactivity, diabetes mellitus, alcohol consumption, psychosocial stress and depression, cardiac disease, and a high apolipoprotein B/A1 ratio [45]. Therefore, maintaining a healthy lifestyle is a critical strategy for stroke prevention.

Finally, 10–15% of strokes occur in young adults (aged 25–50 years), often with underlying comorbidities. In this population, both primary (e.g., management of hypertension, smoking, and dyslipidemia) and secondary prevention (e.g., addressing specific etiological and risk factors) are essential [46].

1.3.2 Pathophysiology

From a pathophysiological perspective, stroke can be classified into two major types: ischemic, which accounts for approximately 85% of cases, and hemorrhagic, which represents the remaining 15% [44]. This distinction is fundamental not only for understanding the underlying mechanisms but also for guiding diagnosis, treatment, and prognosis.

Ischemic Stroke

Ischemic stroke occurs when blood flow to a part of the brain is blocked due to the occlusion of a cerebral artery. This interruption prevents oxygen and nutrients from reaching brain tissue, resulting in neuronal necrosis. A wide range of causes can lead to ischemic stroke, and for etiopathological classification, the TOAST (Trial of Org 10172 in Acute Stroke Treatment) system is frequently used. It identifies five subtypes of ischemic stroke [19]:

- The atherothrombotic subtype is typically caused by stenosis or occlusion of large cerebral arteries and is often associated with atherosclerotic plaques, particularly at the carotid bifurcation. Plaque rupture may lead to the formation of thrombi or emboli that occlude cerebral vessels.
- The lacunar subtype results from the occlusion of small penetrating arteries, commonly due to microangiopathies such as atherosclerosis or cerebral amyloid angiopathy. These lesions are generally located in deep brain structures and can be detected through imaging techniques like MRI or computed tomography (CT) [47].
- The cardioembolic subtype occurs when emboli originating from the heart travel to the brain, obstructing a cerebral artery. Common embolic sources include cardiac chamber abnormalities, valvular disease, and arrhythmias, particularly atrial fibrillation [48]. The stroke of other determined cause subtype includes less frequent etiologies, such as non-atherosclerotic vasculopathies, coagulation disorders, or hematologic diseases, provided that large-vessel atherosclerosis and cardioembolic sources have been excluded [12].
- The cryptogenic subtype refers to cases in which, despite extensive diagnostic work-up, no clear cause can be identified. In some of these cases, an embolic mechanism is suspected but not definitively proven. The Causative Classification System encourages thorough cardiac, vascular, and brain imaging to better characterize these events [49].

A widely used clinical-radiological classification is the Oxfordshire Community Stroke Project system, also known as the Bamford classification, which categorizes ischemic strokes into four syndromes based on clinical features and the affected brain region [50,51]:

- TACS (Total Anterior Circulation Syndrome) indicates extensive involvement of the anterior cerebral territory and is associated with severe clinical presentation, high one-year mortality (60–70%), and significant long-term disability.
- PACS (Partial Anterior Circulation Syndrome) suggests partial involvement of the same territory, with milder outcomes but a higher risk of recurrence.
- LACS (Lacunar Syndromes) are associated with small, deep infarcts and show lower mortality rates (10–15%) but may result in residual disability.
- POCS (Posterior Circulation Syndrome) involves the brainstem or cerebellum and generally has a more favorable prognosis, although it is linked to the highest recurrence risk (annual mortality between 15% and 23%).

Hemorrhagic Stroke

Hemorrhagic stroke occurs when a blood vessel in the brain ruptures, leading to bleeding within the cranial cavity. Depending on the site of the hemorrhage, it is classified as either an intracerebral hemorrhage or a subarachnoid hemorrhage (SAH).

Spontaneous intracerebral hemorrhage can be further divided into two subtypes: deep and lobar. Deep hemorrhages primarily involve the basal ganglia, internal capsule, and brainstem, and are frequently associated with chronic arterial hypertension. Lobar hemorrhages, on the other hand, affect the cortical and subcortical regions of the cerebral lobes and tend to occur in the more superficial areas of the brain. Hypertension may also act as a contributing factor in these cases [44], although these are considered atypical cases, where hypertension plays a less prominent role compared to other underlying conditions such as cerebral amyloid angiopathy, tumors, and others.

SAH accounts for approximately 5% of all stroke cases and is most commonly caused by the rupture of an intracranial aneurysm. Other possible etiologies include drug abuse, coagulation disorders, arteriovenous malformations, and cerebral venous thrombosis. A positive family history may significantly increase the risk of developing SAH [44].

1.3.3 Diagnosis

The diagnosis of stroke is based on an integrated clinical and instrumental assessment. In the acute phase, the first step is a neurological evaluation, often performed using standardized scales such as the National Institutes of Health Stroke Scale (NIHSS) and the modified Rankin Scale (mRS).

The NIHSS is a clinical tool composed of 11 items, with a maximum score of 42, which should be administered within the first ten minutes after the patient's arrival in the emergency department. It allows clinicians to quantify neurological impairment, estimate prognosis, and identify patients eligible for reperfusion therapies. In general, scores below 5 are associated with a favorable prognosis, while scores above 20 indicate a high risk of death or severe disability [47].

The mRS, by contrast, is a seven-level functional scale (from 0 to 6) that assesses the degree of residual disability after a stroke. Compared to its original 1957 version, the updated scale includes grade 0 (no symptoms) and grade 6 (death), thus providing a more comprehensive picture of the patient’s functional status in both the acute and follow-up phases [52].
The scale is as follows:

- 0: No symptoms
- 1: Symptoms present but no significant disability
- 2: Mild disability; functional independence preserved
- 3: Moderate disability; requires some help but able to walk unassisted
- 4: Moderately severe disability; needs assistance with daily activities
- 5: Severe disability; completely dependent
- 6: Death

According to the 2019 AHA/ASA Guidelines, for patients with suspected ischemic stroke, a neuroimaging study is essential before initiating any therapeutic intervention. The initial test is typically a non-contrast computed tomography (NCCT) scan, which helps rule out intracranial hemorrhage. Neurologists and neuroradiologists, after evaluating the NCCT scan, assign it a score from 0 to 10 using the ASPECT score (Alberta Stroke Program Early CT Score) [53], with the aim of numerically quantifying the extent of early ischemic injury in order to assess both prognosis and eligibility for reperfusion treatment. Subsequently, CTA and CT perfusion (CTP) may be performed. These imaging modalities, as part of multimodal CT diagnostics, help to identify the site of vascular occlusion, assess collateral circulation, and evaluate cerebral perfusion parameters [54].

Diffusion-weighted magnetic resonance imaging (DWI-MRI) offers the highest sensitivity for detecting hyperacute ischemic stroke but is less commonly used in emergency settings due to logistical and time constraints. In cases of SAH, transcranial Doppler ultrasound is employed to monitor for vasospasm, a frequent and serious complication in this context [54].

Finally, in some specialized centers, such as the Stroke Unit of Cattinara Hospital in Trieste, electroencephalography (EEG) is also used as a supportive diagnostic tool. Especially in its wireless form, EEG can provide real-time insights into neurophysiological changes due to cerebral hypoperfusion, without interfering with acute treatment [14].

1.3.4 Reperfusion Treatment in Ischemic Stroke

The goal of reperfusion therapy is to restore blood flow, particularly to regions of the ischemic penumbra, areas that are damaged but not yet infarcted. The key to effective treatment is speed, in line with the concept of “time is brain.” Depending on the type of patient, the timing of the event, which vessel is affected by the occlusion, the clinical neurological assessment, and acute neuroimaging, it is possible to determine whether the patient is eligible for reperfusion treatment and which therapy would offer the greatest benefit.

Thrombolysis

Thrombolysis represents a cornerstone of reperfusion therapy in acute ischemic stroke, with Alteplase (rt-PA) being the primary pharmacologic agent employed. When administered within 4.5 hours of the patient’s last known well, Alteplase has demonstrated substantial efficacy in improving functional outcomes. However, recent guidelines have introduced Tenecteplase as a viable alternative. Tenecteplase has shown comparable efficacy, particularly in patients with large vessel occlusion, and offers practical advantages due to its single bolus administration. Its favorable pharmacokinetics, simplified delivery, and potential time and cost benefits suggest it may increasingly be considered a first-line thrombolytic agent in selected cases.

The efficacy of thrombolytic therapy is highly time-dependent. The earlier the treatment is initiated, the better the clinical outcome, both in the short and long term. Delayed administration, even within the allowable 4.5-hour therapeutic window, significantly worsens prognosis. Specifically, for every 15-minute delay in treatment initiation, the

probability of independent ambulation at discharge decreases by 4%, the chance of being discharged home (as opposed to a care facility) declines by 3%, while the risks of in-hospital mortality and hemorrhagic infarction each increase by 4% [55,56]. Moreover, a meta-analysis including 6,756 patients across nine randomized trials compared Alteplase with placebo in the setting of ischemic stroke. The primary outcome was a mRS score of 0–1 at 3 to 6 months, indicating minimal or no disability. The results confirmed that "time to treatment" is the most critical independent predictor of favorable outcomes in thrombolytic therapy [55,57]. Beyond 4.5 hours, however, the balance of benefits and harms shifts unfavorably, with the risks potentially outweighing the benefits [58].

Nevertheless, advanced neuroimaging techniques, including CTP and MRI, have allowed for the extension of the treatment window up to 9 hours after symptom onset, provided there is clear evidence of a substantial ischemic penumbra with salvageable tissue [59]. This is especially relevant for wake-up strokes, in which the exact onset of symptoms is unknown and the last known well time is considered the time of falling asleep, often excluding patients from thrombolysis under conventional criteria.

Regarding safety, the major adverse effects of thrombolytic therapy include angioedema, systemic bleeding, and intracerebral hemorrhage. While the first two are relatively rare and usually clinically insignificant [60,61], intracerebral hemorrhage is a more common and potentially severe complication. The estimated risk of symptomatic intracerebral hemorrhage (sICH) following Alteplase administration is 5–7% [57]. Clinical suspicion should be high in cases of sudden neurological deterioration, decreased consciousness, new-onset headache, nausea, vomiting, or acute hypertension, most commonly within the first 24 hours post-treatment.

Importantly, despite various risk factors (such as age, stroke severity, or hemorrhagic risk), none constitute absolute contraindications within the approved treatment window. Evidence supports that, when administered appropriately, the benefits of Alteplase outweigh the risks across a wide spectrum of patients [55].

Mechanical Thrombectomy

Mechanical thrombectomy has emerged as a pivotal intervention in the management of acute ischemic stroke due to large vessel occlusion (LVO), particularly within the anterior cerebral circulation. This endovascular procedure can be performed either as a standalone intervention or in conjunction with intravenous thrombolysis using Alteplase. Administering thrombolytics before thrombectomy may facilitate partial thrombus dissolution, especially in the case of large clots, thus simplifying the interventional radiologist's task. Moreover, thrombolysis can help dissolve distal emboli that cannot be accessed by mechanical means and may contribute to more rapid neurological recovery [62].

Thrombectomy is primarily indicated in patients with acute ischemic stroke resulting from proximal occlusion of a major artery in the anterior circulation. However, only approximately 10% of patients with ischemic stroke present with this condition within the ideal 6-hour treatment window [63], and an additional 9% present between 6 and 24 hours after symptom onset [64].

Nevertheless, strong evidence supports the efficacy, safety, and disability-reducing benefits of thrombectomy for anterior circulation LVOs treated within six hours of symptom onset [65]. Additionally, studies have shown that selected patients can still benefit from thrombectomy beyond the 6-hour window, even when infarct size is substantial [66–68]. Regardless of geographic or ethnic differences or variability in imaging techniques, thrombectomy in patients with large ischemic strokes (e.g., ASPECTS score of 3–5 or infarct core >50 mL), treated within 24 hours, has been associated with significantly improved outcomes [68].

Thrombectomy is typically performed under general anesthesia and involves femoral artery catheterization, advancing a device through the aorta and internal carotid artery to reach the site of occlusion.

- Stent Retriever Technique: A self-expanding retrievable stent is deployed at the site of the thrombus under fluoroscopic guidance. The stent remains in place for several minutes to entrap the clot within its mesh. Subsequently, the stent is withdrawn under continuous aspiration, helping remove the clot. The most commonly used devices are second-generation stent retrievers, such as the Solitaire Flow Restoration Device and the Trevo Retriever, which have demonstrated enhanced safety and efficacy [69].
- Aspiration Thrombectomy: In this method, a catheter tip is brought into direct contact with the thrombus and aspiration is applied via negative pressure to extract the clot. The process may be repeated for additional clot fragments. If aspiration alone is unsuccessful, a stent retriever can be deployed through the same catheter to complete the recanalization procedure.

Outcomes between stent retriever and aspiration techniques appear to be comparable, with similar rates of revascularization and post-procedure functional improvement [70].

1.4 HEART RATE VARIABILITY AND ECHOCARDIOGRAPHIC FEATURES IN CARDIOVASCULAR ASSESSMENT

During the course of this PhD project, the non invasive obtained parameters were considered to assess cardiac function and investigate potential diagnostic and prognostic indicators. In particular, both linear and non-linear features were derived from heart rate variability (HRV) analysis. Additionally, two key echocardiographic parameters were collected: the left ventricular ejection fraction (LVEF) and the global longitudinal strain (GLS).

HRV is a key indicator of autonomic nervous system function and reflects the balance between sympathetic and parasympathetic activity. Changes in HRV are often associated with various heart diseases, providing valuable prognostic information [71]. Moreover, HRV-based biomarkers are increasingly recognized for their potential role in risk stratification for individuals with suspected heart disease [72]. While HRV alone may not be sufficient to differentiate between specific cardiac conditions such as IHD and DCM, it can

complement other clinical and instrumental parameters, offering a more comprehensive assessment of heart function.

LVEF is one of the most widely used measures for assessing cardiac function and predicting outcomes in patients with cardiovascular conditions, particularly those with DCM [4]. It is essential for evaluating the extent of impaired systolic function, making it valuable for guiding the management of various heart diseases [73]. However, LVEF has several limitations. These include reduced sensitivity in the early stages of heart disease, a tendency to decline primarily in advanced stages, and poor reliability in patients with left ventricular hypertrophy or reduced volume. Furthermore, LVEF is prone to significant inter- and intra-observer variability and difficulties in identifying endocardial borders [4]. Therefore, there is an ongoing need for more reliable non-invasive biomarkers to support early differential diagnosis of DCM and IHD.

GLS is a myocardial deformation parameter that provides valuable insights into cardiac function. Recent studies have shown that GLS is superior to LVEF in detecting early left ventricular dysfunction and degeneration [7,74]. Unlike LVEF, which primarily reflects overall cardiac output, GLS offers a more sensitive measure of myocardial contractility and is particularly useful in the early stages of heart disease.

1.4.1 Heart rate variability

Heart rate (HR), typically expressed in beats per minute (bpm), is calculated by counting the number of R peaks within a one-minute ECG segment. The R peak, representing the ventricular depolarization phase of the cardiac cycle, is a reliable reference for HR measurement. During increased physiological demand, such as physical activity, the overall duration of the cardiac cycle shortens. Although the durations of the P wave, QRS complex, and T wave remain relatively stable, intervals between these components, particularly the R-R interval, decrease to accommodate a higher HR. These temporal fluctuations in R-R intervals are quantified as HRV, which reflects the dynamic interplay between sympathetic and parasympathetic branches of the autonomic nervous system (ANS). The sympathetic system accelerates HR and shortens inter-beat intervals to prepare the body for action, while the parasympathetic (vagal) system slows HR and prolongs intervals, promoting relaxation and recovery. While the sinoatrial and atrioventricular nodes generate the heart's intrinsic rhythm, HRV is predominantly modulated by autonomic regulation rather than intrinsic pacemaker activity.

Physiologically, HRV reflects the adaptability of the cardiovascular system to internal and external stimuli. High HRV indicates robust autonomic function and greater resilience to stress, whereas reduced HRV is associated with autonomic imbalance and increased risk of cardiovascular and chronic diseases. The beat-to-beat variability in HR is never perfectly regular, even under resting conditions, due to the influence of respiration, emotional state, physical activity, and other physiological factors. This variability imparts a complex structure to the cardiac signal, initially interpreted as stochastic in nature. However, emerging evidence suggests that HRV may exhibit deterministic chaotic behavior, meaning that while governed by specific physiological rules, it is highly sensitive to initial conditions and thus appears unpredictable.

This complexity has led to the development of complementary analytical approaches. Classical linear methods, such as time-domain and frequency-domain analyses, are effective for quantifying global trends and average fluctuations in HRV. In contrast, non-linear techniques, such as fractal dimension analysis, Poincaré plots, and the beta exponent, are designed to capture the finer structure, adaptability, and chaotic dynamics of autonomic regulation. These advanced methods provide valuable insights into ANS health and are increasingly used in both clinical and research settings to assess cardiovascular risk and regulatory function.

1.4.1.1 Linear analysis

Linear methods can be divided into two main categories: time and frequency domain methods.

Time domain analysis

Time domain HRV features assess fluctuations in the interbeat interval, which represents the duration between consecutive heartbeats [75]. These measures are obtained through statistical or geometric techniques [76]. Statistical methods, such as the calculation of standard deviation, are applied to RR intervals (RRi) to quantify variability over time intervals that may range from under a minute to up to 24 hours [75,76]. In geometric approaches, a sequence of RRi is transformed into a visual pattern and then evaluated using statistical tools [76]. The most common parameters include: Mean RR intervals (MeanRR), Standard Deviation of Normal-to-Normal RR intervals (SDNN), Root mean square of RR intervals successive differences (RMSSD), Number of pairs of successive NNs that differ by more than 50 ms (NN50), Proportion of NN50 divided by total number of NNs (pNN50).

MeanRR represents the average time (in milliseconds) between consecutive heartbeats over a given recording period. As a core time-domain HRV parameter, MeanRR reflects the inverse of average heart rate and serves as a foundational measure for understanding baseline cardiac activity [77]. It is particularly useful in combination with other HRV features, providing context for interpreting fluctuations in autonomic balance.

SDNN is one of the most recognized time domain HRV parameters, with strong clinical relevance, especially when derived from 24-hour recordings. It is considered the "gold standard" for evaluating cardiac autonomic function and stratifying patients based on cardiac risk [76]. Expressed in milliseconds, SDNN reflects the combined influence of both sympathetic nervous system (SNS) and parasympathetic nervous system (PNS) activity on heart rate dynamics. SDNN has been shown to be a powerful prognostic indicator. Research shows that SDNN values can predict both morbidity and mortality across various patient populations. In particular, 24-hour SDNN measurements offer clear thresholds for health classification: values below 50 ms indicate poor autonomic function and higher cardiac risk; values between 50–100 ms reflect compromised but not critical health; and values exceeding 100 ms are associated with a healthy autonomic profile [78]. This stratification has direct survival implications. Among heart attack survivors, those with SDNN values above 100 ms demonstrated a 5.3-fold reduction in mortality risk over a mean follow-up of 31 months, compared to those with values under 50 ms [78]. Physiologically, SDNN correlates strongly

with frequency domain HRV parameters, including ultra-low-frequency (ULF), very-low-frequency (VLF), low-frequency (LF), and total spectral power [78]. The degree of this correlation depends on the power distribution across HRV frequency bands. In long-term recordings, especially over 24 hours, LF band activity makes a significant contribution to SDNN [78]. When low-frequency components dominate the HRV spectrum, they influence SDNN more than high-frequency (HF) activity.

The RMSSD is a key time domain feature in HRV analysis, particularly valued for its sensitivity to short-term fluctuations in heart rate that are mediated by PNS activity. RMSSD is calculated by first determining the time differences between successive normal-to-normal (NN) heartbeats in milliseconds, squaring these differences, averaging the result, and then taking the square root. This method captures the beat-to-beat variability in heart rate, making RMSSD a direct and reliable index of vagally mediated HRV [76]. It is especially relevant in contexts where rapid autonomic responses are of interest, such as stress, recovery, and sleep studies. RMSSD is the primary time-domain metric for assessing PNS influence on cardiac function. Its value is further underscored by its equivalence to SD1, a non-linear Poincaré plot measure, which also reflects short-term HRV [79]. Moreover, long-term RMSSD measurements (e.g., over 24 hours) correlate strongly with both pNN50 and HF power, all of which are indicators of vagal tone [5].

NN50 and pNN50 quantify, respectively, the number and proportion of successive NN intervals that differ by more than 50 ms. They are established time-domain markers of PNS activity. Among these, pNN50 is particularly noted for its sensitivity to vagal tone and its close association with HF power and RMSSD, all of which reflect heart rate fluctuations that are synchronously linked with respiration, a phenomenon known as respiratory sinus arrhythmia (RSA), and short-term autonomic regulation [78]. Despite their utility, RMSSD is often preferred over pNN50 in research and clinical contexts due to its greater stability, especially in older populations where HR dynamics may be more complex [78]. Studies suggest RMSSD provides a more consistent estimate of RSA, making it the preferred metric in many HRV assessments [78]. Nonetheless, pNN50 remains a valuable measure, particularly when used in conjunction with RMSSD and HF power to triangulate parasympathetic function.

Time domain HRV features are easy to compute and widely accessible for analysis [76,80]. However, they are particularly susceptible to artifacts, especially those caused by supraventricular or ventricular ectopic beats [80]. In addition, accurate time-domain analysis assumes stationarity in the heart rate signal, meaning the average heart rate remains relatively constant over time, a condition that is rarely met in biological systems [80]. Consequently, time-domain measures alone cannot differentiate between sympathetic and parasympathetic nervous system activity [81]. Nevertheless, they remain valuable for evaluating overall ANS function and can offer meaningful clinical insights [80].

Frequency domain analysis

Frequency domain measures analyze fluctuations in RR intervals by converting them into their constituent frequency components. These measures are typically obtained using Fast Fourier Transform (FFT) analysis, which reveals the spectral characteristics of HRV

across a time series [76,80]. The spectral analysis decomposes the HRV signal into several characteristic components, including LF power and HF power.

LF power has historically been interpreted as reflecting both sympathetic and parasympathetic activity, with a presumed dominance of sympathetic influence. However, another research has emphasized that under resting conditions, LF power predominantly reflects baroreflex-mediated parasympathetic (vagal) activity rather than direct sympathetic cardiac innervation [82]. This frequency range has also been referred to as the baroreceptor range, given its close association with blood pressure regulation through baroreflex mechanisms [75]. While LF is often used as an indicator of sympathetic modulation, this interpretation must be made cautiously. Baroreflex activity, which can generate oscillations within the LF range, is largely under parasympathetic control during rest [83,84]. Moreover, respiratory patterns significantly influence LF power. In particular, at slow breathing rates, vagal activity can produce oscillatory effects that extend into the LF range, further complicating attribution solely to sympathetic output [85,86].

HF power is widely recognized as a primary index of parasympathetic modulation of heart rate. As previously noted, HF power, often referred to as the respiratory band, captures the phenomenon of RSA. Since RSA is primarily governed by the vagus nerve, HF power serves as a reliable marker of vagal tone and PNS activity. This measure is strongly correlated with time-domain indices such as RMSSD and pNN50, which also reflect beat-to-beat, vagally mediated changes in HRV [78]. In healthy individuals, HF power tends to follow a circadian rhythm: it increases during sleep (particularly at night) and decreases during daytime hours, reflecting shifts in autonomic balance [87]. Furthermore, reduced HF power is frequently observed in conditions associated with stress, anxiety, panic, and emotional distress, making it a valuable biomarker for assessing both psychological and physiological stress responses. Importantly, HF power reflects the dynamic adaptability of the autonomic nervous system, particularly through vagal modulation of cardiac function. Adequate vagal inhibition plays a crucial role in maintaining cardiovascular stability and enabling adaptive responses to environmental demands. Conversely, reduced vagal activity, as indicated by low HF power, is associated with increased morbidity, including both cardiovascular and psychiatric conditions [88].

To enable comparison across individuals or conditions with differing total HRV power, the LFn and HFn are often calculated. LFn and HFn are derived by dividing LF power and HF power, respectively, by the total spectral power, thereby expressing LF and HF as a proportion of overall HRV. This normalization helps reduce inter-individual variability and better highlights relative autonomic shifts.

The LF/HF ratio is a commonly used HRV feature intended to represent the balance between sympathetic and parasympathetic nervous system activity. It is calculated as the ratio of LF power, which includes both sympathetic and parasympathetic contributions, to HF power, which is primarily vagally mediated [75]. Under this framework, a high LF/HF ratio is often interpreted as indicative of sympathetic dominance or parasympathetic withdrawal, such as during stress or fight-or-flight responses. Conversely, a low LF/HF ratio is thought to reflect parasympathetic predominance, as seen in calm, energy-conserving states [82]. Originally developed for use in 24-hour HRV recordings, the LF/HF ratio was intended to reflect relative autonomic balance across longer periods where both branches of the ANS contribute significantly to HRV [82]. However, this interpretation becomes

problematic in short-term recordings (e.g., 5 minutes), where distinct physiological mechanisms appear to drive LF and HF components and where LF/HF ratios often poorly correlate with 24-hour values [82]. Critics such as Billman [89] have challenged the validity of the LF/HF ratio as a true measure of "sympatho-vagal balance" [90], pointing out several important limitations:

- LF power is not a pure index of sympathetic activity. It is significantly influenced by parasympathetic modulation, particularly via the baroreflex, and can also reflect other undefined factors.
- The interaction between the sympathetic and parasympathetic systems is non-linear and non-reciprocal. In many physiological states, these branches do not simply act in opposition, undermining the assumption that their activity can be inferred from a single ratio.
- Respiratory mechanics and resting heart rate can confound both LF and HF components, further complicating interpretation of their ratio, especially in short-term or uncontrolled breathing conditions.

Given these concerns, Shaffer et al. [82] caution that the LF/HF ratio remains a controversial and often misunderstood metric, especially when applied outside of well-controlled, long-term monitoring contexts. The physiological basis for short-term LF/HF ratio interpretation lacks clarity, and the assumption of a direct SNS/PNS opposition does not consistently hold.

Frequency-domain HRV measures offer valuable insights into ANS function, but their utility depends heavily on careful interpretation within the appropriate physiological and methodological context [75,82]. Furthermore, both frequency- and time-domain analyses are susceptible to artefacts, ectopic beats, and require signal stationarity to ensure valid interpretation [80]. External variables such as posture, stress, and physical movement can significantly influence HRV measurements and should be carefully controlled during data acquisition [75,76,80]. Thus, while HRV frequency-domain indices are powerful tools for assessing autonomic regulation, they should always be interpreted in conjunction with complementary metrics, within a controlled environment, and with a full understanding of their physiological underpinnings.

1.4.1.2 Non-linear analysis

In addition to traditional time- and frequency-domain analyses, non-linear measures of HRV have gained increasing attention for their ability to capture the complex, dynamic nature of cardiovascular regulation. These measures account for non-linear phenomena arising from the interplay of hemodynamic, electrophysiological, and humoral variables, along with autonomic and central nervous system regulation [75,91]. Unlike linear methods, which require signal stationarity and typically model physiological responses on fixed axes, non-linear techniques analyze variability patterns through dynamic, often fractal-based approaches [75,91,92]. This makes them especially valuable in assessing physiological systems that do not behave linearly or consistently over time, conditions common in real-world and clinical settings [92]. Non-linear HRV metrics estimate the quality, correlation, and scaling properties of the heart rate signal, offering insights into its underlying

complexity and structure. While some non-linear indices correlate with conventional HRV measures when generated by similar physiological processes, they also reveal unique features, particularly in pathological conditions. For instance, certain stressors or disorders like diabetes tend to depress non-linear variability, while in post-myocardial infarction patients, elevated non-linear HRV has paradoxically been identified as an independent risk factor for mortality [93]. Importantly, these methods do not rely on the assumption of stationarity and can better reflect dynamic physiological changes, distinguishing between patient groups even when the mechanistic interpretation remains limited [92,94]. The parameters used to measure non-linear properties of HRV included Poincare's plot, Beta exponent (betaExp) and Fractal Dimension (FD).

The Poincaré plot, offers a powerful and intuitive method for visualizing and quantifying the beat-to-beat variability of heart rate. From it, two main nonlinear parameters can be extracted: SD1 and SD2. The SD1 value represents short-term HRV and is closely associated with HF power and RMSSD [79]. In contrast, SD2 reflects both short- and long-term HRV components and correlates with LF power and BRS [95,96]. Finally, the SD1/SD2 ratio provides a dimensionless index of HRV complexity and unpredictability, often interpreted in the context of autonomic balance. When the observation period is sufficiently long and sympathetic tone is elevated, SD1/SD2 tends to mirror the LF/HF ratio, offering a non-linear counterpart to this widely used, though controversial, frequency-domain metric [97].

The FD and betaExp offer valuable insights into the self-affinity and scaling behavior of cardiac dynamics. These parameters reflect the inherent complexity of the physiological systems generating HRV signals, providing information beyond that of traditional linear methods [98]. The betaExp, often derived from the slope of the power spectral density plotted in a log-log scale, quantifies the relationship between signal frequency and spectral power, capturing the long-term scaling properties of the RR interval time series. This measure is particularly relevant in conditions such as heart failure, where changes in autonomic control can significantly alter the scaling properties of HRV signals [98]. Similarly, FD, calculated in the time domain, provides a numerical index of signal complexity by describing how the RR interval signal fills space as its resolution increases. A higher FD suggests more irregularity and complexity, whereas a lower FD indicates a more regular and potentially pathological rhythm. Importantly, FD has been shown to be altered in cardiovascular patients, highlighting its sensitivity to underlying cardiac dysfunction [99]. Both FD and betaExp serve as measures of self-affinity, the idea that the structure of HRV fluctuations remains statistically similar across different time scales. These non-linear metrics are especially useful when the signal lacks stationarity or exhibits complex dynamics that elude linear characterization. Moreover, while FD captures complexity in the temporal structure of the signal, betaExp captures frequency-based scaling behavior, making the two parameters complementary in comprehensive HRV analysis.

Non-linear HRV provide robust insights into the dynamic complexity of autonomic regulation, offering diagnostic value beyond traditional linear measures. By capturing patterns of short- and long-term variability, autoaffinity, and structural irregularities in heart rate dynamics, these indices improve the detection of subtle alterations in cardiovascular health and autonomic balance.

In conclusion, it is generally accepted that HRV is a powerful predictor of cardiac mortality, arrhythmia, and sudden cardiac death, independent of other risk factors such as left ventricular ejection fraction, ventricular extrasystoles, and episodes of non-sustained ventricular tachycardia following myocardial infarction [71,76,100]. Although HRV alone cannot distinguish between specific cardiac conditions, when combined with other clinical and instrumental parameters, it can contribute to a more comprehensive assessment of cardiac function.

1.4.2 Echocardiographic features: LVEF and GLS

Echocardiography encompasses a range of non-invasive and safe techniques that utilize ultrasound waves to assess myocardial integrity and blood flow across cardiac valves. It has become an essential diagnostic tool in cardiology due to its widespread availability, absence of ionizing radiation, and ability to provide real-time anatomical and functional cardiac information [101].

Echocardiography, particularly with the addition of STE, has become the gold standard for evaluating global and regional systolic and diastolic performance, especially of the left ventricle [101]. Numerous studies have demonstrated the strong prognostic value of cardiac volumes and global systolic function across a wide spectrum of cardiovascular diseases [102,103]. In IHD, for instance, global systolic function has been shown to carry a higher prognostic weight than the mere anatomical extent of coronary artery involvement: patients with three-vessel disease but preserved systolic function exhibit a lower mortality rate than those with less extensive coronary disease but more compromised ventricular performance [104]. Similarly, in the setting of cardiomyopathies accurate assessment of systolic function supports both diagnostic classification and the initiation or adjustment of therapy [105,106].

From both 2D echocardiography and 2D STE, a range of parameters can be extracted, including LVEF and GLS, two of the most commonly used and clinically valuable indicators of left ventricular systolic function.

LVEF is a powerful predictor of cardiovascular morbidity and mortality. It plays a crucial role in diagnosing and managing heart failure, determining prognosis after myocardial infarction, and assessing candidacy for coronary revascularization [107,108]. Moreover, one of the most important clinical applications of LVEF is in selecting patients for implantable cardioverter-defibrillators [109]. Beyond these established roles, LVEF also holds significant prognostic value. In patients with DCM, real-time three-dimensional echocardiography has demonstrated that reduced LVEF strongly correlates with increased systolic dyssynchrony and impaired right ventricular function, underscoring its role as a marker of global cardiac dysfunction [110]. Additionally, a large cohort study using 3DE demonstrated that reduced LVEF was significantly associated with increased all-cause mortality and cardiac death, emphasizing its prognostic value across a wide spectrum of cardiovascular diseases [111]. Nevertheless, LVEF should not be viewed in isolation: its prognostic value is best interpreted alongside other clinical and laboratory markers [73].

Studies have shown that GLS is a strong prognostic marker and often superior to traditional parameters such as LVEF. Antoni et al. [32] studied 659 patients post-acute myocardial infarction and found that individuals with a GLS > -15.1% had worse cardiac outcomes. Bertini et al. [112] reported that in 1060 patients with IHD, a GLS < -11.5% was

associated with improved prognosis during follow-up. Ma et al. [113] compared GLS between healthy individuals and those with DCM, demonstrating significantly lower GLS in the DCM group (-7.62% ± 3.03%) compared to healthy controls (-26.20 ± 2.36%). GLS also correlated better with myocardial damage than LVEF. Importantly, some patients showed improved LVEF after therapy but continued to exhibit impaired GLS (>-16%), suggesting persistent subclinical dysfunction. Moreover, several studies have demonstrated the diagnostic utility of GLS in detecting significant coronary artery disease (CAD), particularly in patients presenting with chest pain but inconclusive initial diagnostic workups. One investigation reported high sensitivity and specificity for a GLS cutoff value of $> -18.8\%$ in identifying significant coronary stenosis [114]. In another study involving patients referred to the emergency department with suspected non-ST elevation acute coronary syndrome (NSTE-ACS), left ventricular GLS outperformed traditional echocardiographic parameters in distinguishing between those with and without significant coronary stenosis [115]. Furthermore, research focusing on patients with typical angina symptoms and dynamic cardiac biomarkers found that GLS was independent predictor of CAD in multivariate analysis, reinforcing the clinical relevance of GLS in the early identification of NSTE-ACS [116]. However, Zito et al. [117] advised against the routine use of regional strain due to high intra- and inter-observer variability and reduced reliability.

1.5 Perfusion imaging and EEG biomarkers in the evaluation of stroke

During the course of this PhD research, multiple imaging and neurophysiological parameters were considered to assess cerebral perfusion and investigate their potential diagnostic and prognostic value in acute ischemic stroke. In particular, advanced perfusion neuroimaging techniques, such as computed tomography perfusion (CTP) and arterial spin labeling (ASL), and electroencephalographic (EEG) parameters, have been employed to improve differential diagnosis and potentially predict long-term outcomes.

CTP represents a valuable diagnostic tool in the management of acute ischemic stroke, offering significant advantages in terms of rapid acquisition, widespread availability, and the ability to provide detailed information on cerebral perfusion status. It is particularly useful for delineating the ischemic core and penumbra, thereby supporting timely treatment decisions. However, CTP is not without limitations. Exposure to ionizing radiation and the use of iodinated contrast agents can pose risks, especially for patients with renal impairment or contrast allergies. Furthermore, technical constraints such as limited anatomical coverage, motion artifacts, and potential inaccuracies in the selection of the arterial input function may reduce the reliability of perfusion measurements. Despite its widespread use, the literature remains heterogeneous regarding threshold values used to define ischemic regions, partly due to variability across post-processing software platforms [118].

As a complementary method, ASL provides a completely non-invasive approach to cerebral perfusion imaging by using magnetically labeled arterial blood water as an endogenous tracer. ASL is increasingly recognized as a viable alternative to contrast-based methods such as dynamic susceptibility contrast (DSC) imaging, particularly in patients with contraindications to gadolinium. Although limited by low signal-to-noise ratio and

sensitivity to delayed arrival of blood flow, ASL enables absolute quantification of cerebral blood flow (CBF) and offers high repeatability.

Despite the critical role of perfusion imaging in stroke assessment, these methodologies do not allow for real-time monitoring of cerebral ischemia evolution during the acute phase. In this context, EEG, particularly in its quantitative form (qEEG), emerges as a valuable additional tool. EEG enables the detection of early functional alterations in neuronal activity due to hypoperfusion, reflecting changes in neurovascular coupling and metabolic demand. The integration of EEG with clinical and imaging data enhances the capacity for early risk stratification and outcome prediction. Moreover, qEEG is rapid, portable, radiation-free, and sensitive to subtle changes in cortical function, allowing for non-invasive estimation of neurological deficits, potential disability, and final lesion extent, elements that are particularly relevant given the high interindividual variability observed in stroke patients [14,16].

1.5.1 CT perfusion

Ischemic stroke is characterized by reduced perfusion in the brain regions supplied by the occluded vessel, accompanied by decreased delivery of oxygen and glucose. These alterations can be detected within minutes of symptom onset, making them crucial for diagnosis and therapeutic decision-making [119].

CTP plays a central role in the evaluation of patients with suspected ischemic stroke. It enables rapid detection of these alterations, assessment of the potential benefit from reperfusion therapy, and precise differentiation between the ischemic core—necrotic, non-salvageable tissue—and the ischemic penumbra, tissue at risk but potentially salvageable with timely reperfusion. This information is key for selecting candidates for revascularization, even beyond conventional time windows [120–122].

The introduction of CTP has supported a shift from the traditional time clock approach to the tissue clock paradigm, in which treatment decisions are guided by tissue viability rather than time since onset. This approach has proven effective in identifying additional subgroups, including patients with wake-up strokes, who may still benefit from reperfusion in delayed phases [123].

A particularly relevant parameter derived from CTP is the Mismatch Volume, defined as the volumetric difference between the penumbra and the ischemic core. A large mismatch indicates a wider therapeutic window and can guide the selection of patients for mechanical thrombectomy or systemic thrombolysis in extended time frames [124,125].

Despite its advantages, CTP has limitations. Exposure to ionizing radiation and iodinated contrast agents may pose risks, particularly in patients with renal impairment or contrast allergies. Limited anatomical coverage can prevent complete assessment of the ischemic region, while motion artifacts and errors in arterial input function selection may compromise accuracy.

Although the qualitative delineation of ischemic territories is well established, threshold values for their identification vary across studies, partly due to differences between post-processing software platforms [118]. Commonly accepted thresholds include:

- Ischemic core: rCBF <30% compared to the contralateral hemisphere, CBV <2–2.2 mL/100 g, MTT >8.3 s, Tmax >10 s.
- Penumbra: MTT >145% compared to the healthy hemisphere, rCBF <66%, Tmax >6 s.

This variability complicates the uniform application of treatment selection criteria, although automated algorithms have improved reproducibility and reduced inter-observer variability [118].

Overall, CTP is a valuable diagnostic tool in acute ischemic stroke, offering speed, accessibility, and detailed insight into cerebral perfusion. Its integration with other clinical and imaging data, such as EEG and ASL-MRI parameters, remains essential for a comprehensive patient assessment

1.5.2 Arterial spin labeling

ASL is an MRI technique that enables the acquisition of cerebral perfusion images in a completely non-invasive manner, by using the water in arterial blood as an endogenous tracer. In the context of cerebrovascular disease, ASL represents a promising alternative to bolus DSC imaging for the evaluation of acute ischemic stroke, although it presents certain technical limitations mainly related to low signal intensity and sensitivity to delayed blood flow arrival.

The ASL signal is influenced by technical parameters such as labeling duration and post-labeling delay (PLD). In acute stroke, a perfusion deficit (low or absent ASL CBF signal) is commonly observed in the affected region. A characteristic artifact is the arterial transit artifact (ATA), caused by labeled blood that has not yet reached the capillary bed during image acquisition. ATA appears as a high serpiginous signal in peripheral cortical vessels and is often interpreted as indicative of collateral flow [126,127].

Initially, ASL was considered poorly suited for imaging acute ischemic stroke, as the ASL signal is proportional to CBF, which is markedly reduced in the ischemic core. Additionally, residual flow may be sustained by collateral circulation with prolonged arrival times, rendering the ASL signal unrepresentative of actual CBF due to the rapid decay of the magnetic label (T1 ~1.2–1.8 sec) [126]. Nevertheless, several studies have demonstrated significant diagnostic value of ASL in stroke assessment.

The first study demonstrating the capability of ASL to detect perfusion abnormalities in stroke was conducted by Siewert et al. [128]. Subsequently, Chalela et al. (2000) highlighted the feasibility of ASL in acute stroke, confirming the correlation between reduced CBF and NIHSS score, and identifying ATA as a potential positive prognostic marker [129].

In 2012, three major clinical studies compared ASL with DSC, the standard technique for cerebral perfusion imaging. Zaharchuk et al. demonstrated the clinical feasibility of ASL at 1.5T, reporting good agreement between the methods, although ASL tended to overestimate perfusion deficits due to delayed blood arrival [130]. Bokkers et al., in a larger cohort, showed that ASL at 3T detected perfusion lesions in 82% of cases where DSC showed deficits, with good image quality and 88% agreement in identifying perfusion-diffusion mismatch [131]. Wang et al. confirmed the concordance of ASL with DSC

parameters (Tmax, MTT, relative CBF), emphasizing ASL's higher sensitivity in detecting hyperperfusion [132].

The diffusion-perfusion mismatch approach is crucial in identifying penumbra in patients eligible for revascularization therapies. ASL, when combined with diffusion-weighted imaging (DWI), allows estimation of the penumbra by comparing the hyperintense area on DWI (core) with the hypoperfused area on ASL (penumbra) [127]. However, ASL may overestimate penumbra size, especially in patients with small infarcts [133].

Quantitative studies have identified absolute and relative CBF thresholds for ASL: Bivard et al. proposed a threshold of 40% of contralateral CBF to define critical hypoperfusion, while Niibo et al. used an absolute threshold of 20 ml/100g/min, showing 100% concordance between ASL and DSC in defining mismatch [134,135].

In the presence of arterial occlusion, accumulation of labeled spins in the occluded vessel results in a focal increase in ASL signal, potentially localizing the site of occlusion even in the absence of angiographic or DSC images [127].

Spontaneous or post-treatment reperfusion may be detected as increased ASL signal in the ischemic zone, a phenomenon known as *luxury perfusion*, which is frequently associated with favorable prognosis [126]. In some cases, distinguishing between ATA and true hyperperfusion may be challenging; the absence of a distal hypoperfused territory supports the interpretation of parenchymal hyperperfusion [126].

In TIA, a reduction in ASL signal within a vascular territory may represent the only pathological finding. ASL can enhance diagnostic accuracy by distinguishing TIA from other conditions such as migraine or seizures [136,137]. However, reduced ASL signal is nonspecific and may also be seen in anatomical variants or non-ischemic conditions [138–140].

ASL is useful in differentiating stroke from stroke mimics (e.g., seizures, encephalitis, PRES), often through the identification of atypical or extra-vascular perfusion patterns[141]. In the case of epileptic seizures, ASL can assist in localizing the epileptogenic focus even during the interictal phase[142,143].

Despite inherent limitations, ASL has shown great utility in acute stroke due to its non-invasive nature, repeatability, and ability to provide absolute CBF quantification. Clinical studies demonstrate that, although it may overestimate perfusion deficits, ASL can serve as a valid alternative to DSC, particularly in patients with contraindications to gadolinium. When combined with DWI, ASL enables reliable estimation of the ischemic penumbra, making it a valuable tool in the stratification and management of stroke patients.

1.5.3 Electroencephalography

Perfusion neuroimaging techniques, such as CTP and MRI, are essential for managing stroke patients, but they do not permit real-time monitoring of cerebral ischemia during the acute phase. In this setting, EEG, particularly in its quantitative form (qEEG), offers a valuable complement by providing objective, reproducible measures of hypoperfusion-induced changes in brain electrical activity, thereby supporting standardized assessment and informed therapeutic decision-making [14].

Spectral analysis allows for the measurement of relative power across delta, theta, alpha, and beta frequency bands, as well as the derivation of composite indices such as the Delta/Alpha Ratio (DAR) and the (Delta + Theta)/(Alpha + Beta) Ratio (DTABR), which have demonstrated significant correlations with clinical outcomes and perfusion measurements obtained via CTP[16,18,144].

The study by Ajčević et al. [14] demonstrated a statistically significant correlation between EEG parameters and the extent of hypoperfused volume measured via CTP in patients with hyperacute ischemic stroke. Specifically, relative delta power, DAR, and DTABR were significantly and linearly correlated with both the ischemic core and the hypoperfused area. Conversely, relative alpha power exhibited an equally significant inverse correlation. The analysis was based on EEGs acquired within 4.5 hours from symptom onset, following a multimodal imaging protocol (NCCT, CTA, and CTP) and clinical assessment using the NIHSS scale. Compared to the control group, stroke patients exhibited a significant increase in delta power and a reduction in high-frequency bands (alpha and beta), suggesting that high-frequency activity declines at CBF values around 25–35 mL/100g/min, while an increase in low-frequency activity becomes evident below 17–18 mL/100g/min, a threshold indicative of irreversible neuronal damage[14].

Another study [16] investigated the correlation between EEG parameters recorded using a bedside wireless device in patients with hyperacute anterior ischemic stroke and post-treatment neurological disability. A direct correlation was found between DAR, DTABR, delta power, and NIHSS scores (at 7 days and 12 months) and mRS (at 12 months). In contrast, alpha power showed an inverse correlation with these indices. Furthermore, a favorable outcome (mRS $\leq$ 2 at 12 months) was associated with lower DAR values. Relative delta power, DAR, and DTABR were also significantly correlated with the final lesion volume, measured using a seed-region segmentation algorithm on NCCT images. This suggests that an EEG pattern characterized by relatively preserved alpha activity and only modestly increased delta power may indicate viable tissue and thus a greater likelihood of benefiting from reperfusion therapy [16].

The study by Zhang et al. [144] compared the predictive value of qEEG indices and CTP parameters in 29 patients undergoing mechanical thrombectomy (MT). Results showed that DAR, DTABR, and delta power were significantly associated with clinical scores (NIHSS and mRS), and that EEG parameters outperformed CTP in predicting the 3-month outcome. In particular, delta power measured 24 hours post-MT exhibited the highest predictive value among the EEG indices analyzed. An additional study [18] involving 73 patients who underwent thrombectomy found that the interhemispheric difference in DAR significantly correlated with NIHSS and mRS scores at discharge and at 3 months. This metric proved to be an independent predictor of favorable outcome (mRS $\leq$ 2), even compared to infarct volume. These findings support the role of EEG not only as a diagnostic tool but also as a prognostic instrument in ischemic stroke patients treated with MT.

The integration of EEG with clinical and imaging data can significantly enhance the capacity for risk stratification and outcome prediction in patients affected by ischemic stroke. The use of qEEG in the acute setting offers considerable advantages: it is rapid, portable, radiation-free, and sensitive to early functional changes. Moreover, the ability to non-invasively predict neurological deficits, functional disability, and final lesion extent may

guide more targeted therapeutic choices, particularly in a context characterized by high interindividual variability [14,16].

1.6 Interpretable Machine Learning Models in Healthcare

The growing integration of machine learning (ML) in healthcare has opened significant opportunities for advancing clinical decision-making, particularly in areas such as diagnosis, prognosis, and personalized treatment planning. However, one of the most critical challenges hindering the broader adoption of these technologies in medical settings is the interpretability of the models used. Interpretability, in this context, refers to the ability of a human user, typically a clinician or healthcare professional, to understand the decision-making process of a ML model, including how specific input features influence outputs and what reasoning underlies a given prediction or classification.

These interpretable models aim not only to predict clinical outcomes such as disease risk, readmission probability, or treatment necessity but also to ensure that clinicians can verify and trust the basis of those predictions. In clinical practice, black-box models, such as deep neural networks or ensemble methods, although often highly accurate, fall short in delivering the transparency required for high-stakes decisions. In such settings, incorrect predictions can have life-threatening consequences [145]. Interpretability ensures that end-users can examine, debug, and potentially improve machine learning systems before acting on their outputs. Furthermore, it gives clinicians a reason to either accept or reject the model's suggestions based on a clear understanding of its logic. The limitations of opaque models are well illustrated in a study by Caruana et al. [146], where a neural network was used to predict pneumonia mortality. Despite achieving high predictive accuracy, the model falsely identified asthma patients as lower-risk, presumably because they had received more aggressive treatment leading to better outcomes. This misleading correlation, one that might be overlooked in a black-box model, was corrected once a more interpretable regression model was used. Such examples highlight how lack of interpretability can lead to dangerously flawed conclusions, particularly when the model captures spurious correlations or suffers from data leakage [145].

Consequently, there is a growing preference for inherently interpretable algorithms such as classification trees, logistic regression, and naive Bayes, especially in the medical domain. They are not only capable of providing actionable predictions but also allow clinicians to evaluate the plausibility of model decisions by directly inspecting thresholds, feature interactions, or probabilistic weights. For example, in classification tree models, clinicians can visualize the pathway leading to a decision and assess whether the selected thresholds correspond to known clinical markers or diagnostic criteria. Similarly, linear or logistic regression and naive Bayes models allow for interpretability through coefficients or conditional probabilities, respectively. These characteristics make such models valuable across several medical specialties, including toxicology [147], endocrinology [148], neurology [149], and cardiology [150–152].

In cardiology, the use of interpretable models has demonstrated particular success. Feeny et al. [150], for instance, reported that a naive Bayes classifier incorporating nine

demographic and clinical variables, including New York Heart Association (NYHA) classification and LVEF, was the best model for predicting echocardiographic response to cardiac resynchronization therapy. In a separate study, Salman et al. [151] explored multiple models for predicting hospital mortality among myocardial infarction patients, emphasizing the need for not just accuracy but explainability. Melillo et al. [152] applied a classification and regression tree model for stratifying congestive heart failure patients by risk level, using HRV-based features to distinguish between high-risk and low-risk groups.

Despite these successes, the majority of machine learning applications in healthcare continue to prioritize accuracy over interpretability. This has led to a landscape dominated by complex models that provide little to no insight into why a particular decision was made [145,153]. This opacity is problematic, as it undermines user trust and introduces a barrier to clinical adoption. Moreover, clinicians are often reluctant to integrate such models into their decision-making processes when the rationale behind predictions cannot be clearly articulated or validated against established clinical knowledge [154]. As a result, a strong emphasis is now being placed on the development of clinically plausible ML models.

An important advantage of classification trees is their visual structure, which closely mirrors human decision-making processes. This simplicity allows clinicians to follow a clear set of rules and thresholds for both clinical and HRV-derived variables, facilitating acceptance and usability in real-world settings. Typically, the most influential features are found at the top of the tree, providing immediate insight into what factors are most important for classification. Logistic regression and naive Bayes models, while not inherently visual, can be represented using nomograms, a graphical tool that translates regression coefficients or conditional probabilities into accessible visualizations. This level of interpretability adds substantial value in clinical contexts, enabling clinicians to assess the consistency of model outputs with clinical intuition and empirical evidence.

However, there is little consensus on what "interpretability" precisely entails [155]. Various definitions have been proposed that encompass model transparency, fidelity, user trust, and comprehensibility [145,154–156]. Lipton et al. [155] argue that a fully interpretable system should allow a user to understand its algorithmic mechanism, the semantics of input features, and the influence of parameters. Moreover, interpretability techniques can be classified in multiple ways. One distinction is between intrinsic and post-hoc interpretability [156]. Intrinsic interpretability refers to models that are naturally understandable by their structure, such as decision trees and linear models. Post-hoc interpretability, in contrast, applies explanatory methods after model training, often to decipher black-box models without modifying them. Depending on when they are applied, these techniques may also be classified as pre-model, in-model, or post-model. Pre-model methods, such as data visualization, PCA, and clustering, help in understanding the dataset before model selection. In-model methods embed interpretability into the learning process itself. Post-model methods, such as LIME [157] or SHAP values [158], provide explanations after the model has been trained. Another classification distinguishes model-specific from model-agnostic interpretability approaches [154] (Figure 1.3). Model-specific methods utilize internal model structures to generate explanations and are tailored to specific algorithms, while model-agnostic methods treat the model as a black box and rely only on its outputs.

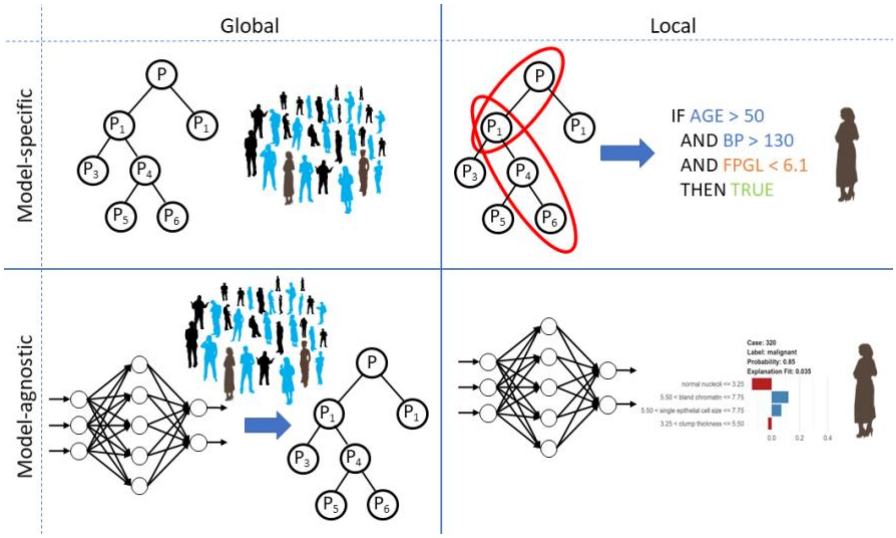

Figure 1.3. *Visual summary of the most representative interpretability approaches for machine learning based predictive modelling in healthcare [141].*

Interpretability methods can also be evaluated by their scope [154]. Local interpretability focuses on explaining individual predictions, important in clinical cases where decisions must be justified for a single patient, whereas global interpretability describes the overall model behavior across the dataset. Historically, global interpretability dominated the field, especially for knowledge extraction and rule-based systems. But in modern personalized medicine, local interpretability has gained traction, particularly in efforts to explain predictions on a per-patient basis.

With the growing integration of ML in healthcare, interpretability has evolved from a desirable characteristic into a clinical and ethical requirement, despite the various definitions and conceptual frameworks found in the literature. Clinicians must be able to understand, trust, and communicate the outputs of predictive models. Interpretable models allow them to validate thresholds, ensure alignment with clinical knowledge, and detect anomalies. Ultimately, the adoption of ML in medicine depends on the ability to bridge the gap between algorithmic power and human understanding. Interpretable models, by offering transparency, trustworthiness, and clinical relevance, are uniquely positioned to fulfill that role.

This part of the thesis provides a critical overview of interpretability in machine learning models applied to healthcare, laying the groundwork for the methods developed in Chapter 2.

Chapter 2. BIOMEDICAL DATA ACQUISITION, PROCESSING AND MODELING PIPELINE

2.1 HRV PROCESSING AND ANALYSIS

The 24-hour Holter ECG recordings were acquired in DCM, IHD and healthy subjects using the ambulatory electrocardiographic recorder SpiderView (Sorin Group, Italy) with a sampling rate of 200 Hz. RR intervals were extracted and labeled using SyneScope analysis software (Sorin Group, Italy), which classified each beat as normal (N), ectopic (E), artifact (A), or calibration (C). Since the estimation of HRV indexes is affected by missing data, noise, arrhythmic events, and ectopic beats, all of which can alter the signal and compromise the reliability and clinical utility of the extracted features, appropriate pre-processing of the RR time series is necessary to mitigate these effects.

The RR interval time series were segmented into non-overlapping 5-minute. This segment length was chosen to ensure the extraction of reliable HRV measures over short durations while also guaranteeing a frequency resolution of 0.01 Hz in spectral analyses.

Two distinct preprocessing strategies were applied depending on whether ectopic beats were considered in the analysis. In the first approach, only NN intervals were retained; RR intervals labeled as ectopic or artifact were excluded. A segment was included only if it contained at least 60 normal beats, ensuring statistical reliability of the computed features. This approach aimed to obtain a "clean" HRV signal, free from physiological artifacts that could otherwise bias standard HRV metrics.

In the second approach, ectopic beats were retained in the RR series to analyze what is referred to as total HRV, a measure that includes both normal and ectopic activity. This choice was motivated by the fact that, in certain pathological conditions, ectopic beats are not merely noise but may provide meaningful prognostic information that could be lost if excluded. However, to preserve signal quality and avoid dominance by noise or arrhythmic runs, a 5-minute segment was accepted for analysis only if the longest contiguous sequence of ectopic or artifact beats did not exceed 10 seconds, and at least 80% of the beats were labeled as normal. RR intervals labeled as calibration (C) were ignored in both strategies.

To enable spectral and other analyses that require regularly sampled signals, the accepted RR segments were interpolated using cubic spline interpolation and resampled at 2 Hz, producing uniformly sampled time series. As a result, two HRV signals were generated for each subject: one including only NN intervals and one including both normal and ectopic beats (total RR series). For both types of signals, linear and non-linear HRV features were extracted from each segment to assess different aspects of autonomic regulation and rhythm dynamics.

Several time-domain linear parameters were calculated directly from the RR sequence to evaluate RR variability. In particular, in a continuous ECG recording, each QRS complex

is identified, and the intervals between neighboring QRS complexes, produced by the sinus node's depolarization, are calculated. Furthermore, more advanced statistical metrics in the time domain can be obtained. These include:

- MeanRR, providing a general measure of heart rate over time [75];
- SDNN, which reflects the overall variability in RR intervals, indicating the consistency of heartbeats [75];
- RMSSD, that captures the magnitude of variations between consecutive RR intervals, offering insights into parasympathetic nervous system activity [75];
- NN50, that highlighting instances of significant heart rate fluctuations [75];
- pNN50, which provides a normalized measure of heart rate variability [75].

Frequency domain features estimate the balance between the sympathetic and parasympathetic branches of the autonomic nervous system. In my research, the power spectral density (PSD) of a time series was estimated using Welch's method [159]. This approach involves dividing the original sequence of data into several equal-length segments. Each segment is then treated as a smaller subsequence for which a PSD is calculated. Instead of analyzing the entire sequence at once, Welch's method computes the PSD for each segment individually and then averages them to produce a more stable and reliable estimate. A window function, specifically the Hamming window, was applied to each segment to minimize the impact of edge effects and to reduce the influence of overlapping samples. This choice helps in suppressing the abrupt changes at the segment boundaries and decreases redundancy due to any overlap between segments [160]. The final PSD estimate is obtained by averaging the results from all segments. This averaging process reduces the variability (or noise) in the PSD estimate. In this study, the segments were not overlapping, and the variability in the final estimate was inversely related to the number of segments used; more segments led to a more stable estimate. This spectral analysis decomposes the HRV signal into the subsequent characteristic components:

- Low Frequency (LF) [ms^2], ranging from 0.04Hz to 0.15Hz,
- Low Frequency normalized (LFn), the normalization is obtained dividing the LF power by the total power spectrum,
- High Frequency (HF) [ms^2], ranging from 0.15Hz to 0.4Hz,
- High Frequency normalized (HFn), the normalization is obtained dividing the HF power by the total power spectrum,
- Ratio between the LF and the HF (LF/HF).

Finally, the non-linear analysis included several advanced measures to capture the complexity and variability of the heart rate signal. The Poincaré plot is constructed by plotting each R–R interval against the preceding interval, forming a scatterplot that reveals patterns and complexity in the time series data that are not readily apparent through linear HRV measures [161]. One of its significant strengths lies in its insensitivity to trends within the R–R intervals, making it more robust in the presence of non-stationary signals compared to frequency-domain analyses [161]. A Poincaré plot can be analyzed geometrically by fitting an ellipse to the cloud of plotted points, from which several non-linear indices are derived. The SD1 value is the standard deviation of points perpendicular to the line of identity ($y = x$). In contrast, SD2 measures the spread of points along the line of identity.

SD1 reflects short-term heart rate variability, the Poincaré plot parameter SD2 represents long-term variability, while their ratio SD1/SD2 indicates their balance [162].

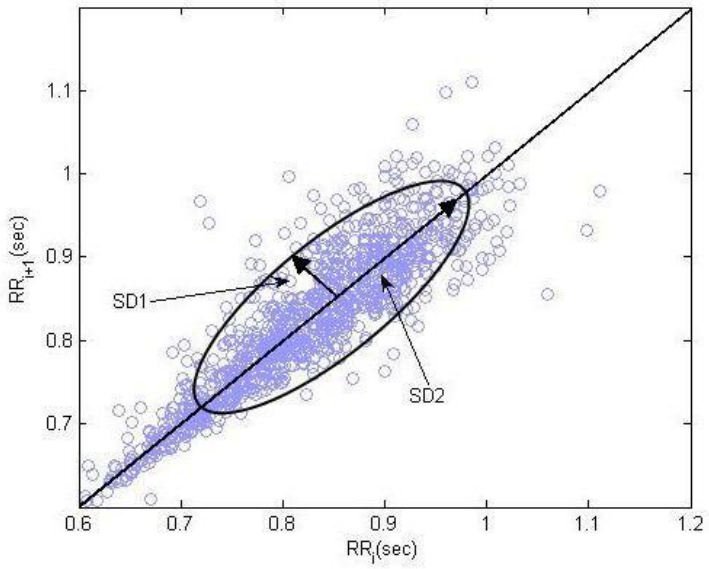

Figure 2.1. *Standard Poincaré plot. A standard Poincaré plot (lag-1) of RR intervals of a healthy person (N = 2000). SD1 and SD2 represents the dispersion along minor and major axis of the fitted ellipse [153].*

The fractal dimension (FD), calculated directly in the time domain, quantifies the self-affinity and complexity of the HRV signal [163]. To determine the fractal dimension (FD) directly from time-domain data, various methods have been proposed [164–166]. Among them, studies have shown that Higuchi's algorithm [163] is one of the most reliable for accurately estimating the FD of waveform signals. This technique involves analyzing how the length of a curve changes depending on the scale at which it is measured. In this research, Higuchi's method was used by applying it to a time series, which was divided into multiple new sequences by sampling at regular intervals. For each of these sequences, the curve's length was estimated, and then an average length was calculated for each interval scale. This process was repeated across a range of scales to capture the complexity of the signal. By plotting the results on a double logarithmic graph, where one axis represents the scale and the other represents the average length, a linear trend can often be observed. The slope of this line corresponds to the negative value of the fractal dimension. In this study, the method was applied to time series containing more than 125 data points, with specific parameters chosen to ensure accurate and reliable FD estimation [164].

A significant portion of HRV is found at frequencies lower than the low-frequency band, specifically below 0.04 Hz. Within the frequency range of approximately 10^{-4} to 10^{-2} Hz, the HRV power spectrum typically lacks distinct periodic patterns and instead displays a power-law distribution [98]. This behavior is characterized by a power exponent, β, which describes the relationship between the PSD and the frequency of HRV. In graphical terms, when the PSD is plotted against frequency on a double logarithmic scale, the resulting line's slope corresponds to the value of β. The exponent β provides insight into the "color" or autocorrelation properties of the signal. A β of 0 indicates no autocorrelation, a β of 2 suggests strong autocorrelation, and a β of 1 represents moderate autocorrelation. Since both the power-law exponent β and the FD reflect similar aspects of signal complexity, there is an

expected relationship between them [167]. This connection allows for the possibility of estimating one metric based on the other. An established model describes this relationship as follows:

$$FD = \frac{(5 - \beta)}{2}, \qquad [1]$$

where β typically ranges from 1 to 3, corresponding to FD values between 1 and 2 [163].

2.2 ECHOCARDIOGRAPHIC IMAGING

Each subject in the study underwent both 2D echocardiography and 2D speckle-tracking echocardiography (STE). In the following section, a brief overview of the two acquisition techniques is provided, followed by a detailed description of the analyses performed to derive the two echocardiographic parameters: LVEF and GLS.

2.2.1 2D echocardiography and 2D Speckle-Tracking Echocardiography

The core technology behind echocardiography is based on the piezoelectric effect, a phenomenon where piezoelectric crystals convert electrical oscillations into mechanical (ultrasound) waves and vice versa [168]. These crystals are embedded within the echocardiographic probe and typically vibrate at frequencies between 1.5 to 7.5 MHz. For transthoracic cardiac imaging, a narrower frequency range of 3 to 5 MHz is generally employed due to the direct relationship between frequency and signal attenuation in tissues. Ultrasound waves generated by the probe traverse the thoracic tissues and reflect back upon encountering boundaries between different tissue types. The speed of sound varies depending on the medium, approximately 330 m/s in air and around 1540 m/s in cardiac tissue [168]. The echocardiographic system measures the time delay of returning echoes and calculates the distance of each interface from the transducer, thereby constructing a two-dimensional grayscale image based on reflection intensity and depth.

Early echocardiographic techniques involved A-mode (amplitude mode) imaging, where reflected wave amplitude was displayed along a single line. This evolved into M-mode (motion mode), which plots depth versus time and offers superior temporal resolution, making it particularly valuable for analyzing fast-moving cardiac structures like the mitral and aortic valves [168]. M-mode continues to complement more advanced 2D and 3D imaging techniques due to its high spatial resolution, especially for measuring ventricular dimensions in systole and diastole [168].

2D echocardiography

2D echocardiography forms the cornerstone of modern cardiac imaging. In this mode, rather than sending sound waves in a fixed line, the scan plane is dynamically swept across

an arc. Data from multiple scan lines are processed to produce tomographic slices of cardiac structures in real time [168]. These dynamic images allow clinicians to assess cardiac chamber sizes, wall motion, valve morphology, and pericardial effusion. 2D echocardiography also serves as a visual guide for complementary techniques such as Doppler imaging, 3D reconstruction, and speckle-tracking analysis. Three major approaches exist for acquiring echocardiographic images [169]:

- Transthoracic echocardiography (TTE): the most commonly used modality where the probe is placed on the chest wall.
- Transesophageal echocardiography (TEE): involves the insertion of an ultrasound probe into the esophagus, providing superior visualization of posterior cardiac structures, especially in technically challenging patients.
- Intracardiac echocardiography (ICE): used less frequently, primarily in interventional cardiology or electrophysiology settings, where the probe is delivered via a catheter into the heart itself.

2D Speckle-Tracking Echocardiography

2D STE represents a significant advancement in myocardial function analysis. Unlike Doppler-based techniques, STE is angle-independent and minimally affected by cardiac translational motion, providing quantitative and objective assessment of myocardial deformation [170]. STE operates by tracking natural acoustic markers known as "speckles", which are unique grayscale patterns generated by the interaction of ultrasound waves with the myocardial tissue. These speckles form stable patterns during a cardiac cycle and can be monitored using dedicated software. Each collection of speckles forms a functional unit (kernel), and their motion throughout the cardiac cycle is used to evaluate myocardial strain.

Prior to the adoption of STE, only cardiac MRI offered precise measurements of myocardial strain and torsion. However, MRI is more expensive, time-consuming, and less accessible than echocardiography. STE bridges this gap, offering reliable assessment of myocardial deformation in longitudinal, radial, and circumferential directions, as well as rotational dynamics of the left ventricle. One of the key strengths of STE is its semi-automated nature, which improves inter- and intra-observer reproducibility. However, its accuracy is heavily dependent on image quality, particularly in achieving clear definition of the endocardial border.

2.2.2 Left Ventricular Ejection Fraction

LVEF is the cornerstone parameter for the assessment of left ventricular systolic function. It represents the percentage of blood ejected by the left ventricle during systole relative to the total volume present at the end of diastole [73].

The American College of Cardiology (ACC) provides a simplified classification of LVEF ranges for clinical use[73]:

- Hyperdynamic: LVEF > 70%
- Normal: LVEF 50–70%

- Mild dysfunction: LVEF 40–49%
- Moderate dysfunction: LVEF 30–39%
- Severe dysfunction: LVEF < 30%

LVEF can be documented either quantitatively (precise percentage value) or qualitatively (e.g., "moderate dysfunction" or visual estimation). While visual assessment is rapid and commonly used in routine clinical practice, quantitative methods are preferred to reduce interobserver variability and improve diagnostic accuracy.

LVEF can be measured using multiple imaging modalities, but echocardiography is the most widely used due to its non-invasive nature, portability, and lack of ionizing radiation [73]. Various echocardiographic techniques (M-mode, 2D, and 3D imaging) offer different levels of precision based on how LV volumes are determined (linear, area, or volumetric measurements).

In this study, LVEF was calculated using the Simpson biplane method applied to 2D echocardiographic images.

2.2.3 Global Longitudinal Strain

GLS is a key parameter in myocardial deformation imaging, representing the longitudinal shortening of myocardial fibers from the base to the apex of the heart during systole [171]. This directional deformation reflects the functional integrity of the subendocardial fibers, which are often the earliest to be affected in various cardiac pathologies.

The GLS is derived from 2D STE and the analysis is typically conducted in apical views, allowing longitudinal motion to be assessed effectively [171]. Speckle tracking offers a non-invasive, reproducible, and angle-independent method to quantify myocardial motion and deformation, enhancing sensitivity in the detection of subclinical myocardial dysfunction[171]. As shown in Figure 2.2:

- V_{long} indicates the longitudinal velocity related to longitudinal strain,
- V_{trasv} relates to radial deformation,
- V_v reflects velocity relative to a user-defined reference point.

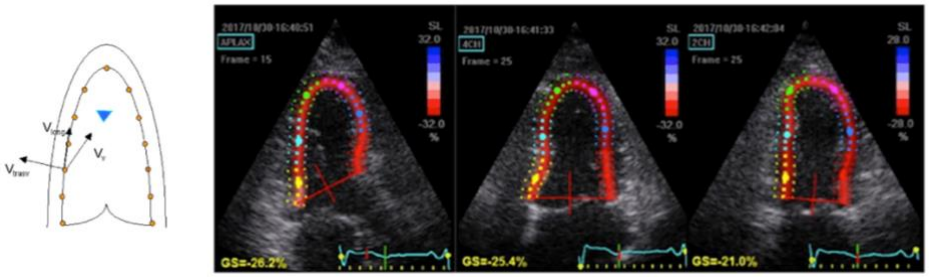

Figure 2.2. *Left: Velocities acquired during the analysis of the apical view. Vlong: longitudinal velocity, Vtrasv: radial velocity, Vv: velocity relative to a manually selected point of interest. Right: GLS measurements by 2D speckle tracking [163].*

Strain values can be calculated for each myocardial segment, typically divided into a 17-segment model. Depending on which strain point is used (e.g., peak systolic, end-systolic), different types of GLS can be obtained. Among these, the peak systolic GLS (PS-GLS) is most commonly used in clinical practice due to its high reproducibility and predictive power.

2.2.4 2D echocardiographic imaging acquisition and processing

The 2D image acquisition was performed using transthoracic echocardiography (TTE). During the examination, patients were positioned in the left lateral decubitus position to bring the heart closer to the chest wall and enhance apical imaging. Standard apical four-chamber (A4C) and apical two-chamber (A2C) views were obtained using a phased-array transducer.

To ensure accurate assessment of LV volumes, care was taken to avoid foreshortening of the apex, which can result in underestimation. It was essential that the long axis of the LV be fully visualized in both views, with the mitral valve and apex clearly defined and aligned in the same imaging plane.

Image optimization parameters were adjusted visually for each patient. For this reason, ranges are reported rather than fixed values. Depth was typically set between 10–20 cm, sector width between 60°–90°, and the focal zone positioned within 4–12 cm of depth. These settings were individually tailored: depth was visually adjusted to clearly display the myocardium while excluding most of the left atrium, focusing on the ventricle immediately below the mitral valve. This distance varies according to the acoustic impedance between the transducer and the heart, which is influenced by the thickness of the chest wall. Similarly, sector width was adapted to ensure all ventricular walls were adequately visualized in a single image. The focal zone was adjusted just below the region of interest to maximize the sharpness of the endocardial borders, again based on visual feedback and acoustic window quality.

Each acquisition covered the full cardiac cycle and included three consecutive heartbeats, synchronized with ECG gating to allow accurate identification of end-diastolic and end-systolic frames. End-diastole was defined as the frame showing the largest LV cavity, immediately before mitral valve closure, whereas end-systole corresponded to the frame with the smallest cavity, typically just prior to mitral valve opening.

For both A4C and A2C views, semi-automated contouring of the endocardial border of the LV was performed. Initially, the operator was prompted by the software to place basal and apical markers: in the A4C view, at the lateral and septal mitral annuli; and in the A2C view, at the inferior and anterior mitral annuli. An apical marker was then placed at the visible apex. Based on these points, the software generated a preliminary region of interest (ROI), which was subsequently reviewed and manually adjusted to align as closely as possible with the actual endocardial border. Special attention was paid to exclude trabeculations and papillary muscles from the LV cavity during tracing.

Simpson biplane method

The biplane method of disks, commonly referred to as the modified Simpson biplane method, is the current gold standard for assessing LVEF using 2D echocardiography, as endorsed by the American Society of Echocardiography [172]. This technique involves acquiring high-quality apical four-chamber and two-chamber views of the heart to allow visualization of the LV cavity in orthogonal planes. During image acquisition, it is critical to avoid foreshortening of the apex and to ensure clear visualization of the endocardial borders at both end-diastole and end-systole [73]. In this study, the endocardial borders in each view were semi-automatically traced, and the resulting contours were used to divide the LV into a stack of approximately 20 cylindrical disks. The volume of each disk was computed using the area-length formula, and total end-diastolic volume (EDV) and end-systolic volume (ESV) were calculated by summing the individual disk volumes. The LVEF was then derived using the formula:

$$LVEF = \frac{Stroke\ Volume}{EDV} \times 100 \qquad [2]$$

where stroke volume is calculated as the difference between EDV and ESV [73].

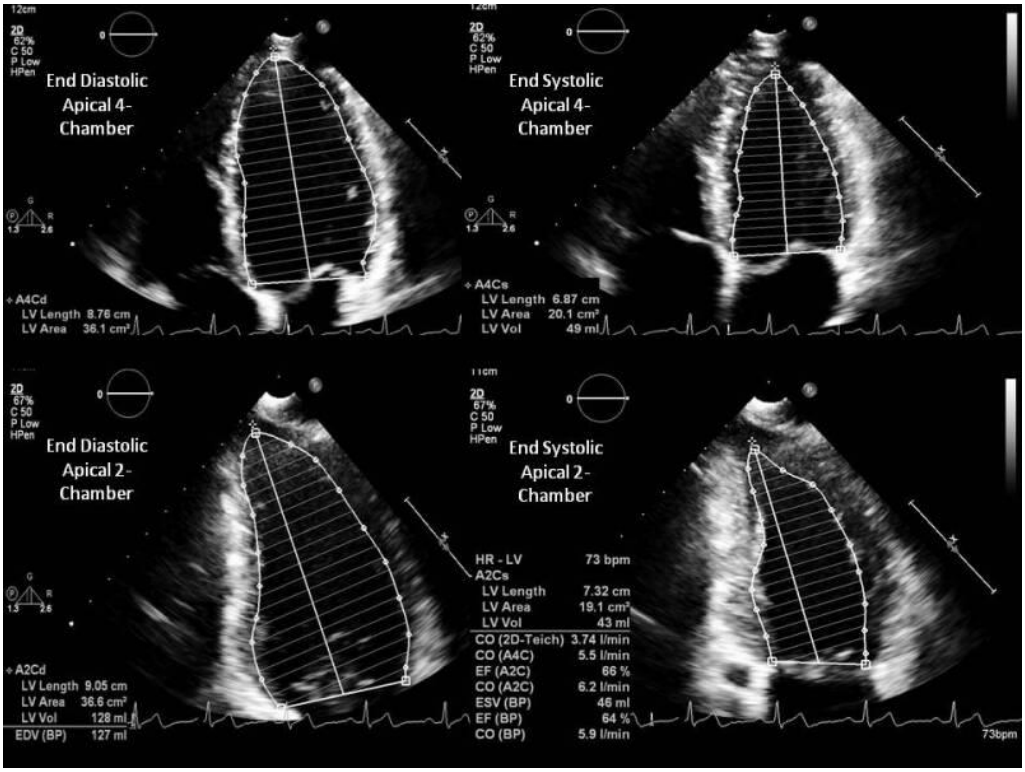

Figure 2.3. *Biplane Simpson Method. The end diastolic and end systolic apical 4- and 2-chamber views were used to estimate LV volume and calculate the ejection fraction [56].*

Compared to older techniques such as the modified Quinones method, which uses linear dimensions from a single plane and assumes a symmetric ellipsoidal LV geometry, the

Simpson method significantly reduces reliance on geometric assumptions and better captures regional and longitudinal contraction, thereby improving diagnostic accuracy, especially in the presence of wall motion abnormalities [172]. The Quinones method, while faster and requiring only mid-ventricular linear measurements, fails to account for asymmetric or segmental dysfunction, and relies on correction factors rather than direct measurements of apical contraction, making it less accurate in cases of ischemic cardiomyopathy or regional wall motion defects [172]. In contrast, the biplane method provides a more physiologically representative estimate of global LV function. Nevertheless, it is not without limitations. It is operator-dependent, more time-consuming, and requires good image quality for accurate tracing [173]. Moreover, errors can arise due to ventricular foreshortening if apical views are not properly aligned, although newer echocardiographic techniques and software aim to mitigate this issue [172]. Despite these challenges, the biplane Simpson method remains the preferred non-invasive modality for LVEF quantification in clinical practice and research due to its balance between accuracy, accessibility, and reproducibility [73,172].

2.2.5 2D STE echocardiographic imaging acquisition and processing

As with 2D echocardiographic acquisitions, all 2D STE acquisitions were also performed using TTE, with the patient positioned in the left lateral decubitus position. In this case, in addition to the A4C and A2C views, the apical three-chamber (A3C) or apical long-axis view was also acquired. As previously described, all views were required to include the entire left ventricular myocardium from base to apex, with clearly defined endocardial and epicardial borders. As in the previous case, particular care was taken to avoid apical foreshortening, which can lead to inaccurate speckle tracking and underestimation of strain values.

The frame rate was set to 80 frames per second to provide an optimal balance between temporal and spatial resolution. Once again, image optimization parameters were adjusted visually for each patient. The optimization settings included a medium gain level, an imaging depth between 10–20 cm, and a sector width between 60°–90°. Additionally, a narrow sector width and a single focal point, positioned at the mid-left ventricular level, were used to further support frame rate adequacy and tracking precision. Each acquisition included three consecutive cardiac cycles and was synchronized with ECG to ensure accurate identification of end-diastolic and end-systolic frames for precise strain analysis.

The echocardiographic data were subsequently processed offline using an acoustic tracking software that enables semi-automated analysis of myocardial deformation. The analysis workflow varies depending on the imaging view used during acquisition; in this case, an apical view was employed. In the apical view, specific anatomical landmarks are identified [174]:

- Left/Right base: the terminal points of the left and right endocardial borders.
- Midbase: the midpoint between the left and right base.
- Apex: the point most distant from the midbase, which can also be manually defined.
- Left/Right ROI: these represent the areas between the corresponding base point (left or right) and the apex.

For accurate tracking of the regions of interest, the software automatically detects the epicardial border, endocardial border, and the mid-myocardial line, which is computed as the average of the two aforementioned contours. During the analysis, these contours can be manually adjusted to optimize the delineation of the myocardial walls for each subject. Proper definition of these borders is essential for the computation of both tangential and radial components of myocardial strain parameters. Furthermore, the ROIs are divided into segments according to the selected analytical model.

In this study, the standardized 17-segment model of the left ventricle was adopted. Starting from the base, each basal and mid-ventricular segment was assigned a length equal to 2/7 of the total length of the corresponding ROI, while the apical region accounted for 1/7. The right and left apical zones were then combined into a single apical segment with a length comparable to the others, in accordance with the conventional segmentation model.

Subsequently, longitudinal strain was calculated for each of the 17 myocardial segments, based on the temporal variation in segmental length throughout the cardiac cycle. The measurement of longitudinal strain is based on the following formula [174]:

$$S_L(t) = \frac{L(t) - L_0}{L_0} \qquad [3]$$

where L_0 represents the length of a speckle-tracking kernel at end-diastole (typically corresponding to the onset of the QRS complex on the ECG), and L(t) is the length of the same kernel at any given time point t. Since L_0 corresponds to the maximal myocardial length, the strain curve typically exhibits a negative deflection during systole, reflecting myocardial shortening.

This deformation can be visualized over time using a strain-time curve (Figure 2.4), which includes the following key reference points [174]:

- P: peak positive strain (pre-systolic expansion).
- S: peak systolic strain.
- ES: end-systolic strain.
- PSS: post-systolic strain, which may occur after aortic valve closure and can be indicative of abnormal myocardial mechanics.

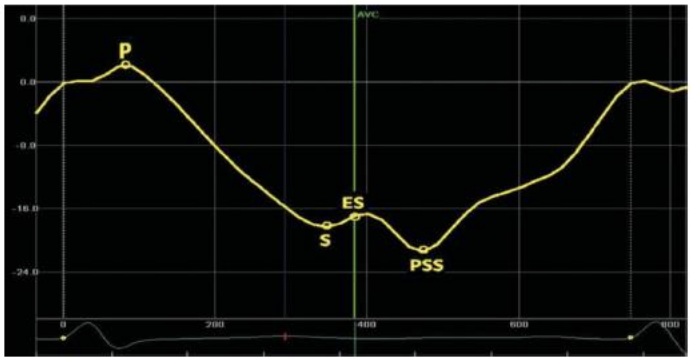

Figure 2.4. *Longitudinal strain trend over time. P: peak positive strain, S: peak systolic strain, ES: end of systolic phase, PSS: post-systolic strain [166].*

The peak systolic strain values from all 17 segments are then averaged to calculate the GLS, which is expressed as a percentage. More negative GLS values are associated with better myocardial function.

2.3 CT PERFUSION

Technological advances in functional imaging are rapidly expanding beyond the assessment of brain morphology and enabling diagnostic evaluation of cerebral hemodynamics, specifically cerebral perfusion. CTP studies have thus become a complementary technique alongside traditional "gold standard" functional imaging modalities such as positron emission tomography (PET) and single photon emission computed tomography (SPECT).

CTP is modeled using the kinetic tracer model, which assumes a single arterial input, capillary transit, and venous outflow, with the contrast remaining intravascular. Knowing the input and output functions allows estimation of tissue perfusion parameters. Perfusion is defined as the blood flow through a given volume of tissue over time. It is quantitatively described using the following parameters:

- Cerebral Blood Flow (CBF): the rate of blood passing through a given volume of brain tissue, encompassing flow within arteries, arterioles, capillaries, venules, veins, and arteriovenous shunts.
- Cerebral Blood Volume (CBV): the volume of blood contained in the tissue, including arterial and venous compartments, excluding stagnant blood.
- Mean Transit Time (MTT): the average time (in seconds) taken by blood to traverse the microvascular bed from arterial to venous end.

These parameters are interrelated by the central volume principle[175]:

$$CBF = \frac{CBV}{MTT} \qquad [4]$$

Perfusion CT relies on dynamic image acquisition following the administration of iodinated contrast and on the analysis of time-density curves obtained through deconvolution algorithms. The mathematical integration of these curves generates voxel-wise perfusion parameter maps, which visually represent regional variations in cerebral blood flow. Each pixel is color-coded based on the value of a specific parameter, enhancing the contrast between areas of differing perfusion levels [176]. The main perfusion parameters calculated and graphically represented include the aforementioned maps, CBF, CBV, and MTT, as well as two additional parameters:

- TTP (Time to Peak): the time required for the contrast agent to reach its peak concentration in the tissue.
- Tmax: the maximum delay between the arrival of the contrast bolus and the peak concentration within a specific voxel [177].

Moreover, one of the most clinically relevant features of CTP is its capacity to differentiate between two critical regions: the ischemic core and the ischemic penumbra [119].

- The ischemic core appears as a region of severely reduced perfusion, characterized by significantly decreased CBF and CBV, with a corresponding increase in MTT and Tmax.
- The ischemic penumbra, on the other hand, shows a less severe perfusion deficit, with reduced CBF and preserved or increased CBV due to compensatory vasodilation via collateral circulation. This tissue remains viable but is at high risk of infarction within 8–10 hours if not treated [119].

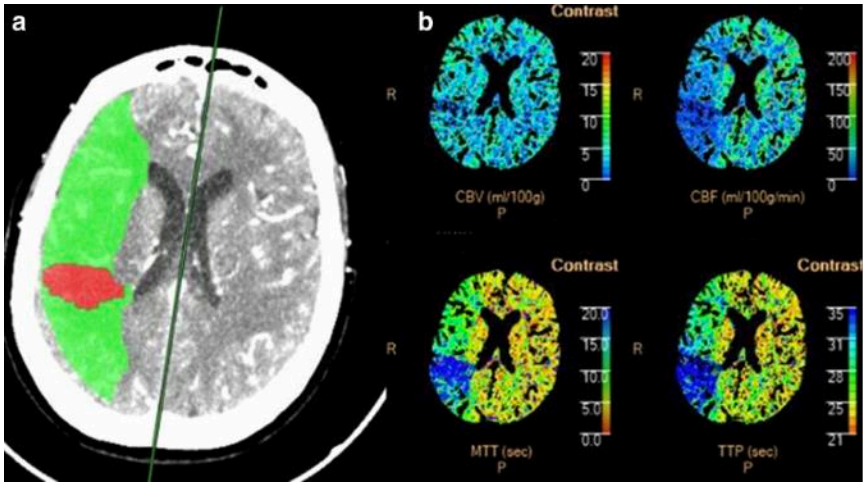

Figure 2.5. CTP maps showing core and penumbra regions.

Additionally, a region of benign oligemia can often be identified surrounding the penumbra. This area exhibits moderate hypoperfusion but is not at risk of infarction and does not require active reperfusion, as it is expected to recover spontaneously [119].

2.3.1 CTP Image Acquisition, Image Processing and Perfusion Analysis

CTP is feasible on spiral CT scanners capable of cine-mode acquisitions [175]. Functional information is obtained by dynamically scanning the brain during the intravenous injection of a contrast bolus via a power injector. When available, a dual-barrel injector is preferred, as it enables a rapid saline flush following contrast administration, thereby increasing bolus compactness and peak enhancement.

In brain CTP, iodinated contrast media improve differentiation between tissues of similar baseline densities. Typically, 35–45 mL of high-concentration contrast agent (350–370 g/mL [178]) is injected at 3–7 mL/s, followed by 20–40 mL of saline at the same rate. This protocol maximizes enhancement and optimizes the signal-to-noise ratio (SNR) for perfusion map generation [178]. Scanning begins immediately before injection to acquire a baseline dataset.

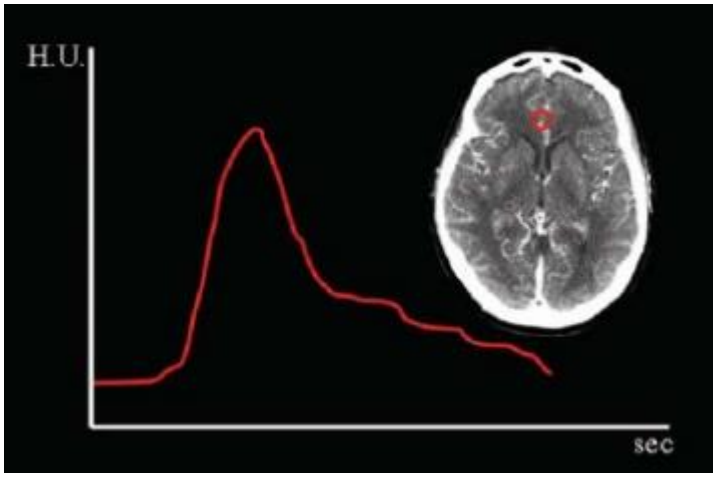

Figure 2.6. *Example of a time-density curve (TDC) generated from the anterior cerebral artery ROI.*

CTP captures the first pass of the contrast bolus through the cerebral capillary bed [124]. Repeated scans over 1–3 minutes enable the generation of time–attenuation curves (TACs), also known as time–density curves (TDCs), based on the proportionality between tissue density and X-ray attenuation [124]. These curves reflect signal intensity before, during, and after contrast injection.

Protocol optimization requires balancing SNR and radiation dose, which depend on tube voltage (kV), current (mAs), scan interval, contrast volume and rate, axial coverage, and acquisition duration [179]. In brain CTP, low peak voltage (≈80 kV) and moderate current (100–200 mAs) are recommended to limit dose while preserving diagnostic quality. Typical doses range from 1.2 mSv to 3.4 mSv, comparable to a standard brain CT (~2.5 mSv). Temporal resolution below 3 s per frame is advised; a 3 s interval with a 40 mL bolus at 4 mL/s provides a good compromise between accuracy and dose [179]. Acquisition usually lasts 50–60 s to cover the first pass, but may be extended to 120–150 s to assess blood–brain barrier (BBB) permeability and kinetic parameters. Raw data are inherently 4D (3D over time), with reconstruction at 10 mm slice thickness (from original 5 mm) to improve SNR.

Post-processing begins with quality control, addressing artifacts such as motion, beam hardening, and partial volume effects [179]. Minor motion can be corrected by automatic coregistration. Beam hardening, caused by preferential attenuation of low-energy photons, produces streak artifacts but is usually mitigated by commercial CT software. Partial volume effects, due to mixed-density structures within a voxel, can be reduced only by thinner slices, at the expense of SNR.

Following artifact correction, an arterial region of interest (ROI) is placed to obtain the arterial input function (AIF), a TDC describing contrast distribution. The first-pass phase corresponds to the interval from injection to the onset of recirculation, followed by the interstitial phase. A typical AIF shows a steep rise and fall within ~50 s. Some software platforms apply thresholds to exclude cerebrospinal fluid and vascular signals, isolating parenchymal perfusion [180].

Quantitative perfusion parameters (CBF, CBV, MTT, Tmax) are computed voxel-by-voxel using semi-automated methods that perform mathematical modeling after initial manual input. Two main computational approaches are used: maximum slope model and deconvolution models.

Maximum Slope Model

Now mostly obsolete due to its relative (non-quantitative) outputs, the maximum slope method uses the ascending limb of the TDC to estimate:

$$CBF = \frac{maximum\ slope\ of\ Q(t)}{maximum\ height\ of\ Ca(t)} \qquad [5]$$

$$CBV = k \cdot \frac{area\ sottostante\ la\ curva\ nella\ ROI\ parenchimale}{\text{area sottostante la curva nella ROI vascolare}} \qquad [6]$$

where Q(t) denotes the amount of CA in the local vascular network, Ca(t) represents the arterial CA concentration over time, and k accounts for differences in red blood cell concentration between peripheral and tissue blood [181].

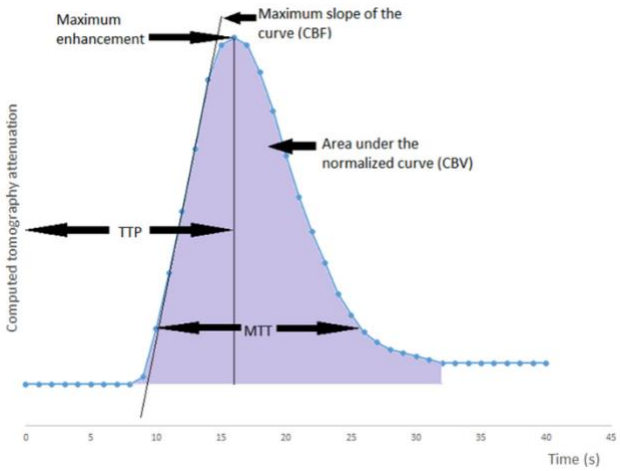

Figure 2.7. *Maximum Slope model showing derivation of perfusion parameters from TDC.*

This model assumes a very rapid contrast injection and is appreciated for its simplicity and speed. However, it lacks the precision and quantitative rigor of deconvolution methods [176].

Deconvolution Models

Deconvolution-based methods, which compare each voxel's TDC with the arterial input (AIF), offer quantitative, PET- and SPECT-validated outputs and tolerate lower contrast injection rates (3–5 ml/s) [176]. Manual AIF selection is often performed using a voxel in the anterior cerebral artery that is almost entirely intravascular [175]. A venous ROI is also placed to extract the venous output function (VOF).

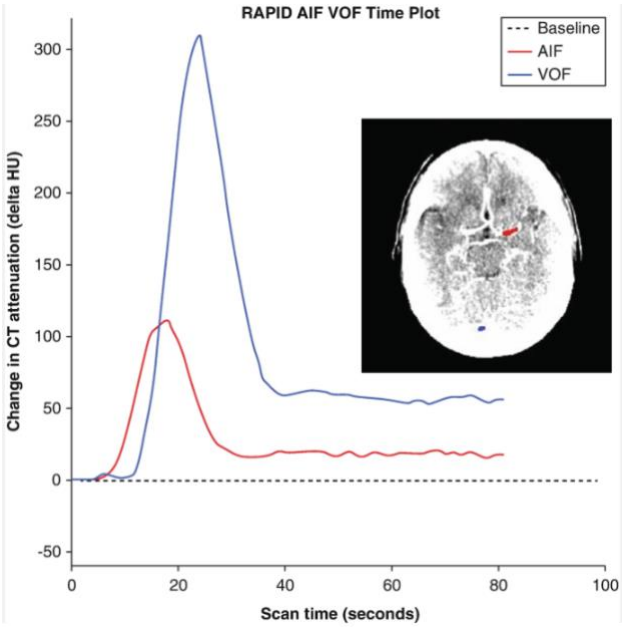

Figure 2.8. *Manual selection of AIF and VOF with resulting TDCs.*

The deconvolution process yields the impulse residue function (IRF), a corrected TDC that removes bolus dispersion effects. The concentration-time curve is modeled as:

$$Q(t) = F \cdot Ca(t) \otimes R(t), \qquad [7]$$

where Q(t) is the tissue TDC, Ca(t) is the AIF, F is CBF, and R(t) is the IRF. A scaled version of IRF, RF(t), is typically used to reflect local tissue hemodynamics independently of arterial input.

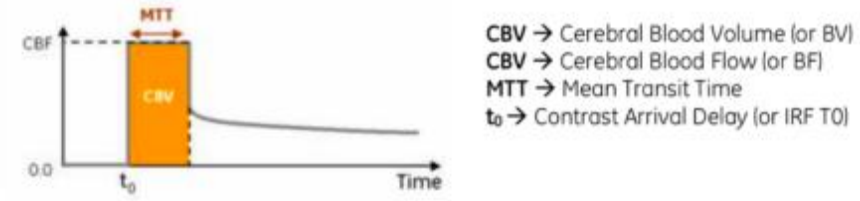

Figure 2.9. *Impulse Residue Function (IRF) used to derive quantitative perfusion parameters.*

There are three main deconvolution algorithms commonly used to analyze perfusion data: the Fourier-based deconvolution, the plug-flow contrast model, and the Johnson-Wilson-Lee model [182]. The Fourier-based method operates in the frequency domain, using mathematical transformations to estimate the tissue residue function by deconvolving the arterial input function from the observed tissue response. In Fourier deconvolution, CBF is the peak of the IRF, CBV is the area under the curve, MTT is derived via the central volume principle, and Tmax is the time-to-peak of the IRF (Figure 2.9). It is computationally efficient but can be sensitive to noise. The plug-flow contrast model, on the other hand, assumes a simplified, idealized flow where contrast moves uniformly through the vascular system without dispersion. While less physiologically accurate, it offers a straightforward

and fast approximation of perfusion parameters. The Johnson-Wilson-Lee model introduces a more complex, physiologically grounded approach, incorporating parameters such as capillary permeability and blood–brain barrier integrity. This model enables a more detailed interpretation of tissue microcirculation, particularly in pathological conditions.

In particular, in this research, all CTP scans were acquired using a 256-slice Philips Brilliance iCT scanner (Philips Healthcare, Best, The Netherlands) at 80 kVp and 150–200 mAs. At the beginning of each scan, 75 mL of contrast agent was administered intravenously at a rate of 4 mL/s, followed by a 40 mL saline flush. Whole-brain axial three-dimensional acquisitions were reconstructed with 5 mm slice thickness. Each individual scan lasted 4 seconds, with a total acquisition time of 60 seconds.

Image processing was performed using the Extended Brilliance Workstation v4.5 (Philips Medical Systems, Best, The Netherlands) and further developed in MATLAB (MathWorks Inc., Natick, MA, USA). Perfusion maps, MTT, CBV, and CBF, were generated from the source CTP images. To obtain a mathematical representation of the time-density curves for each voxel, a Gaussian curve-fitting method based on the least squares algorithm was applied. One arterial input and one venous output were selected, and a convolution algorithm was subsequently applied to generate the MTT map. The CBV map was computed as the area under the time-attenuation curve, while the CBF map was derived by calculating the ratio of CBV to MTT.

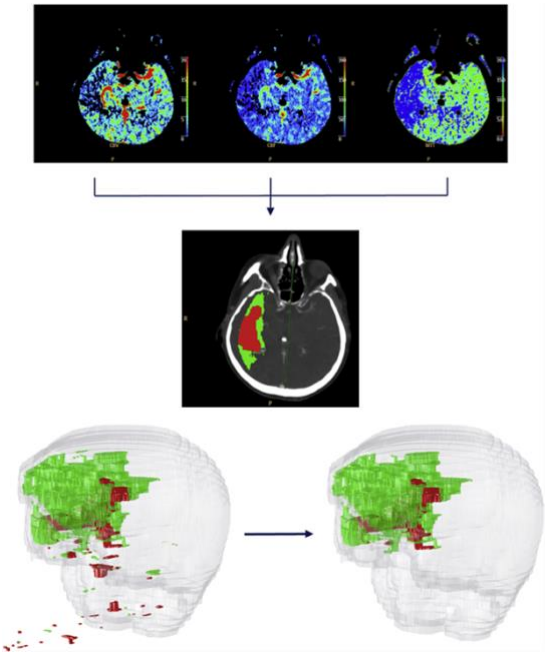

Figure 2.10. *CTP Image Processing.*

2.4 ARTERIAL SPIN LABELING

ASL is an advanced MRI technique used for the non-invasive quantification of cerebral perfusion, conventionally expressed in milliliters of blood per 100 grams of tissue per minute (mL/100 g/min). This parameter enables the assessment of perfusion within a physiological range, typically from 0 to 100 mL/100 g/min.

ASL is inherently non-invasive due to its use of an endogenous contrast agent, namely, magnetically labeled water protons within arterial blood, achieved via the application of tailored radiofrequency (RF) pulses. Labeling is typically performed at the level of the cervical arteries through magnetic inversion of inflowing blood spins.

Three main ASL techniques have been developed, each differing in the temporal characteristics and type of RF pulse used for labeling: pulsed ASL (pASL), continuous ASL (cASL), and pseudo-continuous ASL (pcASL)[183]. In pASL, a single RF pulse labels blood within a defined spatial region, independent of flow duration. In contrast, cASL applies a prolonged RF pulse over a defined period, continuously labeling the flowing blood. pcASL, currently regarded as the preferred approach and endorsed by the ASL White Paper, approximates continuous labeling by employing a series of discrete RF pulses interleaved with gradient pulses, thereby improving labeling efficiency while maintaining hardware compatibility with standard clinical MRI systems.

The pcASL labeling mechanism is illustrated in Figure 2.11. Water molecules within arterial blood exhibit a spatial gradient as they travel from the neck to the brain. When subjected to a constant magnetic gradient in the direction of blood flow, their local resonance frequency is altered. Concurrently, a train of RF pulses is applied at a specific labeling plane. Inversion of the magnetization occurs when the shifted resonance frequency of the flowing spins coincides with the frequency of the applied RF pulse.

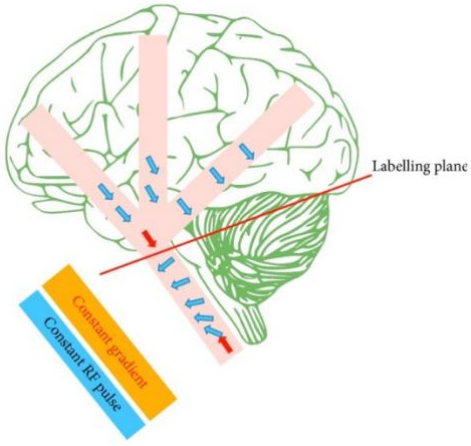

Figure 2.11. *Magnetic inversion in pcASL: a constant gradient shifts blood water resonance; RF pulses at the labeling plane invert spin magnetization [175].*

ASL image acquisition involves the generation of two image types (Figure 2.12):

- The label image, acquired after the labeled blood has perfused the brain tissue.

- The control image, acquired in the absence of labeling and serving as a baseline reference.

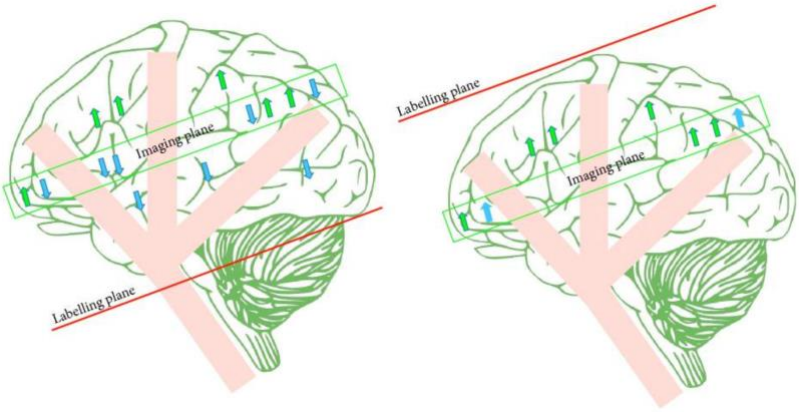

Figure 2.12. *Labeling and imaging planes during label (left) and control (right) acquisitions. Green: static tissue; blue: labeled blood water [175].*

The PLD represents the interval between the conclusion of the labeling pulse and the image acquisition, allowing time for labeled blood to reach the imaging region. The label duration refers to the length of time over which the labeling RF pulse is applied. The sum of these two parameters defines the inversion time (TI), a critical factor influencing the quantification of perfusion[183]:

$$TI = PLD + label\ duration \qquad [8]$$

ASL offers several methodological advantages. It enables the absolute quantification of perfusion in physiological units, facilitates the simultaneous acquisition of co-registered anatomical and functional data, and, most importantly, permits repeated measurements within the same imaging session due to its non-invasive nature and lack of exogenous contrast agents. Nonetheless, ASL also presents certain limitations. The rapid T1 relaxation of labeled spins reduces signal longevity, which can be particularly problematic in patients with slow cerebral blood flow or in the presence of neurovascular disorders. Furthermore, ASL typically exhibits a low SNR, primarily due to its inherently low spatial resolution and limited imaging time.

2.4.1 Perfusion Quantification

The analysis of images acquired through the ASL technique involves three primary steps:

- subtraction of the label and control images,
- kinetic model inversion, and
- calibration.

The first step involves subtracting the label and control images to eliminate the signal from static brain tissue, thereby isolating the signal originating from the labeled blood. However, this subtraction process results in a highly noisy image. To address this, phase-synchronized averaging is applied during acquisition. Specifically, an equal number (greater

than one) of label and control image pairs must be acquired and subtracted. A subsequent averaging process is then performed to obtain the final perfusion-weighted image. The resulting image represents the perfusion signal at each voxel; however, the signal intensity does not yet provide an absolute quantitative measure.

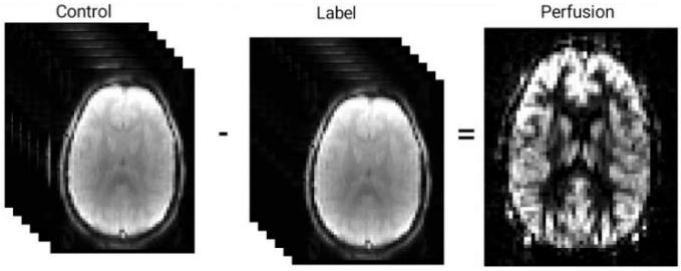

Figure 2.13. *Subtraction of label and control images to obtain the perfusion-weighted image.*

The second step involves kinetic model inversion, which enables analysis of the tracer's dynamic behavior and is expressed mathematically in:

$$\Delta M(t) = AIF(t) * r(t) \cdot F \qquad [9]$$

This equation describes the convolution of the arterial input function (AIF(t)) with the tissue residue function r(t), scaled by the blood delivery rate F.

The arterial input function models the temporal profile of the labeled blood as it travels from the labeling plane to the voxel, taking into account the arterial transit time (ATT), the label duration (defining the width of AIF(t)), and the T1 relaxation time, which reflects signal decay based on the chosen labeling method. As a result, the perfusion signal arriving at the tissue is temporally delayed and reduced in amplitude. The residue function, on the other hand, describes the behavior of the endogenous contrast agent after it reaches the voxel. It typically exhibits exponential decay, under the assumption that the labeled water distributes uniformly in a single tissue compartment, with no dispersion of the bolus, and with a known T1 relaxation time.

Calibration, the final step, is required to express the perfusion signal in absolute units of ml/100g/min. This step involves determining the amplitude of the arterial input function, which depends on the magnetization of arterial blood (denoted as M_0a). Since M_0a cannot be measured directly, it is estimated using an image acquired without labeling or background suppression that reflects the tissue magnetization (M_0t). These values are related by

$$M_0 a = \frac{M_0 t}{\lambda}, \qquad [10]$$

where λ represents the tissue–blood partition coefficient.

Additionally, the calibration must account for the labeling efficiency parameter α, which compensates for imperfect inversion of the blood spins. The M_0a image must also be proton-density weighted (i.e., it should reflect the apparent water proton concentration in each voxel) and acquired with a long repetition time (TR > 5 seconds) to ensure full relaxation. The calibration modifies the kinetic model inversion formula, as shown in Figure 2.14, and is described mathematically by

$$Perfusion\left(\frac{\frac{ml}{100g}}{min}\right) = \frac{perfusion}{M_0 a} \cdot 6000 \qquad [11]$$

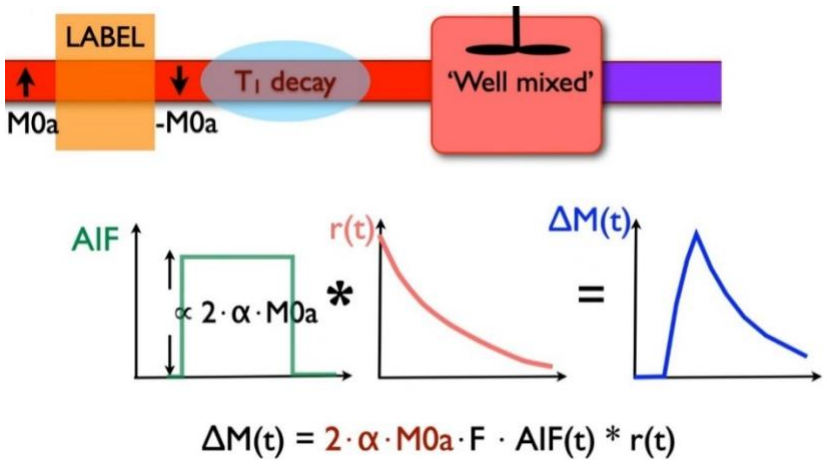

Figure 2.14. *Calibrated kinetic model inversion framework. Illustration of the kinetic model inversion incorporating calibration parameters to enable quantitative estimation of cerebral blood flow in absolute units (ml/100g/min).*

Taking into account the image subtraction, kinetic modeling, and calibration, the final perfusion quantification formula is given in

$$CBF = \frac{6000 \cdot \lambda \cdot (SI_{control} - SI_{label}) \cdot e^{\frac{PLD}{T_{1,blood}}}}{2 \cdot \alpha \cdot T_{1,blood} \cdot M_0 t \cdot \left(1 - e^{-\frac{\tau}{T_{1,blood}}}\right)}, \qquad [12]$$

where $SI_{control}$ rapresent control images, SI_{label} label images and the ratio $\frac{e^{\frac{PLD}{T_{1,blood}}}}{\left(1-e^{-\frac{\tau}{T_{1,blood}}}\right)}$ depicts the kinetic model inversion.

For accurate analysis, the White Paper recommends the following parameter values:

- T_1,tissue = T_1,blood = 1.65 s (3T),
- α = 0.85,
- λ = 0.9 ml/g,
- Label duration = 1.8 s.

In ASL studies, data from individuals with the same pathology may be aggregated to investigate differences or changes in perfusion. However, consistency across images must be ensured. This requires two forms of coherence: spatial and intensity. Spatial coherence involves the normalization of perfusion maps into a common space so that corresponding brain regions align across subjects. Intensity coherence requires the use of quantitative maps in ml/100g/min, which depend on accurate calibration data. Furthermore, intensity

normalization relative to reference values for white and gray matter is necessary to minimize inter-subject variability.

2.4.2 Image correction techniques

In ASL imaging, several artifact correction techniques are employed as part of either the pre-processing or post-processing stages, with the goal of improving the quality and accuracy of CBF quantification. Two of the most commonly used techniques are Partial Volume Correction (PVC) and Motion Correction (MC).

PVC aims to adjust CBF images by accounting for the mixed contributions of different tissue types within each voxel, namely, gray matter (GM), white matter (WM), cerebrospinal fluid (CSF), and the macrovascular component. This technique allows for the generation of separate perfusion maps for gray and white matter. Since voxels inevitably contain a mixture of tissues with different perfusion values, failing to correct for these contributions may lead to an underestimation of gray matter perfusion.

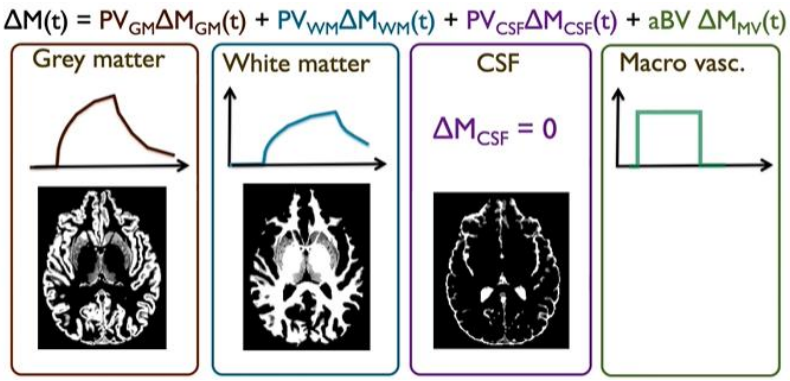

Figure 2.15. *Kinetic model inversion incorporating multiple components.*

This problem can be addressed by modeling multiple tissue components, each with its own perfusion kinetics. Tissue fractions are estimated from the segmented anatomical image, which is then resampled to match the ASL resolution. In the case of multi-PLD (Post Labeling Delay) acquisitions, differences between GM and WM involve not only perfusion values but also kinetic parameters such as ATT and the longitudinal relaxation time (T1). The CSF is typically ignored in the perfusion estimation, as its contribution is negligible. The macrovascular signal becomes problematic when the labeled blood has not yet arrived at the tissue at the time of image acquisition and is still present in large vessels or capillaries; a practical solution is to use a sufficiently long PLD to allow complete delivery of labeled blood.

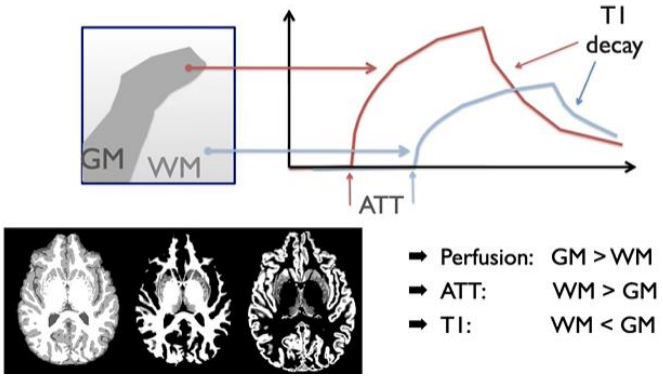

Figure 2.16. *Partial volume correction based on kinetic data.*

MC, on the other hand, addresses motion-related artifacts in ASL data that may arise during image acquisition. This process involves realigning image volumes. To effectively eliminate static tissue signal and enhance the perfusion-weighted contrast, it is essential to apply both background suppression and motion correction. The motion correction algorithm typically uses a rigid-body registration approach with six degrees of freedom (translations and rotations along the x, y, and z axes). Furthermore, it plays a critical role in differentiating between true perfusion signal and apparent motion in multi-PLD datasets, especially in the subtraction of control and label images, where small misalignments may be interpreted as motion artifacts.

In this research, all subjects, both stroke patients and stroke mimics, were scanned on an Ingenia 3T MRI scanner (Philips Health- care, Best, The Netherlands) using a 32-channel head coil. High-resolution whole brain anatomic images were acquired using 3D T1-weighted (3DT1w) scan with TR=8.4 ms, TE=3.9 ms, flip angle=8°, voxel size=1×1×1 mm3 and 180 slices.

ASL-MRI was performed using the pcASL with label duration = 1800 ms, PLD = 2000 ms. 3D gradient and spin-echo (GraSE) pCASL scans with background suppression were obtained with TR/TE = 4.1 s/13 ms, FOV = 240 × 240 mm2, matrix size = 80 × 75, voxel size = 3 × 3 × 5 mm3, 20 slices, flip angle = 90°. Seven label/control image pairs were acquired as well as one calibration M0 image with no background suppression. All subjects were asked to rest and to keep their eyes closed during data acquisition. Stroke patients and stroke mimics were acquired using exactly the same imaging protocol on the same MRI scanner.

The individual steps of ASL data processing and analysis were performed using FSL 6.0.5 (FMRIB, Oxford, United Kingdom) including Bayesian Inference for Arterial Spin Labelling MRI (BASIL) [184]. The head motion correction was carried out with MCFLIRT, non-brain tissue removal was performed with a brain extraction tool (BET). Spatial smoothing was also applied [185]. CBF maps were quantified from perfusion-weighted images (averaged pairwise subtracted control label images) by applying the general kinetic model [186] according to the ASL white paper [187] using voxel-wise calibration with the M0 image. To correct the partial volume effect spatially regularised technique was applied [188]. For each subject native space CBF maps were spatially normalised into the Montreal

Neurological Institute—MNI152 standard-space (2-mm T1-weighted average structural template image).

2.5 ELECTROENCEPHALOGRAPHY

EEG is a non-invasive neurophysiological technique that enables the recording of brain electrical activity with high temporal resolution. It is widely employed in both experimental and clinical settings, particularly for real-time monitoring of brain function in critical contexts, such as the acute phase of stroke.

EEG measures fluctuations in electrical potential resulting from the simultaneous activation of neuronal populations [189]. These fluctuations can be characterized in terms of spectral content (EEG frequency bands or rhythms) or time-domain features (event-related or evoked potentials).

The component waves of the EEG signal are typically classified based on their frequency, as notable variations in this parameter are readily detectable and can serve as fundamental markers for distinguishing physiological from pathological rhythms, or as indicators of specific functional states depending on the clinical or experimental context. Classically, EEG signals are divided into five major frequency bands: Delta (δ) 0.5–4 Hz, Theta (θ) 4–8 Hz, Alpha (α) 8–12 Hz, Beta (β) 12–30 Hz, and Gamma (γ) >30 Hz. Further subdivision into sub-bands is often applied for more refined analyses. Each frequency band conveys distinct information regarding brain function and synchrony.

The Delta band is typically observed during deep non-REM sleep (especially stage N3) and is also associated with physiological restoration processes. Delta activity can also emerge in pathological states such as brain injury or coma. Theta frequencies are associated with the early stages of sleep (N1), deep relaxation, creativity, memory-related processes, and sometimes emotional variability. The Alpha band characterizes a relaxed wakeful state, particularly with closed eyes and in the absence of significant cognitive demands. Beta activity reflects active mental engagement, attention, and problem-solving. Lastly, Gamma frequencies (>30 Hz) are linked to higher-order cognitive functions, such as attention, memory, and complex multisensory integration [190].

Finally, EEG has demonstrated high sensitivity to acute changes in cerebral blood flow (CBF) and neuronal metabolism, making it a valuable tool for investigating neurovascular coupling, i.e., the relationship between neuronal activity and cerebral perfusion. It is well established that CBF reduction in ischemic regions induces marked alterations in the EEG signal, characterized by a significant increase in Delta power and a concurrent reduction in Alpha power [17].

2.5.1 EEG Acquisition and Signal Analysis

EEG signals are acquired using an electroencephalograph, consisting of an acquisition unit, a processing unit, and a display system. Surface electrodes are placed on the patient's scalp using adhesives, conductive pastes, or EEG caps. The most common electrode types include cup electrodes (Sn/AgCl), stainless steel ring electrodes, and disposable Ag/AgCl adhesive electrodes [189].

To ensure standardization and data comparability, the "10–20 system" is employed for electrode placement, involving 16 to 32 electrodes distributed according to defined percentages of cranial distances (nasion-inion and interaural lines). Electrode labels correspond to cortical regions (F = frontal, T = temporal, C = central, P = parietal, O = occipital), with odd numbers referring to the left hemisphere and even numbers to the right. EEG montages can be unipolar, using a common reference electrode (e.g., Cz or mastoids), or bipolar, where the potential difference between pairs of electrodes is measured. Specific configurations, such as anterior–posterior, transverse, or symmetric montages, are selected based on diagnostic requirements [190]. Electrode impedance must be kept below 5 kΩ to ensure high-quality signal acquisition.

The sampling rate depends on the clinical application; however, typical values are 128, 256, or 512 Hz to ensure adequate temporal resolution and faithful representation of the EEG signal [189].

EEG signal analysis consists of several stages: raw signal acquisition, artifact removal, filtering, analog-to-digital conversion, and ultimately clinical classification. Artifacts may arise from patient movements, interfering biological signals, device malfunction, or environmental electromagnetic noise [191].

In the time domain, the analysis focuses on the morphological characteristics of brain waves, examining changes associated with specific events. In the frequency domain, instead, the power spectrum is evaluated, which represents the relative intensity of the various frequency components. The power spectrum can be estimated either directly from the signal data using non-parametric methods or from a signal model using parametric methods. Non-parametric methods can be further subdivided into direct methods, which estimate the spectrum directly from the data, and indirect methods, which first compute the signal's autocorrelation function and then apply its Fourier transform.

The primary non-parametric direct method for power spectrum estimation is Schuster's periodogram, which, for a signal x(n), estimates the power spectral density as:

$$\hat{P}(f) = \frac{1}{NF_s}\left|\sum_{n=0}^{N-1} x(n)e^{-\frac{j2\pi fn}{F_s}}\right|^2 \qquad [13]$$

where F_s is the sampling frequency.

However, this method suffers from poor statistical consistency, as the variance does not approach zero as the number of samples N increases. Therefore, alternative methods such as Bartlett's and Welch's are preferred. These methods divide the signal into segments using a windowing function before computing the periodogram. Bartlett's method partitions the signal into K equal-length segments, computes the periodogram of each segment, and averages the resulting K periodograms. As the number of samples increases, so does the number of segments, leading to more averaging and, consequently, reduced variance. However, this comes at the cost of frequency resolution, since each segment is shorter than the original signal. Welch's method, like Bartlett's, divides the signal into K segments and averages the corresponding periodograms to obtain a consistent spectral estimate. Unlike Bartlett's method, Welch applies a non-rectangular window with smoother transitions at the

edges, which helps reduce spectral leakage, artificial spreading of energy across frequencies caused by the convolution of the signal spectrum with that of the window. Welch's method also employs segment overlap, which minimizes information loss due to attenuation at segment boundaries and allows for more averaging.

Ideally, a window's spectrum should have a narrow main lobe to prevent local smearing of the signal spectrum and low-power side lobes to avoid leakage into other frequencies. However, reducing side-lobe power generally increases the main lobe's width, leading to a trade-off between frequency resolution and spectral leakage.

The rectangular window has the narrowest possible main lobe but relatively high-power side lobes (only 6 dB attenuation between the main lobe and the first side lobe), resulting in minimal dispersion of energy for pure harmonics but substantial leakage for non-harmonic components. Among non-rectangular windows, the Hamming and Hann (also known as Hanning) windows are commonly used. Both belong to the class of raised cosine windows. The Hamming window is defined by:

$$w(n) = 0.54 - 0.46\cos\left(2\pi\frac{n}{N-1}\right), 0 \le n \le N-1 \qquad [14]$$

while the Hann window is given by:

$$w(n) = \frac{1}{2}\left[1 - \cos\left(2\pi\frac{n}{N-1}\right)\right], 0 \le n \le N-1 \qquad [15]$$

This results in a cosine-shaped window with maximum amplitude at the center and zero at the edges.

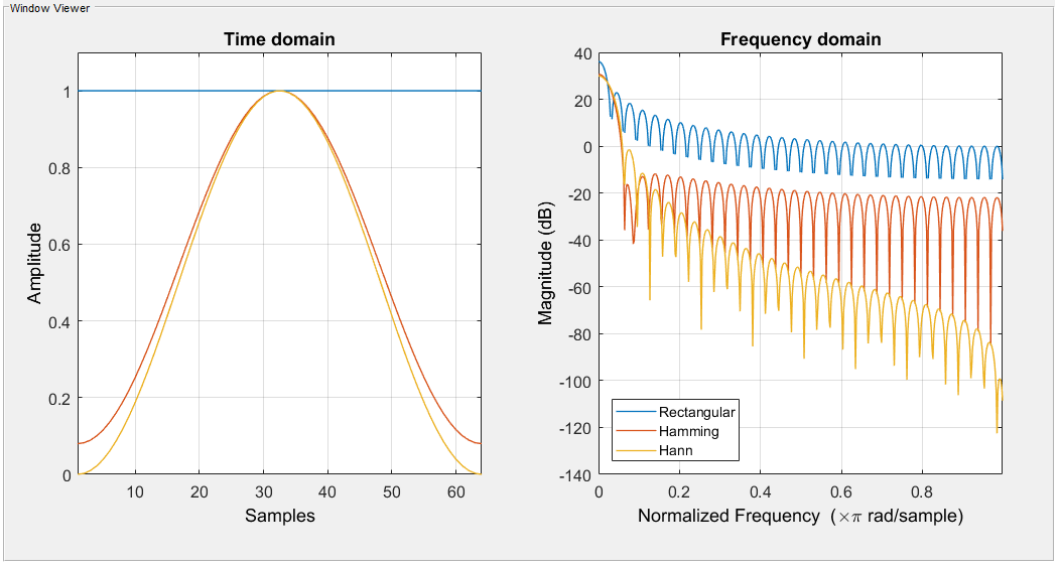

Figure 2.17. Time-domain (top) and frequency-domain (bottom) representations of the rectangular (blue), Hamming (red), and Hann (yellow) windows.

As shown in Figure 2.17, the Hamming and Hann windows are similar in the time domain but differ in the frequency domain. Both show reduced side-lobe energy compared

to the rectangular window. However, in the frequency domain, the Hann window initially exhibits higher side-lobe power than the Hamming window, but this power decreases more rapidly at higher frequencies.

In this thesis, all patients underwent bedside electroencephalographic monitoring using a Be Plus PRO amplifier (EB NEURO, Florence, Italy) with a 19-channel electro-cap equipped with Ag/AgCl electrodes, following the 10-20 system, for a recording duration of 20–30 minutes. Electrode impedance was maintained below 5 kΩ, and the sampling frequency was set at 128 Hz. In some studies, EEG recordings were visually inspected with a computer-based system from the Neurophysiology Unit of the Neurology Clinic (Galileo NT, Eb Neuro S.p.A.) to identify clinically significant epileptiform patterns and alterations in EEG rhythms. The time passed between stroke onset and the initial EEG examination was recorded.

Off-line EEG analysis was performed using in-house scripts developed in MATLAB (MathWorks Inc., Natick, MA). Each signal was filtered with a second-order Butterworth bandpass filter with cutoff frequencies set to 0.5–40 Hz.To estimate the PSD of each EEG electrode, Welch's method was chosen due to its superior performance compared to the simple periodogram. Specifically, the Hann window was employed with a 50% overlap between segments.

Using 20-second intervals, the PSD was computed for each electrode. Absolute power values were calculated for each spectral band (delta: 1–4 Hz; theta: 4–8 Hz; alpha: 8–13 Hz; beta: 13–30 Hz). The absolute power of a frequency band is defined as the integral of the PSD over the frequency range of that band. However, absolute power values may vary across subjects and depend on acquisition conditions. Therefore, relative power was also calculated, defined as the ratio between the absolute power in the band of interest and the total power in the 1–30 Hz range (computed as the integral of the full spectrum).

Finally, two EEG-derived indices were also computed: DAR (Delta/Alpha Ratio) and DTBAR (Delta+Theta)/(Beta+Alpha) Ratio.

2.6 MACHINE LEARNING ALGORITHMS

ML is a computational paradigm that focuses on the development of predictive models capable of learning from data to perform tasks such as decision-making or forecasting, without being explicitly programmed for each specific function. Through the identification of latent patterns and statistical regularities within datasets, ML algorithms can autonomously adapt their internal representations and progressively improve their performance as they are exposed to new information. The methodological framework of ML integrates both classical statistical approaches and modern computational techniques to address a variety of problems, including regression, classification, and, in some cases, data generation. A fundamental objective of ML is generalization, namely the ability to infer underlying relationships from training data and apply them effectively to previously unseen instances. ML techniques are typically categorized according to criteria such as the availability of labeled data, distinguishing between supervised and unsupervised learning, and the nature of the output, whether continuous, categorical, or structural (e.g., clusters). The ML pipeline generally comprises several essential phases: data preprocessing, aimed at

optimizing the quality and structure of the input data; model training, during which algorithms infer predictive rules from labeled examples; model evaluation, which assesses generalization performance using independent test data; and, finally, deployment for real-world prediction, where the trained model is applied to solve practical tasks in an automated or user-assisted setting.

The capacity to learn from experience renders ML particularly suitable for complex domains characterized by high-dimensional and heterogeneous data, such as medical diagnosis and prognosis. Nevertheless, clinicians remain concerned about the limited interpretability of these models, as they often lack transparency at the level of individual input features. Consequently, interpretable models that not only generate diagnostic outputs but also facilitate an intrinsic evaluation of their own validity are preferred within the medical field [154].

2.6.1 Classification tree

The classification tree [192], commonly referred to as a decision tree classifier, represents a fundamental and widely used method for predicting categorical outcomes through recursive data partitioning based on feature-specific decision rules. Conceptually, the classification tree can be envisioned as a hierarchical structure where internal nodes correspond to decision points derived from feature values, branches indicate the possible outcomes of these decisions, and leaf nodes denote the final predicted class labels. This method aims to generate subsets of data that are increasingly homogeneous with respect to the target variable, thereby facilitating accurate classification.

The construction of a classification tree proceeds through two principal phases: tree growth and pruning. During the growth phase, the tree is expanded iteratively by selecting splits that maximize the purity of the resulting nodes, ideally leading to terminal nodes that contain instances of a single class. This process continues recursively, partitioning the dataset until pre-defined stopping criteria, such as a minimum number of observations per node or a maximum tree depth, are met. Following the growth phase, pruning is performed to mitigate overfitting by removing branches that do not substantially contribute to predictive accuracy. Pruning is guided by a cost-complexity function, which balances the complexity of the tree against its classification error, ultimately identifying the optimal subtree that minimizes this trade-off.

A critical aspect of tree construction is the selection of the splitting criterion, which determines how the data is partitioned at each node. Depending on the nature of the target variable, different metrics are employed:

- Information Gain. For categorical target variables, information gain is used to evaluate the reduction in entropy or uncertainty resulting from a potential split. Entropy quantifies node impurity, with a pure node exhibiting instances belonging exclusively to one class. Information gain measures the difference in entropy before and after the split, and the feature that yields the highest information gain is chosen to partition the node.
- Mean Squared Error (MSE). For numeric or continuous target variables, MSE serves as the impurity measure. It calculates the average of the squared deviations between

observed and predicted values within a node. The optimal split is the one that minimizes the MSE, thereby maximizing the homogeneity of the resulting subsets with respect to the target value.

In my studies, information gain was applied to categorical outcomes while MSE was employed for numeric targets, enabling the algorithm to maximize node purity according to the type of variable considered.

Classification trees present several advantages that justify their popularity in various applications. Their interpretability is particularly noteworthy, as the model's decision-making process can be easily visualized and understood, facilitating transparent communication of results. Moreover, classification trees are non-parametric and do not rely on assumptions about data distribution, which grants them flexibility in modeling complex and non-linear relationships between features and outcomes. Additionally, they are naturally capable of handling mixed data types without extensive preprocessing.

However, classification trees also have inherent limitations. One major drawback is their propensity to overfit the training data, especially when trees grow very deep and complex, capturing noise rather than the underlying data patterns. This overfitting leads to reduced generalization performance on unseen data. Furthermore, classification trees exhibit sensitivity to small perturbations in the training dataset, which can cause substantial changes in the tree structure and hence reduce model stability. Another limitation is a bias towards features with many distinct levels or categories, which may be preferentially selected during splitting, potentially resulting in suboptimal trees.

Regarding my specific implementation, I utilized a binary classification tree with forward pruning to balance model complexity and predictive performance. The constructed tree was constrained to a maximum depth of 100 levels and employed a minimum leaf size of two instances. Subsets containing fewer than five instances were not further subdivided. Splitting ceased when a node reached a 95% majority threshold, indicating a strong class dominance. The pruning process was governed by a minimum cost-complexity criterion, which accounted for both the number of nodes and the expected misclassification cost. This approach ensured the derivation of an optimally sized tree that maintains interpretability while mitigating overfitting.

2.6.2 Naïve Bayes

The Naive Bayes classifier is a probabilistic model grounded in Bayesian statistics that leverages the Bayes' theorem of conditional probability to perform classification tasks. Despite its conceptual simplicity and the strong assumption of feature independence, the Naive Bayes algorithm has been shown to perform competitively, even outperforming more complex algorithms, in various real-world applications, particularly within the biomedical domain [193]. At the core of the Naive Bayes algorithm lies the Bayes' theorem, which allows for the computation of the posterior probability of a class given a set of observed features:

$$P(A|B) = \frac{P(B|A) \cdot P(A)}{P(B)}, \qquad [16]$$

where P(A) represents the prior probability of class A, i.e., the general probability of the class occurring in the population, P(B|A) is the likelihood, the probability of observing the evidence B given that class A is true, P(B) is the marginal probability of the evidence, and P(A|B) is the posterior probability of class A given the observed evidence B, which is the quantity of interest in classification problems.

In a typical supervised learning setting, the algorithm receives as input a dataset composed of instances characterized by a set of features (predictors) and their corresponding class labels (targets). For each feature-class pair, the algorithm estimates the prior and conditional probabilities required by Bayes' theorem. The classification of new instances is then achieved by computing the posterior probabilities for each possible class and selecting the one with the highest value.

The model performs particularly well when features are discrete, as it is based on frequency counts of feature values across classes. For continuous features, a discretization step is typically required, or alternatively, distributional assumptions (e.g., Gaussian) can be applied to approximate the likelihoods.

One of the most important characteristics of the Naive Bayes classifier is its interpretability, which makes it especially attractive in medical contexts. Nevertheless, the main limitation of the Naive Bayes model lies in its naivety, namely, the assumption of conditional independence among features. In reality, medical data often involve correlated features, and ignoring such dependencies can lead to suboptimal probability estimates. Despite this, empirical studies have demonstrated that the model often maintains a high level of predictive performance, particularly when the dependencies between features do not dominate the underlying data structure.

In the context of our research, the Naive Bayes algorithm was selected for its efficiency, minimal training data requirements, and the ease with which it can be interpreted by domain experts. These qualities make it well-suited for medical applications, especially when computational resources are limited or rapid model deployment is needed. The classifier was implemented with standard preprocessing procedures and applied to datasets where discretization of continuous features was performed when necessary. Given the high dimensionality and heterogeneity of medical data, the Naive Bayes model provided a robust and computationally efficient approach for probabilistic classification, contributing effectively to clinical decision-support scenarios.

2.6.3 Logistic regression

Logistic regression is a widely used statistical and machine learning model for binary classification tasks. It estimates the probability of an event occurring by modeling the relationship between one or more input variables and a dichotomous outcome. The model is based on a logistic (sigmoid) function, which maps the output of a linear combination of features to a probability value bounded between 0 and 1. This probabilistic interpretation enables logistic regression to classify data points into two categories based on whether the predicted probability surpasses a defined threshold, typically set at 0.5 [194].

From a mathematical standpoint, logistic regression receives as input a dataset composed of N instances, each defined by a feature vector $X = (x_1, x_2, ..., x_n)$ and a binary

label Y∈{0, 1}. During the training phase, the algorithm determines a weight vector W = (w_1, w_2, ..., w_n), which is used to compute a linear combination:

$$Z = W \cdot X = w_1 x_1 + w_2 x_2 + \cdots + w_n x_n. \quad [17]$$

This linear combination is then passed through the sigmoid function defined as:

$$f(Z) = \frac{1}{1 + e^{-Z}} \quad [18]$$

The result is a probability value indicating the likelihood that a given instance belongs to the positive class. If this probability exceeds the threshold, the instance is classified as belonging to class 1; otherwise, it is assigned to class 0. This approach enables the model to not only perform classification but also quantify the confidence of its predictions.

One of the key advantages of logistic regression lies in its interpretability. The coefficients associated with each feature indicate the direction and strength of its influence on the predicted outcome, which is especially valuable in fields like medicine, where understanding model behavior is critical. Moreover, logistic regression is computationally efficient and scales well to large datasets, making it a preferred choice for many practical applications such as disease prediction and diagnostic decision support. Nevertheless, logistic regression has its limitations. It is inherently a linear model, and thus it may perform poorly when the relationship between predictors and the outcome is nonlinear. Furthermore, the model is specifically designed for binary classification problems, and its extension to multi-class settings requires modifications.

In this research, logistic regression was employed with ridge regularization (L2 penalty) to reduce the risk of overfitting. The regularization technique imposes a penalty on large coefficient values, thereby promoting a simpler and more generalizable model. Specifically, the cost strength parameter was set to 1, ensuring a balance between model complexity and training error. This regularized approach proved to be effective in stabilizing the parameter estimates, especially in the presence of multicollinearity or high-dimensional input spaces.

In some of the studies conducted during my PhD, I also included two additional machine learning models: the artificial neural network and the support vector machine (SVM). This choice was made in order to compare the performance of the previously considered interpretable models with that of non-interpretable models, which, according to the literature, often achieve higher classification accuracy.

2.6.4 Artificial neural network

Artificial Neural Networks (ANNs) are computational models inspired by the structure and functioning of the human brain [195]. These systems are composed of numerous interconnected processing units, known as "neurons", which are linked by weighted connections. A widely used architecture is the feed-forward network, typically consisting of three types of layers: an input layer, which receives the input features; one or more hidden layers, where each neuron computes a weighted sum of the inputs and applies a non-linear

activation function; and an output layer, which generates the final predictions of the model [195].

Neural networks are trained through a learning process that can be supervised, unsupervised, or reinforcement based. During training, model parameters, specifically the weights and biases, are iteratively updated through interaction with the input data or the surrounding environment. This parameter adjustment process enables the network to improve its performance on the specific task for which it was designed [195].

One of the key advantages of ANNs is their capacity to learn complex input-output relationships directly from data, without requiring prior assumptions about the underlying statistical distributions. This flexibility makes neural networks particularly suitable for classification and prediction tasks in clinical settings. Furthermore, ANNs are inherently non-linear models, enabling them to represent intricate data patterns and interactions among predictor variables more effectively than linear models. However, neural networks are not without limitations. One major drawback is their reduced interpretability, especially in the presence of large input spaces, which can make them difficult to analyze and explain. Additionally, ANNs are computationally intensive and may require significant training time, particularly with large datasets and numerous features. Another significant challenge is their susceptibility to overfitting, where the model learns the noise in the training data rather than the underlying patterns. Although this can be mitigated by limiting the number of hidden units, such constraints may also reduce the network's ability to model complex relationships [196].

In this study, a neural network was implemented using a multi-layer perceptron (MLP) architecture with a single hidden layer comprising 100 neurons. The network employed the Rectified Linear Unit (ReLU) as the activation function and was trained using a gradient-based stochastic optimizer. The training process was capped at a maximum of 200 iterations. The neural network model was implemented using scikit-learn's MLPClassifier, which is capable of learning both linear and non-linear functions. MLP is a supervised learning algorithm that maps an input vector $f\{x\} = (x1, x2, ..., xm) \in Rm$ to an output $y \in Ro$, learning a function $f: Rm \rightarrow Ro$. Unlike logistic regression, MLPs introduce one or more non-linear hidden layers between the input and output layers, allowing the model to capture more complex patterns. In a standard MLP, the input layer represents the features of the problem. Each neuron in the hidden layer calculates a weighted linear combination of the input values, applies a non-linear activation function (such as the hyperbolic tangent or ReLU), and passes the result to the next layer. The output layer then transforms the values from the last hidden layer into the final predictions, depending on the nature of the task.

2.6.5 Support vector machine

Support Vector Machines (SVMs) are supervised learning models used for both classification and regression tasks [197]. They are grounded in statistical learning theory and designed to maximize generalization performance by implementing the principle of Structural Risk Minimization (SRM). This approach seeks to minimize an upper bound on the generalization error, rather than merely fitting the training data, thereby reducing the risk of overfitting.

At the core of SVMs lies the concept of finding the optimal separating hyperplane that maximizes the margin between two classes in a feature space. This hyperplane is defined such that it is equidistant from the closest data points of each class, known as support vectors. These vectors are critical, as they alone determine the position and orientation of the decision boundary.

To handle cases where the data are not linearly separable in the original feature space, SVMs employ kernel functions, which implicitly map the input data into a higher-dimensional space where a linear separation becomes possible. Common kernel functions include the linear kernel, polynomial kernel, and the Radial Basis Function (RBF) kernel. The optimization objective of SVM includes a regularization parameter, often denoted as C, which controls the trade-off between maximizing the margin and minimizing the classification error.

An important advantage of SVMs is their high predictive performance, especially in high-dimensional spaces or datasets with few instances relative to the number of features. Moreover, SVMs are relatively robust to outliers and can be extended to multi-class classification problems using strategies such as one-vs-one or one-vs-rest. However, SVMs also present certain limitations. They can be computationally intensive, particularly for large-scale datasets, and their performance is sensitive to the choice of kernel and associated parameters. Additionally, the resulting models, especially when non-linear kernels are used, are often less interpretable compared to simpler classifiers such as decision trees or logistic regression.

In this study, the RBF kernel was used, as it is well-suited for non-linear decision boundaries due to its ability to handle complex relationships in the data, and the cost parameter was set to 1, reflecting a balanced approach to this trade-off. Furthermore, the maximum number of training iterations was limited to 100 to constrain computational cost. The model was implemented using the LIBSVM library, a widely adopted and optimized SVM package. LIBSVM provides support for various kernels, multi-class classification, probability estimates, and automatic parameter selection [198].

All analysis was carried out in Python Orange3 Data Mining library and toolbox [199].

2.7 FEATURES SELECTION

The primary objective of feature selection was to improve model generalization, reduce overfitting, and enhance computational efficiency by eliminating irrelevant or redundant variables. In the various studies conducted during my PhD, different feature selection techniques were applied. The methods implemented include Information Gain (IG), Information Gain Ratio (IGR), and the ReliefF algorithm, each of which provides a distinct perspective on feature relevance and is supported by different theoretical assumptions.

Information Gain is a univariate filter method widely used in the context of decision tree learning. It quantifies the expected reduction in entropy, i.e., the amount of uncertainty associated with the target variable, after observing a given feature [200]. Formally, given a dataset D and a feature A, Information Gain is defined as:

$$IG(D, A) = H(D) - H(D \mid A), \quad [19]$$

where H(D) represents the entropy of the dataset and H(D|A) the conditional entropy of the target variable given the values of attribute A. A high Information Gain indicates that the feature contributes significantly to the predictability of the target variable. This method was employed in preliminary analyses to rank features according to their individual discriminatory power with respect to the class label. Its simplicity and computational efficiency made it particularly suitable in scenarios where the dimensionality of the data was relatively low and where model interpretability was a priority.

Despite its effectiveness, Information Gain exhibits a known bias towards features with a high number of distinct values. To mitigate this issue, the Information Gain Ratio (GR) was used. This metric normalizes the raw Information Gain by the intrinsic value of the feature, which captures the information content of the feature itself [201]:

$$GR(D, A) = \frac{IG(D,A)}{H_A(D)}, \quad [20]$$

where HA(D) denotes the intrinsic information of attribute A, i.e., the entropy induced by the distribution of its values. This normalization penalizes attributes that tend to over-partition the data without improving class separation. IGR was particularly useful in datasets containing high-cardinality categorical variables, where the standard Information Gain metric would otherwise select features based on their granularity rather than their actual predictive utility. Its adoption ensured a more balanced and equitable evaluation of all features, regardless of their value distributions.

ReliefF is a multivariate, instance-based feature selection algorithm that evaluates the quality of attributes by considering their ability to distinguish between neighboring instances of different classes [202]. Unlike IG and IGR, which operate on global statistics, ReliefF captures local dependencies and feature interactions, and is capable of handling multiclass problems, noisy data, and missing values effectively. The algorithm works as follows:

- For each randomly sampled instance, ReliefF identifies its k nearest neighbors from the same class (hits) and from different classes (misses).
- Feature weights are updated based on how well each attribute differentiates the selected instance from its misses and how consistently it aligns with its hits.
- The final importance score for each feature reflects its average contribution across all iterations.

ReliefF was adopted in studies involving heterogeneous clinical datasets, where features often exhibit complex, non-linear interactions and are subject to missing or noisy entries. Its local evaluation strategy and robustness to imperfections made it particularly well-suited to biomedical contexts, where variable dependencies are rarely independent or linearly separable.

2.8 CLASSIFICATION PERFORMANCE

To rigorously assess the predictive capabilities of the implemented machine learning models, in most studies, a 5-fold cross-validation procedure was employed. This technique partitions the dataset into five equally sized folds. At each iteration, four folds are used for training the model, while the remaining fold serves as a validation set. This process is repeated five times, ensuring that each fold is used exactly once for validation. Importantly, no individual appears in both the training and validation set within the same iteration, preserving the independence of validation and ensuring a reliable estimate of generalization performance. This approach is particularly suitable when dealing with limited sample sizes, as it maximizes the use of available data without compromising evaluation integrity.

2.8.1 Evaluation Metrics

Model performance was evaluated using multiple metrics, each capturing a different aspect of classification effectiveness. These metrics were computed at each fold of cross-validation and subsequently averaged to produce an overall estimate of performance. In binary classification, predictions are expressed in terms of true positives (TP), false positives (FP), true negatives (TN), and false negatives (FN). The metrics considered include:

- Classification Accuracy (CA): the proportion of correctly classified instances over the total number of samples

$$CA = \frac{TP + TN}{TP + TN + FP + FN} \quad [21]$$

- Precision (PR): the ratio of true positives to all predicted positives, indicating the model's ability to avoid false alarms

$$PR = \frac{TP}{TP + FP} \quad [22]$$

- Recall (Sensitivity): the proportion of true positives out of all actual positive instances, assessing the model's ability to detect the positive class

$$Recall = \frac{TP}{TP + FN} \quad [23]$$

- F1 Score: the harmonic mean of precision and recall, providing a balanced measure especially when classes are imbalanced

$$F_1 = \frac{2}{Recall^{-1} + PR^{-1}} = 2 \cdot \frac{Recall \cdot PR}{Recall + PR} \quad [24]$$

- Specificity (SP): the proportion of true negatives correctly identified, reflecting the model's ability to recognize the negative class

$$SP = \frac{TN}{TN + FP} \quad [25]$$

- Area Under the Receiver Operating Characteristic Curve (AUC): a measure of separability, which reflects the model's ability to distinguish between classes

across all classification thresholds. Higher AUC values indicate better discriminative ability.

2.8.2 Confusion Matrix

A key tool in performance evaluation is the confusion matrix, which provides a granular view of classification results by contrasting actual versus predicted class labels. Its structure is depicted in Figure 2.18.

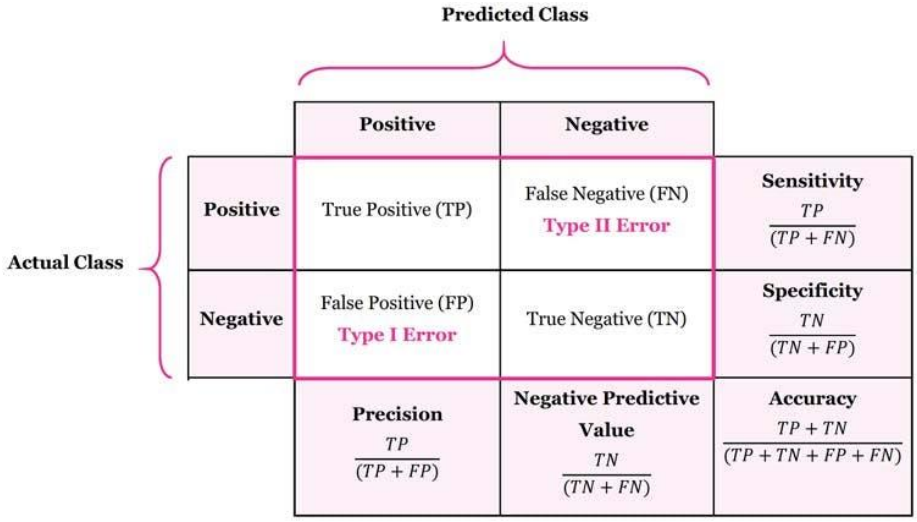

***Figure 2.18**. Structure of a Confusion Matrix: illustrating the relationship between predicted and actual classifications, including true positives (TP), true negatives (TN), false positives (FP), and false negatives (FN).*

Each element of the confusion matrix contributes directly to the computation of the aforementioned performance metrics.

2.8.3 Receiver Operating Characteristic (ROC) Curve

For a more nuanced evaluation, ROC curves were generated for each classifier. These plots depict the trade-off between True Positive Rate (TPR) and False Positive Rate (FPR) at varying classification thresholds:

$$TPR = Recall = \frac{TP}{TP + FN} \quad [26]$$

$$FPR = 1 - Specificity = \frac{FP}{FP + TN} \quad [27]$$

The ROC curve thus allows for an assessment of model performance across all possible decision boundaries. A classifier whose ROC curve closely follows the top-left border of the plot space exhibits high accuracy. The AUC quantifies the overall performance: values close to 1.0 indicate excellent discriminative ability, whereas a value of 0.5 suggests performance equivalent to random guessing.

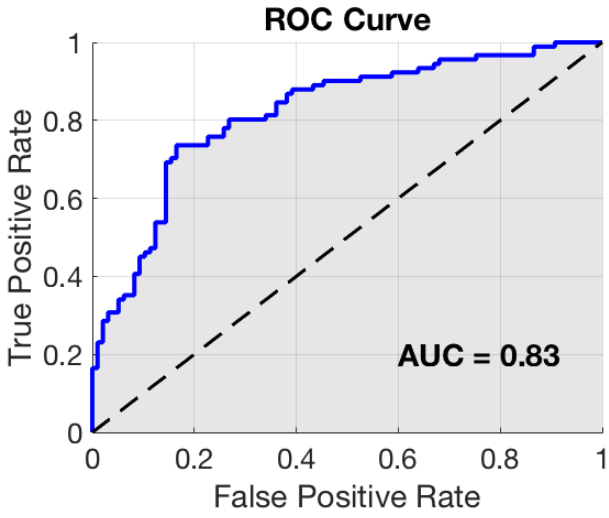

Figure 2.19. *Example of a ROC Curve with an AUC of 0.83: illustrating the model's ability to distinguish between classes, with an Area Under the Curve indicating good discriminatory performance. The x-axis represents the FPR (1 – specificity), while the y-axis shows the TPR (sensitivity).*

All performance metrics were used in concert to guide the selection of the optimal classification model. While accuracy provided a general indication of correctness, metrics such as precision, recall, and specificity offered more detailed insights into the model's behavior under class imbalance. The F1 score, being a composite of precision and recall, proved particularly useful in balancing false positives and false negatives.

2.9 NOMOGRAMS

A nomogram is a graphical calculation tool that represents a multivariable predictive model in a visual format, allowing estimation of an outcome probability without complex computation. The nomogram was originally designed to facilitate the rapid resolution of equations without requiring complex calculations. In medical research and practice, this approach found a pivotal application when Lubsen and colleagues [203] first employed it to interpret a logistic regression model aimed at predicting the risk of acute myocardial infarction. Their work demonstrated how a predictive tool could be effectively printed and used in clinical settings, allowing physicians to derive an immediate and individualized estimate of risk at the bedside.

Beyond the simple provision of a numerical prediction, nomograms derived from logistic regression or naive Bayesian models have the advantage of making the internal structure of the model explicit. The relative importance of each predictor is visually represented by the length of the corresponding scale, which reflects the range of odds ratios associated with that variable. This characteristic enhances transparency, as it allows the clinician not only to compute the probability of an outcome but also to appreciate the contribution of each variable to the final prediction [204,205]. The methodology involves assigning a score to each predictor according to its measured value in the patient under examination. These scores are then summed to yield an overall score, which is subsequently translated into an estimated probability. Such an approach enables both categorical

classification and probabilistic assessment of disease, thereby providing richer information than a binary decision threshold.

The nomogram typically consists of several parallel scales corresponding to individual predictors, each calibrated to a point system reflecting the relative contribution of that variable to the outcome. To use the nomogram, the value of each predictor is located on its respective scale, and a corresponding point value is assigned. The sum of these points is then mapped onto a total points scale, which is linked to a probability scale representing the likelihood of the outcome of interest. The final decision is derived by interpreting the calculated probability in the context of pre-established thresholds or clinical criteria, enabling objective risk stratification and informed decision-making.

Nomograms can also function as practical tools for the validation of predictive models, facilitating more accurate assessment and enabling their integration into routine clinical practice. By visually inspecting threshold points and calibration across different probability ranges, clinicians can assess whether the model performs consistently with empirical evidence. This is particularly relevant in diagnostic contexts where the separation between two conditions is subtle and misclassification has significant clinical implications. The enduring appeal of nomograms lies in their ability to combine predictive accuracy with interpretability, thus bridging the gap between statistical modelling and clinical decision-making.

In the case of logistic regression models, nomogram construction begins with the estimation of regression coefficients, each of which quantifies the effect of a predictor on the log odds of the outcome. These coefficients are then proportionally converted into point scales, with the variable exerting the greatest influence typically assigned the maximum point value. For each example, the observed value of a predictor corresponds to a position on its individual scale, from which the associated points are determined. The points for all predictors are summed to produce a total score, which is then transformed into a predicted probability through the logistic function. This approach preserves the mathematical integrity of the regression model while translating it into a graphical tool that can be applied without computation.

Možina et al. proposed a methodology for visualizing the Naive Bayesian classifier through nomograms [204]. The transformation of the Naive Bayes model into a nomogram begins with the formulation of the log-odds of the target class c given an instance X:

$$logit\ P(c|X) = logit\ P(c) + \sum_i \log \frac{P(a_i|c)}{P(a_i|\bar{c})} \qquad [28]$$

Here, each term $\log \frac{P(a_i|c)}{P(a_i|\bar{c})}$ represents the contribution, or "point score", of a particular attribute value a_i relative to the prior probability. These contributions are calculated as log odds ratios (log ORs) and then rescaled so that the largest absolute log OR corresponds to ±100 points, facilitating a straightforward visual summation of scores across attributes. The total point score, denoted F(c|X), is then converted into a predicted probability via the inverse logistic function:

$$P(c|X) = \left[1 + e^{(-logit\ P(c) - F(c|X))}\right]^{-1} \quad [29]$$

This mapping is displayed at the bottom of the nomogram, enabling direct translation from aggregated points to predicted probability.

In addition to point estimation, the Možina et al. incorporate confidence intervals (CIs) both for the individual contributions of attribute values and for the overall predicted probability. The CIs for each odds ratio are computed using standard formulas:

$$\widehat{OR}(a_i) \pm z_{1-\alpha/2}\sqrt{Var\widehat{OR}(a_i)} \quad [30]$$

where the variance is derived from the counts of positive and negative instances in the training data. These intervals are graphically overlaid on the nomogram's axes, thereby conveying the statistical uncertainty associated with each contribution and the model's final prediction.

In both logistic regression and Naive Bayes nomograms, the underlying process involves quantifying predictor effects, translating these into a standardized point scale, summing the contributions to form an aggregate score, and mapping this score to a predicted probability via the logistic transformation. This parallel structure ensures that, regardless of the modelling approach, the resulting nomogram remains an interpretable, transparent, and practically applicable decision-support tool in clinical settings.

Chapter 3. Development of Predictive Models for the Classification of IHD and DCM Based on HRV and Echocardiographic Features

To reach the aim of the better diagnostic classification in cases of IHD and DCM patients the series of studies were conducted to identify HRV features, estimated through linear and non-linear HRV signal analysis, as well as echocardiographic imaging parameters, such as GLS and LVEF, that support the classification of IHD and DCM, and to assess the influence of HRV preprocessing on diagnostic performance, focusing on feature explainability and model transparency.

In particular, the study presented in section 3.1 [206] focuses on the importance of HRV signal preprocessing. Specifically, it investigates the impact of including or excluding ectopic beats on the features extracted from the HRV signal, as their presence can significantly alter the results.

As discussed extensively in Chapter 1, the clinical adoption of machine learning increasingly emphasizes the need for interpretable models, those that allow clinicians to understand the decision-making process underlying the model's outputs. For this reason, the study described in section 3.2 [207] evaluates three interpretable classification models, logistic regression, naive Bayes, and decision trees, using HRV features and LVEF to support differential diagnosis among patients with IHD, DCM, and healthy controls.

Moreover, while echocardiography is widely used in clinical practice for the diagnosis and prognosis of cardiovascular diseases, particularly DCM, certain parameters such as GLS are still underutilized despite their diagnostic potential. In the study described in the section 3.3 [208], a comparative analysis of the predictive power of LVEF and GLS was performed for distinguishing DCM patients from healthy subjects. The findings demonstrated that, in addition to LVEF, GLS can be a highly valuable diagnostic marker, in some cases even outperforming LVEF. These results provided the rationale for combining LVEF and GLS with features extracted from linear and non-linear HRV analyses to build interpretable models capable of differentiating among IHD, DCM, and healthy subjects. The methodology and results of this investigation are presented in section 3.4 [209].

A particular diagnostic challenge arises in patients whose LVEF falls within the so-called “grey zone.” Moreover, healthy controls may also exhibit LVEF values around 50%, which further reduces the discriminative power of this parameter in borderline cases. To address this issue, the study outlined in section 3.5 [210] proposes a multinomial logistic regression model based on HRV features, GLS, and clinical data to support differential diagnosis among IHD, DCM, and healthy controls within the LVEF range of 40–55%.

The complexity increases further when focusing exclusively on patients with mildly reduced LVEF values (i.e., 40–50%). To address this particularly challenging subgroup, this PhD thesis also explored three interpretable classification models that rely on HRV and GLS

parameters to differentiate between IHD and DCM in this patient subset. The study and its findings are detailed in section 3.6 [211].

3.1 ANALYSIS OF THE IMPACT OF ECTOPIC BEATS ON HRV FEATURES

The changes in tonic vagal activity and sympathetic-parasympathetic disbalance, characteristic of ischemic heart disease [212], can be measured by HRV [5], which reflects the fluctuations in beat-to-beat heart rate (RR interval). As described in the first and second chapters of this thesis, HRV is calculated by analyzing RR intervals from sinoatrial node beats and it can be examined using various methods, including time-domain and frequency-domain analyses, as well as non-linear analyses [82]. HRV can be utilized to assess several cardiac diseases [9,213]. However, there is no consensus on the HRV preprocessing steps, which can potentially bring different results.

One of the issues still debated is the inclusion of ectopic beats in HRV analysis [9,10,214–218]. Ectopic beats are premature heartbeats originating from sites outside the sinoatrial node, such as the atria (premature atrial contractions) or the ventricles (premature ventricular contractions). These beats interrupt the normal rhythm and timing of the heart, and they can occur sporadically in healthy individuals or more frequently in those with underlying heart conditions. Some studies exclude ectopic beats from HRV analysis, considering them biological artifacts [10] or irrelevant due to the fact that they are not generated by sinoatrial nodes [214,215]. Their exclusion, however, creates a challenge for interpolation of the RR intervals and can bias the HRV parameters [9,216,217], especially when these are caused by cardiovascular autonomic tone changes [216]. Indeed, albeit still much debated, such bias and the inclusion of ectopic beats can potentially be relevant for discrimination of IHD [218]. For this reason, the inclusion of ectopic beats should be potentially considered in HRV feature extraction [219].

Therefore, in this study [206] we aimed to investigate the performance of the models for classification of early IHD versus healthy subjects based on HRV features extracted from signals excluding ectopic beats and based on the same features extracted from the signals that contain both ectopic and normal heartbeats.

3.1.1 Methods

In this study, clinical data and processed ECG signals from 385 subjects were analyzed. In particular, the study encompassed 170 patients affected by early IHD (125M/45F, aged 71±11 y) and 215 healthy controls (101M/114F, aged 58±20 y). The assessment of IHD was based on clinical and laboratory findings [39]. Only early-stage IHD were included in the study (patients without cardiac insufficiency symptoms or with cardiac insufficiency symptoms classified by NYHA scale as class 1). IHD patients did not present acute coronary syndrome in the 3 months before the Holter monitoring. Patients with known trigger factors, such as toxic insults from alcohol or drugs, and tachyarrhythmias were also excluded. IHD patients were on beta-blocker pharmacological treatment. The exclusion criteria for healthy controls (HC) were the presence of peripheral artery disease, thyroid disorders, history of

myocardial revascularization, hypertensive heart disease, pulmonary hypertension, or severe valvulopathy.

All subjects underwent 24-hour Holter ECG recording and RR intervals were extracted and labeled as described in the section 2.1. Linear and nonlinear parameters were obtained from HRV signal analysis, in both conditions, including and excluding ectopic beats.

The Logistic Regression (LogReg) method [194] was employed to produce models capable of differentiating between the two groups (IHD and HC). The models were produced considering HRV features obtained from 1) signals after exclusion of ectopic beats ($LogReg_N$) and 2) signals which included both normal and ectopic beats ($LogReg_{NE}$). In both cases, the total number of 10 aforementioned HRV features was considered. The classification performance of the produced models was estimated using 5-fold cross-validation. For each model we calculated the CA, AUC, F1, precision, and recall. Nomograms were used to interpret the obtained logistic regression models.

Moreover, the HRV features represented in the nomograms extracted from signals excluding ectopic beats and obtained from signals which included ectopic beats were compared using the paired t-test. A $p<0.05$ was considered statistically significant.

3.1.2 Results

Classification performance of LogReg models based on HRV features extracted from signals after excluding ectopic beats and features obtained from signals which included normal and ectopic beats are reported in Table 3.1. The CA, AUC, F1, precision, and recall were higher in the model based on features that were extracted from HRV that included both normal and ectopic beats ($LogReg_{NE}$) compared to the logistic regression model constructed with the features obtained from HRV excluding ectopic beats ($LogReg_N$).

Table 3.1 *Classification performance of produced $LogReg_N$ and $LogReg_{NE}$ models.*

Model	AC	AUC	F1	Precision	Recall
$LogReg_N$	0.678	0.714	0.677	0.677	0.678
$LogReg_{NE}$	0.727	0.810	0.725	0.726	0.727

The produced nomograms for $LogReg_{NE}$ and $LogReg_N$ are reported in Figure 3.1 and the features are listed in order of importance allowing to select the subset of most informative features. The most discriminatory features were SD2, SDNN, LF, HF, MeanRR, LF/HF, SD1 and SD2, SDNN, SD1, LF/HF, HF, MeanRR, LF for $LogReg_{NE}$ and $LogReg_N$, respectively.

Mean±SD and comparison between LogRegN and LogRegNE features in HC and IHD subjects are reported in Table 3.2 and Table 3.3, respectively. All features except SDNN and SD1 in HC subjects (Table 3.2), and MeanRR and SD2 in IHD subjects (Table 3.3) were significantly different.

Table 3.2. Mean±SD and comparison between $LogReg_N$ and $LogReg_{NE}$ features in HC subjects.

Features	$LogReg_N$ Mean±SD	$LogReg_{NE}$ Mean±SD	p-value
MeanRR	874±137	879±138	<0.001
SDNN	66±43	69±48	0.058
LF	1165±2386	1042±2470	<0.001
HF	1501±4727	1681±5282	<0.001
LF/HF	2.31±2.06	2.23±2.12	<0.001
SD1	30±25	33±31	0.094
SD2	82±50	82±49	0.022

Table 3.3. Mean±SD and comparison between $LogReg_N$ and $LogReg_{NE}$ features in IHD subjects.

Features	$LogReg_N$ Mean±SD	$LogReg_{NE}$ Mean±SD	p-value
MeanRR	963±151	960±149	0.807
SDNN	81±62	88±72	<0.001
LF	1521±2816	1406±2836	<0.001
HF	3193±6294	4170±9693	<0.001
LF/HF	1.22±1.09	1.10±1.13	<0.001
SD1	40±35	46±44	<0.001
SD2	95 ±69	97±73	0.565

Figure 3.1. Nomograms for IHD output class for (a) LogRegNE and (b) LogRegN models.

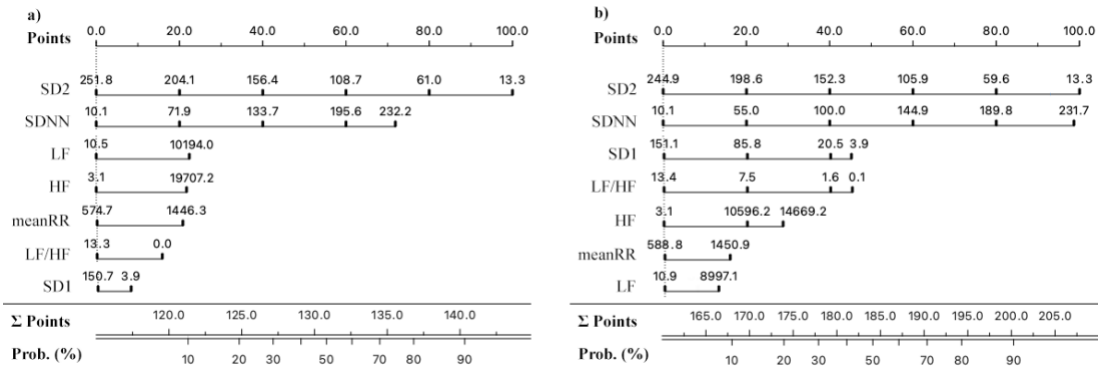

3.1.3 Discussion

The main finding of this study is that the model with the input features extracted from RR segments with normal and ectopic beats, also called total HRV, presented higher

classification performance (72.7%) in comparison to the model that uses features based only on normal heart beats (67.8%).

The nomograms revealed that the most important features were SD2, SDNN, LF, HF, meanRR, LF/HF, and SD1, with SD2 and SDNN emerging as among the most discriminative. Comparable information about autonomic nervous system dysfunction in patients with IHD can also be derived from LF and HF parameters [220], which in our study ranked third and fourth in the $LogReg_{NE}$ nomogram, and fourth and seventh in the $LogReg_{N}$ nomogram.

Given the potential influence of data preprocessing on HRV metrics, we also examined how the exclusion of ectopic beats affected the ranking and stability of these features in both groups. The nomograms showed that SD2 remained invariant regardless of whether ectopic beats were excluded, making it a robust feature for the IHD group. MeanRR displayed similar stability, albeit with lower discriminative power. In contrast, SDNN showed greater variability between preprocessing approaches, consistent with the observed numerical differences in this parameter; however, it still retained its position as the second most important feature. Interestingly, the opposite trend for SD2 and SDNN was observed in the HC group, suggesting that the exclusion of ectopic beats influences these features differently across groups. SD1, which reflects short-term HRV changes, was significantly different in the IHD group but not in the HC group, likely due to the higher number of ectopic beats in IHD patients. Notably, SD1 had greater discriminative power when ectopic beats were excluded, possibly reflecting the effects of RR interval interpolation [216]. LF, HF, and LF/HF were statistically different between preprocessing methods in both groups.

Several of the parameters included in the model may exhibit intercorrelations, potentially leading to multicollinearity issues. For instance, SD2 and LF power are both established indicators of autonomic modulation, whereas SD1 shows a strong correspondence with HF power, reflecting vagal activity. Although these relationships suggest overlapping information, their joint consideration provides a more nuanced understanding of autonomic function. By integrating linear frequency-domain measures with non-linear metrics, the model captures complementary aspects of sympathetic and parasympathetic regulation, enhancing the overall clinical interpretability despite the presence of correlated variables. Nonetheless, careful consideration is needed to avoid model overfitting, and future validation on larger and more diverse study populations will be essential to confirm the robustness and generalizability of these findings.

In conclusion, the results of this study suggest that the inclusion of ectopic beats may enhance the discriminatory power of HRV-based models, particularly in distinguishing between early-stage IHD patients and healthy individuals. However, it is noteworthy that in both scenarios, whether ectopic beats are included or excluded, the models consistently identified the same features as the most relevant, indicating that model development is not substantially affected by this choice. Certain parameters, such as SD2 and meanRR, remained stable regardless of ectopic beat inclusion, while others exhibited divergent behavior between the IHD and healthy control groups. Therefore, although including ectopic beats may improve classification accuracy, the exclusion of such beats, when clinically justified in future applications, would not lead to a significant decrease in model performance. As such, while their inclusion can be recommended to optimize classification, their exclusion does not compromise the overall robustness of the model.

Once the HRV signal preprocessing methods had been assessed, the focus shifted to examining the potential of interpretable machine learning models for classifying IHD and DCM patients.

3.2 Evaluation of Interpretable Machine Learning Models in the Differential Diagnosis Between IHD and DCM

There is growing research interest in the development of machine learning models for computer-aided diagnosis that exploits HRV extracted parameters in combination with other available clinical data [145]. Such models may be used to predict illness risk, readmission risk, and the need for treatment, among other things. However, the limited interpretability of produced models still creates dissatisfaction among the clinicians, as they cannot be evaluated on the level of single input features. For this reason, methods such as classification trees, naive Bayes, and linear/logistic regression algorithms are more desirable in medicine [154]. These approaches are employed in several sectors of healthcare, including also cardiology [150–152]. However, there is a lack of studies that explore HRV parameters to distinguish between IHD and DCM patients.

Nonetheless of the importance of model interpretability, the majority of existing models focus only on accuracy prediction and seldom provide a relevant clinical explanation for their outcomes [145,153]. Interpretability approaches are unquestionably a key issue that must be considered while developing prediction models for healthcare [154]. Hence, the production of clinically plausible machine learning models that can guide diagnosis and can provide information on the feature relevance is desired.

Therefore, this study [207] aimed to develop interpretable and clinically plausible models for early differential diagnosis between DCM and IHD, based on LVEF and HRV parameters and to compare their classification performance.

3.2.1 Methods

In this study, clinical data and processed ECG signals of 313 subjects were analyzed. In particular, the study encompassed 196 patients affected by IHD (145 males, aged 70±11, and 51 females, aged 76±9) and 117 patients suffering from DCM (74 males, aged 57±15, and 43 females, aged 65±14). IHD subjects were diagnosed based on clinical and laboratory observations, and coronary angiography was used to confirm the diagnosis [39]. In the three months prior to Holter monitoring, none of the IHD patients had acute coronary syndrome. LVEF, acquired by echocardiographic examination, was obtained by the Simpson biplane method [173], as described in section 2.2.4. Patients with DCM were included only if coronary artery disease was not sufficient to explain the dysfunction or if LVEF was less than 50% and cannot be explained by pressure or volume overload [24]. Coronary angiography was conducted on all individuals over the age of 35 who had cardiovascular risk factors and/or had a family history of DCM. Patients with established trigger factors such as toxic insults from alcohol or drugs, as well as tachyarrhythmias, were excluded from

the study. Both groups of subjects were receiving beta-blocker medication and were classified as NYHA ≤ 1 according to the New York Heart Association severity scale.

All subjects underwent 24-hour Holter ECG recording and RR intervals were extracted from the ECG signal and automatically labeled. In this study, linear and nonlinear HRV parameters were calculated including ectopic beats. The detailed analysis was presented in Chapter 2.

The models were built considering selected HRV features together with LVEF. The features were chosen based on their correlation with the target parameter, which was computed using the information gain or the expected amount of information. The features that have information gain of at least 0.025 were considered for further modeling.

Classification tree, logistic regression, and naive Bayes methods were employed, as described in section 2.6, to produce models capable of differentiating between the two groups (IHD and DCM). The classification accuracy, the AUC, F1 measure, precision, and recall on the dataset were estimated using 5-fold cross-validation.

3.2.2 Results

Table 3.4 shows the selected features by using the information gain as a metric. The features, LVEF, LF, NN50, pNN50 and meanRR with information gain of 0.109, 0.40, 0.037, 0.030, and 0.025 respectively were then used to produce three different classification models (classification tree, logistic regression, and naive Bayes).

Table 3.4. *The set selected features and corresponding information gain.*

Features	Information Gain
LVEF	0.109
LF	0.040
NN50	0.037
pNN50	0.030
MeanRR	0.025

Table 3.5 reports the performance of the produced models. In particular, the model produced by naive Bayes showed the highest classification accuracy (73.5%) compared to models produced by logistic regression (67.4%) and classification tree (67.1%). Regarding the AUC, naive Bayes again presented the highest value (0.740), followed by classification tree (0.729) and logistic regression (0.674). Figure 3.2 depicts the ROC curves for each of the models and class (DCM Figure 3.2a and IHD Figure 3.2b). The same trend was also observed for F1, precision and recall and reported in Table 3.5.

Table 3.5. *Performance measures of the naive Bayes, logistic regression and classification tree models.*

Model	AC	AUC	F1	Precision	Recall
Classification tree	0.671	0.729	0.669	0.667	0.671
Logistic regression	0.674	0.674	0.636	0.666	0.674
Naive Bayes	0.735	0.740	0.734	0.733	0.735

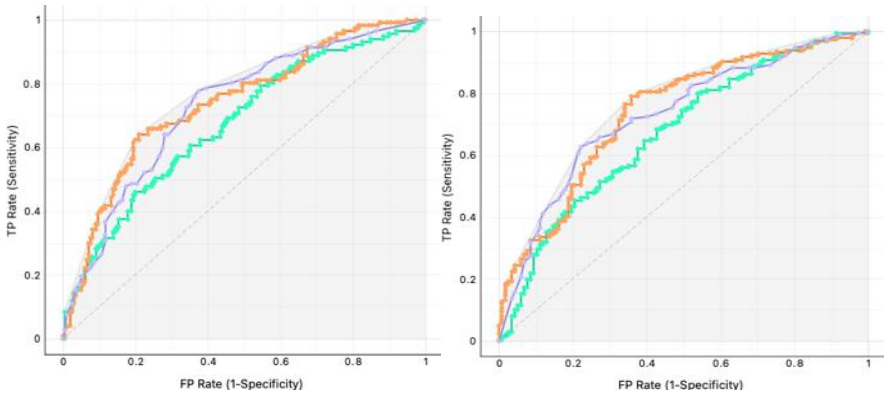

Figure 3.2. *ROC curves for classification tree (purple), logistic regression (green) and naive Bayes (orange) of a) DCM and b) IHD patients.*

Confusion matrices obtained for classification tree, logistic regression and naive Bayes models are reported in Figure 3.3. Confusion matrices show that DCM patients were correctly classified with 53.0% (Figure 3.3a), 29.1% (Figure 3.3b) and 62.4% (Figure 3.3c) with classification tree, logistic regression and naive Bayes, respectively. On the other hand, IHD were correctly classified with 75.5% (Figure 3.3a), 90.3% (Figure 3.3b) and 80.1% (Figure 3.3c) with the same models.

a)	DCM	IHD	Σ
DCM	53.0%	47.0%	117
IHD	24.5%	75.5%	196
Σ	53	260	313

b)	DCM	IHD	Σ
DCM	29.1%	70.9%	117
IHD	9.7%	90.3%	196
Σ	53	260	313

c)	DCM	IHD	Σ
DCM	62.4%	37.6%	117
IHD	19.9%	80.1%	196
Σ	112	201	313

Figure 3.3. *Confusion matrices obtained by a) classification tree; b) logistic regression; c) naive Bayes models.*

The comparison of cross-validation classification accuracies by means of Bayesian comparison of classification algorithms shows that the probability that CA of naive Bayes is higher than CA of the classification tree $p(CA_{naiveBayes}>CA_{tree})$ is 0.923 and classification of logistic regression $p(CA_{naiveBayes} > CA_{logregression})$ is 0.876. The nomogram for naive Bayes approach, that shows the highest classification accuracy, is depicted in Figure 3.4.

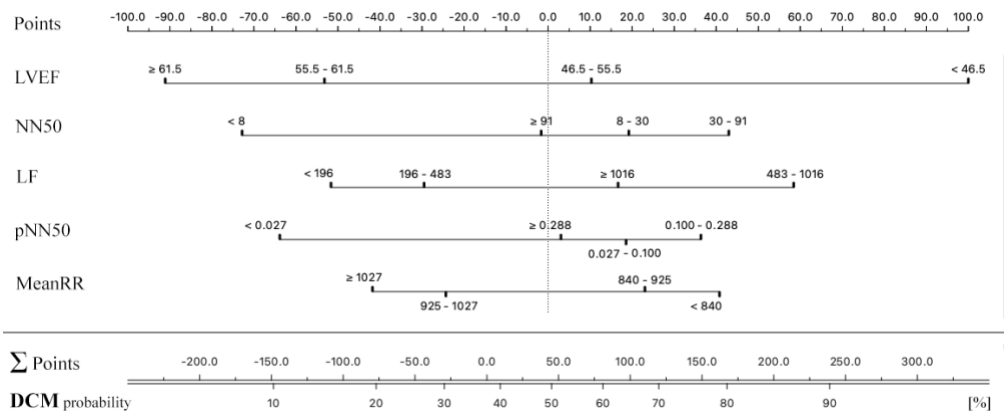

Figure 3.4. Nomogram for naive Bayes classifier for the DCM patients. The scoring can be obtained as a sum of the score of each individual parameter. For IHD the probability with the same scoring obtained by nomogram can be calculated by subtracting DCM probability from 100.

3.2.3 Discussion

The results of this study show that LVEF, LF, NN50, pNN50, and meanRR, used in naive Bayes approach with classification accuracy (73.5%), AUC (0.740), F1 (0.734), precision (0.733), and recall (0.735), outperformed classification trees and logistic regression.

The selection of interpretable machine learning approaches allows for further investigation into the relationship between the parameters selected by the ranking method and the output of the classifier. Accordingly, in the result section, the nomogram of the best performing approach has been reported. The nomogram reveals the structure of the naive Bayes model and the influence of each feature on the class probability. In particular, the longest length of the LVEF feature implies that is the most discriminatory feature between the two groups. The asymmetry around zero suggests that a longer bar on the right side indicates greater relevance for DCM classification, while a longer bar on the left side indicates greater relevance for IHD classification. For example, NN50 and pNN50 are more characteristic of IHD, which is in line with the literature [221], as these HRV time-domain parameters often reflect increased heart rate irregularities.

Moreover, nomograms allow further validation of the produced model by observing clinically meaningful thresholds. For example, clinical literature shows that patients with LVEF $\leq$ 45% [4] have a high probability of DCM. Indeed, our model, depicted in Figure 3.4, demonstrates the same fact: the subjects < 46.5 have the highest probability of being classified as DCM if only that parameter is considered. Similar threshold-based validation can also be performed for other features. Furthermore, nomograms can be printed on paper and used by clinicians to estimate the likelihood of being in the DCM or IHD group. Scoring is performed individually for each feature and then summed to obtain the final probability.

The study has some limitations. Specifically, it is a single-center study with a moderate sample size. The model performance was assessed using 5-fold cross-validation. This approach provides a reliable internal estimate of performance that generally approximates results on an independent test set, and was considered appropriate given the moderate

sample size. Nonetheless, the absence of an external test cohort remains a limitation, and future validation on larger, independent populations is needed to confirm these results.

In conclusion, this study demonstrated that interpretable machine learning models can achieve clinically meaningful classification performance in this specific clinical population, supporting first-line diagnostic decision-making for these pathologies. Furthermore, by identifying relevant features, the study underscores the value of interpretability in machine learning, as clinical plausibility can be assessed at the level of individual variables through the use of nomograms. When examined across multiple features, these models also offer insights into potential threshold values for HRV parameters not yet fully characterized in relation to disease. Finally, the study highlights the utility of nomograms as tools for probabilistic classification, reinforcing their role in supporting differential diagnosis between early-stage IHD and DCM.

This study included the standard echocardiographic parameter LVEF. To further evaluate the discriminatory power and informativeness of additional echocardiographic features, subsequent analyses also incorporated the GLS parameter derived from echocardiographic imaging. The first of these investigations focused on comparing the diagnostic utility of GLS and LVEF in differentiating between patients and healthy controls.

3.3 Discriminatory power of GLS and LVEF for identification of DCM

The LVEF is the most commonly used parameter for evaluating cardiac function and predicting clinical outcomes in patients with DCM [4]. However, despite its widespread use, LVEF presents several inherent limitations. Notably, a decrease in LVEF typically occurs only in the advanced stages of cardiac disease, which limits its utility as an early diagnostic marker. Additionally, LVEF can be unreliable in patients with left ventricular hypertrophy or significant volume reduction, and it suffers from relatively high inter- and intra-observer variability. Accurate identification of endocardial boundaries during image acquisition and analysis also remains a technical challenge, potentially compromising measurement consistency and reliability [4].

Given these drawbacks, there remains a critical need to identify alternative, reliable, and non-invasive biomarkers that can support earlier and more accurate differential diagnosis of DCM. In this context, recent studies have highlighted GLS and HRV as promising echocardiographic and physiological parameters, respectively, for the diagnosis and prognosis of various cardiovascular diseases [6,7,113,219,222].

GLS, a parameter derived from myocardial deformation imaging, quantifies the longitudinal shortening of the myocardium and offers valuable insight into subtle changes in left ventricular function. Unlike LVEF, GLS can detect early myocardial dysfunction, often before structural or volumetric abnormalities become evident. Several studies have demonstrated the superior sensitivity and prognostic value of GLS compared to traditional LVEF measurements, particularly in detecting subclinical ventricular impairment and predicting adverse cardiovascular outcomes [7,74].

Therefore, the aim of this study [208] was to investigate the discriminatory power of GLS and LVEF when used as features in logistic regression models for the identification and early detection of dilated cardiomyopathy.

3.3.1 Methods

The study included 138 DCM patients (81M/57F, aged 61 ± 15 years) and 138 HC (66M/72F, aged 59 ± 19 years). DCM patients were enrolled following clinical assessment. Coronary angiography was systematically performed in patients over 35 years of age with cardiovascular risk factors and/or without a family history of DCM. Patients with known trigger factors, such as toxic insults from alcohol or drug abuse, and those with tachyarrhythmias, were excluded from the study. LVEF was obtained using the Simpson biplane method [173], and GLS was derived via speckle tracking echocardiography, as described in Chapter 2. GLS measurements were performed offline using dedicated software (TomTec Arena v2.0, TomTec Imaging Systems, Unterschleißheim, Germany). Investigators visually assessed the detected endocardial border and, when necessary, manually adjusted the tracing to ensure accurate contour delineation.

All subjects underwent a 24-hour Holter ECG recording, and RR intervals were extracted and labeled as described in the section 2.1. RR interval recordings were segmented into non-overlapping 5-minute intervals. Linear and non-linear HRV features were extracted from each segment, which included both normal and ectopic beats.

For feature selection, the Information Gain method [200] was used. The cut-off value for Information Gain estimates of informative attributes was set at 0.07. Two logistic regression models were developed: one including the selected HRV features, age, sex, and GLS ($LogReg_{GLS}$), and the other including the same features but with LVEF instead of GLS ($LogReg_{LVEF}$). Classification performance was estimated using 5-fold cross-validation, and the average metric values were calculated. Finally, nomograms were created to interpret and validate the resulting models.

3.3.2 Results

The results of features selection analysis showed that the most informative features for classification between DCM and HC listed from higher to lower Information Gain coefficients were GLS, SD1/SD2, RMSSD, betaExp, and LFn for $LogReg_{GLS}$ model and LVEF, SD1/SD2, RMSSD, betaExp and LFn for $LogReg_{LVEF}$. The selected features were used as the set of variables to produce LogReg models.

The classification performance of produced LogReg models based on HRV features and GLS in one case and based on HRV features and LVEF in the other are reported in Table 3.6. The CA, AUC, F1, precision, and recall were higher in the model based on HRV features and GLS ($LogReg_{GLS}$) compared to the logistic regression model constructed with the HRV features and LVEF ($LogReg_{LVEF}$).

Table 3.6. Classification performance of produced LogRegGLS and LogRegLVEF models.

Model	AC	AUC	F1	Precision	Recall
$LogReg_{GLS}$	0.86	0.89	0.85	0.86	0.86
$LogReg_{LVEF}$	0.83	0.87	0.83	0.83	0.83

Confusion matrices obtained for $LogReg_{GLS}$ and $LogReg_{LVEF}$ are reported in Table 3.7. Confusion matrices show that DCM patients were correctly classified with 88.3% (Table 3.7a) and 86.3% (Table 3.7b) with $LogReg_{GLS}$ and $LogReg_{LVEF}$, respectively.

TABLE 3.7. Confusion matrices obtained by (a) $LogReg_{GLS}$ and (b) $LogReg_{LVEF}$ models.

a)	Predicted			
		DCM	**HC**	**Σ**
	DCM	88.3%	16.9%	138
Actual	**HC**	11.7%	83.1%	138
	Σ	128	148	276
b)	Predicted			
		DCM	**HC**	**Σ**
	DCM	86.3%	20.4%	138
Actual	**HC**	13.7%	79.6%	138
	Σ	124	152	276

The produced nomograms for $LogReg_{GLS}$ and $LogReg_{LVEF}$ are reported in Figure 3.5 and the features are listed in order of importance. The produced nomograms can be interactively used to determine the likelihood of being in the DCM or HC group. In particular, for each of the features a score (point) corresponding to the specific features value is assigned. Subsequently the sum of the points of all considered features is converted into the probability that the subject belongs to the specific group. For example, in the Figure 3.5a, if the patient has a GLS value equal to 17.5 (43 points on the scale), betaExp equal to 0.9 (4 points), LFn equal to 0.5 (1 point), RMSSD equal to 87.5 (1.5 points) and SD1/SD2 equal to 0.4 (0.5 points), the total sum of points is equal to 50, which corresponds to probability of 65% that the specific subject is affected by DCM.

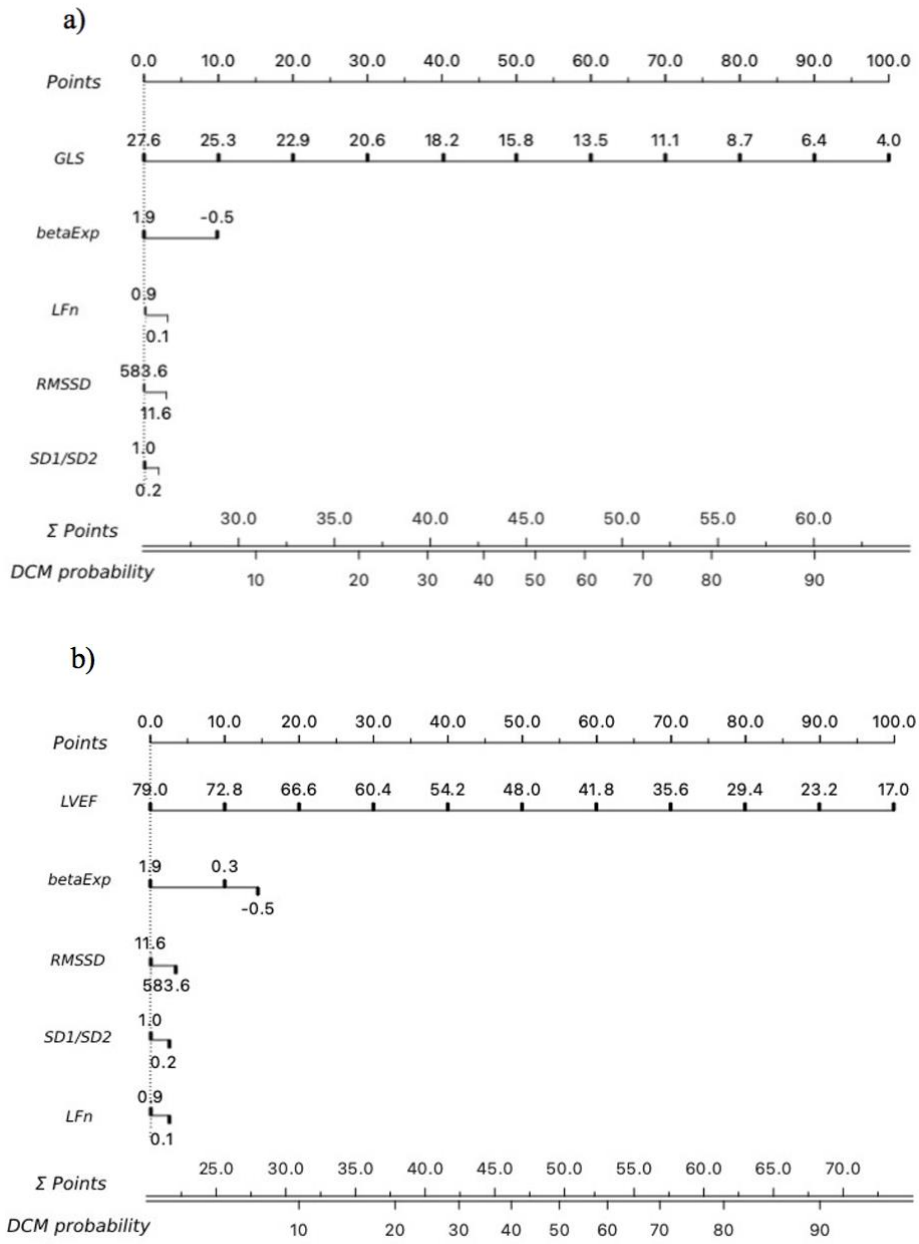

Figure 3.5. *Nomograms for DCM output class for (a)LogReg$_{GLS}$ and (b)LogReg$_{LVEF}$ models.*

3.3.3 Discussion

The results obtained in this study demonstrated that the features SD1/SD2, RMSSD, betaExp, LFn, and GLS in one case, and LVEF in the other, were the most informative for the differential classification of DCM versus HC. The LogReg$_{GLS}$ model achieved an accuracy of 86%, which was slightly higher than the 83% accuracy obtained by the LogReg$_{LVEF}$ model. This finding suggests that the inclusion of GLS as a clinical parameter may offer improved discriminative capacity compared to LVEF alone, partially confirming the hypothesis that GLS can provide more nuanced and early insights into myocardial

dysfunction in DCM. The relevance of GLS, LVEF, and selected HRV features was further supported by the nomograms. In both cases, the clinical parameter, either GLS or LVEF, emerged as the most influential variable in differentiating DCM from HC, reinforcing previous findings in the literature that identify these metrics as essential for the diagnosis of cardiomyopathy [4,113,223].

In conclusion, the slightly better performance of the $LogReg_{GLS}$ model suggests that GLS may be more effective than LVEF in distinguishing DCM patients from healthy individuals, particularly in early disease stages. These findings support the growing recognition of GLS as a reliable and sensitive biomarker for myocardial impairment and advocate for its broader implementation in routine echocardiographic evaluation. Moreover, based on these results, GLS was included, along with HRV parameters and LVEF, in subsequent studies focused on the differential diagnosis of DCM and IHD patients. However, the study is limited by its single-center design and moderate sample size, warranting confirmation of the results in larger, multi-center studies

3.4 Interpretable Model to Support Differential Diagnosis Between Ischemic Heart Disease, Dilated Cardiomyopathy and Healthy Subjects

As previously discussed, chronic IHD and DCM are distinct cardiac conditions that can present with overlapping clinical features, making accurate differential diagnosis challenging, particularly in the absence of invasive or limited-access diagnostic exams. HC may also exhibit early or subclinical signs that further complicate diagnostic clarity. It is crucial to distinguish between DCM and healthy individuals, as early detection enables timely intervention and monitoring to prevent progression to advanced heart failure. Similarly, accurately identifying IHD is essential to initiate appropriate treatment strategies, reduce the risk of acute coronary events, and limit long-term cardiac damage.

Non-invasive diagnostic tools, such as echocardiographic LVEF, GLS, and HRV analysis, have proven useful in detecting various cardiac conditions [6–8,222]. However, these parameters have rarely been used together in a unified diagnostic framework to support differential diagnosis between DCM, IHD, and HC.

Therefore, the aim of this study [209] was to develop an interpretable model that integrates LVEF, GLS, and HRV features to support the differential diagnosis among DCM, IHD, and HC.

3.4.1 Methods

A total of 488 subjects participated in this study, divided into three groups: 146 DCM (60F/86M, aged 61 ± 14y), 182 IHD (44F/138M, aged 73 ± 11y), and 160 HC (80F/80M, aged 61 ± 17y). Patients with DCM were enrolled after clinical evaluation, and those older than 35 years of age, with cardiovascular risk factors and/or without a family history of DCM underwent coronary angiography. The assessment of IHD was based on clinical,

laboratory, and invasive findings [76], and patients with known risk factors such as alcohol or drug abuse, and tachyarrhythmias were excluded from the study. The LVEF was determined using the Simpson biplane method [173], and the GLS was determined using STE. The GLS measurement was performed offline using dedicated software (TomTec Arena v2.0, TomTec Imaging Systems, Unterschleißheim, Germany), with visual assessment of the endocardial border and manual adjustment of the tracing, if necessary, to ensure accurate contour tracing.

As in previous studies, all subjects in this study underwent a 24-hour Holter ECG recording, and both linear and non-linear HRV parameters were extracted from 5-minute segments, as described in Chapter 2.

Subsequently, the dataset was preprocessed to identify potential outliers using the Local Outlier Factor (LOF) detection method. Feature selection was then performed using the Information Gain method, followed by the development of a logistic regression model. The LOF method employed a Hamming distance metric, a contamination rate of 0.1, and a neighborhood size of 20 (k = 20) to estimate local density from the k-nearest neighbors. As a result, 42 subjects were excluded (16 with DCM, 18 with IHD, and 8 HC), leaving a final sample of 130 DCM patients (57F/73M, aged 62 ± 13 years), 164 IHD patients (41F/123M, aged 73 ± 10 years), and 152 HC (77F/75M, aged 61 ± 17 years).

For feature selection, the Information Gain method [200] was applied with a cut-off threshold of 0.086. To evaluate the model's performance, 10-fold cross-validation was used to estimate CA, AUC, F1 score, precision, and recall. Finally, nomograms were created for each group to support interpretation and validation of the resulting model.

3.4.2 Results

The results showed that the most informative features for classification between IHD, DCM e HC, according to obtained Information Gain coefficient were GLS, LVEF, age, FD, SD1/SD2 and sex, listed in order of importance.

The classification performance of produced logistic regression model based on selected features is reported in Table 3.8.

Table 3.8. Performance measures of the logistic regression model.

Model	AUC	CA	F1	Precision	Recall
Logistic Regression	0.83	0.70	0.70	0.71	0.70

The confusion matrix obtained for the logistic regression model is reported in Figure 3.6. The confusion matrix shows that DCM patients were classified with a precision of 78.9%, IHD patients at 65.0%, and HC subjects at 69.4%.

		Predicted			
		DCM	HC	IHD	Σ
Actual	DCM	78.9%	11.9%	14.1%	130
	HC	3.7%	69.4%	20.9%	152
	IHD	17.4%	18.8%	65.0%	164
	Σ	109	160	177	446

Figure 3.6. Confusion matrix obtained by logistic regression model.

The produced nomograms for logistic regression models are reported in Figure 3.7. The features are listed in order of importance allowing us to select the subset of the most informative features.

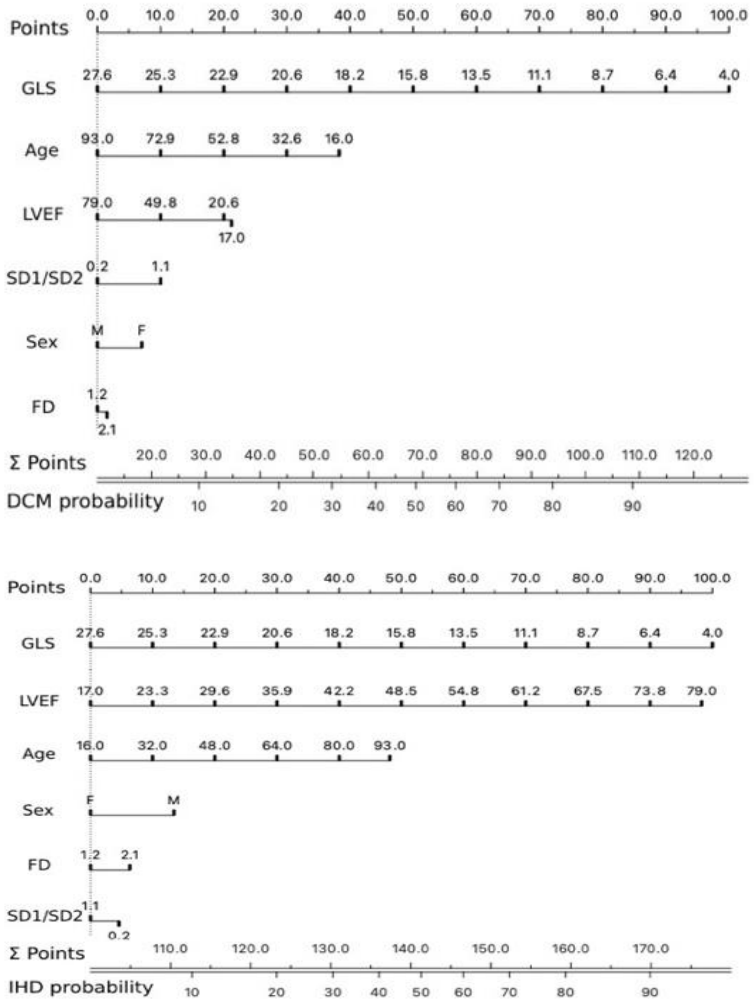

Figure 3.7. Nomograms of the logistic regression model for DCM (top panel) and IHD (bottom panel) groups.

3.4.3 Discussion

This study found that GLS, LVEF, age, FD, SD1/SD2, and sex are the most informative features for accurately classifying DCM, IHD, and HC subjects. The model achieved an accuracy of 70%, and the confusion matrix for the test data showed that the DCM group had the highest precision (78.9%), while the IHD group had the lowest (65.0%). This difference in precision can be explained by the fact that the model's features characterized DCM patients better.

This finding was partially confirmed by the created nomograms for the DCM and IHD groups. In the IHD nomogram, GLS and LVEF appeared to be of equal importance.

However, in the DCM nomogram, GLS was more crucial in the classification of these patients, as evidenced by its more extended line. The model identified GLS < 16 and LVEF < 50 as key thresholds for diagnosing DCM and IHD which are consistent with recent research [224,225], and highlighted age as an important factor, with DCM risk decreasing with age. It is noteworthy to underline that if GLS is less than 16, the probability of developing one of the two disorders increases. Conversely, an LVEF of less than 50 increases the chance of DCM while decreasing the likelihood of IHD.

In conclusion, this preliminary study produced a machine learning model with a reasonably high accuracy for the differential diagnosis of HC, DCM, and IHD. This level of accuracy can aid clinicians in deciding whether further invasive diagnostic tests are necessary. Among the study's limitations are its single-center design and moderate sample size, which suggest that further research with larger cohorts is necessary to confirm these findings. However, given the promising results of this study, the same approach will be applied in future research to differentiate among the three conditions in subjects with a more narrow and diagnostically challenging LVEF range of 40% to 55%, a spectrum that may include cases of IHD, DCM, as well as healthy individuals.

3.5 Development of an Interpretable Model for Improving Differential Diagnosis in Subjects with a Left Ventricular Ejection Fraction Ranging from 40 to 55%

As previously mentioned, LVEF is frequently used to assess heart function and predict outcomes in routine clinical practice [4], although it has inherent limitations. One such limitation is that its diagnostic cut-off has yet to be firmly established, complicating differential diagnosis within the so-called "grey zone" (LVEF: 40–50%) [3], particularly during the early, often asymptomatic stages of disease. Moreover, HC may exhibit LVEF values around 50%, further diminishing the discriminative power of this parameter in borderline cases. Consequently, reliance on LVEF alone may lead to diagnostic uncertainty. Therefore, there is a growing need for additional non-invasive diagnostic tools capable of more accurately distinguishing between DCM, IHD, and HC, especially in patients with LVEF values ranging from 40% to 55%.

For these reasons, this study [210] aimed to develop a multinomial logistic regression model based on HRV, GLS, and clinical features to differentiate between DCM, IHD, and HC in patients with LVEF values within the range of 40–55%.

3.5.1 Methods

The study encompassed 73 DCM patients (45M/28F, aged 61 ± 14 years, LVEF: 46.7 ± 4.3), 71 IHD patients (58M/13F, aged 74 ± 11 years, LVEF: 49.2 ± 4.7), and 70 HC (33M/37F, aged 59 ± 21 years, LVEF: 53.7 ± 1.3). Subjects with an LVEF, obtained by the Simpson biplane method [173] described in Chapter 2, ranging from 40% to 55% were included in the study. The DCM patients were enrolled after clinical assessment. Coronary

angiography was systematically performed in patients older than 35 years and with cardiovascular risk factors and/or without a family history of DCM. The assessment of IHD was based on clinical, laboratory, and invasive findings [76]. IHD patients had not experienced acute coronary syndrome in the three months preceding Holter monitoring. Patients with known trigger factors, such as toxic insults from alcohol or drug abuse, and tachyarrhythmias were excluded from the study. GLS was obtained from STE, following the procedure described in the Chapter 2.

All participants underwent 24-hour Holter ECG monitoring, during which RR intervals were recorded, extracted, and annotated following the procedure outlined in the section 2.1. The RR interval data were divided into consecutive, non-overlapping segments of five minutes each. From each segment, both linear and nonlinear HRV features were computed, also described in the section 2.1.

The dataset was preprocessed to identify the possible outliers using the covariance estimator detection method, subsequently the feature selection was performed using the information gain ratio method, and finally the logistic regression model was produced. In all, 20 subjects were excluded: 7 DCM, 11 IHD, and 2 HC. Therefore, 66 DCM (42M/24F, aged 60 ± 14y), 60 IHD (49M/11F, aged 73 ± 11y), and 68 HC (31M/37F, aged 59 ± 20 y) were considered in the study. The cut-off of the Information Gain Ratio's estimates of the informative attribute was set to 0.044. The CA, AUC, F1, precision, specificity, and recall of the dataset were estimated using 5 random samples with a training set size of 70% of data.

3.5.2 Results

The results showed that the most informative features for classification between the three groups listed in order of importance, according to obtained Information Gain Ratio coefficients were GLS, meanRR, sex, age, and LFn for the logistic regression model. The classification performance of produced logistic regression model based on selected features on the test set is reported in Table 3.9.

Table 3.9. Performance measures of the logistic regression model on test set.

Model	AUC	CA	F1	Prec.	Spec.	Recall
Logistic Regression	0.89	0.73	0.73	0.73	0.87	0.73

The confusion matrix obtained for the logistic regression model considering the test set of data is reported in Figure 3.8. The confusion matrix shows that DCM patients were classified with a precision of 76.2%, IHD patients at 63.5%, and HC subjects at 79.1%.

		Predicted			
		DCM	HC	IHD	Σ
Actual	DCM	76.2%	9.6%	26.0%	100
	HC	4.8%	79.1%	10.4%	105
	IHD	19.0%	11.3%	63.5%	90
	Σ	84	115	96	295

Figure 3.8. Confusion matrix obtained by logistic regression model considering the test set (size of 30%) of data.

The produced nomogram of the logistic regression model for HC, DCM and IHD groups are reported in Figure 3.9. The features are listed in order of importance allowing us to select the subset of the most informative features.

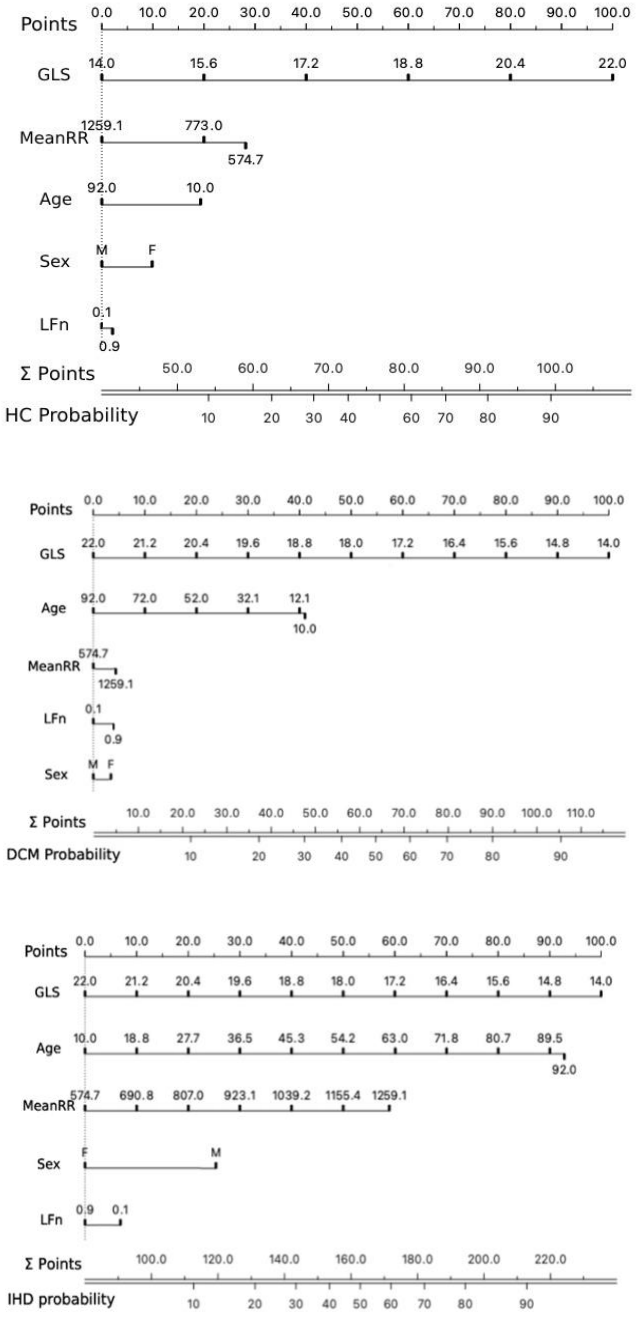

Figure 3.9. *Nomograms of the logistic regression model for HC (top panel), DCM (middle panel) and IHD (bottom panel) groups.*

3.5.3 Discussion

The results of this study showed that GLS, meanRR, sex, age, and LFn are the most informative features for the differential classification of DCM, IHD, and HC with a LVEF between 40% and 55%. The model achieved an accuracy of 73%, and the confusion matrix for the test set indicated that the HC group was classified with the highest precision (79.1%), while the IHD group had the lowest precision (63.5%). As in the previous study [209], this disparity in precision can be attributed to the model's features, which more effectively characterized HC and DCM patients. The constructed nomograms for the three groups showed that, in the HC and DCM nomograms, the longest feature bar corresponds to GLS, indicating that it is the most discriminative feature for these groups. In contrast, the IHD nomogram displays features of similar lengths, suggesting the absence of a single dominant feature for discriminating IHD patients.

The HC nomogram can be particularly useful for the preliminary distinction between healthy individuals and patients. It shows that the probability of being healthy increases with a GLS value greater than 17.5, a low meanRR, and younger age. The other two nomograms can then be used to distinguish between the DCM and IHD groups. Notably, in both nomograms, GLS, age, and meanRR are the first, second, and third features ranked by importance, respectively.

In conclusion, once again, a model with moderately high classification accuracy that can support the diagnostic process was developed. The high precision in identifying healthy individuals is particularly noteworthy, as it may help prevent unnecessary invasive procedures in borderline cases and healthy subjects. Building on this outcome, the subsequent research focused on providing diagnostic support for differentiating between IHD and DCM within a highly challenging "gray zone", specifically, patients with mildly reduced ejection fraction, characterized by a narrower LVEF range (40%–50%).

3.6 Enhancing Differential Diagnosis of IHD and DCM Using Interpretable Machine Learning in Mildly Reduced Ejection Fraction

The differential diagnosis between IHD and DCM can be particularly challenging in the presence of LV systolic dysfunction, typically defined as a LVEF of less than 50%. This diagnostic complexity arises from the necessity to exclude significant coronary artery disease (CAD) in order to establish a definitive diagnosis of DCM. In this context, the decision to perform coronary angiography, a key tool for identifying obstructive CAD, becomes especially nuanced in the outpatient setting, particularly for individuals with mildly reduced ejection fraction (LVEF between 40% and 50%) [3].

Given these diagnostic challenges, GLS has gained attention as a more sensitive indicator of early LV systolic dysfunction compared to LVEF [113,226]. Moreover, patients with both IHD and DCM often exhibit a notable decrease in the cardiac autonomic nervous system's regulation. For this reason, HRV emerges as a potential source of valuable prognostic information [71].

This study [211] aims to assess the discriminative power of GLS and HRV parameters in interpretable machine learning models developed to differentiate between DCM and IHD in patients with mildly reduced ejection fraction.

3.6.1 Methods

This study was conducted on a cohort of consecutive patients who presented to the Heart Failure Clinic at the Cardiovascular Department of Trieste University Hospital between 2019 and 2021. The inclusion criteria were diagnosis of DCM or IHD, LVEF of 40-50% on echocardiogram, a 24-hour Holter ECG performed within three months before or after the echocardiographic assessment, and no recent history of acute myocardial infarction or hospitalization for heart failure.

According to the ESC guidelines the diagnosis of DCM was defined by the presence of impaired contraction of the LV or both ventricles, in the absence of CAD, hypertension, valvular disease, and congenital heart disease sufficient to explain the myocardial abnormality [227]. Coronary angiography was conducted systematically in all patients older than 35 years with cardiovascular risk factors and/or a family history of CAD, and cardiac magnetic resonance imaging was used when necessary to assess the pattern of non-ischemic late gadolinium enhancement and other relevant sequences required for a definitive diagnosis. Additionally, clinical, electrocardiographic, and echocardiographic data were integrated to support the diagnosis.

The final diagnosis of IHD was established based on angiographic evidence of significant flow-limiting atherosclerotic obstruction in at least one epicardial coronary artery (i.e., ≥70% stenosis in one or more main branches and/or ≥50% stenosis in the left main coronary artery). This was further supported by anatomical, physiological, and clinical evidence indicating that the aforementioned obstructive coronary stenoses had either led to regional ischemia requiring invasive treatment [228] in the patient's medical history or precipitated acute myocardial infarction in previous acute settings.

The echocardiographic images were subsequently visually assessed by two cardiologists. GLS was obtained following the procedure described in the Chapter 2. Each subject underwent a 24-hour Holter ECG recording, from which RR intervals were obtained and labeled according to the procedure outlined in the section 2.1. The recordings were then divided into non-overlapping 5-minute segments, and both linear and non-linear HRV features were extracted from each segment, following the approach detailed in Chapter 2.

Descriptive statistics included means ± standard deviations (SDs) for continuous variables, and proportions for categorical variables (n, %). Differences between the variables between IHD and DCM patients were evaluated with the two-sample t-test for continuous parameters and the chi-square test for proportions. Statistical significance was set at $p<0.05$.

Predictive models for classifying DCM and IHD were developed using a set of HRV features, along with sex, age, and GLS. Features with a ReliefF score exceeding 0.010 were retained for modeling to reduce dimensionality and enhance generalizability and three supervised machine learning algorithms, logistic regression, naive Bayes, and decision trees, were employed. Model performance was assessed using 5-fold cross-validation. Performance metrics were averaged across folds and included CA, F1 score, precision,

recall, specificity, and the AUC. The performance of each classifier was evaluated also using ROC curves. The aforementioned performance metrics were used to select the best model.

3.6.2 Results

Among the 3,196 patients consecutively evaluated at the Heart Failure Clinic of the Cardiovascular Department of Trieste University Hospital in the study period, 122 with DCM and 110 with IHD met the inclusion criteria and were included. Forty-four patients (25 with DCM and 19 with IHD) whose images were considered inadequate for GLS measurement were excluded. As a result, the final study population included 188 patients: 97 with DCM and 91 with IHD.

The mean ± SD values of demographic characteristics, as well as LVEF, GLS, and extracted HRV parameters for both DCM and IHD, are reported in Table 3.10. Patients with DCM were significantly younger than those with IHD (57 ±15 vs 71±11 years, p<0.001). Both groups exhibited a predominance of male patients, especially the IHD population (73 males and 18 females for IHD and 63 males and 34 females for DCM; p = 0.019).

Table 3.10. Mean and standard deviation values of the features set and the p-value of each feature for intergroup comparison (p<0.05 in bold). The ReliefF values are also reported and the features with a ReliefF value higher than 0.01 (in bold) were included in the final model.

	DCM	IHD	p-value	ReliefF value
Age	57±15 years	71±11 years	**<0.001**	**0.058**
Sex (M/F)	63/34	73/18	**0.019**	**0.042**
LVEF (%)	44.5±3.1	45.2±3.1	0.166	-
GLS (%)	-15.0±2.5	-14.6±2.4	0.320	**0.012**
HRV				
MeanRR (ms)	694±186	859±22	**<0.001**	**0.025**
SDNN (ms)	57.3±26.9	81.7±52.7	**<0.001**	0.008
RMSSD (ms)	56.0±43.3	99.6±82.1	**<0.001**	0.008
NN50	36.7±44.7	75.2±80.5	**<0.001**	0.004
pNN50	0.11±0.13	0.23±0.22	**<0.001**	**0.012**
LF (ms^2)	1490±2193	2382±4437	0.079	0.003
HF (ms^2)	1652±2545	3500±5775	**0.005**	0.005
LF/HF	2.15±2.41	1.32±1.64	**0.007**	0.001
LFn	0.46±0.18	0.41±0.19	0.064	**0.010**
HFn	0.33±0.13	0.49±0.18	**<0.001**	**0.017**
BetaExp	0.87±0.45	0.67±0.52	**0.005**	0.007
SD1 (ms)	25.9±15.1	42.2±30.4	**<0.001**	**0.011**
SD2 (ms)	72.8±32.2	96.5±59.5	**0.001**	0.007
SD1/SD2	0.28±0.10	0.38±0.14	**<0.001**	**0.012**

FD	1.18±0.32	1.43±0.27	**<0.001**	**0.017**

No significant differences in GLS values were detected between IHD and DCM (-14.6±2.4 vs -15.0±2.5 respectively, p = 0.320). Conversely, all extracted HRV parameters, except for LF and LFn, were statistically different. In particular, the observed HF were significantly greater in IHD compared to the DCM group (3500±5775 vs 1652±2545 respectively, p=0.005) and the LF/HF ratio was notably higher in the DCM group than in the IHD group (2.15±2.41 vs 1.32±1.64 respectively, p = 0.007). Both groups exhibited low mean SDNN values, with a more pronounced reduction in the DCM group compared to the IHD group (57.3±26.9 vs 81.7±52.7 respectively, p < 0.0001). A similar trend, with significantly lower values in the DCM group, was observed across all other time-domain measures, including mean RR, RMSSD, NN50, and pNN50. Regarding non-linear parameters, FD was significantly higher, and Beta exponent was significantly lower in the IHD group compared to the DCM group, indicating a higher complexity of the HRV signal in the IHD population. Additionally, the mean values of SD1 and SD2, which represent short-term and long-term heart rate variability, were significantly lower in the DCM group. The SD1/SD2 ratio, reflecting the relationship between short-term and long-term variability, was also significantly reduced in the DCM compared to the IHD group (0.28±0.10 vs 0.38±0.14 respectively, p < 0.001).

The set of features selected for the final models obtained using the ReliefF method, with a threshold of 0.01, included Sex, Age, MeanRR, FD, HFn, GLS, pNN50, SD1/SD2, SD1, and LFn. The classification performance of the models generated by the three approaches (i.e., logistic regression, naïve Bayes and classification tree) is reported with the corresponding ROC curves in Figure 3.10. Among the interpretable models, the logistic regression model demonstrated the highest classification performance, outperforming the naïve Bayes and classification tree models (Figure 3.10). Specifically, the logistic regression model achieved a classification accuracy of 76% for the differential diagnosis between DCM and IHD, with balanced sensitivity and specificity of 76% each (Figure 3.10). Moreover, for this model, that showed the best performance, the ROC curves for classifying IHD and DCM are reported in Figure 3.11.

Model	AUC	CA	F1	Precision	Recall	Specificity
Logistic regression	0.83	0.76	0.76	0.76	0.76	0.76
Naive Bayes	0.76	0.70	0.70	0.71	0.70	0.69
Tree	0.68	0.65	0.65	0.66	0.65	0.66

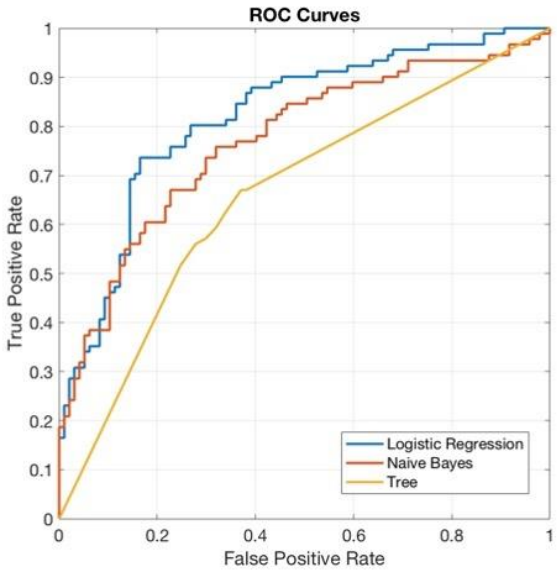

Figure 3.10. *Classification performance measures of the produced logistic regression, naïve Bayes, and classification tree models and corresponding ROC curves (blue, orange and yellow respectively).*

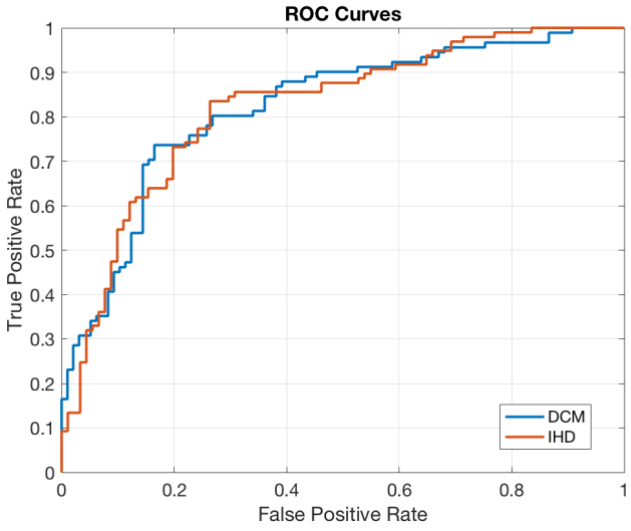

Figure 3.11. *ROC curves of the logistic regression model for classifying IHD (orange) and DCM (blue).*

The nomogram derived from the logistic regression model for differentiating DCM from IHD in patients with mildly reduced ejection fraction is shown in Figure 3.12. The total score, reflecting the probability of DCM compared to IHD, is calculated by summing the points assigned to each individual feature. Notably, Age, MeanRR, Sex, SD1, and GLS were

identified as the most important contributing features. We provided two explicative examples of its application. In the first case, preserved GLS and normal HRV parameters suggest maintained parasympathetic activity, indicating a pattern more typical of IHD. In contrast, the second case shows severe autonomic dysfunction with sympathetic dominance typical of DCM, despite family history suggesting IHD. The preserved GLS in this case may indicate early-stage DCM or a variant with maintained longitudinal function, highlighting the complexity of diagnosis in certain patients.

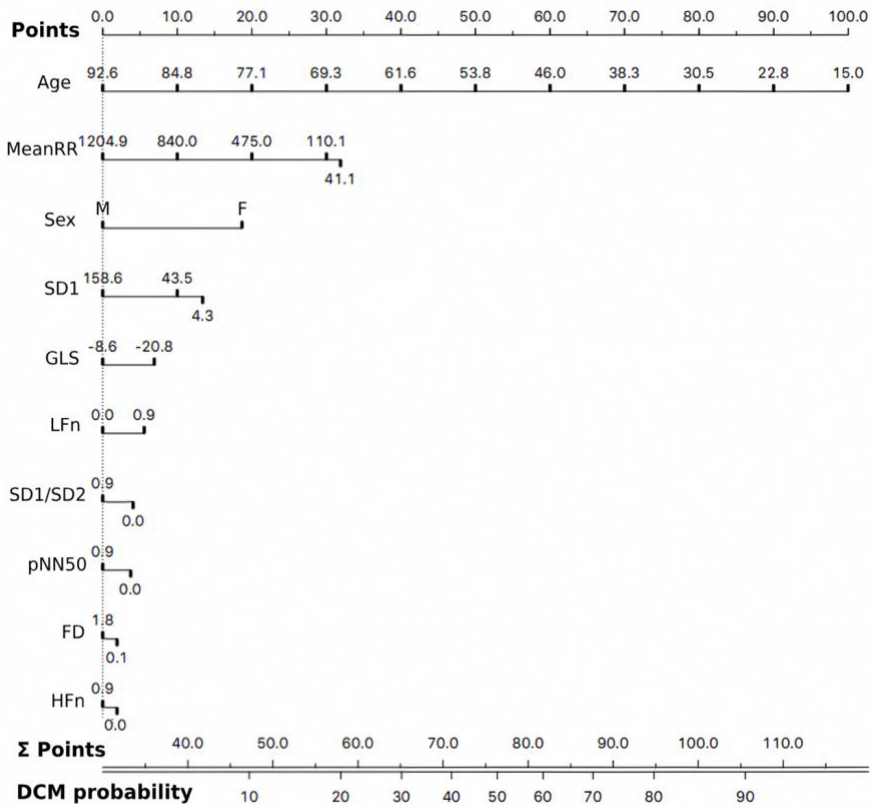

Figure 3.12*. The nomogram derived from the logistic regression model. It estimates the probability of DCM by summing points assigned to individual features. The IHD probability is determined by subtracting the DCM probability from 100. Two opposite clinical scenarios:* ***1)*** *70-year-old male with mild to moderate cardiovascular risk, no IHD history. Echocardiography shows mildly dilated left ventricle, slightly depressed function, GLS -11%. HRV parameters: mean RR 1000 ms, SD1 50 ms, SD1/SD2 0.5, LFn 50 nu, PNN50 50-60%, HFn 20 nu, FD 1. Model scoring: 0 (sex), 29 (age), 2 (GLS), 23 (HRV); total 54 points. Probability: 16% DCM, 84% IHD.* ***2)*** *45-year-old female, strong family history of early-onset IHD and sudden cardiac death, no significant cardiovascular risk factors. Echocardiography: mildly reduced ejection fraction and dilation, GLS -17%. HRV parameters: mean RR 450 ms, SD1 43 ms, SD1/SD2 0.4, LFn 80 nu, PNN50 30%, HFn 30 nu, FD 1.4. Model scoring: 18 (sex), 61 (age), 5 (GLS), 41 (HRV); total 125 points. Probability: 96% DCM.*

3.6.3 Discussion

The main finding of this study is the development of an interpretable machine learning model based on HRV, GLS, and demographic features that can assist in the differential diagnosis between DCM and IHD in subjects with mildly reduced ejection fraction. The logistic regression model achieved a classification accuracy of 76% in distinguishing DCM

from IHD, with balanced sensitivity and specificity, both at 76%. Sex, Age, MeanRR, FD, HFn, GLS, pNN50, SD1/SD2, SD1, and LFn were identified as the most important features in distinguishing between IHD and DCM.

These results underscore the value of a novel integrative approach that combines HRV features with GLS to differentiate cardiac pathologies in this patient population. Nevertheless, the distinction in GLS between DCM and IHD remains debated [229,230]. Since GLS and LVEF are correlated [231], GLS values may fall within a constrained range in cases of mildly reduced ejection fraction, potentially limiting their discriminative power. However, this limitation does not diminish the utility of GLS when it is used as part of a composite predictive model alongside other relevant features.

Importantly, the most novel contribution of this study concerns the significant HRV predictors identified to differentiate between DCM and IHD, which improve the accuracy in distinguishing IHD from DCM patients with an early decrease in LVEF. In particular, the key predictive features identified were MeanRR, SD1, LFn, SD1/SD2, pNN50, FD, and HFn.

Our study has some limitations. Firstly, although the study population is statistically powered, it is small, partly due to the specific focus of the study. Additionally, 44 subjects were excluded due to the inability to obtain the GLS value, a crucial parameter for our analysis. The small sample size did not allow us to test the performance on external test set, however, the 5-fold cross-validation approach we employed provides a robust internal estimate of model's performance. Secondly, the exclusion of ectopic beats from the HRV signal prevents the application of the constructed model to patients with a high number of extrasystoles. Another limitation is the non-systematic availability of cardiac magnetic resonance. Furthermore, due to the small sample size and monocentric design, the study results should be confirmed in larger clinical studies.

In conclusion, this study demonstrates the added value of integrating HRV metrics with myocardial deformation parameters for the differential diagnosis of DCM and IHD in patients with mildly reduced ejection fraction. The proposed machine learning model effectively captures complex interactions among demographic, autonomic, and myocardial functional parameters, potentially improving diagnostic accuracy and supporting clinical decision-making. These findings not only offer an interpretable model but also highlight the valuable interplay between HRV and myocardial function, information that can significantly aid clinicians in distinguishing between these two conditions. This approach may help avoid unnecessary, invasive, and costly procedures, enabling earlier diagnosis and ultimately leading to better patient management and improved clinical outcomes.

3.7 DISCUSSION AND CONCLUSIONS

One of the aims of this thesis was to improve the differential diagnosis between IHD and DCM by leveraging HRV features and echocardiographic imaging parameters, obtained by signal and image processing, within interpretable machine learning models. Through a series of studies, the work systematically addressed key aspects of this challenge, ranging from the influence of HRV signal preprocessing to the comparative diagnostic value of both established (LVEF) and underutilized (GLS) echocardiographic markers, as well as linear

and non-linear HRV features. Particular attention was given to diagnostically challenging subgroups, such as patients with mildly reduced ejection fraction, where traditional diagnostic criteria often fail to provide a definitive diagnosis without relying on invasive or less readily available techniques.

Although HRV is used in several studies to support the diagnosis of various cardiovascular conditions, there is still no consensus on preprocessing methodologies, which can significantly influence the final results. One of the most debated issues is whether to include or exclude ectopic beats in HRV signal analysis. The results of this thesis demonstrated that the model based on HRV features including ectopic beats achieved superior classification performance compared to the model that relied solely on features derived from normal beats. However, it is noteworthy that in both scenarios, regardless of whether ectopic beats were included or excluded, the models consistently identified the same features as the most relevant. This suggests that model development is not substantially influenced by this preprocessing choice. Indeed, certain parameters remained stable irrespective of ectopic beat inclusion, indicating that in some cases, the decision to include or exclude ectopic beats may have limited impact on the model's effectiveness. On the other hand, statistical analysis comparing parameters with and without ectopic beats across the two groups revealed opposite trends for some features, suggesting that the exclusion of ectopic beats affects HRV parameters differently in healthy individuals compared to patients with IHD. Therefore, while our findings indicate a potential advantage in retaining ectopic beats for model training, their exclusion, when clinically justified, would not result in a significant decrease in model performance.

The subsequent objective of this research was to develop clinically interpretable predictive models. Specifically, three machine learning techniques (classification trees, naïve Bayes, and logistic regression) were employed to determine the most effective method for distinguishing patients with IHD from those with DCM in the early stages of disease. The findings demonstrated that interpretable machine learning models can achieve clinically meaningful classification performance in this specific patient population, providing valuable support for first-line diagnostic decision-making. By identifying the most relevant features, the study also underscores the importance of interpretability in machine learning, as clinical plausibility can be evaluated at the level of individual variables through the use of nomograms. When assessed across multiple features, such models further offer insights into potential threshold values for HRV parameters that are not yet fully characterized in relation to disease. Indeed, with the growing integration of machine learning into clinical practice, interpretability has shifted from a desirable feature to a clinical and ethical necessity, despite the variety of definitions and conceptual frameworks discussed in the literature [145,154–156]. Clinicians must be able to understand, trust, and effectively communicate the outputs of predictive models. Interpretable models enable them to validate thresholds, ensure consistency with established clinical knowledge, and detect potential anomalies. By offering transparency, reliability, and clinical relevance, interpretable models are uniquely positioned to fulfill this role, and the findings of this thesis support this claim.

This PhD thesis also aimed to assess the predictive value of parameters extracted from echocardiographic images. Specifically, two fundamental parameters were considered: LVEF and GLS. LVEF is the most commonly used parameter for evaluating cardiac function and predicting clinical outcomes, particularly in patients with DCM. However,

despite its widespread use, LVEF has several inherent limitations. GLS, on the other hand, provides valuable insights into subtle changes in left ventricular function, and several studies have demonstrated its superior sensitivity and prognostic value compared to traditional LVEF measurements [7,74]. The findings described in this thesis also suggest that the inclusion of GLS as an imaging parameter may enhance discriminative capacity compared to the use of LVEF alone. This partially confirms the hypothesis that GLS provides more nuanced and earlier insights into myocardial dysfunction. In particular, GLS appears to be more effective than LVEF in distinguishing patients with DCM from healthy individuals, especially in the early stages of the disease [208].

Moreover, our results suggest that GLS is valuable in the differential diagnosis of DCM and IHD in patients with mildly reduced LVEF, although the extent of the difference in GLS values between these two groups remains debated. In studies that considered unselected populations of IHD and DCM patients without LVEF restrictions, Mohamed et al. reported significantly higher GLS values in IHD patients compared to those with DCM [229]. Conversely, Vietheer et al. did not observe a statistically significant difference in GLS between the two groups, although ischemic patients still tended to exhibit higher GLS values [230].

In the study that was conducted during the PhD period [211], no statistically significant differences were observed in GLS values between IHD and DCM patients with LVEF ranging from 40% to 50% ($p = 0.320$). This finding may be attributable to the narrow LVEF range of the considered sample. Given the known correlation between LVEF and GLS [231], it is plausible that GLS values were similarly constrained, potentially limiting their capacity to reveal pronounced intergroup differences. Nevertheless, this does not diminish the potential diagnostic utility of GLS when incorporated into multivariable predictive models alongside other parameters examined in the context of this thesis.

Specifically, GLS emerged as a significant predictor, with decreasing values associated with a higher probability of DCM. While GLS has already been established as a reliable prognostic marker in DCM patients [232], who typically exhibit lower GLS values than their ischemic counterparts [229,230], this results reinforce its utility by demonstrating significant and disproportionate alterations in GLS even among patients with comparable ejection fraction values [233,234]. These findings support the growing consensus that GLS constitutes a sensitive and robust biomarker for myocardial impairment and advocate for its broader adoption in routine echocardiographic assessment.

The results obtained in this thesis have underscored the high diagnostic value of parameters derived from both linear and nonlinear analyses of HRV signals in differentiating between patients with IHD, those with DCM, and healthy subjects. In particular, two HRV parameters, namely, the SD1/SD2 ratio and the nonlinear measure FD, emerged as especially important in supporting the differential diagnosis among these three groups [209].

These parameters were also found in the results of this thesis to be significant in distinguishing between IHD and DCM patients with mildly reduced ejection fraction. Previous studies showed that lower FD values were generally associated with DCM [235], whereas higher FD values were indicative of IHD [236]. This finding suggests distinct patterns of neuro-autonomic regulation of heart rate between the two pathologies, as well as an overall reduction in the complexity of physiological variability in diseased states [236].

Additionally, in our study, within this subgroup, DCM patients exhibited more severe autonomic dysfunction and impaired cardiovascular adaptability compared to IHD patients, as reflected by a more pronounced reduction in short-term HRV (SD1) [237,238]. Consequently, both SD1 and the SD1/SD2 ratio were identified as significant predictors for differential diagnosis, with lower values being more strongly associated with DCM.

Two HRV parameters that proved particularly relevant for the differential diagnosis of subjects with LVEF in the gray zone, across two studies conducted during the doctoral research, were meanRR and LFn. Specifically, in one study which was part of this project, meanRR successfully distinguished between pathological subjects and healthy controls [209], while in another, it differentiated between patients with IHD and those with DCM [207]. Notably, meanRR also proved significant in differentiating DCM from IHD patients regardless of the LVEF values.

In detail, meanRR was found to be significantly lower in DCM patients compared to those with IHD, both in cases where patients had an LVEF between 40% and 50%, and when no LVEF limitation was applied. This reduction in meanRR in DCM is likely attributable to more frequent alterations in the cardiac electrical conduction system, which are commonly observed in this condition. Conversely, patients with IHD typically exhibit a more stable heart rhythm, possibly due to a relatively preserved autonomic nervous system response [239], resulting in longer meanRR intervals.

Furthermore, elevated LFn values were consistently observed in DCM patients, whereas reduced LFn values were more characteristic of those with IHD. Elevated LFn reflects sympathetic nervous system dominance and is generally associated with worse clinical outcomes [76]. In contrast, reduced LFn has been linked to increased mortality rates in both ischemic and non-ischemic patients with compromised left ventricular function [221,240].

Lastly, another parameter that effectively differentiated between IHD and DCM, regardless of whether patients presented with mildly reduced ejection fraction or not, was the time-domain HRV measure pNN50. This parameter, which is associated with parasympathetic nervous system activity [75], was also found to be lower in DCM patients. Such a finding may suggest an autonomic imbalance characterized by sympathetic dominance, which appears to be more frequently impaired in DCM than in IHD. Supporting this, a recent study demonstrated that lower pNN50 values are indicative of DCM in comparison to healthy individuals [241]. Additionally, previous research has associated reduced pNN50 with an increased risk of death due to progressive pump failure [242].

In conclusion, this thesis highlights the added value of integrating HRV features with myocardial deformation parameters, such as GLS and LVEF, for the differential diagnosis of DCM and IHD. The findings demonstrate that interpretable machine learning models not only allow clinicians to understand the rationale behind the model's predictions and assess parameter thresholds, but also underscore the informative interplay between autonomic regulation and myocardial function. This integrated approach offers significant clinical utility, particularly in diagnostically challenging cases involving patients with mildly reduced ejection fraction, where conventional diagnostic criteria may be insufficient. Therefore, these models have the potential to facilitate earlier and more accurate diagnoses, while minimizing the need for unnecessary, invasive, and costly procedures, thereby enhancing clinical decision-making and patient outcomes.

Chapter 4. NON-INVASIVE EEG AND ASL-MRI APPROACHES IN ACUTE AND POST-STROKE CARE

An increasingly recognized priority in acute stroke care is to improve characterization of patients and to identify a novel and reliable biomarkers for predicting functional outcomes. While neuroimaging plays a central role in the diagnosis of ischemic stroke and in guiding reperfusion treatment decisions, predicting both short- and long-term outcomes remains a significant clinical challenge. In this context, there is growing research interest for novel, non-invasive prognostic tools.

EEG, despite its potential, remains underutilized in routine stroke unit practice. In particular, the prevalence and prognostic value of epileptiform patterns in EEG, especially interictal epileptiform discharges (IEDs), have been poorly investigated in ischemic stroke patients. The first study presented in the section 4.1 [243] addresses this gap by applying interpretable machine learning models to evaluate the predictive value of epileptiform EEG patterns recorded within the first 72 hours post-stroke, with respect to 3-month functional outcomes measured using mRS.

Given the potential prognostic role of these EEG patterns, and recognizing that continuous EEG monitoring may not be feasible for all stroke patients, it becomes essential to stratify the population to identify those most likely to benefit from EEG monitoring. Therefore, a second study, depicted in the section 4.2 [244], explores the use of machine learning classifiers to predict the presence of epileptiform EEG activity based on clinical features, and evaluates the impact of dataset balancing techniques, such as over-sampling and under-sampling, on model performance.

A particularly understudied subgroup within the stroke population includes patients undergoing mechanical thrombectomy. In cases of successful reperfusion, this intervention leads to a rapid reopening of large vessel occlusions (LVO), which may restore normal neuronal activity in accordance with the neurovascular coupling principle. Thus, early normalization of EEG activity post-thrombectomy could serve as a potential marker of favorable prognosis. The study presented in section 4.3 investigates spectral features extracted from EEG recordings acquired shortly after reperfusion therapy, integrating these data with clinical and neuroimaging variables into interpretable models for outcome prediction.

One of the key diagnostic challenges in acute stroke management is distinguishing true ischemic strokes from stroke mimics in patients presenting with isolated aphasia, a symptom commonly associated with either ischemia or seizures. Although CT perfusion imaging facilitates early diagnosis, its limited repeatability underscores the need for non-invasive alternatives. To address this, the study presented in section 4.4 investigates the use of ASL MRI to track perfusion changes over time, with the aim of identifying imaging biomarkers that enable accurate and timely differential diagnosis.

4.1 Prognostic Value of Early Interictal Epileptiform EEG Patterns in Ischemic Stroke: A Predictive Model for Functional Outcomes

An accurate prediction of clinical outcomes in acute ischemic stroke is essential for improving patient management. This prediction is particularly complex, as it depends on various clinical, radiological, and neurophysiological characteristics [245,246]. In this context, neurophysiological biomarkers derived from EEG are emerging as promising tools for predicting patients' functional outcome [16,247]. Indeed, acute stroke is a neurological emergency characterized by a reduction in regional cerebral blood perfusion, leading to alterations in the brain's electrical activity [14,248], which reflects the phenomenon of neurovascular coupling [15].

Besides EEG slowing abnormalities, increasing evidence suggests the presence of epileptiform patterns in patients with acute ischemic stroke. Recent studies have investigated the prevalence of IEDs and seizures during the acute and subacute phases of stroke [20,21]. However, data on IEDs during the acute ischemic stroke phase remain insufficient, particularly regarding their predictive value in patients without clinical seizures, a history of epilepsy, or anticonvulsant treatment.

Therefore, the aim of this study [243] was to investigate whether the presence of the IEDs in the EEG in the first 72 hours make contribute to the prediction of clinical functional outcome, as measured by the mRS at three months, in treated stroke patients and produce the predictive model.

4.1.1 Methods

This study retrospectively analyzed clinical, neurophysiological, and neuroimaging data from a cohort of acute stroke patients admitted to the Stroke Unit of the Neurological Clinic at Trieste University Hospital. The inclusion criteria were the patients with ischemic stroke who underwent reperfusion treatment and had an EEG within the first three days of the sub-acute phase, irrespective of age or gender. Exclusion criteria included stroke mimics, prior epileptic seizures, ongoing anti-epileptic treatment, or logistical issues preventing EEG recording.

Initial evaluations included NCCT upon admission, with some patients also undergoing CTA or CTP scans. MRI was performed for patients without confirmed lesions on follow-up CT. Data collected included demographic details, stroke risk factors (e.g., atrial fibrillation, diabetes, hypertension, smoking, chronic heart failure), clinical features (e.g., NIHSS on admission and discharge, mRS at discharge and 3 months), and lesion characteristics (e.g., cortical involvement, infarct location, side, sum of lobes with an infarct area, and lobe involvement).

Standardized clinical and diagnostic assessments were conducted during hospitalization and at 3 months post-stroke. Outcomes were determined via phone interviews or follow-up

exams by two neurologists. Neurologic impairment was evaluated using the NIHSS, recorded on the 7th day or earlier if discharged, and functional outcomes were assessed using the mRS at 3 months.

The EEG signal was acquired and processed as detailed in the Chapter 2. IEDs were identified in accordance with the guidelines of the International Federation of Clinical Neurophysiology and defined as di- or tri-phasic sharp waves followed by a characteristic slow after-wave [249].

Feature selection was performed using the GR method and only features with a GR value higher than 0.03 were included. Odds ratios (OR) with corresponding 95% confidence intervals (CI) were calculated for the selected features. Five different machine learning models were considered in the study: classification tree, logistic regression, naïve Bayes, artificial neural network and SVM. The CA, AUC, F1 score, precision, recall, and specificity were evaluated using 5-fold cross-validation. Additionally, confusion matrices and ROC analyses were generated for each model.

4.1.2 Results

The study sample consisted of 228 stroke patients (74±14 year, 122 females; 127 patients with good outcome and 101 patients with poor outcome) who underwent EEG within the first 72 hours. The features identified as highly predictive by the GR method were NIHSS at admission (GR = 0.13), mRS anamnestic (GR = 0.05), chronic heart failure (GR = 0.05), acute infectious disease (GR = 0.05), sum of lobes (GR = 0.04), atrial fibrillation (GR = 0.03), and IEDs (GR = 0.03). This set of selected features was used to develop the machine learning models.

Table 4.1 reports the performance metrics of developed classification models and the ROC curves are depicted in Figure 4.1. All models demonstrated medium-to-high performance, with the logistic regression model, an interpretable approach, achieving the highest accuracy. Specifically, the logistic regression model, which integrates clinical parameters and risk factors along with IEDs, predicted the outcomes of treated stroke patients with an accuracy of 81%.

Table 4.1. *Performance measures of the five produced models.*

Models	CA	AUC	F1	Prec.	Recall	Spec.
Logistic Regression	0.81	0.83	0.80	0.81	0.81	0.79
SVM	0.79	0.84	0.79	0.80	0.79	0.77
Neural Network	0.79	0.84	0.79	0.79	0.79	0.77
Tree	0.77	0.77	0.77	0.78	0.77	0.75
Naïve Bayes	0.76	0.83	0.76	0.76	0.76	0.74

Table 4.2 presents the confusion matrix for the best-performing model, the logistic regression model. The confusion matrix demonstrates that this model correctly predicts the outcomes of 81% of stroke patients.

Table 4.2. *Confusion matrix obtained by the best-performing model, the logistic regression.*

	Good outcome	**Poor outcome**	∑
Good outcome	113	14	127
Poor outcome	30	71	101
∑	143	185	228

Finally, the association between significant features and the poor outcome identified by the logistic regression model that presented the best performance was expressed as odds ratios with 95% confidence intervals. In particular, higher NIHSS scores at admission (OR: 1.03, 95% CI: 1.02–1.04) and greater pre-stroke functional disability, as measured by the anamnestic mRS (OR: 1.10, 95% CI: 1.04–1.15), are significant predictors of poor outcomes. Chronic heart failure (OR: 1.07, 95% CI: 0.96–1.19), atrial fibrillation (OR: 1.07, 95% CI: 0.96–1.31), and acute infectious disease (OR: 1.12, 95% CI: 0.96–1.30) showed slightly elevated odds, with confidence intervals exceeding 1. The cumulative burden of lobar pathologies (Sum of Lobs) shows a marginal association with poor outcomes (OR: 1.04, 95% CI: 1.00 - 1.08). Importantly, the presence of IEDs is associated with a higher likelihood of poor outcomes (OR: 1.13, 95% CI: 1.00 - 1.28).

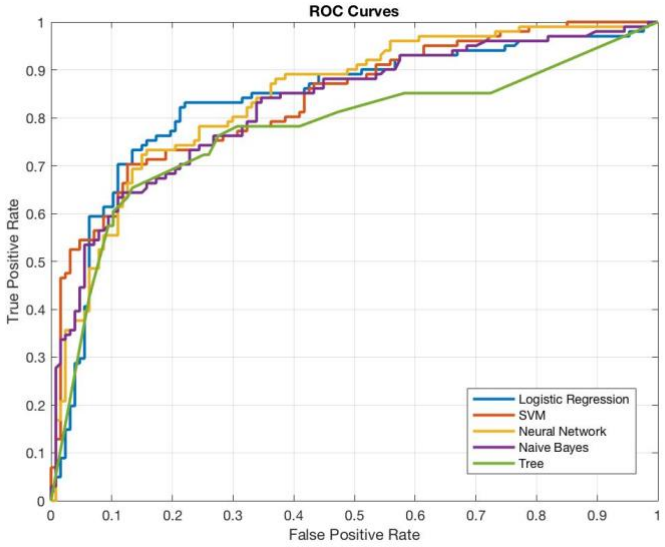

Figure 4.1. *ROC curves for the five produced models.*

4.1.3 Discussion

The results of this study highlight that the presence of IEDs, as an EEG biomarker, is a strong predictor of poor outcomes and may enhance the prediction of functional prognosis when considered alongside other clinical and radiological features, such as NIHSS at admission, anamnestic mRS, chronic heart failure, acute infectious disease, sum of affected lobes, and atrial fibrillation, identified through feature selection. All models evaluated in this study demonstrated moderate to high performance, with the logistic regression model emerging as the best, achieving an accuracy of 81% and an AUC of 0.83.

In general, the absence of pathological EEG alterations may serve as a surrogate marker of tissue reperfusion and favorable clinical outcomes. Patients with EEG abnormalities exhibit a hypermetabolic neural pattern resembling that observed during seizures in epileptic disorders [250]. These phenomena, blood flow dysregulation and associated metabolic alterations, may plausibly contribute to reduced functional status, even in the absence of overt seizures.

Several additional clinical parameters were significantly associated with 3-month outcomes. Specifically, lower NIHSS scores at admission and lower anamnestic mRS values were strongly associated with favorable outcomes, in line with findings from previous studies [19,251]. Conversely, chronic heart failure and atrial fibrillation were linked to worse outcomes, while a greater number of affected lobes increased the likelihood of an mRS > 2. These findings reinforce the prognostic importance of clinical and radiological features and underscore the added predictive value of interictal EEG epileptiform patterns in stroke outcome assessment.

This study's single-center nature and moderate sample size represent important limitations that may affect the generalizability of the findings. These constraints underscore the need for further validation through larger, multi-center investigations that can provide more robust and widely applicable results.

In conclusion, our study demonstrates that EEG derived biomarkers, particularly IEDs, can significantly contribute to predicting 3-month outcomes in patients with ischemic stroke. Given their predictive value, identifying individuals most likely to exhibit these patterns is crucial to improving patient assessment and guiding clinical decision-making.

4.2 Optimizing machine learning models for classification of stroke patients with epileptiform EEG pattern: the impact of dataset balancing techniques

As demonstrated by the previous study in this thesis, biomarkers obtained from EEG recordings, particularly IEDs, are valuable in predicting three-month functional outcomes following ischemic stroke. Moreover, accurate detection and classification of EEG patterns are crucial for timely intervention and treatment planning [11,252]. Therefore, classifying stroke patients to identify those with a high probability of epileptiform EEG patterns may improve stroke management. However, there is a problem: as often happens in medical datasets, patients with epileptiform patterns are outnumbered by stroke patients without these patterns.

The quality and balance of the dataset used to train classifiers often determine their effectiveness. The balance of a dataset refers to the distribution of samples across different classes or categories. Imbalance of the data-set is a primary factor contributing to decreased generalization in machine learning algorithms [253] and presents challenges in developing effective classifiers [254]. Indeed, the classifiers built on the basis of an unbalanced dataset tend to bias their predictions towards the majority classes, often ignoring the minority ones.

As a result, the performance of classifiers can be severely impacted, leading to suboptimal results, particularly for the minority classes.

Therefore, the aim of the study [244] is to investigate the impact of dataset balancing strategies on the classification performance of machine learning models for identifying stroke patients with epileptiform EEG patterns. We compare the performance of models trained on imbalanced datasets against those trained on balanced datasets using various balancing techniques.

4.2.1 Methods

The study encompassed 455 consecutive stroke patients including both ischemic and hemorrhagic stroke admitted at stroke unit of neurological clinic of Trieste University Hospital, 349 (149F/200M, aged: 75 ± 14) without epileptiform EEG patterns observed and 106 (66F/40M, aged: 76 ± 12) with epileptiform EEG patterns detected. All included patients underwent common neurologic stroke workup, stroke risk factors assessment, neurological examination at admission including NIHSS, as well as neuroimaging assessment at admission and 24h follow-up. All patients underwent EEG at least two recordings during the first week from admission and the epileptiform EEG patterns were assessed by three experienced neurologists, in order to define the two classification groups. The following set of features to be considered for the development of classification models were extracted: sex, age, NIHSS at admission, hypercholesterolemia, atrial fibrillation, diabetes, heart failure, smoke, renal failure, hypertension, coronary disease, previous cognitive impairment, acute infectious state, previous ischemic or hemorrhagic stroke, type of stroke (ischemic or hemorrhagic), cortex lesion, supratentorial stroke, number of interested lobes, reperfusion treatment.

Before applying the sampling techniques, a test set corresponding to 10% of the original dataset was randomly extracted. Four different sampling techniques were then employed on the training set, composed by the 90% of the original dataset: an oversampling technique, SMOTENC; an undersampling technique, NearMiss; and two techniques that combine over- and undersampling methods, SMOTEToken and SMOTEENN.

SMOTENC - Synthetic Minority Over-sampling Technique for Nominal and Continuous [255]. SMOTENC is a version of the SMOTE algorithm that considers datasets containing both numeric and categorical characteristics. This oversampling approach, just like SMOTE, increases the representation of the minority class by generating "synthetic" instances in a way that is less tailored to specific applications, working within "feature space" rather than "data space". The minority class is upsampled by incorporating synthetic instances along the line segments connecting the nearest neighbors of the minority class. Synthetic samples are produced by calculating the difference between the feature vector (sample) and its nearest neighbor, then multiplying this difference by a random number ranging from 0 to 1, and finally adding the resulting value to the feature vector. This process selects a random point along the line segment between two specific elements. Consequently, this method broadens the decision region of the minority class, enhancing its overall generality. Thus, synthetic examples encourage the classifier to create larger and less specific decision regions.

NearMiss [256]. NearMiss is a subsampling technique. Specifically, it encompasses three distinct NearMiss algorithms, each relying on some heuristic rules for subsampling. NearMiss-1 identifies samples from the majority class where the average distance to the k' nearest samples of the minority class is minimized. In contrast, NearMiss-2 identifies samples of the majority class where the average distance to the farthest samples of the minority class is minimized. The third method, NearMiss-3, operates in two stages: initially, it retains the m nearest neighbors for each minority sample; subsequently, it selects majority samples based on their maximum average distance to the k nearest neighbors. When conducting under-sampling on a particular class, the NearMiss-1 method may be influenced by noise. NearMiss-2, on the other hand, remains impervious to noise as it prioritizes the farthest samples over the nearest ones, although the presence of noise could potentially influence the sampling process, particularly in the context of marginal outliers. NearMiss-3 is likely to be the least impacted by noise, primarily because of its initial step in sample selection. Also, for this reason, the third algorithm, NearMiss-3, was used in the study.

SMOTETomek [257]. Applying only over- or undersampling sometimes does not lead to an optimal result. Frequently, class boundaries are ambiguous, with instances of predominant classes encroaching upon minority class territories, while minority class interpolations might extend the boundaries of the minority group, inadvertently inserting artificial instances into the majority class domain. Training a classifier under such circumstances can result in overfitting. Improving the definition of class clusters can be achieved by employing Tomek links as a data cleaning technique on the oversampled training set using SMOTE. Tomek links [258] can be defined as follows: considering E_i and E_j two examples from distinct classes, and $d(E_i,E_j)$ like the distance between them, a pair (E_i,E_j) constitutes a Tomek link if there no exists another example, E_l, such that the distance between E_i and E_l is less than $d(E_i,E_j)$, or the distance between E_j and E_l is less than $d(E_i,E_j)$. In the case of SMOTEToken, rather of only removing instances from the majority classes forming Tomek links, istances from both classes are removed. In particular, the initial dataset is upsampled through SMOTE, followed by the identification and removal of Tomek links, resulting in a balanced dataset characterized by distinct class clusters.

SMOTEENN [257]. This method, similar to SMOTEToken, combines over- and under-sampling using SMOTE and another undersampling technique, Edited Nearest Neighbours (ENN) [259]. The ENN algorithm cleans the dataset by removing examples situated near the decision boundary, discarding any example whose class label differs from the class of at least two of its three nearest neighbors. This method involves training a K-Nearest Neighbors model on the entire dataset to identify each observation's K closest neighbors, particularly focusing on the targeted classes. It then proceeds to remove observations if the majority of their neighbors belong to a different class, thus purifying the dataset by eliminating instances near the decision boundary. Therefore, the ENN method retains instances from the majority class when the majority, or all, of their neighbors share the same class. ENN typically removes a greater number of instances compared to Tomek links, offering a more comprehensive data cleaning approach. Similar to what was done with SMOTEToken, the initial dataset is upsampled with SMOTE and then cleaned with the ENN algorithm, ultimately providing a dataset with two well-balanced classes.

By applying these techniques, four new datasets were created. In particular, with the SMOTENC oversampling technique, 219 subjects with epileptic patterns in the EEG were

added. Through the NearMiss subsampling technique, 219 patients without epileptic patterns in the EEG were excluded from the analysis. The SMOTETomek technique added 167 subjects with epileptic patterns and eliminated 52 subjects without epileptic patterns. Finally, with SMOTEEEN, 121 patients with epileptic patterns in the EEG were created and 98 patients without these patterns were excluded. These datasets were used to build the models based on the machine learning techniques described in the following section.

The features selection was made using the ReliefF scoring method [202] and only features that presented a contribution value greater than 0.01 were utilized for model construction. Five different machine learning models were considered in the study: classification tree, logistic regression, naïve Bayes, artificial neural network and support vector machine. The produced models were trained on the resampled training sets as well as on the original training set. Subsequently, the classification performance of the produced models was evaluated by the following metrics on previously unseen data (test set): the CA, the AUC, F1 measure, precision, recall, and specificity. Moreover, the confusion matrix and ROC analysis were executed for each model.

4.2.2 Results

In Table 4.3 the performances of the produced models considering the original training set, without application of any of balancing methods are reported.

Table 4.3. Performance measures of the models produced considering original training set and evaluated by the test set.

Models	CA	AUC	F1	Prec.	Recall	Spec.
Tree	0.69	0.54	0.69	0.68	0.69	0.40
LogReg	0.77	0.67	0.71	0.72	0.77	0.30
Naïve Bayes	0.74	0.67	0.72	0.72	0.74	0.43
NN	0.75	0.62	0.72	0.71	0.75	0.39
SVM	0.76	0.60	0.71	0.70	0.76	0.31

Although the overall accuracy values were moderately high for the specific clinical research question, the AUC and the specificity were very low. The underperformance observed for the AUC and specificity indicates that the models were affected by the fact that the two classes are not balanced; in fact, subjects with epileptiform graphs are much fewer than those without.

Table 4.4 presents the performance of the produced models considering the different under- and oversampling balancing techniques (SMOTENC, NearMiss, SMOTETomek, SMOTEENN).

Table 4.4. Performance measures of the models produced considering under- and oversampling balancing techniques SMOTENC, NearMiss, SMOTETomek, SMOTEENN and evaluated by the test set.

Models	CA	AUC	F1	Prec	Rec	Spec.
SMOTENC						
Tree	0.60	0.46	0.62	0.63	0.60	0.37
LogReg	0.72	0.75	0.73	0.74	0.72	0.54
NaïveBayes	0.72	0.76	0.74	0.79	0.72	0.73
NN	0.74	0.77	0.75	0.79	0.74	0.69
SVM	0.65	0.53	0.67	0.70	0.65	0.52
NearMiss						
Tree	0.49	0.53	0.53	0.65	0.49	0.52
LogReg	0.60	0.64	0.63	0.71	0.60	0.60
NaïveBayes	0.49	0.48	0.53	0.63	0.49	0.47
NN	0.57	0.63	0.60	0.72	0.57	0.64
SVM	0.62	0.68	0.65	0.76	0.62	0.70
SMOTETomek						
Tree	0.62	0.44	0.61	0.61	0.62	0.23
LogReg	0.65	0.56	0.67	0.70	0.65	0.52
NaïveBayes	0.63	0.60	0.65	0.68	0.63	0.47
NN	0.63	0.63	0.65	0.69	0.63	0.52
SVM	0.66	0.52	0.65	0.65	0.66	0.34
SMOTEENN						
Tree	0.43	0.46	0.47	0.64	0.43	0.55
LogReg	0.48	0.59	0.51	0.66	0.48	0.56
NaïveBayes	0.55	0.66	0.58	0.76	0.55	0.73
NN	0.57	0.66	0.60	0.74	0.57	0.68
SVM	0.63	0.69	0.66	0.76	0.63	0.70

Among the considered dataset balanced techniques, SMOTENC showed better results compared to other techniques and original dataset. In particular, the models utilizing the SMOTEC balancing technique demonstrated superior performance compared to those employing other balancing methods. While the accuracy values remained comparable to models trained on the original dataset, notable improvements were observed in terms of AUC and specificity values. Figure 4.2 represents the ROC curves of all the models built using the training set resampled with SMOTENC technique.

By observing the ROC curves and classification performance reported in Table 4.4, the naive Bayes presented the best performance when considering both overall accuracy which was comparable to neural network and logistic regression, while showing the notably better performance in terms of specificity compared to logistic regression and slightly better specificity then neural network. In Figure 4.3 the comparison between ROC curves for the two best models (naïve Bayes and neural network) against the results obtained from models produced the same classification techniques on the original training set was reported.

From the Figure 4.3 it can be observed that the models constructed from the resampled training set using the oversampling technique outperform those obtained from the unbalanced training set. Furthermore, when exclusively considering the models trained on the original dataset, we observe that, once again, the Naive Bayes model demonstrates slight classification superiority. To support the previous findings, in Table 4.5 we report also a

comparative analysis of the confusion matrices for Naive Bayes models constructed using the original dataset and another employing SMOTENC resampled data.

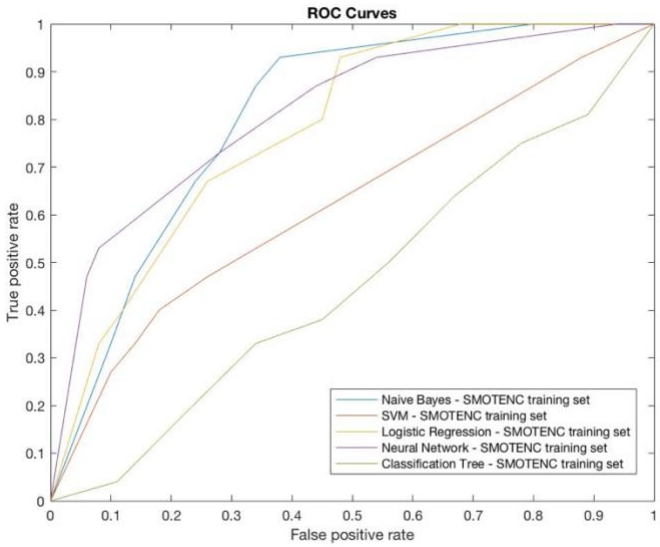

Figure 4.2. *ROC curves of all models built using the training set resampled with SMOTENC technique.*

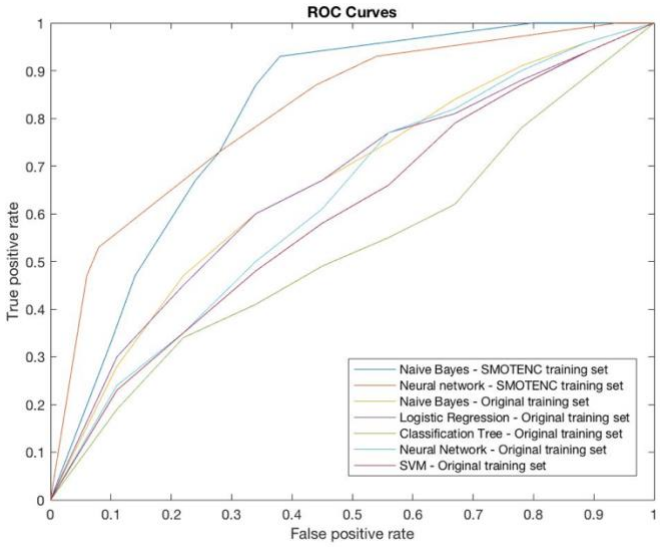

Figure 4.3. *ROC curves for the two best models (naïve Bayes and neural network) against the results obtained from models produced the same classification techniques on the original training set.*

Table 4.5. *Confusion matrices obtained by (a) Naïve Bayes model constructed with training set resampled with SMOTENC technique; (b) Naïve Bayes model constructed with original training set.*

a)	**noEPI**	**EPI**	**Σ**	b)	**noEPI**	**EPI**	**Σ**
noEPI	72%	28%	35	**noEPI**	87%	13%	35
EPI	27%	73%	11	**EPI**	70%	30%	11
Σ	28	18	46	**Σ**	38	8	46

Table 4.6 shows the selected features, in order of their importance, utilizing the ReliefF method as the metric for each training sets derived from different sampling techniques. The data reported in the table shows how various sampling techniques implicate different set of most significant features.

Table 4.6. The set of selected features for each sampling technique.

Training dataset	Features
Original	Reperfusion treatment, Hypercholesterolemia, Cortex lesion, Sex, Supratentorial stroke, NIHSS at admission, Diabetes, Smoke, Acute infectious state, Number of interested lobes, Type of stroke (ischemic or hemorrhagic), Renal failure, Age, Previous ischemic or hemorrhagic stroke, Coronary disease
SMOTENC	Sex, Type of stroke (ischemic or hemorrhagic), Age, NIHSS at admission, Atrial fibrillation, Diabetes, Supratentorial stroke, Hypercholesterolemia, Previous cognitive impairment, Heart failure, Cortex lesion, Hypertension, Number of interested lobes
NearMiss	Sex, Hypertension, NIHSS at admission, Acute infectious state, Supratentorial stroke, Age, Previous cognitive impairment, Reperfusion treatment
SMOTETomek	NIHSS at admission, Age, Hypercholesterolemia, Reperfusion treatment, Type of stroke (ischemic or hemorrhagic), Number of interested lobes, Supratentorial stroke, Diabetes, Hypertension, Cortex lesion, Heart failure, Coronary disease
SMOTEENN	NIHSS at admission, Hypercholesterolemia, Reperfusion treatment, Cortex lesion, Sex, Age, Number of interested lobes, Diabetes, Type of stroke (ischemic or hemorrhagic), Acute infectious state, Smoke, Previous ischemic or hemorrhagic stroke, Renal failure, Coronary disease

4.2.3 Discussion

The study results indicate that the SMOTENC oversampling technique improved the classification performance also for the minority classes such as stroke patients with epileptiform EEG patterns. In particular, we observed the improvement of the AUC and specificity while maintaining the overall classification accuracy compared to the original dataset. In addition, the model produced with naive Bayes approach showed the best classification performance among others on SMOTENC oversampling dataset.

Models trained on the SMOTENC balanced training set outperformed those trained on the original, imbalanced set. While accuracy values were higher then 70%, specificity and AUC values did not exhibit the same level of performance. This discrepancy is further highlighted by the ROC curves, which notably lag behind those generated by the Naive

Bayes and Neural Network models trained with the SMOTENC-enhanced dataset. The obtained confusion matrices also indicate that the Naive Bayes model trained with the SMOTENC training set outperforms those trained with the original training set, particularly in classifying the minority group, namely stroke subjects with epileptiform EEG patterns. The underlying cause is undoubtedly the class imbalance inherent in the original dataset. Studies have consistently shown that machine learning classifiers trained on imbalanced datasets tend to exhibit bias towards the majority classes while neglecting the minority ones [260,261]. This imbalance can significantly impair classifier performance, leading to suboptimal results, particularly for the underrepresented classes. Consequently, it is imperative to address this issue by adopting techniques such as under- or oversampling. These methods aim to balance the class distribution within the dataset, thus mitigating the bias towards the majority classes and improving the classifier's ability to accurately predict outcomes across all classes.

Finally, the study results reveal that different balancing techniques yield distinct selections of features for model construction. Specifically, employing the SMOTENC oversampling technique prioritizes features in the following order of importance: sex, type of stroke (ischemic or hemorrhagic), age, NIHSS at admission, atrial fibrillation, diabetes, supratentorial stroke, hypercholesterolemia, previous cognitive impairment, heart failure, cortex lesion, hypertension, number of interested lobes. Notably, these selected features hold clinical significance, as they can effectively gauge the severity of stroke, often associated with complications such as epileptic EEG patterns.

In conclusion, our study underscores the importance of employing dataset balancing techniques, particularly SMOTENC oversampling, to enhance machine learning models performance in classifying minority groups such as stroke patients with epileptiform EEG patterns. The superior performance of models trained on balanced datasets, highlighted by the Naive Bayes model constructed using SMOTENC oversampling, not only emphasizes the efficacy of these techniques but also underscores their potential to improve clinical decision-making by accurately identifying crucial features associated with stroke severity and complications, such as epileptic EEG patterns.

It is therefore evident that epileptiform EEG patterns may hold significant value for patient prognosis and management. More generally, EEG is emerging as a promising tool for both diagnostic assessment and outcome prediction in this population. Within this context, patients undergoing mechanical thrombectomy remain a particularly underexplored subgroup. In cases of successful reperfusion, this procedure leads to the rapid reopening of LVO, which may facilitate the restoration of normal neuronal function through neurovascular coupling. Accordingly, early normalization of EEG activity following thrombectomy may serve as a valuable biomarker for favorable prognosis.

4.3 Prognostic Value of Quantitative EEG for Three-Month Functional Outcome Following Endovascular Thrombectomy

Among available interventions, endovascular thrombectomy (EVT) has demonstrated strong efficacy in treating LVO, leading to improved functional outcomes and reduced brain injury and disability levels [65]. However, predicting and monitoring responses to EVT remain challenging, and the identification of reliable recovery predictors could enhance personalized care strategies.

Clinical evaluations, such as neurological scales and assessments of daily and cognitive functions, are commonly employed to predict outcomes following recanalization [262]. Advances in imaging, particularly CTP, have enabled more precise visualization of ischemic regions, with certain CTP parameters showing potential as predictors of successful recanalization [263]. Nonetheless, CTP's limitations in continuous monitoring are addressed by EEG, whose high temporal resolution allows real-time assessment of brain function and the detection of neuroelectrical changes following therapeutic interventions [14,16].

Quantitative EEG (qEEG), through power spectrum analysis, provides objective data that support consistent and reliable patient evaluation, reducing subjectivity and aiding clinical decision-making. Notably, qEEG parameters have shown significant correlations with CTP measures of hypoperfused tissue, reinforcing their value as indicators of cerebral function [14]. Recent studies have further highlighted the relevance of EEG-derived parameters in relation to functional outcomes in ischemic stroke [16–18,144].

This study aims to evaluate the predictive value of EEG parameters in forecasting clinical functional outcomes, measured by the mRS at three months, in stroke patients who have undergone treatment.

4.3.1 Methods

This retrospective study included patients with LVO admitted to the Stroke Unit at the University Hospital of Trieste, Italy, between August 2017 and March 2020. Inclusion criteria were patients who underwent EVT, had a CTP study, and received EEG recordings within five days of symptom onset. Patients were excluded if they had a history of cerebral ischemic events, hemorrhagic stroke, TIA, stroke mimics, tandem or bilateral intracranial occlusions, or status epilepticus identified during EEG monitoring.

All patients underwent neurological examination at admission, including the NIHSS, and a multimodal CT imaging protocol comprising NCCT, CTA, and CTP. All patients included in the analysis met the eligibility criteria for EVT in accordance with the European Stroke Organisation (ESO) guidelines [264]. The success of the procedure was assessed using the modified Thrombolysis in Cerebral Infarction (mTICI) score, with successful recanalization defined as mTICI 2b–3, and unsuccessful treatment as mTICI 0–2a [60].

The following variables were collected for each patient: age, sex, vascular risk factors (hypertension, dyslipidemia, atrial fibrillation, diabetes, ischemic cardiomyopathy), site of

vascular occlusion, stroke etiology based on the TOAST classification [66], wake-up stroke status, time from symptom onset to reperfusion, occurrence of clinical seizures, and clinical parameters including NIHSS at admission, anamnestic mRS, and 3-month mRS. A "good outcome" was defined as an mRS ≤2 at three months.

All CT scans were acquired using a 256-slice Philips Brilliance iCT scanner (Philips Healthcare, Best, The Netherlands). CTP acquisition and processing were performed as described in the Methods chapter. To complete the assessment, NCCT was performed post-procedure and at 24 hours following treatment. Symptomatic intracranial hemorrhage (sICH) was reported according to the ECASS II trial criteria [265]. The NCCT evaluation included the ASPECTS and assessment for the hyperdense artery sign [266].

Following treatment, all patients underwent bedside electroencephalographic monitoring. EEG acquisition and signal analysis were performed as detailed in the 2.5 section.

Following statistical analyses were conducted. The Kolmogorov–Smirnov test was used to assess the normality of variable distributions. Continuous variables with normal distribution are presented as means and standard deviations (SD), while those with skewed distributions are reported as medians and interquartile ranges (IQRs), representing the 1st and 3rd quartiles. Categorical variables are presented as counts and percentages. Differences between the two outcome groups (mRS ≤2 vs. mRS >2 at three months) were analyzed using the Student's t-test for normally distributed continuous variables, the Mann–Whitney U test for non-normally distributed variables, and the Chi-square test for categorical data.

Univariate logistic regression analyses were performed on a selected subset of features to identify predictors of poor outcome. Variables with p-values <0.05 in the univariate analysis were considered potential input parameters for the predictive models.

Five different Naive Bayes models were developed, each incorporating a different number of parameters. In one model, all variables found to be significant in the univariate analysis were included, excluding EEG features. In the remaining models, one EEG parameter was added at a time: Alpha, Delta, DAR (Delta/Alpha Ratio), and DTABR (Delta + Theta)/(Alpha + Beta Ratio). Classification performance was assessed using five-fold cross-validation, evaluating metrics including CA, AUC, F1 score, precision, recall, and specificity.

4.3.2 Results

Of the 224 patients consecutively hospitalized in the Stroke Unit of the ASUGI Neurological Clinic from June 2017 to December 2020, 94 met all inclusion criteria and were included in the study.

The median age of the sample was 77 years (IQR 62–83), with 52 female patients (55%) and 86 (91%) experiencing anterior circulation strokes. The median ASPECT score was 9 (IQR 8–10). Post-treatment, 62 patients (66%) achieved successful recanalization, although 5 patients (5%) developed sICH. The median NIHSS at admission was 14.5 (IQR 9–20), with an anamnestic mRS of 0 (IQR 0–0). At three months, the median mRS was 3 (IQR 1–5), with 44 patients (46%) achieving a good outcome. The median time from onset to needle

was 180 minutes (IQR 150–270), and from onset to the first EEG recording was 1.5 days (IQR 1–4).

The results of the comparison of clinical, demographic, CT, and EEG characteristics between patients with good and poor outcomes are presented in Table 4.7.

Table 4.7. Demographics, clinical and neuroimaging characteristics of stroke patients with good and poor clinical outcomes. Statistically significant differences are highlighted in bold.

	3-months mRS≤ 2 n = 44	**3-months mRS>2 n = 50**	**Sig.**
Age (years) [median (range)]	74.5 (57-80.5)	79.5 (73-83)	**0.023**
Females [n (%)]	23 (52)	29 (58)	0.577
Risk factors [n (%)]			
Hypertension	24 (55)	43 (86)	**0.001**
Diabetes mellitus	2 (5)	7 (14)	0.120
Dyslipidaemia	24 (55)	30 (60)	0.594
Ischemic cardiopathy	3 (7)	6 (12)	0.494
Atrial fibrillation	23 (52)	19 (38)	0.165
Clinical features			
NIHSS at baseline [median (range)]	12 (5-17)	17 (11-22)	**0.004**
mRS anamnestic [median (range)]	0 (0-0)	0 (0-0)	0.152
TOAST classification [n (%)]			
Cardioembolic	24 (55)	21 (42)	0.224
Atherothrombotic	7 (16)	13 (26)	0.232
Cryptogenic	8 (18)	14 (28)	0.261
Other cause	5 (11)	2 (4)	0.246
Anterior circulation stroke [n (%)]	42 (96)	44 (88)	0.196
Wake up stroke [n(%)]	12(27)	12 (24)	0.717
Clinical Seizure [n(%)]	1 (2)	6 (12)	0.116
Neuroimaging			
Hyperdense arterial sign [n(%)]	29 (66)	39 (78)	0.191
ASPECTS [median (range)]	9 (8.5-10)	9.5 (8-10)	0.705
Core (mL)	10.9 (2.30-30.90)	11.00 (1.95-28.20)	0.696
Penumbra (mL)	76.70 (41.00-122.70)	72.70 (39.90-112.50)	0.674
Final infarct volume (mL)	7.45 (2.57-15.02)	30.44 (10.31-124.00)	**<0.001**
SICH [n (%)]	0 (0%)	5 (10%)	0.058

Treatment			
Onset-needle (minutes)	173 (138-265)	190 (150-285)	0.437
TICI 2b/3[n (%)]	38 (86)	24 (48)	**<0.001**
EEG parameters [median (range)]			
Timing Stroke-EEG (days)	2 (1-4)	1 (1-3)	0.057
Delta	0.46 (0.36-0.61)	0.62 (0.50-0.71)	**<0.001**
Theta	0.16 (0.12-0.24)	0.19 (0.14-0.24)	0.351
Alpha	0.16 (0.10-0.24)	0.07 (0.05-0.11)	**<0.001**
Beta	0.12 (0.06-0.17)	0.07 (0.04-0.11)	**0.006**
DAR	3.73 (1.69-7.50)	10.16 (5.10-19.07)	**<0.001**
DTABR	3.09 (1.22-5.18)	6.25 (3.94-11.92)	**<0.001**

Patients with poor outcomes were generally older, with a median age of 79.5 years compared to 74.5 years in the good outcome group. Key risk factors, such as hypertension and dyslipidemia, were prevalent in both groups, though slightly higher among patients with poor outcomes. Baseline NIHSS scores, a measure of stroke severity, were significantly higher in the poor outcome group (median 17 vs. 12), suggesting more severe initial presentations among these patients. Neuroimaging data showed that patients with poor outcomes had a larger final infarct volume (median 30.44 mL vs. 7.45 mL) and a higher rate of symptomatic intracranial hemorrhage (10% vs. 0%). EEG parameters, particularly those reflecting brainwave frequency alterations, also revealed significant differences between groups. The DAR and the DTABR were markedly elevated in the poor outcome group, with median DAR values of 10.16 compared to 3.73 in the good outcome group. Similarly, DTABR values were significantly higher (median 6.25 vs. 3.09), highlighting more pronounced slow-wave activity associated with poorer outcomes.

Univariate regression analysis identified age (OR: 1.011, $p = 0.006$), TICI (OR: 0.654, $p < 0.001$), sICH (OR: 1.639, $p = 0.031$), NIHSS at admission (OR: 1.022, $p = 0.003$), hypertension (OR: 1.466, $p = 0.001$), Delta (OR: 2.703, $p < 0.001$), Alpha (OR:0.153, $p < 0.001$), Beta (OR: 0.261, $p = 0.013$), DAR (OR: 1.013, $p = 0.001$), and DTABR (OR: 1.018, $p = 0.002$) as significant parameters associated with patient outcomes.

Table 4.8 reports the performance metrics of five developed Naive Bayes models. As shown in the table, model performance improves when an EEG parameter is included. Specifically, the model without EEG features achieved the lowest classification accuracy, at 73%. Including the Delta or DTABR parameter led to an accuracy of 77%. Similarly, adding the Alpha or DAR parameter increased accuracy by 10% and 11%, respectively. Beyond accuracy, overall model performance improved significantly, underscoring the predictive value of the EEG parameters.

Table 4.8. Performance measures of the five produced models.

Models	CA	AUC	F1	Prec.	Recall	Spec.
$NaïveBayes_{NoEEG}$	0.73	0.85	0.73	0.73	0.73	0.73
$NaïveBayes_{Alpha}$	0.83	0.89	0.83	0.83	0.83	0.82
$NaïveBayes_{Delta}$	0.77	0.87	0.77	0.77	0.77	0.76
$NaïveBayes_{DAR}$	0.84	0.90	0.84	0.84	0.84	0.84
$NaïveBayes_{DTABR}$	0.77	0.87	0.77	0.77	0.77	0.76

The nomogram for the $NaiveBayes_{DAR}$ model, which achieved the highest classification accuracy and overall best performance, is presented in Figure 4.4.

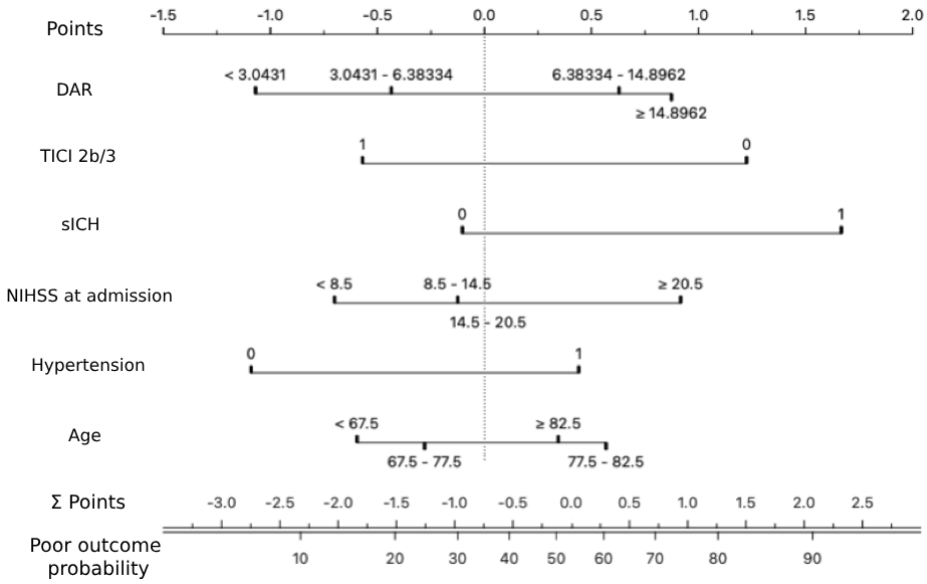

Figure 4.4. The nomogram for the poor outcome of the best model, the $NaiveBayes_{DAR}$ model.

4.3.3 Discussion

In this study, univariate analysis confirmed a significant association between the clinical outcomes of stroke patients treated with thrombectomy and several factors: age, NIHSS score at admission, presence of hypertension, successful recanalization (TICI), occurrence of sICH, and EEG parameters (Delta, Alpha, Beta, DAR, and DTABR).

Our findings demonstrated that electroencephalographic indices possess substantial discriminative power in distinguishing between patients with good and poor functional outcomes. In particular, the DAR, representing the balance between pathological slowing and preserved or recovered activity following reperfusion, and Alpha power, reflecting the

preservation or rapid restoration of normal rhythm after recanalization, emerged as two key quantitative EEG parameters for outcome classification.

The inclusion of EEG parameters in predictive models significantly enhanced their performance. The NaïveBayes$_{DAR}$ model achieved the highest classification accuracy (84%) and the highest AUC (0.90), demonstrating that incorporating DAR notably improves the model's ability to discriminate between good and poor outcomes. Other EEG parameters (Alpha, Delta, DTABR) also contributed to improved model performance compared to the baseline clinical model without EEG features, which achieved an accuracy of only 73%.

The study has some limitations. Once again, is a single-center study with a moderate sample size, though clinically relevant. Moreover, the small sample size did not allow us to test the performance on external test set, however, the 5-fold cross-validation approach we employed provides a robust internal estimate of model's performance. Therefore, the results need to be confirmed in larger, future studies.

In conclusion, these results suggest that the integration of EEG data, particularly indices such as DAR and Alpha, provides valuable additional information for predicting functional outcomes in thrombectomy-treated stroke patients. The strong association between early EEG alterations and poor prognosis highlights the potential role of EEG as an accessible and non-invasive tool for clinical monitoring after reperfusion therapy in acute ischemic stroke with LVO.

4.4 DISTINCT BRAIN PERFUSION PATTERN EVOLUTION ASSESSED BY ASL-MRI IN ACUTE ISOLATED APHASIA: A COMPARISON BETWEEN ISCHEMIC STROKE AND SEIZURE-RELATED STROKE MIMICS

Stroke mimics encompass a heterogeneous group of conditions that clinically resemble acute ischemic stroke but are not caused by cerebrovascular ischemia [267]. It is estimated that between 1% and 41% of patients presenting with stroke-like symptoms at Emergency Department admission are ultimately diagnosed with a stroke mimic [268]. Among the most frequent etiologies are seizures, migraine with aura, and functional disorders such as conversion disorder [269]. Other less common causes include metabolic disturbances, infections, neurodegenerative diseases, peripheral neuropathies, and syncope [269].

One of the most diagnostically challenging presentations is acute isolated aphasia without accompanying focal neurological deficits. This symptom may result from a variety of underlying conditions, including ischemic stroke, epileptic seizures, migraine, or functional disorders. Notably, in the majority of cases, isolated aphasia is attributable either to ischemia or seizure activity [269]. The clinical overlap between these two conditions complicates the acute diagnostic process, especially when time-sensitive decisions regarding reperfusion therapies must be made.

Advanced neuroimaging techniques, particularly CTP, have become critical tools in emergency decision-making. However, the utility of CTP in differentiating stoke mimics from acute ischemic stroke remains under debate [270–273]. A previous study has shown that while many acute ischemic stroke patients exhibit clear hypoperfusion patterns on CTP, patients with seizure-related stroke mimics often display mild hyperperfusion or, less frequently, slight hypoperfusion [23]. Nevertheless, the limitations of CTP, including radiation exposure and limited repeatability, highlight the need for alternative imaging modalities to support early differential diagnosis.

ASL, a non-invasive MRI-based technique that enables quantitative assessment of cerebral perfusion without the use of contrast agents, offers a promising alternative. Its repeatability, rapid acquisition time, and ability to monitor perfusion dynamics make it a valuable tool in the acute setting. Particularly, ASL may help characterize the temporal evolution of perfusion abnormalities, potentially enhancing the accuracy of etiological diagnosis in patients with isolated aphasia.

This preliminary study aimed to evaluate the evolution of brain perfusion alterations using ASL-MRI in patients with acute isolated aphasia, comparing those with ischemic stroke to those with seizure-related stroke mimics. By investigating perfusion patterns over time, we seek to provide further insights into the role of ASL in early differential diagnosis and patient management in emergency neurology.

4.4.1 Methods

We analyzed brain perfusion changes between 48 and 96 hours after symptom onset in 21 patients with acute isolated aphasia, diagnosed with either ischemic stroke (n=14) or seizure-related stroke mimics (n=7), using ASL-MRI. All scans were acquired on an Ingenia 3T MRI scanner (Philips Healthcare, Best, The Netherlands) with a 32-channel head coil. High-resolution anatomical images were obtained using a 3D T1-weighted sequence (TR=8.4 ms, TE=3.9 ms, flip angle=8°, voxel size=1×1×1 mm^3, 180 slices).

Perfusion imaging was performed using pcASL with label duration of 1800 ms and PLD of 2000 ms. 3D GraSE sequences with background suppression were used (TR/TE = 4.1 s/13 ms, FOV = 240×240 mm^2, matrix = 80×75, voxel size = 3×3×5 mm^3, 20 slices, flip angle = 90°), acquiring seven label/control pairs and one M0 calibration image. Subjects were instructed to rest with eyes closed.

ASL data were processed with FSL 6.0.5 (FMRIB, Oxford, UK), using BASIL [188]. Preprocessing included motion correction (MCFLIRT), brain extraction (BET), and spatial smoothing [185]. CBF maps were computed using the general kinetic model [186] and voxel-wise calibration with the M0 image, following the ASL white paper guidelines [187]. Partial volume correction was applied using spatial regularization techniques [188]. CBF maps were normalized to MNI152 standard space (2-mm T1-weighted template).

Baseline perfusion was assessed via CTP at admission using a 256-slice Philips Brilliance iCT scanner (80 kVp, 150–200 mAs). Seventy-five mL of contrast agent was

injected at 4 mL/s, followed by 40 mL of saline. Whole-brain 3D acquisitions were reconstructed in 5-mm slices over a 60-second scan.

CTP data were processed using Extended Brilliance Workstation v4.5 and MATLAB (MathWorks, Natick, MA, USA). Perfusion maps for MTT, CBV, and CBF were generated via Gaussian curve fitting and deconvolution using arterial and venous input functions. CBF was derived from the CBV/MTT ratio. Perfusion findings were compared between ischemic stroke and seizure-related SM groups, integrating both MRI and CTP data.

4.4.2 Results

In patients with ischemic stroke, ASL-MRI performed between 48 and 96 hours after symptom onset revealed focal areas of hyperperfusion corresponding to regions that initially showed significant hypoperfusion on baseline CTP scans (Figure 4.5).

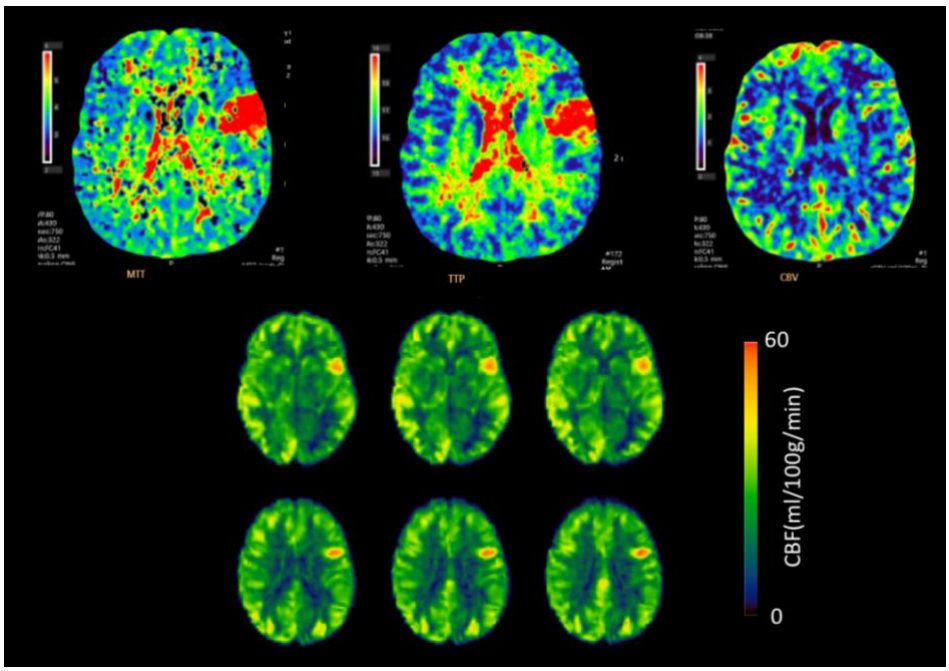

Figure 4.5. *Top: MTT, CBF, and CBV maps from a stroke patient obtained via CT perfusion. Bottom: Selected CBF perfusion slices from the same patient acquired using ASL-MRI.*

For each subject, a coarse ROI mask was created for both the dominant and contralateral hemispheres, enabling intra-subject perfusion comparisons. Mean CBF values within these ROIs are reported in Table 4.9.

Table 4.9. *Mean CBF values in the selected ROIs of the right and left lobes for each stroke patient.*

Subject	Mean CBF right lobe [ml/100g/min]	Mean CBF left lobe [ml/100g/min]
S1	23.50	52.00
S2	25.98	51.59
S3	32.65	54.47

S4	27.82	44.32
S5	24.27	34.26
S6	30.89	54.88
S7	16.30	21.37
S8	11.95	27.56
S9	26.79	67.50
S10	21.01	30.29
S11	24.83	36.60
S12	32.25	50.55
S13	22.68	35.40
S14	34.80	48.70

A statistical comparison of perfusion values between the left and right lobes was conducted using the Wilcoxon signed-rank test for paired data. Median values, interquartile ranges, and associated p-values are presented in Table 4.10. A p-value < 0.05 was considered statistically significant.

Table 4.10. *Median CBF values in the right and left lobes across all stroke patients, with corresponding p-value.*

Median CBF right lobe [ml/100g/min]	Median CBF left lobe [ml/100g/min]	p-value
25.405 (11.95 – 34.80)	46.510 (21.37 – 67.5)	**<0.001**

To further localize perfusion abnormalities, diffusion-weighted imaging (DWI) scans were coregistered to MNI152 standard space. This allowed for accurate identification of ischemic lesions across subjects. The analysis demonstrated that the hyperperfusion detected by ASL was perilesional in nature, spatially surrounding the infarcted core (Figure 4.6).

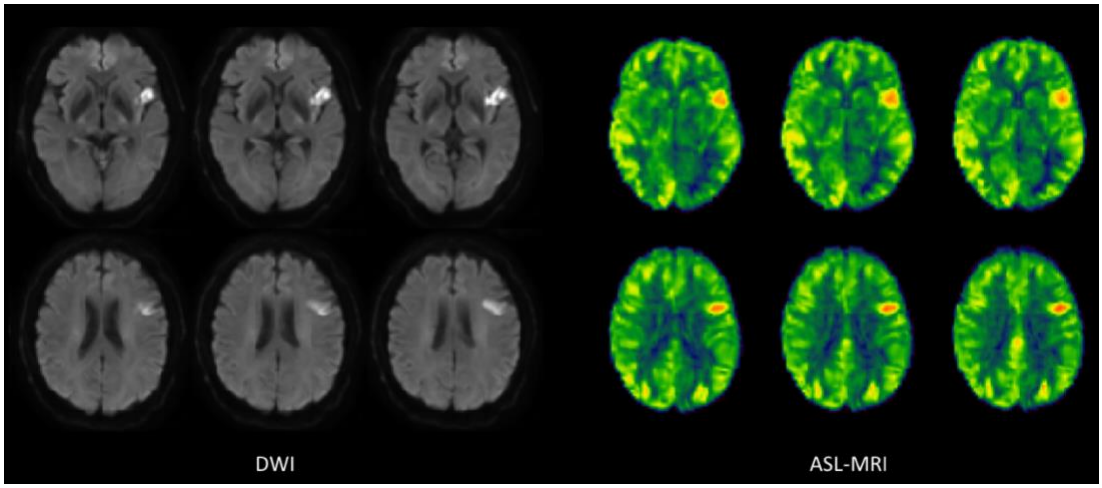

Figure 4.6. *DWI and ASL-MRI images of a stroke patient illustrating perilesional hyperperfusion.*

In contrast, patients with seizure-related stroke mimics exhibited a more diffuse pattern of hyperperfusion on ASL-derived CBF maps, often involving bilateral or unilateral hemispheric regions. An example is depicted in Figure 4.7.

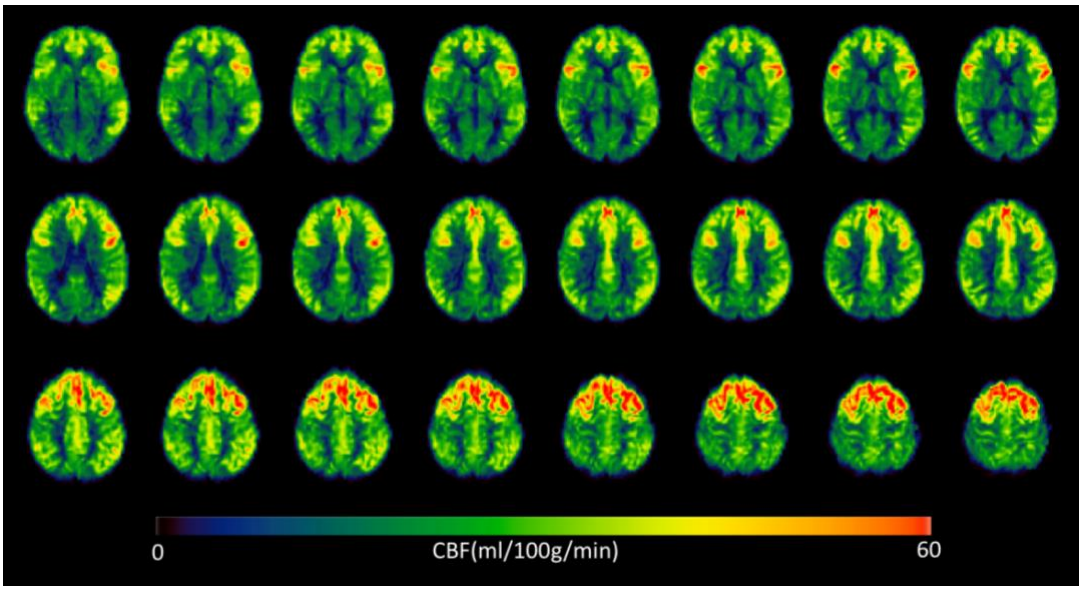

Figure 4.7. *CBF map of a patient with seizure-related stroke mimic.*

These distinct patterns between the two groups were also evident in the averaged CBF images, shown in Figures 4.8 and 4.9.

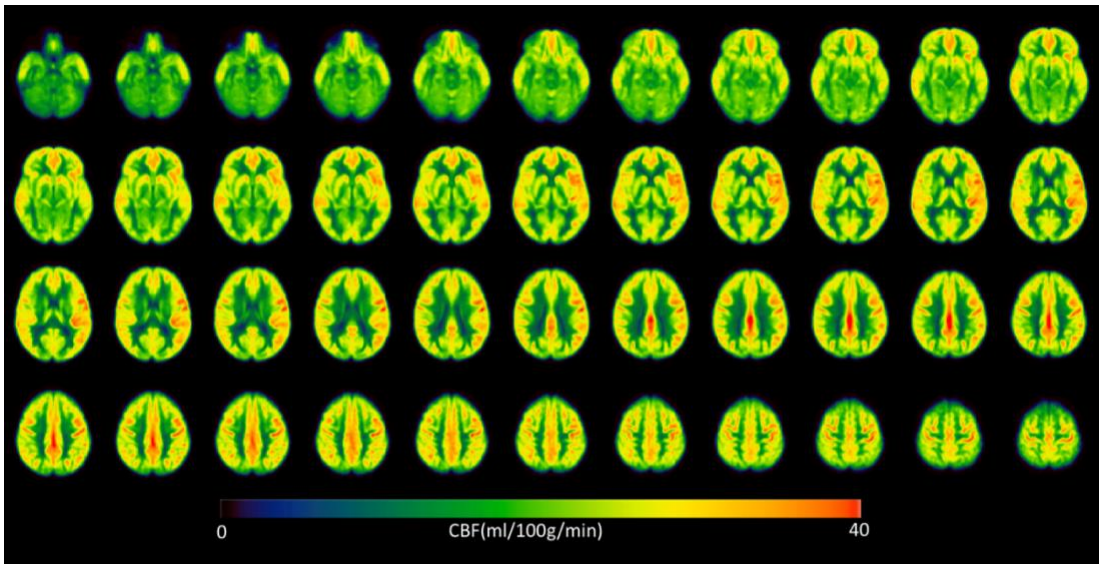

Figure 4.8. *Group-averaged CBF map of stroke patients.*

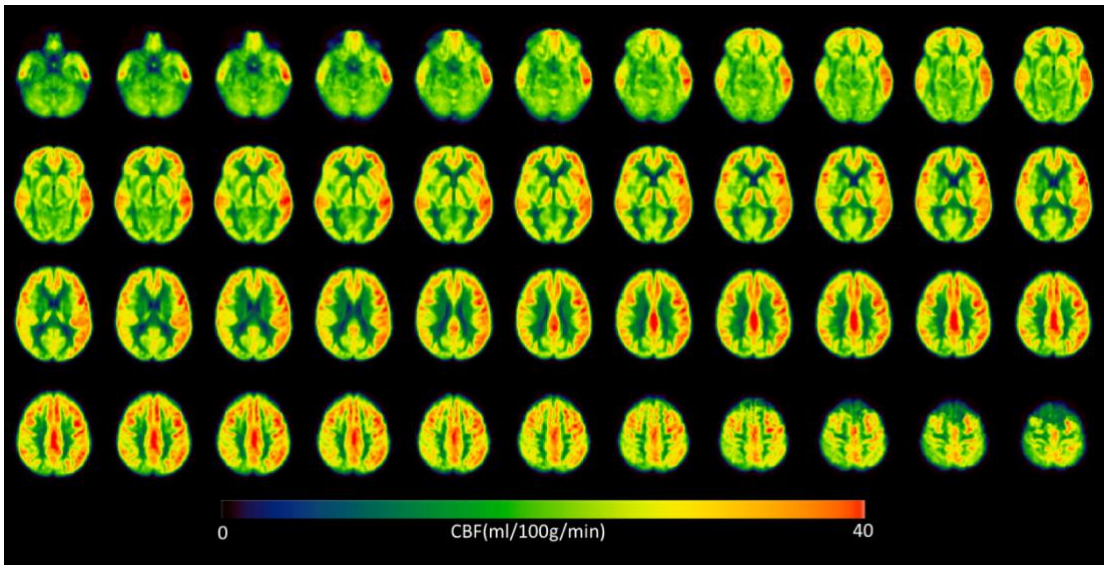

Figure 4.9. *Group-averaged CBF map of patients with seizure-related stroke mimics showing diffuse, non-territorial hyperperfusion.*

These findings did not conform to vascular territories and followed more heterogeneous baseline perfusion profiles, with both hypo- and hyperperfused regions observed without clear localization.

4.4.3 Discussion

This study highlights the utility of ASL-MRI in differentiating perfusion patterns in patients with acute isolated aphasia, revealing distinct temporal perfusion evolutions between ischemic stroke and seizure-related stroke mimics. In patients with confirmed ischemic stroke, ASL-MRI performed between 48 and 96 hours after symptom onset consistently demonstrated focal hyperperfusion in regions previously identified as hypoperfused on baseline CTP imaging. This hyperperfusion was predominantly perilesional, surrounding the infarct core as defined by coregistered DWI, and did not correspond to specific vascular territories.

Quantitative comparisons of CBF between hemispheres, based on ROI analyses, further support the focal nature of post-ischemic hyperperfusion. In particular, the presence of perilesional hyperperfusion in our ischemic stroke cohort suggests a potential reactive or compensatory vascular mechanism in the subacute phase, which may not be captured in earlier imaging windows. This emphasizes the relevance of ASL-MRI as a non-invasive, repeatable modality capable of detecting dynamic perfusion changes that can enhance differential diagnosis, particularly when conventional imaging is inconclusive.

In contrast, patients with seizure-related stroke mimics exhibited a markedly different perfusion profile. ASL-derived CBF maps in these individuals showed more diffuse hyperperfusion patterns, frequently extending across unilateral or bilateral hemispheres and lacking a clear association with ischemic lesions or vascular territories. These diffuse changes likely reflect the metabolic and hemodynamic effects of seizure activity, rather than

true ischemia. Importantly, these findings were apparent both in individual and group averaged CBF maps, further distinguishing seizure mimics from ischemic stroke.

This study presents some limitations. First, the relatively small sample size and the single-center design may limit the generalizability of the findings. Moreover, further analyses, such as a voxelwise comparison of CBF maps between groups, could provide a more detailed understanding of regional perfusion differences and reinforce the current results.

In conclusion, this preliminary study demonstrated that ASL-MRI can detect evolving perfusion patterns in patients with acute isolated aphasia, distinguishing perilesional hyperperfusion in ischemic stroke from diffuse, non-territorial hyperperfusion in seizure-related stroke mimics. These findings suggest that ASL-MRI may support the differential diagnosis between ischemic stroke and stroke mimics, serving as a valuable tool for detecting perfusion alterations underlying these two neurological conditions. This approach may be particularly useful when initial anatomical and functional imaging fails to provide a clear clinical picture.

4.5 DISCUSSION AND CONCLUSIONS

This thesis underscores the critical need for improved prognostic tools in acute ischemic stroke care, particularly through the integration of neurophysiological and neuroimaging biomarkers. Specifically, the studies presented in this thesis contribute to this evolving field by demonstrating the potential of EEG features, especially epileptiform patterns such as IEDs and quantitative parameters derived from spectral analysis, to predict three-month functional outcomes. Moreover, by addressing practical limitations related to the practicability of continuous EEG monitoring, this research identifies clinical predictors to stratify patients most likely to benefit from EEG-based assessments. Finally, a novel imaging approach, ASL-MRI, was investigated to assess its capability to differentiate ischemic strokes from stroke mimics in challenging clinical scenarios, thereby expanding the repertoire of non-invasive, clinically applicable biomarkers.

First and foremost, the results highlight that the presence of IEDs, when considered as an EEG biomarker, serves as a strong predictor of poor outcomes. When combined with other clinical and neuroimaging features, such as NIHSS score at admission, pre-stroke mRS, chronic heart failure, acute infections, number of affected lobes, and atrial fibrillation, identified through feature selection, IEDs significantly contribute to predicting functional outcome. Prior work has shown that patients with IEDs may exhibit localized hypermetabolism, similar to seizure activity, which reflects disrupted neurovascular coupling and metabolic stress, even in the absence of clinical seizures [246], and this may contribute to worse functional recovery.

Several prior studies have explored the use of machine learning for predicting functional outcomes in stroke patients [274–276]. One such study focusing on younger patients found that initial mRS score, living alone, and high NIHSS score at discharge were independent predictors of poor three-month outcomes, achieving promising AUC values [274]. However, only 9% of the study population experienced poor outcomes, which led to a low positive

predictive value and poor F1 scores due to class imbalance. Indeed, one of our studies emphasized that in such cases, dataset-balancing techniques should be employed [244]. Another study, conducted on a cohort of 293 stroke patients who underwent mechanical thrombectomy, developed four different machine learning models and achieved an AUC of 0.84. The key features contributing to the models included age, baseline NIHSS, occlusion side, degree of brain atrophy, early ischemic core volume, and collateral circulation deficit as seen on CTA [276]. Similarly, a logistic regression-based model used to predict three-month outcomes in 256 stroke patients achieved medium-to-high AUC values ranging from 0.79 to 0.88 [275]. Our findings confirm the importance of the aforementioned clinical and radiological features while also highlighting the predictive value of interictal EEG epileptiform patterns for stroke outcome prediction.

These initial results suggest that classifying stroke patients based on their likelihood of exhibiting epileptiform EEG patterns could enhance patient management. However, a significant challenge arises: as is typical in medical datasets, patients with epileptiform EEG patterns represent a minority compared to those without. For this reason, it was investigated the impact of dataset balancing techniques on the performance of machine learning classifiers in identifying stroke patients with epileptiform EEG patterns.

The results showed that the SMOTENC method improved model performance for the minority class without compromising overall accuracy. Specifically, we observed improvements in AUC and specificity compared to models trained on the original, imbalanced dataset.

It is well established that machine learning models trained on imbalanced datasets tend to be biased towards the majority class, thereby neglecting the minority class [260,261]. This imbalance can significantly degrade the model's ability to generalize and produce accurate predictions for underrepresented subgroups. Addressing this issue through appropriate sampling techniques, whether oversampling or undersampling, is therefore essential. These methods aim to rebalance class distributions, improve model fairness, and enhance the model's capacity to detect and predict rare but clinically significant outcomes.

Numerous studies have demonstrated the benefits of oversampling techniques [277–279]. For instance, Alahmari investigated the impact of class imbalance using a real-world dataset focused on autism spectrum disorder screening [277]. His findings illustrated that oversampling techniques, particularly when applied during pre-processing, improved specificity, sensitivity, and precision. Using Random Forest and Naïve Bayes classifiers, the study showed that resampling via random oversampling and SMOTE mitigated class imbalance bias and improved performance across multiple metrics. Similarly, Mohamed et al. demonstrated that oversampling techniques outperform undersampling across various classifiers, consistently yielding superior results across evaluation metrics [278]. In another comprehensive study, Khushi et al. evaluated 23 class balancing techniques in the context of lung cancer prediction [279]. This study encompassed ten undersampling methods, seven oversampling methods, and several hybrid systems. Oversampling techniques, particularly random oversampling combined with Random Forest models, emerged as the most effective, achieving the highest AUC values. In contrast, models employing the NearMiss subsampling method exhibited the poorest performance, an observation consistent with our own findings.

This thesis underscores the necessity of not only applying such balancing techniques but also understanding their impact on classification performance. The improved results obtained using balanced datasets highlight the potential of these approaches to enhance clinical decision-making, especially in identifying critical features linked to stroke severity and complications, such as epileptiform EEG activity.

The results obtained in this thesis have underscored the high prognostic value of quantitative EEG (qEEG). In particular, the use of qEEG as a prognostic tool in acute ischemic stroke has gained increasing attention due to its non-invasive nature, bedside applicability, and the objective insights it provides into cortical function. Among the various qEEG indices, the Delta/Alpha Ratio (DAR) has consistently demonstrated strong prognostic utility across multiple studies, including the work presented in this thesis.

The findings of this study demonstrated that electroencephalographic indices possess substantial discriminative power in distinguishing patients with good versus poor clinical outcomes at 3 months. Specifically, the DAR, which reflects the ratio between pathological slowing and preserved or recovered activity post-reperfusion, and alpha power, indicative of the preservation or rapid restoration of normal rhythmic activity following recanalization, emerged as two pivotal quantitative EEG markers for classifying patient outcomes.

Crucially, the inclusion of EEG features, particularly DAR, in predictive models significantly enhanced classification performance. The addition of other EEG-derived metrics, including alpha power, delta power, and DTABR, also contributed to improved model performance. These findings confirm the additive prognostic value of qEEG parameters when combined with traditional clinical and imaging variables.

Moreover, these results are consistent with previous studies. Ajčević et al. found that relative delta power and alpha power, DAR, and DTABR, recorded using wireless EEG in the hyperacute pre-thrombolysis phase, strongly correlated with both short-term and long-term clinical outcomes (NIHSS and mRS), as well as with final infarct volume, suggesting that qEEG can detect early cortical dysfunction even before reperfusion therapy is initiated [16]. Similarly, Dickey et al. highlighted the prognostic relevance of interhemispheric DAR differences in patients undergoing mechanical thrombectomy, demonstrating that these qEEG metrics were independent predictors of outcome even after controlling for infarct volume [18]. In contrast, the global DAR did not correlate significantly with any of the clinical outcomes considered when evaluated as continuous variables [18]. Zhang et al. also confirmed the superiority of qEEG indices over CT perfusion parameters in predicting 3-month outcomes, with delta power identified as the most predictive features [144].

Taken together, these growing evidences underscores that qEEG parameters, in particular DAR, are not only robust indicators of current cerebral dysfunction but also reliable predictors of long-term functional recovery. Its clinical value lies in its simplicity, reproducibility, and strong physiological rationale, reflecting cortical slowing secondary to ischemia. Moreover, qEEG metrics such as DAR and alpha power can be readily acquired using portable or bedside EEG systems, making them highly suitable for clinical monitoring following reperfusion therapy in acute ischemic stroke patients with LVO.

This thesis demonstrates also that ASL-MRI can effectively capture the evolution of cerebral perfusion patterns in patients with acute isolated aphasia, offering critical insights

into the differential diagnosis between ischemic stroke and seizure-related stroke mimics. In our cohort, patients with ischemic stroke exhibited a statistically significant perilesional hyperperfusion between 48 and 96 hours after symptom onset, in contrast to the diffuse, non-territorial hyperperfusion observed in patients with seizure-related aphasia. Notably, previous ASL studies in aphasic stroke patients have reported decreased perilesional perfusion, particularly within 6 mm of the lesion in frontal, temporal, and parietal regions [280–282]. However, perilesional hyperperfusion has been documented in other neurological conditions, such as post-surgical epilepsy and brain tumors. For example, Galazzo et al. [283] identified perilesional hyperperfusion in drug-resistant epilepsy patients using both ASL and electrical source imaging, underscoring the value of ROI-based analyses for detecting inter-hemispheric asymmetries. Similarly, Sunwoo et al. [284] and Weber et al. [285] reported significant peritumoral hyperperfusion in glioblastoma, which proved useful for differentiating it from brain metastases.

These comparisons underscore the potential pathophysiological relevance of perilesional hyperperfusion in ischemic stroke and affirm the utility of ASL-MRI in capturing such perfusion dynamics. Crucially, our findings support the notion that ASL-MRI may aid early differentiation between ischemic and epileptic etiologies in cases of isolated aphasia—particularly when traditional neuroimaging (e.g., CTP) yields inconclusive results or is limited by factors such as radiation exposure and poor repeatability. As prior studies have shown, patients with seizure-related stroke mimics often present with mild hyperperfusion or no clear perfusion deficit on CTP [23]. In this context, ASL-MRI not only provides a non-invasive, contrast-free alternative but also enables dynamic assessment of perfusion over time.

This thesis demonstrates that both EEG and ASL-MRI can enhance the diagnosis and prognosis of ischemic stroke patients. In particular, both qualitative and quantitative EEG significantly improve the predictive accuracy of stroke outcome models. Quantitative EEG offers an objective, neurophysiological complement to clinical and neuroimaging assessments. As a real-time, bedside tool, EEG supports early risk stratification, informs treatment decisions, and guides patient counseling. Moreover, this thesis highlights the importance of early identification of perfusion patterns using ASL-MRI as diagnostic red flags for differentiating ischemic stroke from stroke mimics in patients with isolated aphasia. Timely recognition of the underlying etiology is critical to ensure appropriate therapeutic decisions, especially when overt neurological deficits are absent. In conclusion, incorporating EEG and ASL-MRI into standard diagnostic workflows may represent an important step toward more personalized and precise stroke care.

Chapter 5. CONCLUSIONS

Cardiovascular and neurovascular diseases continue to represent a major global health burden due to their high prevalence, mortality, and long-term disability. In this context, the present PhD thesis contributes to the identification of novel non-invasive biomarkers derived from image and signal processing, as well as to the development of interpretable predictive models based on these biomarkers to support differential diagnosis and patient management in cardiovascular and neurovascular diseases.

The findings demonstrate that the integration of HRV features with myocardial deformation measures, particularly GLS, significantly improves the differential diagnosis between DCM and IHD, even in patients with comparable ejection fraction values. GLS emerged as a highly sensitive indicator of myocardial dysfunction, supporting its broader implementation in routine echocardiographic assessments. Similarly, both linear and nonlinear analyses of HRV signals proved to be valuable in distinguishing among healthy subjects, DCM patients, and those with IHD. The parameters extracted from the HRV signal were particularly effective in distinguishing DCM and IHD patients with mildly reduced LVEF, highlighting the importance of these features when differential diagnosis becomes even more challenging. The developed interpretable machine learning models further enhanced diagnostic accuracy by capturing complex interactions between demographic, physiological, and clinical variables, such as age, sex, HRV characteristics, and myocardial strain, offering valuable support for clinical decision-making.

In the neurovascular domain, the introduction of non-invasive EEG and ASL-MRI derived features can improve both diagnosis and outcome prediction in patients with ischemic stroke. Quantitative EEG, in particular, provided objective, neurophysiological insights that complemented traditional clinical and imaging assessments, enabling real-time, bedside risk stratification and guiding treatment decisions. ASL-MRI proved especially valuable in detecting perfusion patterns indicative of stroke or stroke mimics in cases of isolated aphasia, where overt neurological signs may be absent and timely etiological clarification is critical.

Despite these promising results, some limitations must be acknowledged. All studies were conducted in a single center with a moderate sample size, though clinically relevant. Therefore, future multicenter studies with larger cohorts are needed to confirm and expand upon these findings.

In conclusion, the quantitative analysis of physiological signals such as HRV and EEG, obtained through non-invasive and widely available tools but often underused in clinical practice, combined with advanced imaging techniques and interpretable machine learning models, has shown strong potential to improve the diagnosis, characterization, and prognosis of cardiovascular and neurovascular diseases. This integrated approach may represent a significant step toward more precise, personalized, and effective patient care.

REFERENCES

[1]E. Olvera Lopez, B.D. Ballard, A. Jan, Cardiovascular Disease, in: StatPearls, StatPearls Publishing, Treasure Island (FL), 2022. http://www.ncbi.nlm.nih.gov/books/NBK535419/ (accessed April 1, 2022).

[2]GBD 2019 Stroke Collaborators, Global, regional, and national burden of stroke and its risk factors, 1990-2019: a systematic analysis for the Global Burden of Disease Study 2019, Lancet Neurol 20 (2021) 795–820. https://doi.org/10.1016/S1474-4422(21)00252-0.

[3]A.C. Solal, P. Assyag, P. Clerson, C. Contre, M. Guenoun, P. Poncelet, J.F. Thebaut, L. Irina, 092 "Grey Zone" of 40-50% ejection fraction in ambulatory patient with Heart Failure. Who are these patients? Lessons from the DEVENIR study, Archives of Cardiovascular Diseases Supplements 2 (2010) 31. https://doi.org/10.1016/S1878-6480(10)70094-X.

[4]I.H. Jung, J.H. Park, J.A. Lee, G.S. Kim, H.Y. Lee, Y.S. Byun, B.O. Kim, Left Ventricular Global Longitudinal Strain as a Predictor for Left Ventricular Reverse Remodeling in Dilated Cardiomyopathy, J Cardiovasc Imaging 28 (2020) 137–149. https://doi.org/10.4250/jcvi.2019.0111.

[5]G. Ernst, Heart-Rate Variability—More than Heart Beats?, Front Public Health 5 (2017) 240. https://doi.org/10.3389/fpubh.2017.00240.

[6]A. Accardo, L. Restivo, M. Ajčević, A. Miladinović, K. Iscra, G. Silveri, M. Merlo, G. Sinagra, Toward a diagnostic CART model for Ischemic heart disease and idiopathic dilated cardiomyopathy based on heart rate total variability, Med Biol Eng Comput 60 (2022) 2655–2663. https://doi.org/10.1007/s11517-022-02618-9.

[7]F. Ferrari, W.R. Menegazzo, Global Longitudinal Strain or Measurement of Ejection Fraction: Which Method is Better in Stratifying Patients with Heart Failure?, Arq Bras Cardiol 113 (2019) 195–196. https://doi.org/10.5935/abc.20190151.

[8]M.C. Pastore, G.E. Mandoli, F. Contorni, L. Cavigli, M. Focardi, F. D'Ascenzi, G. Patti, S. Mondillo, M. Cameli, Speckle Tracking Echocardiography: Early Predictor of Diagnosis and Prognosis in Coronary Artery Disease, Biomed Res Int 2021 (2021) 6685378. https://doi.org/10.1155/2021/6685378.

[9]L. Zhao, P. Li, J. Li, C. Liu, Influence of Ectopic Beats on Heart Rate Variability Analysis, Entropy (Basel) 23 (2021) 648. https://doi.org/10.3390/e23060648.

[10]M.A. Salo, H.V. Huikuri, T. Seppänen, Ectopic beats in heart rate variability analysis: effects of editing on time and frequency domain measures, Ann Noninvasive Electrocardiol 6 (2001) 5–17. https://doi.org/10.1111/j.1542-474x.2001.tb00080.x.

[11]J.I. Doerrfuss, T. Kilic, M. Ahmadi, M. Holtkamp, J.E. Weber, Quantitative and Qualitative EEG as a Prediction Tool for Outcome and Complications in Acute Stroke Patients, Clin EEG Neurosci 51 (2020) 121–129. https://doi.org/10.1177/1550059419875916.

[12]P. Amarenco, J. Bogousslavsky, L.R. Caplan, G.A. Donnan, M.G. Hennerici, Classification of stroke subtypes, Cerebrovasc Dis 27 (2009) 493–501. https://doi.org/10.1159/000210432.

[13]N.W. Manning, C.D. Warne, P.M. Meyers, Reperfusion and Clinical Outcomes in Acute Ischemic Stroke: Systematic Review and Meta-Analysis of the Stent-Retriever-Based, Early Window Endovascular Stroke Trials, Front Neurol 9 (2018) 301. https://doi.org/10.3389/fneur.2018.00301.

[14]M. Ajčević, G. Furlanis, A. Miladinović, A. Buoite Stella, P. Caruso, M. Ukmar, M.A.

Cova, M. Naccarato, A. Accardo, P. Manganotti, Early EEG Alterations Correlate with CTP Hypoperfused Volumes and Neurological Deficit: A Wireless EEG Study in Hyper-Acute Ischemic Stroke, Ann Biomed Eng 49 (2021) 2150–2158. https://doi.org/10.1007/s10439-021-02735-w.

[15]P.M. Rossini, C. Altamura, A. Ferretti, F. Vernieri, F. Zappasodi, M. Caulo, V. Pizzella, C. Del Gratta, G.-L. Romani, F. Tecchio, Does cerebrovascular disease affect the coupling between neuronal activity and local haemodynamics?, Brain 127 (2004) 99–110. https://doi.org/10.1093/brain/awh012.

[16]M. Ajčević, G. Furlanis, M. Naccarato, A. Miladinović, A. Buoite Stella, P. Caruso, T. Cillotto, A. Accardo, P. Manganotti, Hyper-acute EEG alterations predict functional and morphological outcomes in thrombolysis-treated ischemic stroke: a wireless EEG study, Med Biol Eng Comput 59 (2021) 121–129. https://doi.org/10.1007/s11517-020-02280-z.

[17]K.G. Jordan, Emergency EEG and continuous EEG monitoring in acute ischemic stroke, J Clin Neurophysiol 21 (2004) 341–352.

[18]A.S. Dickey, P.D. Mitsias, W.M. Olango, M.C. Agan, W.P. Roche, J.R. Thomas, G.M. Rodrigues, M.R. Frankel, J.J. Ratcliff, R.G. Nogueira, D.C. Haussen, I. Karakis, The Prognostic Value of Quantitative EEG in Patients Undergoing Mechanical Thrombectomy for Acute Ischemic Stroke, J Clin Neurophysiol 39 (2022) 276–282. https://doi.org/10.1097/WNP.0000000000000769.

[19]H.P. Adams, P.H. Davis, E.C. Leira, K.-C. Chang, B.H. Bendixen, W.R. Clarke, R.F. Woolson, M.D. Hansen, Baseline NIH Stroke Scale score strongly predicts outcome after stroke, Neurology 53 (1999) 126–126. https://doi.org/10.1212/WNL.53.1.126.

[20]O. Mecarelli, S. Pro, F. Randi, S. Dispenza, A. Correnti, P. Pulitano, N. Vanacore, E. Vicenzini, D. Toni, EEG patterns and epileptic seizures in acute phase stroke, Cerebrovasc Dis 31 (2011) 191–198. https://doi.org/10.1159/000321872.

[21]S. Abe, T. Tanaka, K. Fukuma, S. Matsubara, R. Motoyama, M. Mizobuchi, H. Yoshimura, T. Matsuki, Y. Manabe, J. Suzuki, H. Ishiyama, M. Tojima, K. Kobayashi, A. Shimotake, K. Nishimura, M. Koga, K. Toyoda, S. Murayama, R. Matsumoto, R. Takahashi, A. Ikeda, M. Ihara, PROPOSE Study Investigators, Interictal epileptiform discharges as a predictive biomarker for recurrence of poststroke epilepsy, Brain Commun 4 (2022) fcac312. https://doi.org/10.1093/braincomms/fcac312.

[22]M.M. Rahman, D.N. Davis, Addressing the Class Imbalance Problem in Medical Datasets, IJMLC (2013) 224–228. https://doi.org/10.7763/IJMLC.2013.V3.307.

[23]P. Manganotti, G. Furlanis, M. Ajčević, P. Polverino, P. Caruso, M. Ridolfi, R.A. Pozzi-Mucelli, M.A. Cova, M. Naccarato, CT perfusion and EEG patterns in patients with acute isolated aphasia in seizure-related stroke mimics, Seizure 71 (2019) 110–115. https://doi.org/10.1016/j.seizure.2019.07.005.

[24]P. Elliott, B. Andersson, E. Arbustini, Z. Bilinska, F. Cecchi, P. Charron, O. Dubourg, U. Kühl, B. Maisch, W.J. McKenna, L. Monserrat, S. Pankuweit, C. Rapezzi, P. Seferovic, L. Tavazzi, A. Keren, Classification of the cardiomyopathies: a position statement from the European Society Of Cardiology Working Group on Myocardial and Pericardial Diseases, Eur Heart J 29 (2008) 270–276. https://doi.org/10.1093/eurheartj/ehm342.

[25]M. Merlo, A. Cannatà, M. Gobbo, D. Stolfo, P.M. Elliott, G. Sinagra, Evolving concepts in dilated cardiomyopathy, Eur J Heart Fail 20 (2018) 228–239. https://doi.org/10.1002/ejhf.1103.

[26]M. Merlo, M. Gigli, S. Poli, D. Stolfo, F. Brun, G. Lardieri, B. Pinamonti, M. Zecchin, A. Pivetta, G. Vitrella, A.D. Lenarda, G. Sinagra, La cardiomiopatia dilatativa come malattia dinamica:

storia naturale, rimodellamento inverso e stratificazione prognostica, Giornale Italiano di Cardiologia 17 (2016) 15–23.

[27]R.G. Weintraub, C. Semsarian, P. Macdonald, Dilated cardiomyopathy, Lancet 390 (2017) 400–414. https://doi.org/10.1016/S0140-6736(16)31713-5.

[28]R.E. Hershberger, D.J. Hedges, A. Morales, Dilated cardiomyopathy: the complexity of a diverse genetic architecture, Nat Rev Cardiol 10 (2013) 531–547. https://doi.org/10.1038/nrcardio.2013.105.

[29]D. Reichart, C. Magnussen, T. Zeller, S. Blankenberg, Dilated cardiomyopathy: from epidemiologic to genetic phenotypes, Journal of Internal Medicine 286 (2019) 362–372. https://doi.org/10.1111/joim.12944.

[30]N.K. Lakdawala, J.R. Winterfield, B.H. Funke, Dilated Cardiomyopathy, Circ Arrhythm Electrophysiol 6 (2013) 228–237. https://doi.org/10.1161/CIRCEP.111.962050.

[31]E. Kinova, D. Somleva-Todorova, A. Goudev, Left Ventricular Strain and Rotation in Patients with Dilated Cardiomyopathy and Severe Systolic Dysfunction, Cardiology 145 (2020) 1–12. https://doi.org/10.1159/000503682.

[32]M.L. Antoni, S.A. Mollema, V. Delgado, J.Z. Atary, C.J.W. Borleffs, E. Boersma, E.R. Holman, E.E. van der Wall, M.J. Schalij, J.J. Bax, Prognostic importance of strain and strain rate after acute myocardial infarction, Eur Heart J 31 (2010) 1640–1647. https://doi.org/10.1093/eurheartj/ehq105.

[33]G. Sinagra, M. Merlo, B. Pinamonti, eds., Dilated Cardiomyopathy: From Genetics to Clinical Management, Springer, Cham (CH), 2019. http://www.ncbi.nlm.nih.gov/books/NBK553850/ (accessed June 11, 2025).

[34]M. Merlo, S.A. Pyxaras, B. Pinamonti, G. Barbati, A. Di Lenarda, G. Sinagra, Prevalence and prognostic significance of left ventricular reverse remodeling in dilated cardiomyopathy receiving tailored medical treatment, J Am Coll Cardiol 57 (2011) 1468–1476. https://doi.org/10.1016/j.jacc.2010.11.030.

[35]N. Townsend, L. Wilson, P. Bhatnagar, K. Wickramasinghe, M. Rayner, M. Nichols, Cardiovascular disease in Europe: epidemiological update 2016, Eur Heart J 37 (2016) 3232–3245. https://doi.org/10.1093/eurheartj/ehw334.

[36]A.S. Go, D. Mozaffarian, V.L. Roger, E.J. Benjamin, J.D. Berry, W.B. Borden, D.M. Bravata, S. Dai, E.S. Ford, C.S. Fox, S. Franco, H.J. Fullerton, C. Gillespie, S.M. Hailpern, J.A. Heit, V.J. Howard, M.D. Huffman, B.M. Kissela, S.J. Kittner, D.T. Lackland, J.H. Lichtman, L.D. Lisabeth, D. Magid, G.M. Marcus, A. Marelli, D.B. Matchar, D.K. McGuire, E.R. Mohler, C.S. Moy, M.E. Mussolino, G. Nichol, N.P. Paynter, P.J. Schreiner, P.D. Sorlie, J. Stein, T.N. Turan, S.S. Virani, N.D. Wong, D. Woo, M.B. Turner, Heart Disease and Stroke Statistics—2013 Update, Circulation 127 (2013) e6–e245. https://doi.org/10.1161/CIR.0b013e31828124ad.

[37]D. Lloyd-Jones, R.J. Adams, T.M. Brown, M. Carnethon, S. Dai, G. De Simone, T.B. Ferguson, E. Ford, K. Furie, C. Gillespie, A. Go, K. Greenlund, N. Haase, S. Hailpern, P.M. Ho, V. Howard, B. Kissela, S. Kittner, D. Lackland, L. Lisabeth, A. Marelli, M.M. McDermott, J. Meigs, D. Mozaffarian, M. Mussolino, G. Nichol, V.L. Roger, W. Rosamond, R. Sacco, P. Sorlie, R. Stafford, T. Thom, S. Wasserthiel-Smoller, N.D. Wong, J. Wylie-Rosett, American Heart Association Statistics Committee and Stroke Statistics Subcommittee, Executive summary: heart disease and stroke statistics--2010 update: a report from the American Heart Association, Circulation 121 (2010) 948–954. https://doi.org/10.1161/CIRCULATIONAHA.109.192666.

[38]R.V. Jensen, M.V. Hjortbak, H.E. Bøtker, Ischemic Heart Disease: An Update, Semin Nucl Med 50 (2020) 195–207. https://doi.org/10.1053/j.semnuclmed.2020.02.007.

[39]J. Knuuti, W. Wijns, A. Saraste, D. Capodanno, E. Barbato, C. Funck-Brentano, E. Prescott, R.F. Storey, C. Deaton, T. Cuisset, S. Agewall, K. Dickstein, T. Edvardsen, J. Escaned, B.J. Gersh, P. Svitil, M. Gilard, D. Hasdai, R. Hatala, F. Mahfoud, J. Masip, C. Muneretto, M. Valgimigli, S. Achenbach, J.J. Bax, ESC Scientific Document Group, 2019 ESC Guidelines for the diagnosis and management of chronic coronary syndromes, Eur Heart J 41 (2020) 407–477. https://doi.org/10.1093/eurheartj/ehz425.

[40]S.J. Murphy, D.J. Werring, Stroke: causes and clinical features, Medicine (Abingdon) 48 (2020) 561–566. https://doi.org/10.1016/j.mpmed.2020.06.002.

[41]K.K. Panuganti, P. Tadi, F. Lui, Transient Ischemic Attack, in: StatPearls, StatPearls Publishing, Treasure Island (FL), 2025. http://www.ncbi.nlm.nih.gov/books/NBK459143/ (accessed June 11, 2025).

[42]J.D. Easton, J.L. Saver, G.W. Albers, M.J. Alberts, S. Chaturvedi, E. Feldmann, T.S. Hatsukami, R.T. Higashida, S.C. Johnston, C.S. Kidwell, H.L. Lutsep, E. Miller, R.L. Sacco, American Heart Association, American Stroke Association Stroke Council, Council on Cardiovascular Surgery and Anesthesia, Council on Cardiovascular Radiology and Intervention, Council on Cardiovascular Nursing, Interdisciplinary Council on Peripheral Vascular Disease, Definition and evaluation of transient ischemic attack: a scientific statement for healthcare professionals from the American Heart Association/American Stroke Association Stroke Council; Council on Cardiovascular Surgery and Anesthesia; Council on Cardiovascular Radiology and Intervention; Council on Cardiovascular Nursing; and the Interdisciplinary Council on Peripheral Vascular Disease. The American Academy of Neurology affirms the value of this statement as an educational tool for neurologists, Stroke 40 (2009) 2276–2293. https://doi.org/10.1161/STROKEAHA.108.192218.

[43]A.P. Coupland, A. Thapar, M.I. Qureshi, H. Jenkins, A.H. Davies, The definition of stroke, J R Soc Med 110 (2017) 9–12. https://doi.org/10.1177/0141076816680121.

[44]P. Tadi, F. Lui, Acute Stroke, in: StatPearls, StatPearls Publishing, Treasure Island (FL), 2025. http://www.ncbi.nlm.nih.gov/books/NBK535369/ (accessed June 11, 2025).

[45]M.J. O'Donnell, D. Xavier, L. Liu, H. Zhang, S.L. Chin, P. Rao-Melacini, S. Rangarajan, S. Islam, P. Pais, M.J. McQueen, C. Mondo, A. Damasceno, P. Lopez-Jaramillo, G.J. Hankey, A.L. Dans, K. Yusoff, T. Truelsen, H.-C. Diener, R.L. Sacco, D. Ryglewicz, A. Czlonkowska, C. Weimar, X. Wang, S. Yusuf, INTERSTROKE investigators, Risk factors for ischaemic and intracerebral haemorrhagic stroke in 22 countries (the INTERSTROKE study): a case-control study, Lancet 376 (2010) 112–123. https://doi.org/10.1016/S0140-6736(10)60834-3.

[46]D. Smajlović, Strokes in young adults: epidemiology and prevention, Vasc Health Risk Manag 11 (2015) 157–164. https://doi.org/10.2147/VHRM.S53203.

[47]T.F. Hasan, H. Hasan, R.E. Kelley, Overview of Acute Ischemic Stroke Evaluation and Management, Biomedicines 9 (2021) 1486. https://doi.org/10.3390/biomedicines9101486.

[48]M.C. Leary, L.R. Caplan, Cardioembolic stroke: An update on etiology, diagnosis and management, Ann Indian Acad Neurol 11 (2008) S52–S63.

[49]S. Yaghi, M.S.V. Elkind, Cryptogenic stroke: A diagnostic challenge, Neurol Clin Pract 4 (2014) 386–393. https://doi.org/10.1212/CPJ.0000000000000086.

[50]G.E. Mead, S.C. Lewis, J.M. Wardlaw, M.S. Dennis, C.P. Warlow, How well does the

Oxfordshire community stroke project classification predict the site and size of the infarct on brain imaging?, J Neurol Neurosurg Psychiatry 68 (2000) 558–562. https://doi.org/10.1136/jnnp.68.5.558.

[51]J. Iłzecka, Z. Stelmasiak, [Practical significance of ischemic stroke OCSP (Oxfordshire Community Stroke Project) classification], Neurol Neurochir Pol 34 (2000) 11–22.

[52]J.L. Banks, C.A. Marotta, Outcomes Validity and Reliability of the Modified Rankin Scale: Implications for Stroke Clinical Trials, Stroke 38 (2007) 1091–1096. https://doi.org/10.1161/01.STR.0000258355.23810.c6.

[53]P.A. Barber, A.M. Demchuk, J. Zhang, A.M. Buchan, Validity and reliability of a quantitative computed tomography score in predicting outcome of hyperacute stroke before thrombolytic therapy. ASPECTS Study Group. Alberta Stroke Programme Early CT Score, Lancet 355 (2000) 1670–1674. https://doi.org/10.1016/s0140-6736(00)02237-6.

[54]O. Shafaat, H. Sotoudeh, Stroke Imaging, in: StatPearls, StatPearls Publishing, Treasure Island (FL), 2025. http://www.ncbi.nlm.nih.gov/books/NBK546635/ (accessed June 11, 2025).

[55]K.R. Lees, E. Bluhmki, R. von Kummer, T.G. Brott, D. Toni, J.C. Grotta, G.W. Albers, M. Kaste, J.R. Marler, S.A. Hamilton, B.C. Tilley, S.M. Davis, G.A. Donnan, W. Hacke, ECASS, ATLANTIS, NINDS and EPITHET rt-PA Study Group, K. Allen, J. Mau, D. Meier, G. del Zoppo, D.A. De Silva, K.S. Butcher, M.W. Parsons, P.A. Barber, C. Levi, C. Bladin, G. Byrnes, Time to treatment with intravenous alteplase and outcome in stroke: an updated pooled analysis of ECASS, ATLANTIS, NINDS, and EPITHET trials, Lancet 375 (2010) 1695–1703. https://doi.org/10.1016/S0140-6736(10)60491-6.

[56]J.L. Saver, G.C. Fonarow, E.E. Smith, M.J. Reeves, M.V. Grau-Sepulveda, W. Pan, D.M. Olson, A.F. Hernandez, E.D. Peterson, L.H. Schwamm, Time to treatment with intravenous tissue plasminogen activator and outcome from acute ischemic stroke, JAMA 309 (2013) 2480–2488. https://doi.org/10.1001/jama.2013.6959.

[57]J. Emberson, K.R. Lees, P. Lyden, L. Blackwell, G. Albers, E. Bluhmki, T. Brott, G. Cohen, S. Davis, G. Donnan, J. Grotta, G. Howard, M. Kaste, M. Koga, R. von Kummer, M. Lansberg, R.I. Lindley, G. Murray, J.M. Olivot, M. Parsons, B. Tilley, D. Toni, K. Toyoda, N. Wahlgren, J. Wardlaw, W. Whiteley, G.J. del Zoppo, C. Baigent, P. Sandercock, W. Hacke, Stroke Thrombolysis Trialists' Collaborative Group, Effect of treatment delay, age, and stroke severity on the effects of intravenous thrombolysis with alteplase for acute ischaemic stroke: a meta-analysis of individual patient data from randomised trials, Lancet 384 (2014) 1929–1935. https://doi.org/10.1016/S0140-6736(14)60584-5.

[58]K.R. Lees, J. Emberson, L. Blackwell, E. Bluhmki, S.M. Davis, G.A. Donnan, J.C. Grotta, M. Kaste, R. von Kummer, M.G. Lansberg, R.I. Lindley, P. Lyden, G.D. Murray, P.A.G. Sandercock, D. Toni, K. Toyoda, J.M. Wardlaw, W.N. Whiteley, C. Baigent, W. Hacke, G. Howard, Stroke Thrombolysis Trialists' Collaborators Group, Effects of Alteplase for Acute Stroke on the Distribution of Functional Outcomes: A Pooled Analysis of 9 Trials, Stroke 47 (2016) 2373–2379. https://doi.org/10.1161/STROKEAHA.116.013644.

[59]G. Thomalla, C.Z. Simonsen, F. Boutitie, G. Andersen, Y. Berthezene, B. Cheng, B. Cheripelli, T.-H. Cho, F. Fazekas, J. Fiehler, I. Ford, I. Galinovic, S. Gellissen, A. Golsari, J. Gregori, M. Günther, J. Guibernau, K.G. Häusler, M. Hennerici, A. Kemmling, J. Marstrand, B. Modrau, L. Neeb, N. Perez de la Ossa, J. Puig, P. Ringleb, P. Roy, E. Scheel, W. Schonewille, J. Serena, S. Sunaert, K. Villringer, A. Wouters, V. Thijs, M. Ebinger, M. Endres, J.B. Fiebach, R. Lemmens, K.W. Muir, N. Nighoghossian, S. Pedraza, C. Gerloff, WAKE-UP Investigators, MRI-Guided Thrombolysis for Stroke with Unknown Time of Onset, N Engl J Med 379 (2018) 611–622. https://doi.org/10.1056/NEJMoa1804355.

[60]W.J. Powers, A.A. Rabinstein, T. Ackerson, O.M. Adeoye, N.C. Bambakidis, K. Becker, J. Biller, M. Brown, B.M. Demaerschalk, B. Hoh, E.C. Jauch, C.S. Kidwell, T.M. Leslie-Mazwi, B. Ovbiagele, P.A. Scott, K.N. Sheth, A.M. Southerland, D.V. Summers, D.L. Tirschwell, Guidelines for the Early Management of Patients With Acute Ischemic Stroke: 2019 Update to the 2018 Guidelines for the Early Management of Acute Ischemic Stroke: A Guideline for Healthcare Professionals From the American Heart Association/American Stroke Association, Stroke 50 (2019) e344–e418. https://doi.org/10.1161/STR.0000000000000211.

[61]B.M. Demaerschalk, D.O. Kleindorfer, O.M. Adeoye, A.M. Demchuk, J.E. Fugate, J.C. Grotta, A.A. Khalessi, E.I. Levy, Y.Y. Palesch, S. Prabhakaran, G. Saposnik, J.L. Saver, E.E. Smith, American Heart Association Stroke Council and Council on Epidemiology and Prevention, Scientific Rationale for the Inclusion and Exclusion Criteria for Intravenous Alteplase in Acute Ischemic Stroke: A Statement for Healthcare Professionals From the American Heart Association/American Stroke Association, Stroke 47 (2016) 581–641. https://doi.org/10.1161/STR.0000000000000086.

[62]J.L. Saver, O. Adeoye, Intravenous Thrombolysis Before Endovascular Thrombectomy for Acute Ischemic Stroke, JAMA 325 (2021) 229–231. https://doi.org/10.1001/jama.2020.22388.

[63]N.H. Chia, J.M. Leyden, J. Newbury, J. Jannes, T.J. Kleinig, Determining the Number of Ischemic Strokes Potentially Eligible for Endovascular Thrombectomy: A Population-Based Study, Stroke 47 (2016) 1377–1380. https://doi.org/10.1161/STROKEAHA.116.013165.

[64]A.P. Jadhav, S.M. Desai, C.L. Kenmuir, M. Rocha, M.T. Starr, B.J. Molyneaux, B.A. Gross, B.T. Jankowitz, T.G. Jovin, Eligibility for Endovascular Trial Enrollment in the 6- to 24-Hour Time Window: Analysis of a Single Comprehensive Stroke Center, Stroke 49 (2018) 1015–1017. https://doi.org/10.1161/STROKEAHA.117.020273.

[65]O.A. Berkhemer, P.S.S. Fransen, D. Beumer, L.A. van den Berg, H.F. Lingsma, A.J. Yoo, W.J. Schonewille, J.A. Vos, P.J. Nederkoorn, M.J.H. Wermer, M.A.A. van Walderveen, J. Staals, J. Hofmeijer, J.A. van Oostayen, G.J. Lycklama à Nijeholt, J. Boiten, P.A. Brouwer, B.J. Emmer, S.F. de Bruijn, L.C. van Dijk, L.J. Kappelle, R.H. Lo, E.J. van Dijk, J. de Vries, P.L.M. de Kort, W.J.J. van Rooij, J.S.P. van den Berg, B.A.A.M. van Hasselt, L.A.M. Aerden, R.J. Dallinga, M.C. Visser, J.C.J. Bot, P.C. Vroomen, O. Eshghi, T.H.C.M.L. Schreuder, R.J.J. Heijboer, K. Keizer, A.V. Tielbeek, H.M. den Hertog, D.G. Gerrits, R.M. van den Berg-Vos, G.B. Karas, E.W. Steyerberg, H.Z. Flach, H.A. Marquering, M.E.S. Sprengers, S.F.M. Jenniskens, L.F.M. Beenen, R. van den Berg, P.J. Koudstaal, W.H. van Zwam, Y.B.W.E.M. Roos, A. van der Lugt, R.J. van Oostenbrugge, C.B.L.M. Majoie, D.W.J. Dippel, MR CLEAN Investigators, A randomized trial of intraarterial treatment for acute ischemic stroke, N Engl J Med 372 (2015) 11–20. https://doi.org/10.1056/NEJMoa1411587.

[66]H.P. Adams, B.H. Bendixen, L.J. Kappelle, J. Biller, B.B. Love, D.L. Gordon, E.E. Marsh, Classification of subtype of acute ischemic stroke. Definitions for use in a multicenter clinical trial. TOAST. Trial of Org 10172 in Acute Stroke Treatment, Stroke 24 (1993) 35–41. https://doi.org/10.1161/01.str.24.1.35.

[67]G.W. Albers, M.P. Marks, S. Kemp, S. Christensen, J.P. Tsai, S. Ortega-Gutierrez, R.A. McTaggart, M.T. Torbey, M. Kim-Tenser, T. Leslie-Mazwi, A. Sarraj, S.E. Kasner, S.A. Ansari, S.D. Yeatts, S. Hamilton, M. Mlynash, J.J. Heit, G. Zaharchuk, S. Kim, J. Carrozzella, Y.Y. Palesch, A.M. Demchuk, R. Bammer, P.W. Lavori, J.P. Broderick, M.G. Lansberg, DEFUSE 3 Investigators, Thrombectomy for Stroke at 6 to 16 Hours with Selection by Perfusion Imaging, N Engl J Med 378 (2018) 708–718. https://doi.org/10.1056/NEJMoa1713973.

[68]Q. Li, M. Abdalkader, J.E. Siegler, S. Yaghi, A. Sarraj, B.C.V. Campbell, A.J. Yoo, O.O. Zaidat, J. Kaesmacher, D. Pujara, R.G. Nogueira, J.L. Saver, L. Li, Q. Han, Y. Dai, H. Sang, Q. Yang, T.N. Nguyen, Z. Qiu, Mechanical Thrombectomy for Large Ischemic Stroke: A Systematic Review

and Meta-analysis, Neurology 101 (2023) e922–e932. https://doi.org/10.1212/WNL.0000000000207536.

[69]J.L. Saver, R. Jahan, E.I. Levy, T.G. Jovin, B. Baxter, R.G. Nogueira, W. Clark, R. Budzik, O.O. Zaidat, SWIFT Trialists, Solitaire flow restoration device versus the Merci Retriever in patients with acute ischaemic stroke (SWIFT): a randomised, parallel-group, non-inferiority trial, Lancet 380 (2012) 1241–1249. https://doi.org/10.1016/S0140-6736(12)61384-1.

[70]A.S. Turk, A. Siddiqui, J.T. Fifi, R.A. De Leacy, D.J. Fiorella, E. Gu, E.I. Levy, K.V. Snyder, R.A. Hanel, A. Aghaebrahim, B.K. Woodward, H.R. Hixson, M.I. Chaudry, A.M. Spiotta, A.T. Rai, D. Frei, J.E.D. Almandoz, M. Kelly, A. Arthur, B. Baxter, J. English, I. Linfante, K.M. Fargen, J. Mocco, Aspiration thrombectomy versus stent retriever thrombectomy as first-line approach for large vessel occlusion (COMPASS): a multicentre, randomised, open label, blinded outcome, non-inferiority trial, Lancet 393 (2019) 998–1008. https://doi.org/10.1016/S0140-6736(19)30297-1.

[71]R.E. Kleiger, J.P. Miller, J.T. Bigger, A.J. Moss, Decreased heart rate variability and its association with increased mortality after acute myocardial infarction, Am J Cardiol 59 (1987) 256–262. https://doi.org/10.1016/0002-9149(87)90795-8.

[72]A.S. Shah, R. Lampert, J. Goldberg, J.D. Bremner, L. Li, M.D. Thames, V. Vaccarino, A.J. Shah, Alterations in heart rate variability are associated with abnormal myocardial perfusion, Int J Cardiol 305 (2020) 99–105. https://doi.org/10.1016/j.ijcard.2020.01.069.

[73]A. Kosaraju, A. Goyal, Y. Grigorova, A.N. Makaryus, Left Ventricular Ejection Fraction, in: StatPearls, StatPearls Publishing, Treasure Island (FL), 2024. http://www.ncbi.nlm.nih.gov/books/NBK459131/ (accessed February 4, 2024).

[74]K. Ashish, M. Faisaluddin, D. Bandyopadhyay, A. Hajra, E. Herzog, Prognostic value of global longitudinal strain in heart failure subjects: A recent prototype, Int J Cardiol Heart Vasc 22 (2018) 48–49. https://doi.org/10.1016/j.ijcha.2018.11.009.

[75]F. Shaffer, J.P. Ginsberg, An Overview of Heart Rate Variability Metrics and Norms, Front Public Health 5 (2017) 258. https://doi.org/10.3389/fpubh.2017.00258.

[76]M. Malik, J.T. Bigger, A.J. Camm, R.E. Kleiger, A. Malliani, A.J. Moss, P.J. Schwartz, Heart rate variability: Standards of measurement, physiological interpretation, and clinical use, European Heart Journal 17 (1996) 354–381. https://doi.org/10.1093/oxfordjournals.eurheartj.a014868.

[77]N. Chattipakorn, T. Incharoen, N. Kanlop, S. Chattipakorn, Heart rate variability in myocardial infarction and heart failure, International Journal of Cardiology 120 (2007) 289–296. https://doi.org/10.1016/j.ijcard.2006.11.221.

[78]R.E. Kleiger, P.K. Stein, J.T. Bigger, Heart rate variability: measurement and clinical utility, Ann Noninvasive Electrocardiol 10 (2005) 88–101. https://doi.org/10.1111/j.1542-474X.2005.10101.x.

[79]A.B. Ciccone, J.A. Siedlik, J.M. Wecht, J.A. Deckert, N.D. Nguyen, J.P. Weir, Reminder: RMSSD and SD1 are identical heart rate variability metrics, Muscle Nerve 56 (2017) 674–678. https://doi.org/10.1002/mus.25573.

[80]A.J.E. Seely, P.T. Macklem, Complex systems and the technology of variability analysis, Crit Care 8 (2004) R367-384. https://doi.org/10.1186/cc2948.

[81]B.W. Johnston, R. Barrett-Jolley, A. Krige, I.D. Welters, Heart rate variability: Measurement and emerging use in critical care medicine, J Intensive Care Soc 21 (2020) 148–157.

https://doi.org/10.1177/1751143719853744.

[82]F. Shaffer, R. McCraty, C.L. Zerr, A healthy heart is not a metronome: an integrative review of the heart's anatomy and heart rate variability, Front Psychol 5 (2014) 1040. https://doi.org/10.3389/fpsyg.2014.01040.

[83]G.A. Reyes del Paso, W. Langewitz, L.J.M. Mulder, A. van Roon, S. Duschek, The utility of low frequency heart rate variability as an index of sympathetic cardiac tone: a review with emphasis on a reanalysis of previous studies, Psychophysiology 50 (2013) 477–487. https://doi.org/10.1111/psyp.12027.

[84]D.S. Goldstein, O. Bentho, M.-Y. Park, Y. Sharabi, Low-frequency power of heart rate variability is not a measure of cardiac sympathetic tone but may be a measure of modulation of cardiac autonomic outflows by baroreflexes, Exp Physiol 96 (2011) 1255–1261. https://doi.org/10.1113/expphysiol.2010.056259.

[85]W.A. Tiller, R. McCraty, M. Atkinson, Cardiac coherence: a new, noninvasive measure of autonomic nervous system order, Altern Ther Health Med 2 (1996) 52–65.

[86]T.E. Brown, L.A. Beightol, J. Koh, D.L. Eckberg, Important influence of respiration on human R-R interval power spectra is largely ignored, J Appl Physiol (1985) 75 (1993) 2310–2317. https://doi.org/10.1152/jappl.1993.75.5.2310.

[87]R. McCraty, F. Shaffer, Heart Rate Variability: New Perspectives on Physiological Mechanisms, Assessment of Self-regulatory Capacity, and Health risk, Glob Adv Health Med 4 (2015) 46–61. https://doi.org/10.7453/gahmj.2014.073.

[88]J.F. Thayer, S.S. Yamamoto, J.F. Brosschot, The relationship of autonomic imbalance, heart rate variability and cardiovascular disease risk factors, Int J Cardiol 141 (2010) 122–131. https://doi.org/10.1016/j.ijcard.2009.09.543.

[89]G.E. Billman, The LF/HF ratio does not accurately measure cardiac sympatho-vagal balance, Front Physiol 4 (2013) 26. https://doi.org/10.3389/fphys.2013.00026.

[90]M. Pagani, F. Lombardi, S. Guzzetti, G. Sandrone, O. Rimoldi, G. Malfatto, S. Cerutti, A. Malliani, Power spectral density of heart rate variability as an index of sympatho-vagal interaction in normal and hypertensive subjects, J Hypertens Suppl 2 (1984) S383-385.

[91]R. Sassi, S. Cerutti, F. Lombardi, M. Malik, H.V. Huikuri, C.-K. Peng, G. Schmidt, Y. Yamamoto, Advances in heart rate variability signal analysis: joint position statement by the e-Cardiology ESC Working Group and the European Heart Rhythm Association co-endorsed by the Asia Pacific Heart Rhythm Society, Europace 17 (2015) 1341–1353. https://doi.org/10.1093/europace/euv015.

[92]B. Francesco, B. Maria Grazia, G. Emanuele, F. Valentina, C. Sara, F. Chiara, M. Riccardo, F. Francesco, Linear and nonlinear heart rate variability indexes in clinical practice, Comput Math Methods Med 2012 (2012) 219080. https://doi.org/10.1155/2012/219080.

[93]P.K. Stein, A. Reddy, Non-Linear Heart Rate Variability and Risk Stratification in Cardiovascular Disease, Indian Pacing Electrophysiol J 5 (2005) 210–220.

[94]J. Pumprla, K. Howorka, D. Groves, M. Chester, J. Nolan, Functional assessment of heart rate variability: physiological basis and practical applications, Int J Cardiol 84 (2002) 1–14. https://doi.org/10.1016/s0167-5273(02)00057-8.

[95]M. Brennan, M. Palaniswami, P. Kamen, Do existing measures of Poincaré plot geometry reflect nonlinear features of heart rate variability?, IEEE Trans Biomed Eng 48 (2001) 1342–1347.

https://doi.org/10.1109/10.959330.

[96]M.P. Tulppo, T.H. Mäkikallio, T. Seppänen, R.T. Laukkanen, H.V. Huikuri, Vagal modulation of heart rate during exercise: effects of age and physical fitness, Am J Physiol 274 (1998) H424-429. https://doi.org/10.1152/ajpheart.1998.274.2.H424.

[97]P. Guzik, J. Piskorski, T. Krauze, R. Schneider, K.H. Wesseling, A. Wykretowicz, H. Wysocki, Correlations between the Poincaré plot and conventional heart rate variability parameters assessed during paced breathing, J Physiol Sci 57 (2007) 63–71. https://doi.org/10.2170/physiolsci.RP005506.

[98]M. Cusenza, A. Accardo, G. D'Addio, G. Corbi, Relationship between fractal dimension and power-law exponent of heart rate variability in normal and heart failure subjects, in: 2010 Computing in Cardiology, 2010: pp. 935–938.

[99]G. Captur, A.L. Karperien, A.D. Hughes, D.P. Francis, J.C. Moon, The fractal heart — embracing mathematics in the cardiology clinic, Nat Rev Cardiol 14 (2017) 56–64. https://doi.org/10.1038/nrcardio.2016.161.

[100]G.E. Billman, Heart rate variability - a historical perspective, Front Physiol 2 (2011) 86. https://doi.org/10.3389/fphys.2011.00086.

[101]G. Corrado, G. Foglia-Manzillo, VALUTAZIONE ECOCARDIOGRAFICA DELLE DIMENSIONI E DELLA FUNZIONE SISTOLICA GLOBALE DEL VENTRICOLO SINISTRO, (n.d.).

[102]L.P. Fernandes, A.T.F. Barreto, M.G. Neto, E.J.N. Câmara, A.R. Durães, L. Roever, R. Aras-Júnior, Prognostic power of conventional echocardiography in individuals without history of cardiovascular diseases: A systematic review and meta-analysis, Clinics (Sao Paulo) 76 (2021). https://doi.org/10.6061/clinics/2021/e2754.

[103]C. Russo, Z. Jin, M.S.V. Elkind, T. Rundek, S. Homma, R.L. Sacco, M.R. Di Tullio, Prevalence and prognostic value of subclinical left ventricular systolic dysfunction by global longitudinal strain in a community-based cohort, Eur J Heart Fail 16 (2014) 1301–1309. https://doi.org/10.1002/ejhf.154.

[104]P.G. Supino, J.S. Borer, E.M. Herrold, C. Hochreiter, Prognostication in 3-Vessel Coronary Artery Disease Based on Left Ventricular Ejection Fraction During Exercise, Circulation 100 (1999) 924–932. https://doi.org/10.1161/01.CIR.100.9.924.

[105]L. Trasca, M.R. Popescu, A.C. Popescu, S.M. Balanescu, Echocardiography in the Diagnosis of Cardiomyopathies: Current Status and Future Directions, Rev Cardiovasc Med 23 (2022) 280. https://doi.org/10.31083/j.rcm2308280.

[106]B. Bozkurt, M. Colvin, J. Cook, L.T. Cooper, A. Deswal, G.C. Fonarow, G.S. Francis, D. Lenihan, E.F. Lewis, D.M. McNamara, E. Pahl, R.S. Vasan, K. Ramasubbu, K. Rasmusson, J.A. Towbin, C. Yancy, On behalf of the American Heart Association Committee on Heart Failure and Transplantation of the Council on Clinical Cardiology; Council on Cardiovascular Disease in the Young; Council on Cardiovascular and Stroke Nursing; Council on Epidemiology and Prevention; and Council on Quality of Care and Outcomes Research, Current Diagnostic and Treatment Strategies for Specific Dilated Cardiomyopathies: A Scientific Statement From the American Heart Association, Circulation 134 (2016) e579–e646. https://doi.org/10.1161/CIR.0000000000000455.

[107]L. Song, C. Brezden-Masley, V. Ramanan, N. Ghugre, J.J. Barfett, K.K.W. Chan, R. Haq, T. Petrella, V. Dhir, L. Jimenez-Juan, B.R. Chacko, V. Kotha, K.A. Connelly, A.T. Yan, Serial Measurements of Left Ventricular Systolic and Diastolic Function by Cardiac Magnetic Resonance

Imaging in Patients with Early Stage Breast Cancer on Trastuzumab, Am J Cardiol 123 (2019) 1173–1179. https://doi.org/10.1016/j.amjcard.2018.12.046.

[108]Real-life data on heart failure before and after implantation of resynchronization and/or defibrillation devices - the Síncrone study - PubMed, (n.d.). https://pubmed.ncbi.nlm.nih.gov/30685295/ (accessed June 12, 2025).

[109]E.R. Duque, A. Briasoulis, P.A. Alvarez, Heart failure with preserved ejection fraction in the elderly: pathophysiology, diagnostic and therapeutic approach, J Geriatr Cardiol 16 (2019) 421–428. https://doi.org/10.11909/j.issn.1671-5411.2019.05.009.

[110]K. Tong, J. Zhang, J. Wang, X. Zhou, X. Lei, Y. Xu, G. Zhi, [Quantification of left and right ventricular systolic function in patients with dilated cardiomyopathy using real-time three-dimensional echocardiography], Zhong Nan Da Xue Xue Bao Yi Xue Ban 37 (2012) 561–566. https://doi.org/10.3969/j.issn.1672-7347.2012.06.004.

[111]E. Surkova, D. Muraru, D. Genovese, P. Aruta, C. Palermo, L.P. Badano, Relative Prognostic Importance of Left and Right Ventricular Ejection Fraction in Patients With Cardiac Diseases, J Am Soc Echocardiogr 32 (2019) 1407-1415.e3. https://doi.org/10.1016/j.echo.2019.06.009.

[112]M. Bertini, A.C.T. Ng, M.L. Antoni, G. Nucifora, S.H. Ewe, D. Auger, N.A. Marsan, M.J. Schalij, J.J. Bax, V. Delgado, Global longitudinal strain predicts long-term survival in patients with chronic ischemic cardiomyopathy, Circ Cardiovasc Imaging 5 (2012) 383–391. https://doi.org/10.1161/CIRCIMAGING.111.970434.

[113]J. Ma, L. Guan, L. Yang, A. Mahemuti, Y. Mu, Relationship Between Myocardial Perfusion and Myocardial Function in Dilated Cardiomyopathy by Shown Ultrasonography, Int Heart J 62 (2021) 792–800. https://doi.org/10.1536/ihj.20-599.

[114]J. Schroeder, S. Hamada, N. Gründlinger, T. Rubeau, E. Altiok, K. Ulbrich, A. Keszei, N. Marx, M. Becker, Myocardial deformation by strain echocardiography identifies patients with acute coronary syndrome and non-diagnostic ECG presenting in a chest pain unit: a prospective study of diagnostic accuracy, Clin Res Cardiol 105 (2016) 248–256. https://doi.org/10.1007/s00392-015-0916-2.

[115]T. Dahlslett, S. Karlsen, B. Grenne, C. Eek, B. Sjøli, H. Skulstad, O.A. Smiseth, T. Edvardsen, H. Brunvand, Early assessment of strain echocardiography can accurately exclude significant coronary artery stenosis in suspected non-ST-segment elevation acute coronary syndrome, J Am Soc Echocardiogr 27 (2014) 512–519. https://doi.org/10.1016/j.echo.2014.01.019.

[116]A. Atici, H.A. Barman, E. Durmaz, K. Demir, R. Cakmak, S. Tugrul, A. Elitok, İ. Onur, İ. Sahin, A. Oncul, Predictive value of global and territorial longitudinal strain imaging in detecting significant coronary artery disease in patients with myocardial infarction without persistent ST-segment elevation, Echocardiography 36 (2019) 512–520. https://doi.org/10.1111/echo.14275.

[117]C. Zito, L. Longobardo, R. Citro, M. Galderisi, L. Oreto, M.L. Carerj, R. Manganaro, M. Cusmà-Piccione, M.C. Todaro, G. Di Bella, E. Imbalzano, B.K. Khandheria, S. Carerj, Ten Years of 2D Longitudinal Strain for Early Myocardial Dysfunction Detection: A Clinical Overview, Biomed Res Int 2018 (2018) 8979407. https://doi.org/10.1155/2018/8979407.

[118]V. A, W. M, N. K, B. A, P. M, G. Aw, K. P, Automated CT perfusion imaging for acute ischemic stroke: Pearls and pitfalls for real-world use, Neurology 93 (2019). https://doi.org/10.1212/WNL.0000000000008481.

[119]L. Lin, A. Bivard, M.W. Parsons, Perfusion patterns of ischemic stroke on computed

tomography perfusion, J Stroke 15 (2013) 164–173. https://doi.org/10.5853/jos.2013.15.3.164.

[120]P. Vilela, H.A. Rowley, Brain ischemia: CT and MRI techniques in acute ischemic stroke, Eur J Radiol 96 (2017) 162–172. https://doi.org/10.1016/j.ejrad.2017.08.014.

[121]M.R. Etherton, A.D. Barreto, L.H. Schwamm, O. Wu, Neuroimaging Paradigms to Identify Patients for Reperfusion Therapy in Stroke of Unknown Onset, Front. Neurol. 9 (2018). https://doi.org/10.3389/fneur.2018.00327.

[122]H. Ma, B.C.V. Campbell, M.W. Parsons, L. Churilov, C.R. Levi, C. Hsu, T.J. Kleinig, T. Wijeratne, S. Curtze, H.M. Dewey, F. Miteff, C.-H. Tsai, J.-T. Lee, T.G. Phan, N. Mahant, M.-C. Sun, M. Krause, J. Sturm, R. Grimley, C.-H. Chen, C.-J. Hu, A.A. Wong, D. Field, Y. Sun, P.A. Barber, A. Sabet, J. Jannes, J.-S. Jeng, B. Clissold, R. Markus, C.-H. Lin, L.-M. Lien, C.F. Bladin, S. Christensen, N. Yassi, G. Sharma, A. Bivard, P.M. Desmond, B. Yan, P.J. Mitchell, V. Thijs, L. Carey, A. Meretoja, S.M. Davis, G.A. Donnan, Thrombolysis Guided by Perfusion Imaging up to 9 Hours after Onset of Stroke, New England Journal of Medicine 380 (2019) 1795–1803. https://doi.org/10.1056/NEJMoa1813046.

[123]G. Furlanis, M. Ajčević, A. Buoite Stella, T. Cillotto, P. Caruso, M. Ridolfi, M.A. Cova, M. Naccarato, P. Manganotti, Wake-up stroke: thrombolysis reduces ischemic lesion volume and neurological deficit, J Neurol 267 (2020) 666–673. https://doi.org/10.1007/s00415-019-09603-7.

[124]D. Václavík, O. Volný, P. Cimflová, K. Švub, K. Dvorníková, M. Bar, The importance of CT perfusion for diagnosis and treatment of ischemic stroke in anterior circulation, J Integr Neurosci 21 (2022) 92. https://doi.org/10.31083/j.jin2103092.

[125]B.C.V. Campbell, C.B.L.M. Majoie, G.W. Albers, B.K. Menon, N. Yassi, G. Sharma, W.H. van Zwam, R.J. van Oostenbrugge, A.M. Demchuk, F. Guillemin, P. White, A. Dávalos, A. van der Lugt, K.S. Butcher, A. Cherifi, H.A. Marquering, G. Cloud, J.M. Macho Fernández, J. Madigan, C. Oppenheim, G.A. Donnan, Y.B.W.E.M. Roos, J. Shankar, H. Lingsma, A. Bonafé, H. Raoult, M. Hernández-Pérez, A. Bharatha, R. Jahan, O. Jansen, S. Richard, E.I. Levy, O.A. Berkhemer, M. Soudant, L. Aja, S.M. Davis, T. Krings, M. Tisserand, L. San Román, A. Tomasello, D. Beumer, S. Brown, D.S. Liebeskind, S. Bracard, K.W. Muir, D.W.J. Dippel, M. Goyal, J.L. Saver, T.G. Jovin, M.D. Hill, P.J. Mitchell, HERMES collaborators, Penumbral imaging and functional outcome in patients with anterior circulation ischaemic stroke treated with endovascular thrombectomy versus medical therapy: a meta-analysis of individual patient-level data, Lancet Neurol 18 (2019) 46–55. https://doi.org/10.1016/S1474-4422(18)30314-4.

[126]G. Zaharchuk, Arterial Spin Labeled Perfusion Imaging in Acute Ischemic Stroke, Stroke 45 (2014) 1202–1207. https://doi.org/10.1161/STROKEAHA.113.003612.

[127]L. Daftari Besheli, A. Ahmed, O. Hamam, L. Luna, L.R. Sun, V. Urrutia, A.E. Hillis, A. Tekes-Brady, V. Yedavalli, Arterial Spin Labeling technique and clinical applications of the intracranial compartment in stroke and stroke mimics - A case-based review, Neuroradiol J 35 (2022) 437–453. https://doi.org/10.1177/19714009221098806.

[128]B. Siewert, B.M. Bly, G. Schlaug, D.G. Darby, V. Thangaraj, S. Warach, R.R. Edelman, Comparison of the BOLD- and EPISTAR-technique for functional brain imaging by using signal detection theory, Magnetic Resonance in Medicine 36 (1996) 249–255. https://doi.org/10.1002/mrm.1910360212.

[129]J.A. Chalela, D.C. Alsop, J.B. Gonzalez-Atavales, J.A. Maldjian, S.E. Kasner, J.A. Detre, Magnetic resonance perfusion imaging in acute ischemic stroke using continuous arterial spin labeling, Stroke 31 (2000) 680–687. https://doi.org/10.1161/01.str.31.3.680.

[130]G. Zaharchuk, I.S. El Mogy, N.J. Fischbein, G.W. Albers, Comparison of Arterial Spin

Labeling and Bolus Perfusion-Weighted Imaging for Detecting Mismatch in Acute Stroke, Stroke 43 (2012) 1843–1848. https://doi.org/10.1161/STROKEAHA.111.639773.

[131]R.P.H. Bokkers, D.A. Hernandez, J.G. Merino, R.V. Mirasol, M.J. van Osch, J. Hendrikse, S. Warach, L.L. Latour, National Institutes of Health Stroke Natural History Investigators, Whole-brain arterial spin labeling perfusion MRI in patients with acute stroke, Stroke 43 (2012) 1290–1294. https://doi.org/10.1161/STROKEAHA.110.589234.

[132]D.J.J. Wang, J.R. Alger, J.X. Qiao, Q. Hao, S. Hou, R. Fiaz, M. Gunther, W.B. Pope, J.L. Saver, N. Salamon, D.S. Liebeskind, UCLA Stroke Investigators, The value of arterial spin-labeled perfusion imaging in acute ischemic stroke: comparison with dynamic susceptibility contrast-enhanced MRI, Stroke 43 (2012) 1018–1024. https://doi.org/10.1161/STROKEAHA.111.631929.

[133]Y.-C. Huang, H.-L. Liu, J.-D. Lee, J.-T. Yang, H.-H. Weng, M. Lee, M.-Y. Yeh, Y.-H. Tsai, Comparison of Arterial Spin Labeling and Dynamic Susceptibility Contrast Perfusion MRI in Patients with Acute Stroke, PLoS One 8 (2013) e69085. https://doi.org/10.1371/journal.pone.0069085.

[134]A. Bivard, V. Krishnamurthy, P. Stanwell, C. Levi, N.J. Spratt, S. Davis, M. Parsons, Arterial spin labeling versus bolus-tracking perfusion in hyperacute stroke, Stroke 45 (2014) 127–133. https://doi.org/10.1161/STROKEAHA.113.003218.

[135]T. Niibo, H. Ohta, K. Yonenaga, I. Ikushima, S. Miyata, H. Takeshima, Arterial spin-labeled perfusion imaging to predict mismatch in acute ischemic stroke, Stroke 44 (2013) 2601–2603. https://doi.org/10.1161/STROKEAHA.113.002097.

[136]S.J. Mendelson, S. Prabhakaran, Diagnosis and Management of Transient Ischemic Attack and Acute Ischemic Stroke: A Review, JAMA 325 (2021) 1088–1098. https://doi.org/10.1001/jama.2020.26867.

[137]J.M. Pollock, H. Tan, R.A. Kraft, C.T. Whitlow, J.H. Burdette, J.A. Maldjian, Arterial spin-labeled MR perfusion imaging: clinical applications, Magn Reson Imaging Clin N Am 17 (2009) 315–338. https://doi.org/10.1016/j.mric.2009.01.008.

[138]J.M. Pollock, A.R. Deibler, J.H. Burdette, R.A. Kraft, H. Tan, A.B. Evans, J.A. Maldjian, Migraine associated cerebral hyperperfusion with arterial spin-labeled MR imaging, AJNR Am J Neuroradiol 29 (2008) 1494–1497. https://doi.org/10.3174/ajnr.A1115.

[139]F.B. Pizzini, P. Farace, P. Manganotti, G. Zoccatelli, L.G. Bongiovanni, X. Golay, A. Beltramello, A. Osculati, G. Bertini, P.F. Fabene, Cerebral perfusion alterations in epileptic patients during peri-ictal and post-ictal phase: PASL vs DSC-MRI, Magn Reson Imaging 31 (2013) 1001–1005. https://doi.org/10.1016/j.mri.2013.03.023.

[140]T. Noguchi, Y. Yakushiji, M. Nishihara, O. Togao, K. Yamashita, K. Kikuchi, M. Matsuo, S. Azama, H. Irie, Arterial Spin-labeling in Central Nervous System Infection, Magn Reson Med Sci 15 (2016) 386–394. https://doi.org/10.2463/mrms.mp.2015-0140.

[141]B. H Buck, N. Akhtar, A. Alrohimi, K. Khan, A. Shuaib, Stroke mimics: incidence, aetiology, clinical features and treatment, Ann Med 53 (2021) 420–436. https://doi.org/10.1080/07853890.2021.1890205.

[142]Various pathophysiological states of acute symptomatic seizures immediately after ischemic stroke, namely “onset seizures,” shown by complementary use of peri-ictal magnetic resonance imaging and electroencephalography - Murao - 2017 - Neurology and Clinical Neuroscience - Wiley Online Library, (n.d.). https://onlinelibrary.wiley.com/doi/10.1111/ncn3.12160 (accessed June 12, 2025).

[143]R.-E. Yoo, T.J. Yun, B.-W. Yoon, S.K. Lee, S.-T. Lee, K.M. Kang, S.H. Choi, J.-H. Kim, C.-H. Sohn, S.-W. Park, M.H. Han, Identification of cerebral perfusion using arterial spin labeling in patients with seizures in acute settings, PLoS One 12 (2017) e0173538. https://doi.org/10.1371/journal.pone.0173538.

[144]N. Zhang, F. Chen, X. Xie, Z. Xie, D. Hong, J. Li, T. Ouyang, Application of quantitative EEG in acute ischemic stroke patients who underwent thrombectomy: A comparison with CT perfusion, Clin Neurophysiol 141 (2022) 24–33. https://doi.org/10.1016/j.clinph.2022.06.007.

[145]M.A. Ahmad, C. Eckert, A. Teredesai, Interpretable Machine Learning in Healthcare, in: Proceedings of the 2018 ACM International Conference on Bioinformatics, Computational Biology, and Health Informatics, Association for Computing Machinery, New York, NY, USA, 2018: pp. 559–560. https://doi.org/10.1145/3233547.3233667.

[146]R. Caruana, Y. Lou, J. Gehrke, P. Koch, M. Sturm, N. Elhadad, Intelligible Models for HealthCare: Predicting Pneumonia Risk and Hospital 30-day Readmission, in: Proceedings of the 21th ACM SIGKDD International Conference on Knowledge Discovery and Data Mining, Association for Computing Machinery, New York, NY, USA, 2015: pp. 1721–1730. https://doi.org/10.1145/2783258.2788613.

[147]H. Zhang, J.-X. Ma, C.-T. Liu, J.-X. Ren, L. Ding, Development and evaluation of in silico prediction model for drug-induced respiratory toxicity by using naïve Bayes classifier method, Food and Chemical Toxicology 121 (2018) 593–603. https://doi.org/10.1016/j.fct.2018.09.051.

[148]S. Sossi Alaoui, B. Aksasse, Y. Farhaoui, Data Mining and Machine Learning Approaches and Technologies for Diagnosing Diabetes in Women, in: Y. Farhaoui (Ed.), Big Data and Networks Technologies, Springer International Publishing, Cham, 2020: pp. 59–72. https://doi.org/10.1007/978-3-030-23672-4_6.

[149]Y. Zhang, Y. Ma, Application of supervised machine learning algorithms in the classification of sagittal gait patterns of cerebral palsy children with spastic diplegia, Comput Biol Med 106 (2019) 33–39. https://doi.org/10.1016/j.compbiomed.2019.01.009.

[150]A.K. Feeny, J. Rickard, D. Patel, S. Toro, K.M. Trulock, C.J. Park, M.A. LaBarbera, N. Varma, M.J. Niebauer, S. Sinha, E.Z. Gorodeski, R.A. Grimm, X. Ji, J. Barnard, A. Madabhushi, D.D. Spragg, M.K. Chung, Machine Learning Prediction of Response to Cardiac Resynchronization Therapy: Improvement Versus Current Guidelines, Circ Arrhythm Electrophysiol 12 (2019) e007316. https://doi.org/10.1161/CIRCEP.119.007316.

[151]I. Salman, Heart attack mortality prediction: an application of machine learning methods, Turk J Elec Eng & Comp Sci 27 (2019) 4378–4389.

[152]P. Melillo, N. De Luca, M. Bracale, L. Pecchia, Classification tree for risk assessment in patients suffering from congestive heart failure via long-term heart rate variability, IEEE J Biomed Health Inform 17 (2013) 727–733. https://doi.org/10.1109/jbhi.2013.2244902.

[153]R. Elshawi, M.H. Al-Mallah, S. Sakr, On the interpretability of machine learning-based model for predicting hypertension, BMC Medical Informatics and Decision Making 19 (2019) 146. https://doi.org/10.1186/s12911-019-0874-0.

[154]G. Stiglic, P. Kocbek, N. Fijacko, M. Zitnik, K. Verbert, L. Cilar, Interpretability of machine learning-based prediction models in healthcare, WIREs Data Mining and Knowledge Discovery 10 (2020) e1379. https://doi.org/10.1002/widm.1379.

[155]Z.C. Lipton, The Mythos of Model Interpretability: In machine learning, the concept of interpretability is both important and slippery., Queue 16 (2018) 31–57.

https://doi.org/10.1145/3236386.3241340.

[156]D.V. Carvalho, E.M. Pereira, J.S. Cardoso, Machine Learning Interpretability: A Survey on Methods and Metrics, Electronics 8 (2019) 832. https://doi.org/10.3390/electronics8080832.

[157]M.T. Ribeiro, S. Singh, C. Guestrin, "Why Should I Trust You?": Explaining the Predictions of Any Classifier, in: Proceedings of the 22nd ACM SIGKDD International Conference on Knowledge Discovery and Data Mining, Association for Computing Machinery, New York, NY, USA, 2016: pp. 1135–1144. https://doi.org/10.1145/2939672.2939778.

[158]E. Štrumbelj, I. Kononenko, Explaining prediction models and individual predictions with feature contributions, Knowl Inf Syst 41 (2014) 647–665. https://doi.org/10.1007/s10115-013-0679-x.

[159]P. Welch, The use of fast Fourier transform for the estimation of power spectra: A method based on time averaging over short, modified periodograms, IEEE Transactions on Audio and Electroacoustics 15 (1967) 70–73. https://doi.org/10.1109/TAU.1967.1161901.

[160]R.M. Rangayyan, S. Krishnan, Biomedical Signal Analysis, John Wiley & Sons, 2024.

[161](PDF) Ictal Heart Rate Variability Assessment with Focus on Secondary Generalized and Complex Partial Epileptic Seizures, ResearchGate (n.d.). https://www.researchgate.net/publication/259918751_Ictal_Heart_Rate_Variability_Assessment_with_Focus_on_Secondary_Generalized_and_Complex_Partial_Epileptic_Seizures (accessed June 12, 2025).

[162]M.A. Woo, W.G. Stevenson, D.K. Moser, R.B. Trelease, R.M. Harper, Patterns of beat-to-beat heart rate variability in advanced heart failure, Am Heart J 123 (1992) 704–710. https://doi.org/10.1016/0002-8703(92)90510-3.

[163]T. Higuchi, Approach to an irregular time series on the basis of the fractal theory, Physica D. Nonlinear Phenomena (1988). https://doi.org/10.1016/0167-2789(88)90081-4.

[164]A. Accardo, M. Affinito, M. Carrozzi, F. Bouquet, Use of the fractal dimension for the analysis of electroencephalographic time series, Biol Cybern 77 (1997) 339–350. https://doi.org/10.1007/s004220050394.

[165]B.S. Raghavendra, D. Narayana Dutt, A note on fractal dimensions of biomedical waveforms, Comput Biol Med 39 (2009) 1006–1012. https://doi.org/10.1016/j.compbiomed.2009.08.001.

[166]R. Esteller, G. Vachtsevanos, J. Echauz, B. Litt, A comparison of waveform fractal dimension algorithms, IEEE Trans. Circuits Syst. I 48 (2001) 177–183. https://doi.org/10.1109/81.904882.

[167]L. Rankine, N. Stevenson, M. Mesbah, B. Boashash, A nonstationary model of newborn EEG, IEEE Trans Biomed Eng 54 (2007) 19–28. https://doi.org/10.1109/TBME.2006.886667.

[168]I. Ahmed, N. Sasikumar, Echocardiography Imaging Techniques, in: StatPearls, StatPearls Publishing, Treasure Island (FL), 2025. http://www.ncbi.nlm.nih.gov/books/NBK572130/ (accessed June 13, 2025).

[169]Ecocardiografia - Disturbi dell'apparato cardiovascolare, Manuali MSD Edizione Professionisti (n.d.). https://www.msdmanuals.com/it/professionale/disturbi-dell-apparato-cardiovascolare/esami-e-procedure-cardiovascolari/ecocardiografia (accessed June 13, 2025).

[170]S. Mondillo, M. Galderisi, D. Mele, M. Cameli, V.S. Lomoriello, V. Zacà, P. Ballo, A. D'Andrea, D. Muraru, M. Losi, E. Agricola, A. D'Errico, S. Buralli, S. Sciomer, S. Nistri, L. Badano,

Echocardiography Study Group Of The Italian Society Of Cardiology (Rome, Italy), Speckle-tracking echocardiography: a new technique for assessing myocardial function, J Ultrasound Med 30 (2011) 71–83. https://doi.org/10.7863/jum.2011.30.1.71.

[171]S. Cimino, E. Canali, V. Petronilli, F. Cicogna, L. De Luca, M. Francone, G. Sardella, C. Iacoboni, L. Agati, Global and regional longitudinal strain assessed by two-dimensional speckle tracking echocardiography identifies early myocardial dysfunction and transmural extent of myocardial scar in patients with acute ST elevation myocardial infarction and relatively preserved LV function, European Heart Journal - Cardiovascular Imaging 14 (2013) 805–811. https://doi.org/10.1093/ehjci/jes295.

[172]T.A. Foley, S.V. Mankad, N.S. Anavekar, C.R. Bonnichsen, M.F. Morris, T.D. Miller, P.A. Araoz, Measuring Left Ventricular Ejection Fraction - Techniques and Potential Pitfalls, (2012). https://www.ecrjournal.com/articles/measuring-left-ventricular-ejection-fraction-techniques-and-potential-pitfalls?language_content_entity=en (accessed May 28, 2025).

[173]J.E. Otterstad, Measuring left ventricular volume and ejection fraction with the biplane Simpson's method, Heart 88 (2002) 559–560. https://doi.org/10.1136/heart.88.6.559.

[174]J.-U. Voigt, G. Pedrizzetti, P. Lysyansky, T.H. Marwick, H. Houle, R. Baumann, S. Pedri, Y. Ito, Y. Abe, S. Metz, J.H. Song, J. Hamilton, P.P. Sengupta, T.J. Kolias, J. d'Hooge, G.P. Aurigemma, J.D. Thomas, L.P. Badano, Definitions for a common standard for 2D speckle tracking echocardiography: consensus document of the EACVI/ASE/Industry Task Force to standardize deformation imaging, Eur Heart J Cardiovasc Imaging 16 (2015) 1–11. https://doi.org/10.1093/ehjci/jeu184.

[175]M. Wintermark, R. Sincic, D. Sridhar, J.D. Chien, Cerebral perfusion CT: technique and clinical applications, J Neuroradiol 35 (2008) 253–260. https://doi.org/10.1016/j.neurad.2008.03.005.

[176]A.A. Konstas, G.V. Goldmakher, T.-Y. Lee, M.H. Lev, Theoretic basis and technical implementations of CT perfusion in acute ischemic stroke, part 1: Theoretic basis, AJNR Am J Neuroradiol 30 (2009) 662–668. https://doi.org/10.3174/ajnr.A1487.

[177]J. Demeestere, A. Wouters, S. Christensen, R. Lemmens, M.G. Lansberg, Review of Perfusion Imaging in Acute Ischemic Stroke: From Time to Tissue, Stroke 51 (2020) 1017–1024. https://doi.org/10.1161/STROKEAHA.119.028337.

[178]A.A. Konstas, G.V. Goldmakher, T.-Y. Lee, M.H. Lev, Theoretic basis and technical implementations of CT perfusion in acute ischemic stroke, part 2: technical implementations, AJNR Am J Neuroradiol 30 (2009) 885–892. https://doi.org/10.3174/ajnr.A1492.

[179]Frontiers | Quantitative functional imaging with CT perfusion: technical considerations, kinetic modeling, and applications, (n.d.). https://www.frontiersin.org/journals/physics/articles/10.3389/fphy.2023.1246973/full (accessed June 13, 2025).

[180]Deconvolution-Based CT and MR Brain Perfusion Measurement: Theoretical Model Revisited and Practical Implementation Details - Fieselmann - 2011 - International Journal of Biomedical Imaging - Wiley Online Library, (n.d.). https://onlinelibrary.wiley.com/doi/10.1155/2011/467563 (accessed June 13, 2025).

[181]C. Baumgartner, K. Gautsch, C. Böhm, S. Felber, Functional Cluster Analysis of CT Perfusion Maps: A New Tool for Diagnosis of Acute Stroke?, J Digit Imaging 18 (2005) 219–226. https://doi.org/10.1007/s10278-004-1048-9.

[182]K.J. Chung, D. De Sarno, T.-Y. Lee, CT perfusion stroke lesion threshold calibration

between deconvolution algorithms, Sci Rep 13 (2023) 21458. https://doi.org/10.1038/s41598-023-48700-6.

[183]A. Alsaedi, D. Thomas, S. Bisdas, X. Golay, Overview and Critical Appraisal of Arterial Spin Labelling Technique in Brain Perfusion Imaging, Contrast Media Mol Imaging 2018 (2018) 5360375. https://doi.org/10.1155/2018/5360375.

[184]M.A. Chappell, A.R. Groves, B. Whitcher, M.W. Woolrich, Variational Bayesian Inference for a Nonlinear Forward Model, IEEE Transactions on Signal Processing 57 (2009) 223–236. https://doi.org/10.1109/TSP.2008.2005752.

[185]A.R. Groves, M.A. Chappell, M.W. Woolrich, Combined spatial and non-spatial prior for inference on MRI time-series, Neuroimage 45 (2009) 795–809. https://doi.org/10.1016/j.neuroimage.2008.12.027.

[186]R.B. Buxton, L.R. Frank, E.C. Wong, B. Siewert, S. Warach, R.R. Edelman, A general kinetic model for quantitative perfusion imaging with arterial spin labeling, Magn Reson Med 40 (1998) 383–396. https://doi.org/10.1002/mrm.1910400308.

[187]D.C. Alsop, J.A. Detre, X. Golay, M. Günther, J. Hendrikse, L. Hernandez-Garcia, H. Lu, B.J. MacIntosh, L.M. Parkes, M. Smits, M.J.P. van Osch, D.J.J. Wang, E.C. Wong, G. Zaharchuk, Recommended implementation of arterial spin-labeled perfusion MRI for clinical applications: A consensus of the ISMRM perfusion study group and the European consortium for ASL in dementia, Magn Reson Med 73 (2015) 102–116. https://doi.org/10.1002/mrm.25197.

[188]M.A. Chappell, A.R. Groves, B.J. MacIntosh, M.J. Donahue, P. Jezzard, M.W. Woolrich, Partial volume correction of multiple inversion time arterial spin labeling MRI data, Magn Reson Med 65 (2011) 1173–1183. https://doi.org/10.1002/mrm.22641.

[189]A. Ferraioli, Manuale di ingegneria biomedicale - Dispositivi medici, normative, apparecchiature elettromedicali e nozioni fondamentali: Una guida completa per gli addetti ai lavori, per gli studenti di ingegneria Biomedica e per tecnici Biomedici, Dario Flaccovio Editore, 2020.

[190]Y. Sun, C. Wei, V. Cui, M. Xiu, A. Wu, Electroencephalography: Clinical Applications During the Perioperative Period, Front Med (Lausanne) 7 (2020) 251. https://doi.org/10.3389/fmed.2020.00251.

[191]J.S. Kumar, P. Bhuvaneswari, Analysis of Electroencephalography (EEG) Signals and Its Categorization–A Study, Procedia Engineering 38 (2012) 2525–2536. https://doi.org/10.1016/j.proeng.2012.06.298.

[192]L. Breiman, J.H. Friedman, R.A. Olshen, C.J. Stone, Classification And Regression Trees, Routledge, Boca Raton, 1984. https://doi.org/10.1201/9781315139470.

[193]I. Rish, An empirical study of the naive Bayes classifier, in: IJCAI 2001 Workshop on Empirical Methods in Artificial Intelligence, 2001: pp. 41–46.

[194]A. Urso, A. Fiannaca, M. La Rosa, V. Ravì, R. Rizzo, Data Mining: Prediction Methods, in: S. Ranganathan, M. Gribskov, K. Nakai, C. Schönbach (Eds.), Encyclopedia of Bioinformatics and Computational Biology, Academic Press, Oxford, 2019: pp. 413–430. https://doi.org/10.1016/B978-0-12-809633-8.20462-7.

[195]A.D.Dongare, R.R.Kharde, A. D.Kachare, Introduction to Artificial Neural Network, in: 2012. https://www.semanticscholar.org/paper/Introduction-to-Artificial-Neural-Network-A.D.Dongare-R.R.Kharde/04d0b6952a4f0c7203577afc9476c2fcab2cba06 (accessed May 13, 2024).

[196]C.M. Bishop, Neural Networks for Pattern Recognition, Clarendon Press, 1995.

[197]Tutorial On Support Vector Machine (SVM): Abstract | PDF, Scribd (n.d.). https://www.scribd.com/doc/184091412/SVMTutorial-doc (accessed May 13, 2024).

[198]C.-C. Chang, C.-J. Lin, LIBSVM: A library for support vector machines, ACM Trans. Intell. Syst. Technol. 2 (2011) 27:1-27:27. https://doi.org/10.1145/1961189.1961199.

[199]J. Demšar, T. Curk, A. Erjavec, Č. Gorup, T. Hočevar, M. Milutinovič, M. Možina, M. Polajnar, M. Toplak, A. Starič, M. Štajdohar, L. Umek, L. Žagar, J. Žbontar, M. Žitnik, B. Zupan, Orange: Data Mining Toolbox in Python, Journal of Machine Learning Research 14 (2013) 2349–2353.

[200]S. Lei, A Feature Selection Method Based on Information Gain and Genetic Algorithm, in: 2012 International Conference on Computer Science and Electronics Engineering, 2012: pp. 355–358. https://doi.org/10.1109/ICCSEE.2012.97.

[201]J. Gao, Z. Wang, T. Jin, J. Cheng, Z. Lei, S. Gao, Information gain ratio-based subfeature grouping empowers particle swarm optimization for feature selection, Knowledge-Based Systems 286 (2024) 111380. https://doi.org/10.1016/j.knosys.2024.111380.

[202]I. Kononenko, E. Šimec, M. Robnik-Sikonja, Overcoming the Myopia of Inductive Learning Algorithms with RELIEFF, Applied Intelligence 7 (1997) 39–55. https://doi.org/10.1023/A:1008280620621.

[203]J. Lubsen, J. Pool, E. van der Does, A practical device for the application of a diagnostic or prognostic function, Methods Inf Med 17 (1978) 127–129.

[204]M. Možina, J. Demšar, M. Kattan, B. Zupan, Nomograms for Visualization of Naive Bayesian Classifier, in: J.-F. Boulicaut, F. Esposito, F. Giannotti, D. Pedreschi (Eds.), Knowledge Discovery in Databases: PKDD 2004, Springer, Berlin, Heidelberg, 2004: pp. 337–348. https://doi.org/10.1007/978-3-540-30116-5_32.

[205]Nomogram — Orange Documentation v2.7.8, (n.d.). https://docs.biolab.si/orange/2/widgets/rst/classify/nomogram.html (accessed April 1, 2022).

[206]K. Iscra, A. Miladinović, M. Ajcevic, L. Restivo, S. Kresevic, M. Merlo, G. Sinagra, A. Accardo, Does Ectopic Beats Bring More Discriminatory Information to Diagnose Ischemic Heart Disease?, (2022). https://doi.org/10.22489/cinc.2022.199.

[207]K. Iscra, A. Miladinović, M. Ajčević, S. Starita, L. Restivo, M. Merlo, A. Accardo, Interpretable machine learning models to support differential diagnosis between Ischemic Heart Disease and Dilated Cardiomyopathy, Procedia Computer Science 207 (2022) 1378–1387. https://doi.org/10.1016/j.procs.2022.09.194.

[208]K. Iscra, A. Miladinović, M. Ajčević, L. Munaretto, J.G. Rizzi, M. Merlo, A. Accardo, Discriminatory power of Global Longitudinal Strain and Left Ventricular Ejection Fraction for Identification of Dilated Cardiomyopathy, Convegno Nazionale Di Bioingegneria (2023). https://www.scopus.com/inward/record.uri?eid=2-s2.0-85175809429&partnerID=40&md5=6a64d2b79e35c49f1acaf68828e9af80.

[209]K. Iscra, M. Ajčević, A. Miladinović, L. Munaretto, J. Rizzi, M. Merlo, A. Accardo, Interpretable Model to Support Differential Diagnosis Between Ischemic Heart Disease, Dilated Cardiomyopathy and Healthy Subjects, in: 2023: pp. 343–349. https://doi.org/10.1007/978-3-031-37132-5_43.

[210]K. Iscra, M. Ajčević, A. Miladinović, L. Munaretto, J.G. Rizzi, M. Merlo, A. Agostino, Development of an Interpretable Model for Improving Differential Diagnosis in Subjects with a Left

Ventricular Ejection Fraction Ranging from 40 to 55%, in: A. Badnjević, L. Gurbeta Pokvić (Eds.), MEDICON'23 and CMBEBIH'23, Springer Nature Switzerland, Cham, 2024: pp. 41–48. https://doi.org/10.1007/978-3-031-49062-0_5.

[211] K. Iscra, L. Munaretto, J. Rizzi, A. Miladinović, M. Zecchin, L. Dalla Libera, C. Baggio, A. Accardo, G. Sinagra, M. Ajčević, M. Merlo. (2025) enhancing differential diagnosis of ihd and dcm using interpretable machine learning in mildly reduced ejection fraction, Accepted to Journal of Cardiovascular Medicine

[212]K. Sroka, On the genesis of myocardial ischemia, Z Kardiol 93 (2004) 768–783. https://doi.org/10.1007/s00392-004-0137-6.

[213]A. Accardo, G. Silveri, M. Ajčević, A. Miladinović, L. Pascazio, Influence of smoking and other cardiovascular risk factors on heart rate circadian rhythm in normotensive and hypertensive subjects, PLOS ONE 16 (2021) e0257660. https://doi.org/10.1371/journal.pone.0257660.

[214]B. Singh, D. Singh, A.K. Jaryal, K.K. Deepak, Ectopic beats in approximate entropy and sample entropy-based HRV assessment, International Journal of Systems Science 43 (2012) 884–893. https://doi.org/10.1080/00207721.2010.543478.

[215]P. Albrecht, R.J. Cohen, Estimation of heart rate power spectrum bands from real-world data: dealing with ectopic beats and noisy data, in: Proceedings. Computers in Cardiology 1988, 1988: pp. 311–314. https://doi.org/10.1109/CIC.1988.72624.

[216]N. Lippman, K.M. Stein, B.B. Lerman, Comparison of methods for removal of ectopy in measurement of heart rate variability, Am J Physiol 267 (1994) H411-418. https://doi.org/10.1152/ajpheart.1994.267.1.H411.

[217]J. Mateo, P. Laguna, Analysis of heart rate variability in the presence of ectopic beats using the heart timing signal, IEEE Trans Biomed Eng 50 (2003) 334–343. https://doi.org/10.1109/TBME.2003.808831.

[218]S.M. Al-Khatib, W.G. Stevenson, M.J. Ackerman, W.J. Bryant, D.J. Callans, A.B. Curtis, B.J. Deal, T. Dickfeld, M.E. Field, G.C. Fonarow, A.M. Gillis, C.B. Granger, S.C. Hammill, M.A. Hlatky, J.A. Joglar, G.N. Kay, D.D. Matlock, R.J. Myerburg, R.L. Page, 2017 AHA/ACC/HRS Guideline for Management of Patients With Ventricular Arrhythmias and the Prevention of Sudden Cardiac Death: Executive Summary, Circulation 138 (2018) e210–e271. https://doi.org/10.1161/CIR.0000000000000548.

[219]A. Accardo, G. Silveri, M. Merlo, L. Restivo, M. Ajčević, G. Sinagra, Detection of subjects with ischemic heart disease by using machine learning technique based on heart rate total variability parameters, Physiol Meas (2020). https://doi.org/10.1088/1361-6579/abc321.

[220]J.T. Korpelainen, K.A. Sotaniemi, A. Mäkikallio, H.V. Huikuri, V.V. Myllylä, Dynamic Behavior of Heart Rate in Ischemic Stroke, Stroke 30 (1999) 1008–1013. https://doi.org/10.1161/01.STR.30.5.1008.

[221]H.V. Huikuri, T.H. Mäkikallio, Heart rate variability in ischemic heart disease, Auton Neurosci 90 (2001) 95–101. https://doi.org/10.1016/S1566-0702(01)00273-9.

[222]E. Agliari, A. Barra, O.A. Barra, A. Fachechi, L. Franceschi Vento, L. Moretti, Detecting cardiac pathologies via machine learning on heart-rate variability time series and related markers, Sci Rep 10 (2020) 8845. https://doi.org/10.1038/s41598-020-64083-4.

[223]M. Jiménez-Blanco, D. Cordero, J.L. Zamorano, Left ventricular ejection fraction… What else?, Cardiol J 27 (2020) 6–7. https://doi.org/10.5603/CJ.2020.0014.

[224]W.-T. Chang, C.H. Lin, C.-S. Hong, C.-T. Liao, Y.-W. Liu, Z.-C. Chen, J.-Y. Shih, The predictive value of global longitudinal strain in patients with heart failure mid-range ejection fraction, Journal of Cardiology 77 (2021) 509–516. https://doi.org/10.1016/j.jjcc.2020.10.018.

[225]N. D'Elia, S. Caselli, W. Kosmala, P. Lancellotti, D. Morris, D. Muraru, M. Takeuchi, A. van den Bosch, R.W.J. van Grootel, H. Villarraga, T.H. Marwick, Normal Global Longitudinal Strain: An Individual Patient Meta-Analysis, JACC Cardiovasc Imaging 13 (2020) 167–169. https://doi.org/10.1016/j.jcmg.2019.07.020.

[226]E. Potter, T.H. Marwick, Assessment of Left Ventricular Function by Echocardiography: The Case for Routinely Adding Global Longitudinal Strain to Ejection Fraction, JACC: Cardiovascular Imaging 11 (2018) 260–274. https://doi.org/10.1016/j.jcmg.2017.11.017.

[227]E. Arbelo, A. Protonotarios, J.R. Gimeno, E. Arbustini, R. Barriales-Villa, C. Basso, C.R. Bezzina, E. Biagini, N.A. Blom, R.A. de Boer, T. De Winter, P.M. Elliott, M. Flather, P. Garcia-Pavia, K.H. Haugaa, J. Ingles, R.O. Jurcut, S. Klaassen, G. Limongelli, B. Loeys, J. Mogensen, I. Olivotto, A. Pantazis, S. Sharma, J.P. Van Tintelen, J.S. Ware, J.P. Kaski, ESC Scientific Document Group, 2023 ESC Guidelines for the management of cardiomyopathies, Eur Heart J 44 (2023) 3503–3626. https://doi.org/10.1093/eurheartj/ehad194.

[228]S.S. Virani, L.K. Newby, S.V. Arnold, V. Bittner, L.C. Brewer, S.H. Demeter, D.L. Dixon, W.F. Fearon, B. Hess, H.M. Johnson, D.S. Kazi, D. Kolte, D.J. Kumbhani, J. LoFaso, D. Mahtta, D.B. Mark, M. Minissian, A.M. Navar, A.R. Patel, M.R. Piano, F. Rodriguez, A.W. Talbot, V.R. Taqueti, R.J. Thomas, S. van Diepen, B. Wiggins, M.S. Williams, Peer Review Committee Members, 2023 AHA/ACC/ACCP/ASPC/NLA/PCNA Guideline for the Management of Patients With Chronic Coronary Disease: A Report of the American Heart Association/American College of Cardiology Joint Committee on Clinical Practice Guidelines, Circulation 148 (2023) e9–e119. https://doi.org/10.1161/CIR.0000000000001168.

[229]A.A.M. Mohamed Abdalgaleel Mohamed, Role of Speckle Tracking Echocardiography in Differentiating between Ischemic and Non-ischemic Cardiomyopathy, (2024). https://doi.org/10.4274/ijca.2023.18209.

[230]J. Vietheer, L. Lehmann, C. Unbehaun, U. Fischer-Rasokat, J.S. Wolter, S. Kriechbaum, M. Weferling, B. von Jeinsen, A. Hain, C. Liebetrau, C.W. Hamm, T. Keller, A. Rolf, CMR-derived myocardial strain analysis differentiates ischemic and dilated cardiomyopathy-a propensity score-matched study, Int J Cardiovasc Imaging 38 (2022) 863–872. https://doi.org/10.1007/s10554-021-02469-9.

[231]S. Romano, R.M. Judd, R.J. Kim, H.W. Kim, I. Klem, J.F. Heitner, D.J. Shah, J. Jue, B.E. White, R. Indorkar, C. Shenoy, -Far Afshin Farzaneh, Feature-Tracking Global Longitudinal Strain Predicts Death in a Multicenter Population of Patients With Ischemic and Nonischemic Dilated Cardiomyopathy Incremental to Ejection Fraction and Late Gadolinium Enhancement, JACC: Cardiovascular Imaging 11 (2018) 1419–1429. https://doi.org/10.1016/j.jcmg.2017.10.024.

[232]A. Faggiano, C. Avallone, D. Gentile, G. Provenzale, F. Toriello, M. Merlo, G. Sinagra, S. Carugo, Echocardiographic Advances in Dilated Cardiomyopathy, J Clin Med 10 (2021) 5518. https://doi.org/10.3390/jcm10235518.

[233]O.A. Smiseth, O. Rider, M. Cvijic, L. Valkovič, E.W. Remme, J.-U. Voigt, Myocardial Strain Imaging: Theory, Current Practice, and the Future, JACC Cardiovasc Imaging (2024) S1936-878X(24)00301–2. https://doi.org/10.1016/j.jcmg.2024.07.011.

[234]P. Collier, D. Phelan, A. Klein, A Test in Context: Myocardial Strain Measured by Speckle-Tracking Echocardiography, J Am Coll Cardiol 69 (2017) 1043–1056.

https://doi.org/10.1016/j.jacc.2016.12.012.

[235]M. Ng, H. Ae, P. M, G. Y, S. I, W. Je, M. Mm, H. Hv, M. Wj, Fractal correlation properties of R-R interval dynamics in asymptomatic relatives of patients with dilated cardiomyopathy, European Journal of Heart Failure 4 (2002). https://doi.org/10.1016/s1388-9842(01)00227-6.

[236]G. Krstacic, A. Krstacic, A. Smalcelj, D. Milicic, M. Jembrek-Gostovic, The “Chaos Theory” and nonlinear dynamics in heart rate variability analysis: does it work in short-time series in patients with coronary heart disease?, Ann Noninvasive Electrocardiol 12 (2007) 130–136. https://doi.org/10.1111/j.1542-474X.2007.00151.x.

[237]A. Voss, R. Schroeder, S. Truebner, M. Goernig, H.R. Figulla, A. Schirdewan, Comparison of nonlinear methods symbolic dynamics, detrended fluctuation, and Poincare plot analysis in risk stratification in patients with dilated cardiomyopathy, Chaos 17 (2007) 015120. https://doi.org/10.1063/1.2404633.

[238]P. van de Borne, N. Montano, M. Pagani, R. Oren, V.K. Somers, Absence of low-frequency variability of sympathetic nerve activity in severe heart failure, Circulation 95 (1997) 1449–1454. https://doi.org/10.1161/01.cir.95.6.1449.

[239]D. Noronha Osório, R. Viana-Soares, J.P. Marto, M.D. Mendonça, H.P. Silva, C. Quaresma, M. Viana-Baptista, H. Gamboa, H.L.A. Vieira, Autonomic nervous system response to remote ischemic conditioning: heart rate variability assessment, BMC Cardiovasc Disord 19 (2019) 211. https://doi.org/10.1186/s12872-019-1181-5.

[240]P. Ponikowski, S.D. Anker, T.P. Chua, R. Szelemej, M. Piepoli, S. Adamopoulos, K. Webb-Peploe, D. Harrington, W. Banasiak, K. Wrabec, A.J. Coats, Depressed heart rate variability as an independent predictor of death in chronic congestive heart failure secondary to ischemic or idiopathic dilated cardiomyopathy, Am J Cardiol 79 (1997) 1645–1650. https://doi.org/10.1016/s0002-9149(97)00215-4.

[241]G. Silveri, M. Merlo, L. Restivo, M. Ajčević, G. Sinagra, A. Accardo, A big - data classification tree for decision support system in the detection of dilated cardiomyopathy using heart rate variability, Procedia Computer Science 176 (2020) 2940–2948. https://doi.org/10.1016/j.procs.2020.09.209.

[242]S. Bm, van V. Dj, van der V. N, B. J, D.G. Pa, C. Hj, Prognostic value of heart rate variability in chronic congestive heart failure secondary to idiopathic or ischemic dilated cardiomyopathy, The American Journal of Cardiology 79 (1997). https://doi.org/10.1016/s0002-9149(97)00026-x.

[243]K. Iscra, E. Ricci, A. Bonini, G. Furlanis, M. Malesani, P. Caruso, M. Naccarato, P. Manganotti, A. Accardo, M. Ajčević, Prognostic Value of Early Interictal Epileptiform EEG Patterns in Ischemic Stroke: A Predictive Model for Functional Outcomes, in: P. Ladyzynski, D.G. Pijanowska, A. Liebert (Eds.), Joint 20th Nordic-Baltic Conference on Biomedical Engineering & 24th Polish Conference on Biocybernetics and Biomedical Engineering, Springer Nature Switzerland, Cham, 2025: pp. 403–411. https://doi.org/10.1007/978-3-031-96538-8_34.

[244]K. Iscra, A. Biscontin, A. Miladinovic, A. Bonini, G. Furlanis, G. Prandin, M. Malesani, M. Naccarato, P. Manganotti, A. Accardo, M. Ajčević, Optimizing machine learning models for classification of stroke patients with epileptiform EEG pattern: the impact of dataset balancing techniques, Procedia Computer Science 246 (2024) 4600–4609. https://doi.org/10.1016/j.procs.2024.09.324.

[245]D. Rajashekar, M.D. Hill, A.M. Demchuk, M. Goyal, J. Fiehler, N.D. Forkert, Prediction

of Clinical Outcomes in Acute Ischaemic Stroke Patients: A Comparative Study, Front Neurol 12 (2021) 663899. https://doi.org/10.3389/fneur.2021.663899.

[246]P.W. Duncan, H.S. Jorgensen, D.T. Wade, Outcome measures in acute stroke trials: a systematic review and some recommendations to improve practice, Stroke 31 (2000) 1429–1438. https://doi.org/10.1161/01.str.31.6.1429.

[247]C. Bentes, A.R. Peralta, P. Viana, H. Martins, C. Morgado, C. Casimiro, A.C. Franco, A.C. Fonseca, R. Geraldes, P. Canhão, T. Pinho E Melo, T. Paiva, J.M. Ferro, Quantitative EEG and functional outcome following acute ischemic stroke, Clin Neurophysiol 129 (2018) 1680–1687. https://doi.org/10.1016/j.clinph.2018.05.021.

[248]L. Stragapede, G. Furlanis, M. Ajčević, M. Ridolfi, P. Caruso, M. Naccarato, M. Ukmar, P. Manganotti, Brain oscillatory activity and CT perfusion in hyper-acute ischemic stroke, J Clin Neurosci 69 (2019) 184–189. https://doi.org/10.1016/j.jocn.2019.07.068.

[249]L.J. Hirsch, M.W.K. Fong, M. Leitinger, S.M. LaRoche, S. Beniczky, N.S. Abend, J.W. Lee, C.J. Wusthoff, C.D. Hahn, M.B. Westover, E.E. Gerard, S.T. Herman, H.A. Haider, G. Osman, A. Rodriguez-Ruiz, C.B. Maciel, E.J. Gilmore, A. Fernandez, E.S. Rosenthal, J. Claassen, A.M. Husain, J.Y. Yoo, E.L. So, P.W. Kaplan, M.R. Nuwer, M. van Putten, R. Sutter, F.W. Drislane, E. Trinka, N. Gaspard, American Clinical Neurophysiology Society's Standardized Critical Care EEG Terminology: 2021 Version, J Clin Neurophysiol 38 (2021) 1–29. https://doi.org/10.1097/WNP.0000000000000806.

[250]A.F. Struck, M.B. Westover, L.T. Hall, G.M. Deck, A.J. Cole, E.S. Rosenthal, Metabolic Correlates of the Ictal-Interictal Continuum: FDG-PET During Continuous EEG, Neurocrit Care 24 (2016) 324–331. https://doi.org/10.1007/s12028-016-0245-y.

[251]T.J. Quinn, M. Taylor-Rowan, A. Coyte, A.B. Clark, S.D. Musgrave, A.K. Metcalf, D.J. Day, M.O. Bachmann, E.A. Warburton, J.F. Potter, P.K. Myint, Pre-Stroke Modified Rankin Scale: Evaluation of Validity, Prognostic Accuracy, and Association with Treatment, Front Neurol 8 (2017) 275. https://doi.org/10.3389/fneur.2017.00275.

[252]F.O. Lima, J.A.G. Ricardo, A.C. Coan, D.C. Soriano, W.M. Avelar, L.L. Min, Electroencephalography Patterns and Prognosis in Acute Ischemic Stroke, Cerebrovasc Dis 44 (2017) 128–134. https://doi.org/10.1159/000477674.

[253]M.S. Kim, An Effective Under-Sampling Method for Class Imbalance Data Problem, 한국지능시스템학회 국제학술대회 발표논문집 (2007) 825–829.

[254]Cluster-based majority under-sampling approaches for class imbalance learning | IEEE Conference Publication | IEEE Xplore, (n.d.). https://ieeexplore.ieee.org/document/5609385 (accessed May 13, 2024).

[255]N.V. Chawla, K.W. Bowyer, L.O. Hall, W.P. Kegelmeyer, SMOTE: Synthetic Minority Over-sampling Technique, Jair 16 (2002) 321–357. https://doi.org/10.1613/jair.953.

[256]A. Kasem, A. Ammar Ghaibeh, H. Moriguchi, Empirical Study of Sampling Methods for Classification in Imbalanced Clinical Datasets, in: S. Phon-Amnuaisuk, T.-W. Au, S. Omar (Eds.), Computational Intelligence in Information Systems, Springer International Publishing, Cham, 2017: pp. 152–162. https://doi.org/10.1007/978-3-319-48517-1_14.

[257]G.E.A.P.A. Batista, R.C. Prati, M.C. Monard, A study of the behavior of several methods for balancing machine learning training data, SIGKDD Explor. Newsl. 6 (2004) 20–29. https://doi.org/10.1145/1007730.1007735.

[258]F. Provost, G.M. Weiss, Learning When Training Data are Costly: The Effect of Class Distribution on Tree Induction, Jair 19 (2003) 315–354. https://doi.org/10.1613/jair.1199.

[259]D.L. Wilson, Asymptotic Properties of Nearest Neighbor Rules Using Edited Data, IEEE Transactions on Systems, Man, and Cybernetics SMC-2 (1972) 408–421. https://doi.org/10.1109/TSMC.1972.4309137.

[260]V. Ganganwar, An overview of classification algorithms for imbalanced datasets, International Journal of Emerging Technology and Advanced Engineering 2 (2012) 42–47.

[261]H. Ali, M.N.M. Salleh, R. Saedudin, K. Hussain, M.F. Mushtaq, Imbalance class problems in data mining: a review, Indonesian Journal of Electrical Engineering and Computer Science 14 (2019) 1552–1563. https://doi.org/10.11591/ijeecs.v14.i3.pp1552-1563.

[262]B.A. Drozdowska, S. Singh, T.J. Quinn, Thinking About the Future: A Review of Prognostic Scales Used in Acute Stroke, Front Neurol 10 (2019) 274. https://doi.org/10.3389/fneur.2019.00274.

[263]S. Hirai, H. Sato, T. Yamamura, K. Kato, M. Ishikawa, H. Sagawa, J. Aoyama, S. Fujii, K. Fujita, T. Arai, K. Sumita, Correlation between the CT Perfusion Parameter Values and Response to Recanalization in Patients with Acute Ischemic Stroke, J Neuroendovasc Ther 16 (2022) 577–585. https://doi.org/10.5797/jnet.oa.2022-0026.

[264]T. G, B. P, F. U, K. P, L. K, M. M, S. Pd, T. D, de V. J, W. P, F. J, European Stroke Organisation (ESO) - European Society for Minimally Invasive Neurological Therapy (ESMINT) Guidelines on Mechanical Thrombectomy in Acute Ischemic Stroke, Journal of Neurointerventional Surgery 15 (2023). https://doi.org/10.1136/neurintsurg-2018-014569.

[265]W. Hacke, M. Kaste, C. Fieschi, R. von Kummer, A. Davalos, D. Meier, V. Larrue, E. Bluhmki, S. Davis, G. Donnan, D. Schneider, E. Diez-Tejedor, P. Trouillas, Randomised double-blind placebo-controlled trial of thrombolytic therapy with intravenous alteplase in acute ischaemic stroke (ECASS II). Second European-Australasian Acute Stroke Study Investigators, Lancet 352 (1998) 1245–1251. https://doi.org/10.1016/s0140-6736(98)08020-9.

[266]G. Mair, E.V. Boyd, F.M. Chappell, R. von Kummer, R.I. Lindley, P. Sandercock, J.M. Wardlaw, IST-3 Collaborative Group, Sensitivity and specificity of the hyperdense artery sign for arterial obstruction in acute ischemic stroke, Stroke 46 (2015) 102–107. https://doi.org/10.1161/STROKEAHA.114.007036.

[267]S. Mehta, N. Vora, R.C. Edgell, H. Allam, A. Alawi, J. Koehne, A. Kumar, E. Feen, S. Cruz-Flores, A. Alshekhlee, Stroke mimics under the drip-and-ship paradigm, J Stroke Cerebrovasc Dis 23 (2014) 844–849. https://doi.org/10.1016/j.jstrokecerebrovasdis.2013.07.012.

[268]J.G. Merino, M. Luby, R.T. Benson, L.A. Davis, A.W. Hsia, L.L. Latour, J.K. Lynch, S. Warach, Predictors of acute stroke mimics in 8187 patients referred to a stroke service, J Stroke Cerebrovasc Dis 22 (2013) e397-403. https://doi.org/10.1016/j.jstrokecerebrovasdis.2013.04.018.

[269]O.Y. Chernyshev, S. Martin-Schild, K.C. Albright, A. Barreto, V. Misra, I. Acosta, J.C. Grotta, S.I. Savitz, Safety of tPA in stroke mimics and neuroimaging-negative cerebral ischemia, Neurology 74 (2010) 1340–1345. https://doi.org/10.1212/WNL.0b013e3181dad5a6.

[270]F. Austein, M. Huhndorf, J. Meyne, H. Laufs, O. Jansen, T. Lindner, Advanced CT for diagnosis of seizure-related stroke mimics, Eur Radiol 28 (2018) 1791–1800. https://doi.org/10.1007/s00330-017-5174-4.

[271]C.-H. Lie, M. Seifert, J. Poggenborg, G.R. Fink, L. Burghaus, Perfusion computer

tomography helps to differentiate seizure and stroke in acute setting, Clin Neurol Neurosurg 113 (2011) 925–927. https://doi.org/10.1016/j.clineuro.2011.06.009.

[272]V.S. Hedna, P.P. Shukla, M.F. Waters, Seizure Mimicking Stroke: Role of CT Perfusion, J Clin Imaging Sci 2 (2012) 32. https://doi.org/10.4103/2156-7514.97728.

[273]M. Ridolfi, A. Granato, P. Polverino, G. Furlanis, M. Ukmar, I. Zorzenon, P. Manganotti, Migrainous aura as stroke-mimic: The role of perfusion-computed tomography, Clin Neurol Neurosurg 166 (2018) 131–135. https://doi.org/10.1016/j.clineuro.2018.01.032.

[274]L. Mbarek, S. Chen, A. Jin, Y. Pan, X. Meng, X. Yang, Z. Xu, Y. Jiang, Y. Wang, Predicting 3-month poor functional outcomes of acute ischemic stroke in young patients using machine learning, Eur J Med Res 29 (2024) 494. https://doi.org/10.1186/s40001-024-02056-3.

[275]K.C. Johnston, A.F. Connors, D.P. Wagner, W.A. Knaus, X. Wang, E.C. Haley, A predictive risk model for outcomes of ischemic stroke, Stroke 31 (2000) 448–455. https://doi.org/10.1161/01.str.31.2.448.

[276]M.S. Jabal, O. Joly, D. Kallmes, G. Harston, A. Rabinstein, T. Huynh, W. Brinjikji, Interpretable Machine Learning Modeling for Ischemic Stroke Outcome Prediction, Front Neurol 13 (2022) 884693. https://doi.org/10.3389/fneur.2022.884693.

[277]F. Alahmari, A Comparison of Resampling Techniques for Medical Data Using Machine Learning, J. Info. Know. Mgmt. 19 (2020) 2040016. https://doi.org/10.1142/S021964922040016X.

[278]R. Mohammed, J. Rawashdeh, M. Abdullah, Machine Learning with Oversampling and Undersampling Techniques: Overview Study and Experimental Results, in: 2020 11th International Conference on Information and Communication Systems (ICICS), 2020: pp. 243–248. https://doi.org/10.1109/ICICS49469.2020.239556.

[279]M. Khushi, K. Shaukat, T.M. Alam, I.A. Hameed, S. Uddin, S. Luo, X. Yang, M.C. Reyes, A Comparative Performance Analysis of Data Resampling Methods on Imbalance Medical Data, IEEE Access 9 (2021) 109960–109975. https://doi.org/10.1109/ACCESS.2021.3102399.

[280]M.V. Ivanova, I. Pappas, B. Inglis, A.L. Pracar, T.J. Herron, J.V. Baldo, A.S. Kayser, M. D'Esposito, N.F. Dronkers, Cerebral perfusion in post-stroke aphasia and its relationship to residual language abilities, Brain Commun 6 (2024) fcad252. https://doi.org/10.1093/braincomms/fcad252.

[281]M. Walenski, Y. Chen, K.A. Litcofsky, D. Caplan, S. Kiran, B. Rapp, T.B. Parrish, C.K. Thompson, Perilesional Perfusion in Chronic Stroke-Induced Aphasia and Its Response to Behavioral Treatment Interventions, Neurobiol Lang (Camb) 3 (2022) 345–363. https://doi.org/10.1162/nol_a_00068.

[282]C.K. Thompson, M. Walenski, Y. Chen, D. Caplan, S. Kiran, B. Rapp, K. Grunewald, M. Nunez, R. Zinbarg, T.B. Parrish, Intrahemispheric Perfusion in Chronic Stroke-Induced Aphasia, Neural Plast 2017 (2017) 2361691. https://doi.org/10.1155/2017/2361691.

[283]I. Boscolo Galazzo, S.F. Storti, A. Del Felice, F.B. Pizzini, C. Arcaro, E. Formaggio, R. Mai, M. Chappell, A. Beltramello, P. Manganotti, Patient-specific detection of cerebral blood flow alterations as assessed by arterial spin labeling in drug-resistant epileptic patients, PLoS One 10 (2015) e0123975. https://doi.org/10.1371/journal.pone.0123975.

[284]L. Sunwoo, T.J. Yun, S.-H. You, R.-E. Yoo, K.M. Kang, S.H. Choi, J.-H. Kim, C.-H. Sohn, S.-W. Park, C. Jung, C.-K. Park, Differentiation of Glioblastoma from Brain Metastasis: Qualitative and Quantitative Analysis Using Arterial Spin Labeling MR Imaging, PLoS One 11 (2016) e0166662. https://doi.org/10.1371/journal.pone.0166662.

[285]M.-A. Weber, C. Thilmann, M.P. Lichy, M. Günther, S. Delorme, I. Zuna, A. Bongers, L.R. Schad, J. Debus, H.-U. Kauczor, M. Essig, H.-P. Schlemmer, Assessment of irradiated brain metastases by means of arterial spin-labeling and dynamic susceptibility-weighted contrast-enhanced perfusion MRI: initial results, Invest Radiol 39 (2004) 277–287. https://doi.org/10.1097/01.rli.0000119195.50515.04.